Technische Universität München
Lehrstuhl für Energiesysteme

Effects of Tars on Solid Oxide Fuel Cells

Michael Maximilian Hauser

Vollständiger Abdruck der von der Fakultät für Maschinenwesen der Technischen Universität München zur Erlangung des akademischen Grades eines

Doktor-Ingenieurs

genehmigten Dissertation.

Vorsitzender:	Prof. Dr.-Ing. Birgit Vogel-Heuser
Prüfer der Dissertation:	1. Prof. Dr.-Ing. Hartmut Spliethoff
	2. Hon.-Prof. Dr.-Ing. Norbert H. Menzler

Die Dissertation wurde am 01.10.2020 bei der Technischen Universität München eingereicht und durch die Fakultät für Maschinenwesen am 02.02.2021 angenommen.

Danksagung

Diese Dissertation entstand während meiner Tätigkeit als wissenschaftlicher Mitarbeiter am Lehrstuhl für Energiesysteme der Technischen Universität München. Neben den excellenten Arbeitsbedingungen haben viele herausragende Menschen zum Gelingen dieser Arbeit beigetragen. Letzteren möchte ich an dieser Stelle meinen Dank aussprechen.

Meinem Doktorvater Prof. Dr.-Ing. Harmut Spliethoff danke ich für Möglichkeit zu promovieren und für die Freiheit, die man an seinem Lehrstuhl bei der Umsetzung von Forschungsvorhaben genießt. Für die Finanzierung des Projekts, auf dem diese Doktorarbeit basiert, danke ich der Deutschen Forschungsgemeinschaft.

Besonderer Dank gilt meinem "Vorgänger" Stephan Herrmann, welcher sehr viel Inspiration zu dieser Arbeit geliefert hat. Als späterer SOFC-Gruppenleiter konnte ich jederzeit mit seiner Unterstützung bei fachlichen, nicht-fachlichen, administrativen und sonstigen Anliegen rechnen. Selbes gilt für den Leiter der Biomassegruppe, Sebastian Fendt, welchem ich neben meiner Einstellung am LES auch meine Wohnung verdanke. Gleichzeitig möchte ich mich bei allen am SynSOFC-Projekt beteiligten Personen am Forschungszentrum Jülich für die ausgezeichnete Kooperation bedanken, allen voran Hyeondeck "Doc" Jeong, Christian Lenser und Norbert H. Menzler.

Die Technikumsversuche mit Stack und Vergaser wären ohne meine Kollegen Felix Fischer und Maximilian Hauck nicht möglich gewesen, wofür ich beiden zu größtem Dank verpflichtet bin. Meinem Nachfolger Benjamin Steinrücken danke ich dafür, dass SynSOFC bei ihm in den bestmöglichen Händen ist. Allen anderen Kollegen, die den LES zu dem machen was er ist, möchte ich ebenfalls danken. Die Grundstimmung der gegenseitigen Hilfsbereitschaft kann man nicht zu hoch wertschätzen und die vielen gemeinsamen Aktivitäten, ob offizieller oder inoffizieller Art, werde

ich sicherlich sehr vermissen. Meinen Bürokollegen Clemens Griebel und Vincent Dieterich danke ich außerdem für die immer witzige und bei Bedarf konzentrierte Arbeitsatmosphäre.

Während der Zeit am LES habe ich mich nicht nur fachlich, sondern auch musikalisch weiterentwickeln dürfen. Für letzteres möchte ich mich bei allen aktuellen und ehemaligen Mitgliedern der LES-Band bedanken. Ich hoffe, dass die Bandauftritte auch weiterhin ein fester Bestandteil von Sommerfesten und Weihnachtsfeiern bleiben und freue mich darauf, die zukünftigen Hits zu hören.

Ein großer Dank gilt allen Studentinnen und Studenten, die ich während meiner Zeit am LES betreuen durfte und die im Rahmen von Studienarbeiten viel aktiven Input geleistet haben, aber auch ein stetiger Antrieb waren, sich mit Fragestellungen überhaupt zu beschäftigen und Dinge zu hinterfragen und anzupacken.

Ebenso bedanken möchte ich mich bei den Kollegen aus der Werkstatt für die Hilfe bei allen technischen Problemen, sowie bei den Kolleginnen aus dem Sekretariat für die Abwicklung organisatorischer Belangen. Nicht wegzudenken aus dem Lehrstuhlteam ist Athula Rathnayake, der durch seine unbeschwerte bis aggressive Art täglich zur guten Stimmung beträgt. Ich wünsche ihm viel Erfolg für das Hotel und ein schönes Wochenende.

Meinen Eltern und Geschwistern danke ich für den ununterbrochenen und starken Rückhalt seit Beginn meines Lebens. Meiner Mutter danke ich für das gründliche Lektorat dieser Thesis und meiner Paper. Meine Freund*innen von zuhause, aus der Schule und aus dem Studium haben stets für willkommene Ablenkungen vom Arbeitsleben gesorgt, was ihnen allen nicht hoch genug anzurechnen ist. Dem kleinen Janosch danke ich für den Ansporn, die Promotion schnell abzuschließen. Der größte Dank geht an dich, Ursi, dafür dass du nicht zugelassen hast, dass ich zu viel jammere und dass du immer, besonders in den intensiven Phasen der Promotion, für mich da warst.

München, im September 2020

Abstract

The operation of solid oxide fuel cells (SOFCs) with bio-syngas from the gasification of biomass is a promising approach to highly efficient and sustainable power generation. At the same time, the coupling is challenging as several biogenic impurities in the bio-syngas have a negative effect on the anode of the SOFC. In order to be able to further improve SOFCs with regard to their robustness, it is necessary to show the existing weaknesses by means of systematic degradation through model contaminants.

For this thesis the impacts of the tar compounds naphthalene and phenol on anode-supported solid oxide fuel cells were investigated experimentally. Single-cell and short-stack experiments were performed at 700 °C under load with simulated bio-syngas consisting of hydrogen, carbon monoxide, carbon dioxide, methane and water vapour. Naphthalene and phenol showed significantly different negative effects on the performance of the SOFC.

Naphthalene caused a pronounced voltage drop at all applied concentrations. It blocked electrochemical hydrogen oxidation as well as the reforming of methane and the shift of carbon monoxide. Using electrochemical impedance spectroscopy it could be shown that naphthalene initially inhibited mass transport to the three-phase boundaries and later also fuel transport through the anode substrate. The latter effect could be attributed to the absence of hydrogen from the catalytic conversion of methane and carbon monoxide in the anode substrate. The cell voltage increased again when the naphthalene supply was stopped. A complete recovery of performance could be achieved by increasing the operating temperature to 900 °C.

Phenol, on the other hand, led to heavy carbon deposition and irreversibly damaged the structure of the anode substrate. With the exception of the highest dosed

phenol concentrations this form of degradation was not visible in the electrochemical operational data. Metal dusting was identified as the underlying degradation mechanism which is caused by the high solubility of carbon in the nickel grains of substrate and anode.

Keywords: Solid oxide fuel cell, SOFC, naphthalene, phenol, impedance spectroscopy, EIS, metal dusting

Kurzfassung

Der Betrieb von Festoxidbrennstoffzellen (engl. solid oxide fuel cell = SOFC) mit Bio-Syngas aus der Vergasung von Biomasse ist ein vielversprechender Ansatz zur hocheffizienten und nachhaltigen Stromerzeugung. Gleichzeitig ist die Kopplung komplex, da sich diverse biogene Verunreinigungen im Bio-Syngas schädigend auf die Anode der SOFC auswirken. Um SOFCs hinsichtlich ihrer Robustheit weiterentwickeln zu können, ist es notwendig, die bestehenden Schwachstellen durch gezielte Degradation durch Modellverunreinigungen aufzuzeigen.

Im Rahmen dieser Thesis wurden die Auswirkungen der Teerverbindungen Naphthalin und Phenol auf anodengestützte Festoxidbrennstoffzellen experimentell untersucht. Es wurden Einzelzell- und Shortstackversuche bei 700 °C unter Last mit simuliertem Bio-Syngas, bestehend aus Wasserstoff, Kohlenstoffmonoxid, Kohlenstoffdioxid, Methan und Wasserdampf, durchgeführt. Dabei zeigten Naphthalin und Phenol deutlich unterschiedliche negative Auswirkungen auf die Leistung der SOFC.

Naphthalin verursachte bei allen angewendeten Konzentrationen eine ausgeprägte Spannungsabnahme. Es hemmte sowohl die elektrochemische Wasserstoffoxidation als auch die Reformierung von Methan und den Shift von Kohlenstoffmonoxid. Mit Hilfe elektrochemischer Impedanzspektroskopie konnte gezeigt werden, dass Naphthalin zunächst den Stofftransport zu den Dreiphasengrenzen und später auch den Stofftransport von Brenngas durch das Anodensubstrat behinderte. Letzterer Effekt konnte auf den Wegfall von Wasserstoff aus der katalytischen Umsetzung von Methan und Kohlenstoffmonoxid im Anodensubstrat zurückgeführt werden. Die Zellspannung stieg wieder, wenn die Napthalinzufuhr gestoppt wurde. Eine vollständige Wiederherstellung der Leistung konnte durch eine Erhöhung der Betriebstemperatur auf 900 °C erreicht werden.

Phenol führte demgegenüber zu starken Kohlenstoffablagerungen und schädigte die Struktur des Anodensubstrats irreversibel. Außer bei den höchsten dosierten Phenolkonzentrationen war diese Form der Degradation nicht in den elektrochemischen Betriebsdaten zu sehen. Als zugrundliegender Degradationsmechanismus wurde Metal Dusting identifiziert, welches durch die gute Löslichkeit von Kohlenstoff im Nickel von Substrat und Anode hervorgerufen wird.

Schlagwörter: Festoxidbrennstoffzelle, SOFC, Naphthalin, Phenol, Impedanzspektroskopie, EIS, Metal Dusting

As Darwin demonstrated, evolution is not an unremitting race towards perfection. It is a haphazard wander around good enough.

Kelly Clancy, Neuroscientist

Contents

List of Figures

List of Tables

Abbreviations and Nomenclature

Abbreviations:

ASC	anode-supported cell
ASR	area-specific resistance [Ωcm^2]
AU	air utilisation
B-IGFC	biomass integrated gasification fuel cell (system)
BOP	balance of plant
CHP	combined heat and power
CPO(x)	catalytic partial oxidation
DCM	dichloromethane
DECO	direct electrochemical oxidation
DIR	direct internal reforming
DRT	distribution of relaxation times
ECM	equivalent circuit model
EIS	electrochemical impedance spectroscopy
ESC	electrolyte-supported cell
FICFB	fast internal circulating fluid bed (gasifier)
FID	flame ionisation detector
FPS	fuel processing system
FU	fuel utilisation
GDC	gadolinia doped ceria
HF	high frequency
HPH	high point (maximum) of the high frequency arc
HPL	high point (maximum) of the low frequency arc
KK-test	Kramers Kronig test
LES	Lehrstuhl für Energiesysteme = Chair for Energy Systems
LF	low frequency

LHV	lower heating value
LP	low point (minimum) between high and low frequency arc
LSCF	lanthanum strontium cobalt ferrite
LSM / LSMO	lanthanum strontium manganite
NDIR	non-dispersive infra-red absorption
MIEC	mixed-ionic-electronic conductivity
MFC	mass flow controller
MSC	metal-supported cell
Nl	one litre of gas at standard conditions
Nm^3	one cubic meter of gas at standard conditions
OCC	open circuit conditions
OCV	open circuit voltage
PAH	polycyclic aromatic hydrocarbons
PTFE	Polytetrafluoroethylene
SEM	scanning electron microscope
SNG	synthetic natural gas
SOFC	solid oxide fuel cell
SPA	solid phase adsorption (method)
TPA	triple phase area
TPB	triple phase boundary
TEC	coefficient of thermal expansion
TMS	tar mixing station
WLD	thermal conductivity detector
WGS	water gas shift reaction
XRD	x-ray diffraction
YSZ	yttria stabilised zirconia

Latin symbols:

A	cm^2	(cell) area
b	var	(fitting) parameters
c	g/Nm^3	concentration
d	μm	layer thickness
F	C/mol	Faraday constant

f	Hz	frequency (DRT calculation)
g	J/mol	Gibbs free energy
h	J/mol	(reaction) enthalpy
I	A	electric current
i	A/cm^2	current density
i_0	A/cm^2	excitation amplitude
i_{load}	A/cm^2	applied current density
j		imaginary unit
MW	g/mol	molar weight
$\dot{n}$	mol/s	molar flow
n_e	-	number of transferred electrons
p	bar	pressure
R	J/molK	ideal gas constant
R	Ω	resistance
R_0	Ωcm^2	ohmic contribution to ASR (minZ_{real})
R_{pol}	Ωcm^2	polarisation resistance
R_{tot}	Ωcm^2	total ASR $R_0 + R_{\text{pol}}$ (maxZ_{real})
s	J/molK	entropy
T	°C, K	temperature
t	s, min, h	time
U	V	voltage
U_{cell}	V	measured cell voltage
$\dot{V}$	Nl/min	volume flow
$V_{\text{mol,ig}}$	l/mol	volume of 1 mole of ideal gas
y	-	molar share
Z	Ωcm^2	impedance

Greek symbols:

$\gamma(\tau)$	-	distribution function
λ	-	regularisation parameter
ν	-	stoichiometric coefficient
τ	s	relaxation time
ϕ	-	phase shift

ω	Hz	(excitation) frequency

Subscripts and superscripts:

0	standard, ohmic
A	anode
C	cathode
cg	carrier gas
fit	fitted
i	components
imag	imaginary part of $Z\,(=Z'')$
k	index
in	inlet
L	limiting
out	outlet
pol	polarisation
tot	total ($\max Z_{\mathrm{real}}$)
R	reaction
ref	reference
real	real part of $Z\,(=Z')$

Chapter 1

Introduction

Although climate change and sustainable energy supply are currently attracting much public attention, the growth of global energy consumption is apparently unabated. In its world energy outlook 2019 the International Energy Agency (IEA) assumes that electricity demand will have increased by 58 % by 2040 [1]. This trend is driven among other things by a growth of world population combined with globally increasing prosperity, an expansive use of air conditioning and a growing number of data centres [2]. The predicted de-fossilisation of the chemical industry will also require enormous amounts of electricity for the production of hydrogen [3]. In order to cover this additional demand for electricity and reverse the simultaneous increase in CO_2 emissions, the power generation capacity of renewable energies must be expanded drastically. At the same time the way biomass is used for power generation must become much more efficient.

One type of biomass is woody biomass in the form of wood, fast-growing natural resources and wood residues. Most electricity from woody biomass in Germany is currently generated in biomass combustion plants with an output <5 MW [4]. The electrical efficiency of such small plants is very low (20-25 %) [5]. In addition around a quarter of timber harvested in Germany in 2016 was used in private households for space heating and was therefore lost for electricity production [4]. Taking into consideration that the energetic use is in competition with its material use as building material and as raw material for chemical products in bio-refineries, wood and its residues are actually too valuable and scarce to be burned.

1.1 Generation of Bio-Syngas by Gasification of Solid Biomass

Electricity can be generated with a higher degree of efficiency if the biomass is first gasified and the resulting bio-syngas is converted into electricity in gas engines, gas turbines, micro turbines or fuel cells. In addition to wood, wood residues and fast-growing energy crops gasifiers can also work with crop residues, empty fruit bunches or straw [6]. In principle municipal solid waste and plastic waste can also be used as raw materials [7].

Bio-syngas mainly consists of hydrogen (H_2), methane (CH_4), carbon monoxide (CO), carbon dioxide (CO_2), water (H_2O) and nitrogen (N_2). In a gasifier the thermochemical decomposition of lignin and hemi-celluloses takes place with a gasification medium, e.g. air, oxygen, steam or CO_2 at temperatures of 500-1600 °C and pressures up to 50 bar. The composition of the bio-syngas depends on the type of gasifier, the gasification medium and on pressure and temperature. A distinction is made between fixed-bed, fluidised-bed, entrained-flow and plasma gasification. Fixed-bed gasifiers are divided into updraft (biomass and gasification agent in counter-current) and downdraft (biomass and gasification agent in co-current); fluidised-bed gasifiers are divided into stationary and circulating fluidised-bed gasifiers. Due to their endothermic character the gasification reactions depend on a heat source. In autothermal concepts this is provided by the partial combustion of biomass in the gasifier; in allothermal concepts heat is supplied to the gasifier from outside, either by electric heating, combustion of part of the supplied biomass or by using the waste heat from a high-temperature fuel cell. [8, 9]

In addition to the main gas components, the raw bio-syngas contains impurities in the form of particles, sulphur, alkali and chlorine compounds and tars [10–12]. In this context tars are higher hydrocarbons which result from the incomplete conversion of complex biogenic macro-molecules in the gasifier. Depending on the intended use of the bio-syngas, it is necessary to remove the contaminants. Particles in the form of ash and bed material must always be separated with filters or cyclones in order to prevent blockages of downstream equipment.

A successful gasifier concept is the FICFB (fast internal circulating fluid bed) gasifier developed by the University of Vienna, which is operated commercially at several locations in Europe. The FICFB is a two-stage allothermal fluidised-bed gasifier in which the actual gasification takes place in one reactor and heat is generated by burning biomass in a second reactor. Sand plus mineral compounds like dolomite or olivine serve as heat transfer medium and as catalytic fluidised-bed agent. The FICFB plant in Güssing/Austria works with a biomass input of 8 MW (17,000 t/year wood chips) and produces 4.5 MWth and 2 MWel in a gas engine. The bio-syngas contains on average 35-45 vol% of H_2, 20-30 vol% CO, 15-25 vol% CO_2, 8-12 vol% CH_4 and 3-5 vol% N_2, which is representative for steam blown fluidised-bed gasifiers. [13]

There are various arguments in respect to an economically and ecologically reasonable plant size for biomass gasifiers. One approach is that the demand for the operation of the gasifier should be covered exclusively by locally available resources in order to prevent long transport distances. For 8 MW_{th} input as required by the gasifier in Güssing a calculated area of 14 km^2 of rapid turnover plantations would have to be managed or residual wood collected in 160 km^2 of forest[1] [4]. Small plants involve a lower investment risk, and planning and implementation can be carried out more quickly. For large plants with an input of > 100 MW_{th} the specific investment costs are lower which at the same time allows the implementation of additional features helping to increase efficiency. In order to cover the resource input of such a plant it is necessary to import biomass from densely wooded regions. As the area estimate from above shows, the biomass collection area can be so large even for medium-sized plants that biomass imports from another country may be cheaper. In addition to the higher investment risk the planning effort for large gasification plants including the necessary biomass logistics is greater.

As an alternative for the generation of electricity, bio-syngas can also be used for the synthesis of chemicals and fuels [14]. Some experts even demand that available biomass should only be used as a source of carbon and that energetic utilisation should only take place for residues that cannot be used for nutrition or chemical syntheses [15]. Since the chemical industry must also become climate

[1] Gross annual fuel yield in GJ/(ha · a)[4]: 185 (rapid turnover plantations), 15.6 (forest residual wood).

neutral in the decades to come [3] large biomass gasifiers must already be designed as poly-generation plants in which both electricity and chemical products can be co-generated. Small to medium-sized gasification plants are therefore preferable in the current situation: they can be realised more easily due to lower investment costs and can be dismantled if the purely energetic utilisation of biomass is no longer economical.

1.2 Efficient Power Generation from Bio-Syngas in SOFCs

Solid oxide fuel cells (SOFC) are very well suited for the conversion of bio-syngas into electricity. With an exergetic efficiency of up to 90 % the SOFC is currently the most efficient device for power generation [16]. The main advantage over e.g. gas turbines is that SOFCs are very efficient even at small plant sizes [17]. At an operating temperature of 500-1000 °C the chemical energy of the bio-syngas is directly converted into electrical power [18]. Fuel is oxidised at the anode with oxygen. The oxygen is transported from the cathode side through the electrolyte which is conductive for oxygen ions. In contrast to low-temperature fuel cells CO and CH_4 are not poisons here but are also converted into electricity. The high operating temperature of the SOFC allows heat integration with the gasifier and gas cleaning as well as extraction of high temperature heat to external consumers, which increases overall efficiency. Solid oxide cells can be operated reversibly, i.e. by applying electrical current H_2 and CO can be generated from water vapour and CO_2 at high efficiency. Because of this property SOFCs will play an important role in energy storage in the future [19].

The interconnection of gasifier and SOFC is called biomass integrated gasification fuel cell system (B-IGFC). Figure 1.1 shows a simplified flow scheme of such a system. Biomass is fed into the gasifier and the resulting bio-syngas is converted into electricity in the SOFC. In addition to gasifier and SOFC further components are required. Since the SOFC cannot completely convert the fuel, remaining H_2, CO and CH_4 in the anode exhaust gas are after-burnt in a burner with the hot cathode exhaust gas (air). The resulting heat is fed to the gasifier or tar removal

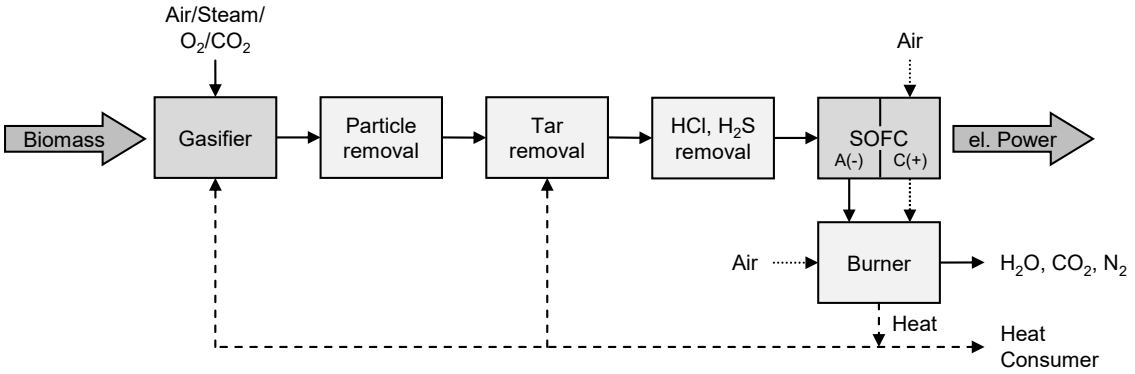

Figure 1.1: Scheme of a B-IGFC. A(-): Anode, C(+): Cathode.

to allow biomass or tar reforming. A very high electrical efficiency of 63 $\%_{\mathrm{LHV}}$ can be achieved at a total exergetic efficiency of 55 % for an optimised interconnection, in which the heat of the post-combustion and a part of the waste heat of the SOFC are introduced into the gasifier via heat pipes and a part of the anode exhaust gas is recycled [20].

1.3 Main Challenge for a B-IGFC System

As already mentioned, the bio-syngas contains various biogenic contaminants that can cause severe damage to the anode of the cells or other equipment of the system. Even at low concentrations in the ppm range H_2S and HCl lower the performance of the SOFC [21] and have to be removed from the bio-syngas. Tars can potentially block catalytic centres for both electrochemical and reforming reactions, inhibit the diffusion of fuel, or lead to mechanical deterioration of the cell [22]. But at the same time they could be reformed at the SOFC anode and serve as a fuel.

The extent of gas cleaning increases the complexity and consequently the costs of the overall system and accordingly the costs of the generated power. Furthermore, additional process steps raise the risk of failure and reduce efficiency. In order to realise economically competitive B-IGFC systems less complex gas cleaning is therefore desirable. Therefore it is critical to make the SOFC itself more resistant

to the influence of contaminants. To achieve this it is necessary to characterise the impact of biogenic contaminants on state-of-the-art SOFCs. With these results as a base the weak spots can be identified and consequently be overcome by adapting anode compositions and microstructure parameters.

Chapter 2

Fundamentals

In this chapter the basics for understanding the results of this thesis are given. In the first section the functional principle of SOFCs, their design and electrochemistry are described. The second section addresses the formation of tars and how they can be handled. In the last section literature regarding the tolerance of SOFCs towards biogenic tars is reviewed.

2.1 Solid Oxide Fuel Cells

In fuel cells the chemical energy of a fuel is directly converted into electrical energy [18]. Compared to thermal power engines the electrical efficiency is higher because it is not limited by the Carnot factor since chemical energy is not converted into thermal energy first. For the same reason no moving parts are necessary which enables low-noise and low-maintenance operation. Since individual SOFCs are interconnected to form stacks and stacks are connected to form larger modules in order to increase the power output, fuel cell systems already provide electrical energy in the kW range with a high degree of efficiency [23].

Like MCFC (molten carbonate fuel cell) SOFCs are among the high-temperature fuel cells. In contrast to low-temperature fuel cells (PEMFC – polymer electrolyte membrane fuel cell, DMFC – direct methanol fuel cell, AFC – alkaline fuel cell, PAFC – phosphoric acid fuel cell), SOFCs can be operated not only on pure hy-

drogen, but also with gases containing CH_4 and CO. The latter can be converted internally to H_2 at SOFC operating temperatures of 500 to 1000 °C by steam-reforming or the water-gas-shift reaction (WGS) [18].

Disadvantages of the high operating temperature are longer start-up times and high mechanical and chemical stress on the materials used at the stack and in the periphery. Reducing the operating temperature is supposed to solve these problems. This is why intense research has been undertaken in the last years to enable so called intermediate temperature SOFCs (IT-SOFC) that can be operated at temperatures between 500 and 750 °C [24, 25].

2.2 Principle of Operation

Figure 2.1 shows on the left the scheme of an SOFC. It is a galvanic element consisting of the air electrode (cathode), the electrolyte, and the fuel electrode (anode). [18]

Air and fuel are continuously fed to the cell where they flow in parallel to cathode and anode and take part in the respective electrode reactions. At the cathode oxygen is reduced to oxygen ions by receiving electrons:

$$\frac{1}{2}O_2 + 2e^- \longleftrightarrow O^{2-}. \tag{2.1}$$

Since the electrolyte is conductive for O^{2-}, the ions are transported to the anode. This material flow is driven by the oxygen partial pressure gradient between cathode and anode, which also determines the cell's potential. The cell potential can be measured in form of the cell voltage. At the anode the ions react exothermically with hydrogen, which is oxidised and releases electrons:

$$H_2 + O^{2-} \longleftrightarrow H_2O + 2e^-. \tag{2.2}$$

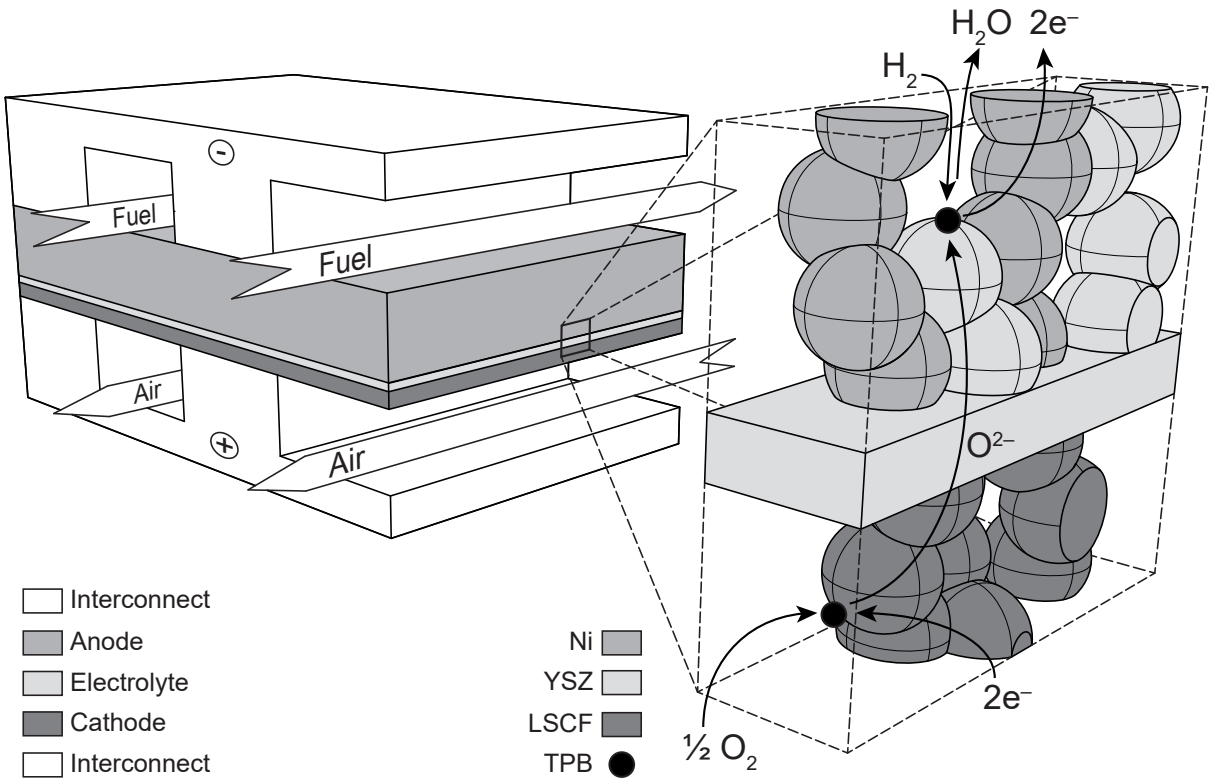

Figure 2.1: Scheme of an SOFC. Zoom on the right shows the schematic structure around the electrolyte for an SOFC with Ni/YSZ anode and LSCF cathode. Exemplary triple phase boundaries (TPB) at anode and cathode and the flow of reaction partners of the electrochemical oxidation of hydrogen (H_2) are indicated.

Addition of equations 2.1 and 2.2 delivers the overall cell reaction:

$$H_2 + \frac{1}{2}O_2 \longleftrightarrow H_2O \qquad \Delta^R h = -241.8\,\mathrm{kJ/mol}. \tag{2.3}$$

The electrons are led back to the cathode via an external circuit, where they in turn participate in the reduction of oxygen. The current flow via the external circuit represents the usable current of the fuel cell. The electrolyte must be gas-tight to prevent a direct reaction of oxygen and fuel, and it must also be electrically insulating so that the electrons only flow through the external circuit.

Oxidation and reduction of fuel and oxygen take place at the interfaces between the gas phase and the electrode material, more precisely at the triple phase boundaries

(TPB)[1]. For the commonly used anode material Ni/YSZ, a mixture of nickel (Ni) and yttrium-stabilised zirconium (YSZ), the three phases involved – Ni, YSZ and gas – and their function are shown in Figure 2.1. Fuel is transported to and reaction products away from the TPB through the gas phase; oxygen ions are transported to the TPB in YSZ; nickel is responsible for the discharge of the electrons released by O^{2-} during electrochemical oxidation at the TPB. As for most heterogeneous catalytic processes the interaction of the mechanisms at the TPB and the influence of material parameters are complex and still not fully understood, even for Ni/YSZ anodes [26].

2.2.1 Functional Layers

Depending on which component of the cell provides mechanical stability SOFC types can be differentiated between anode-supported (ASC) and electrolyte-supported (ESC). In recent years metal-supported cells (MSC) have also been developed to market maturity [27] in which all functional layers are applied to an electrochemically inert porous metal support.

All functional layers should be as thin, inexpensive and easy to produce as possible. In addition, the coefficient of thermal expansion of all layers must be similar in order to minimise stress in the SOFC during temperature changes. All layers can degrade in different ways and thus lead to a decrease in cell performance [21, 28, 29]. The long-term stability of SOFCs is an important research topic as it is crucial for the commercial success of the technology. The maximum tolerable degradation that must be maintained for commercial use in stationary systems is 10 % per 40000 h, i.e. 0.25 %V/1000 h[2] [30]. The following description of the individual layers of an SOFC is largely based on [25, 31, 32].

[1] Electrode materials with mixed-ionic-electronic-conductivity (MIEC) possess triple phase areas (TPA).

[2] Degradation rate is commonly given in %V/1000 h which indicates the percentage decrease of voltage per 1000 hours.

Cathode

The cathode must have a high catalytic activity for the reduction of oxygen. Like any catalyst the cathode microstructure must be porous in order to facilitate mass transport and have a high number of active sites. The cathode material must conduct both ions and electrons; the former in the direction of the electrolyte and the latter from the electrical contact. By optimising the cathode material and its microstructure the performance of SOFC has been significantly improved in recent years while at the same time lowering the operating temperature [33]. Today the state of the art is lanthanum strontium cobalt ferrite (LSCF) as cathode material. Since LSCF forms an insulating $SrZrO_3$ phase with YSZ, a barrier layer of gadolinium doped ceria (GDC) is applied between cathode and electrolyte to prevent interdiffusion between the two layers [34].

Electrolyte

As mentioned before the electrolyte must conduct oxygen ions and at the same time be impermeable to other gases and also act as an electric insulator. The ceramic electrolyte in state-of-the-art cells usually consists of zirconium stabilized with 8 mol% yttrium (8YSZ). The yttrium ensures that a sufficient number of defects are present in the zirconium lattice. This makes the material conductive for oxygen ions which can migrate from defect to defect, driven by the oxygen gradient between cathode and anode. The oxygen ion conductivity of YSZ is strongly temperature and thickness dependent[3]. This is the reason why ESC require higher operating temperatures than ASC since their electrolyte is significantly thicker. To limit the total resistance and lower the operating temperature of the SOFC the electrolyte must be as thin as possible.

Anode and anode support

The requirements for the anode are similar to those for the cathode despite other reactions taking place. It must have a high conductivity for ions and electrons, the

[3]The resistance of YSZ at 600 °C is 10 times higher than at 900 °C. Correlation from [35].

structure must be porous to obtain a high number of TPB and the catalytic activity must be high. Since the atmosphere is reducing during operation but oxidising during production or air ingress during malfunctions, the anode must remain stable even after repeated re-oxidation. In the case of hydrocarbon-containing fuels reforming activity and tolerance to carbon deposits must also be high.

State-of-the-art materials are cermets (ceramic plus metal) made of Ni/YSZ or Ni/GDC. Ni/YSZ cermet is currently the anode material with the best performance and long-term stability [36]. Since the patenting of the Ni-YSZ cermet anode by Spacil 50 years ago [37], this material combination has been continuously optimised. Ni is the electrically conductive component; YSZ provides mechanical stability also during redox-cycles and ensures that the nickel particles remain dispersed even at high temperatures [26]. A disadvantage of the Ni/YSZ anode is the low stability during re-oxidation since nickel oxide takes up more volume than reduced nickel. While Ni is only electrically conductive, GDC is mixed-ion-electron-conductive (MIEC) with a higher ionic conductivity than YSZ. Due to this fact Ni/YSZ anodes have triple phase boundaries where nickel, YSZ and gas phase adjoin each other while Ni/GDC anodes have a triple phase area. This makes Ni/GDC anodes less susceptible to poisoning by adsorbing contaminants such as sulphur. In addition, cerium can probably oxidise hydrocarbons directly. However, GDC is also about 10 times more expensive than Ni [38].

Since the ionic conductivity of YSZ is significantly lower than the electrical conductivity of Ni, the penetration depth of the oxygen ions into the anode is very low [39]. As a consequence electrochemical oxidation mainly takes place near the electrolyte. For a cell with high performance a large number of TPB must therefore be present as close as possible to the electrolyte; at the same time the mass transport must not be hindered by a structure that is too fine. In state-of-the-art ASC, the anode is therefore divided into two areas: the electrochemically more active anode layer near the electrolyte and the substrate layer. The substrate (500-1000 μm) gives the cell mechanical stability and has a coarser structure for better fuel mass transport; the anode layer ($\approx$10 μm) is finer and has a high density of TPB [40].

Interconnects

In the strict sense interconnects are not a functional layer of the SOFC, but they perform important tasks. Since a single SOFC only supplies a voltage of < 1 V during operation, many cells are connected in series in a stack for technical applications. Interconnects serve as bipolar plates between the individual cell planes and are made of (high-temperature) steels or ceramics. Since they separate fuel gas and air, they must be chemically stable in both reducing and oxidising atmospheres. In addition, interconnects must divert the current from the cells and pass it on to the adjacent repeating unit. Machined channels ensure even distribution of fuel and air. The coefficient of thermal expansion must be compatible with the cell materials in order to avoid stress in the event of temperature changes. The evaporation of chromium compounds from the steel must be prevented as these lead to poisoning of the cathode and thus to degradation of the SOFC. Protective coatings can significantly reduce the evaporation rate [41].

Due to the many requirements the interconnects can be the most expensive components of the stack. In intermediate temperature SOFCs at T <750 °C significantly cheaper steels can be used as chromium evaporation rate is reduced at lower temperatures [42]. These steels are also easier to process which further reduces manufacturing costs. As ESC have only a low performance at intermediate temperatures due to the poor conductivity of the electrolyte research on intermediate temperature ASC and MSC has been increasing in recent years.

2.2.2 Electrochemistry

Nernst voltage

The potential in an electrochemical cell in reaction equilibrium can be given with the Nernst equation as a function of temperature T, pressure p_0 and partial pressures $p_i = y_i \cdot p_0$ of reactants and products [43].

$$U_{\mathrm{Nernst}} = -\frac{\Delta^R g(T)}{\mathrm{F} \cdot n_{\mathrm{e}}} - \frac{\mathrm{R}T}{\mathrm{F} \cdot n_{\mathrm{e}}} \ln \left(\frac{p_i}{p_0} \right)^{\nu_i} \tag{2.4}$$

The derivation of the Nernst equation via the reaction equilibrium can be found for example in [31]. F = 96485.309 C/mol (= As/mol = W/V · s/mol = J/V/mol) is the Faraday constant and n_e the number of electrons transferred in the electrochemical reaction; ν_i are the stoichiometric coefficients; $\Delta^R g = \Delta^R h - T\Delta^R s$ is the gibbs free energy belonging to reaction 2.3. Using the partial pressures and the stoichiometric coefficients from Eq. 2.3 the Nernst equation for a hydrogen fuelled cell becomes:

$$U_{\text{Nernst}} = -\frac{\Delta^R g(T)}{\text{F} \cdot n_e} - \frac{\text{R}T}{\text{F} \cdot n_e} \ln\left(\frac{p_{\text{H}_2\text{O}} \cdot p_0^{0.5}}{p_{\text{H}_2} \cdot p_{\text{O}_2}^{0.5}}\right). \tag{2.5}$$

The first term is called standard cell potential or theoretical cell voltage. The ln-term leads to $U_{\text{Nernst}} \to \infty$ for $y_{\text{H}_2\text{O}} \to 0$ and $U_{\text{Nernst}} \to -\infty$ for $y_{\text{H}_2\text{O}} \to 1$ ($= y_{\text{H}_2} \to 0$). Since real gases always contain certain amounts of water vapour, this divergence for $y_{\text{H}_2\text{O}} \to 0$ cannot be observed on real cells. The measured cell voltage is normally <1.3 V instead.

Fuel utilisation

For each water molecule electrochemically produced at the anode one hydrogen molecule is consumed and two electrons must be transported back to the cathode. The maximum current I_{max} that can be supplied by a fuel cell can be calculated from the supplied molar hydrogen flow $\dot{n}_{\text{H}_2,\text{feed}}$:

$$I_{\text{max}} = n_e \text{F} \dot{n}_{\text{H}_2,\text{feed}}. \tag{2.6}$$

If a current I_{load} is set on the cell, the ratio to I_{max} results in the fuel utilisation FU:

$$FU = \frac{I_{\text{load}}}{I_{\text{max}}} \sim \frac{\dot{n}_{\text{H}_2,\text{R}}}{\dot{n}_{\text{H}_2,\text{feed}}}, \tag{2.7}$$

where $\dot{n}_{\text{H}_2,\text{R}}$ is the molar flow of consumed fuel gas which is equal to the molar flow of produced water $\dot{n}_{\text{H}_2\text{O},\text{R}}$. If CH_4 and CO are also present in the fuel gas, FU_{CH_4} and FU_{CO} can be calculated in the same way or it is assumed that these are first

converted to hydrogen which adds up to $\dot{n}_{H_2,feed}$. The air utilisation (AU) can be calculated analogously. Real stacks are usually operated using a very large excess of air to cool the stack which results in a low AU.

While the FU is calculated on the basis of the current generated over the entire cell there are locally differing gas compositions as hydrogen concentration decreases and water concentration increases from the gas inlet to the gas outlet. If the overall fuel utilisation is too high and there is not enough hydrogen left in an area of the cell, oxidation of the anode or substrate can occur.

Cell voltage of a real SOFC

If no current is drawn from the cell (OCC – open circuit conditions), the cell is in equilibrium and the cell voltage (OCV – open circuit voltage) corresponds to the Nernst voltage. When operating an SOFC under load, however, hydrogen is constantly being consumed and additional water is formed. Therefore the cell voltage decreases when the current is increased and the cell is no longer in reaction equilibrium. In addition, loss mechanisms in the form of activation, ohmic losses and concentration losses occur. These cause the measured cell voltage to always be lower than the Nernst voltage. The difference is called polarisation or over-voltage. [44]

The dependence of the over-voltage on the current density $i = I/A_{Cell}$ is determined experimentally by recording I-V-curves: at a constant operation point the current is increased and the cell voltage is measured. The course of this I-V-curve can be used to make statements about the state or quality of the cell or to compare cell types. The slope ($\Delta U/\Delta i$) of the measured I-V-curve corresponds to the area-specific resistance (ASR) according to Ohm's law. The ASR of an SOFC should not exceed 0.3 to 0.4 Ωcm^2 in order to be able to use it in technical systems [45]. From the over-voltage determined by means of the I-V-curve it is not possible to determine the proportions of the individual loss mechanisms; this requires the use of electrochemical impedance spectroscopy (EIS), see chapter 5 of this thesis. In addition, the contributions of the individual losses are – like the FU – locally distributed over the cell.

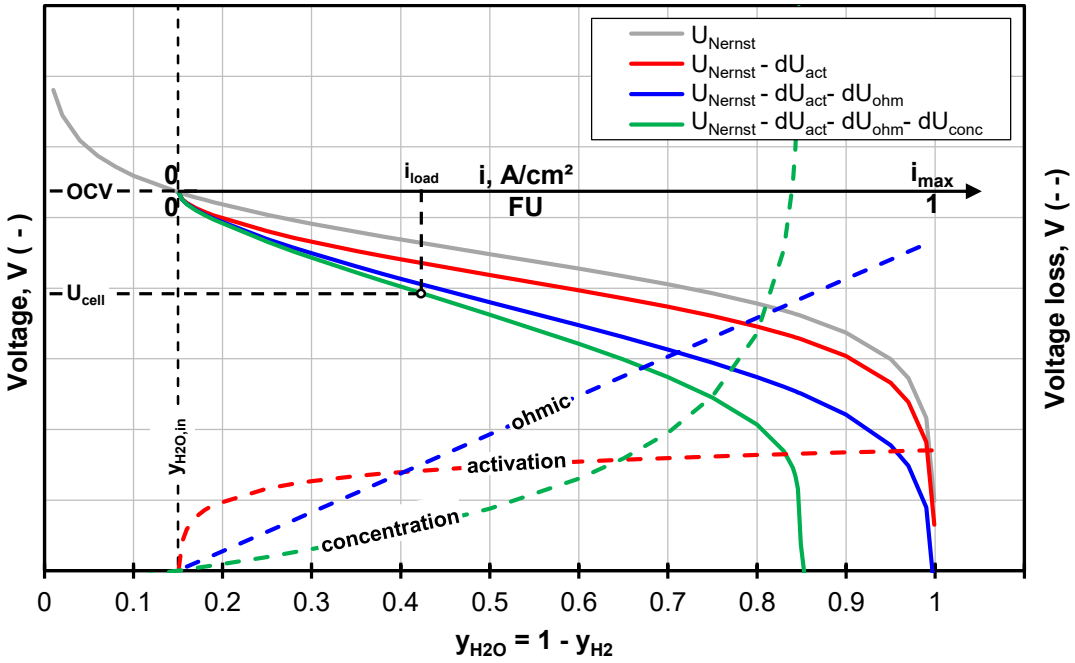

Figure 2.2: Nernst voltage of an H_2/ H_2O fueled SOFC (grey). Starting from an inlet steam share of 15 vol%, loss contributions (activation loss (red), ohmic loss (blue), concentration loss (green)) due to operation under load are indicated. Parameters for the calculation of losses are not according to reality but chosen for best visibility.

The grey curve in Figure 2.2 shows the Nernst voltage of an SOFC operated at the anode on H_2/H_2O as a function of the steam fraction y_{H_2O}. In addition, the diagram shows the influence of the current density on the cell voltage starting with a feed-vapour fraction of 15 vol%. The contributions of the loss mechanisms are plotted on the right y-axis; the parameters for their calculation were chosen in such a way that all mechanisms are clearly visible and therefore do not correspond to reality. The individual mechanisms are explained qualitatively in the following. Formulas for the quantitative description of the loss mechanisms are summarised in [31].

Activation losses: As with any chemical reaction the activation energy for the reactions at the electrolyte-electrode interface must first be overcome. This leads to a drop in cell voltage for $i > 0$. In contrast to low-temperature fuel cells like PEM-FCs these activation losses are small for SOFCs and do not lead to such a pronounced over-voltage as illustrated in Figure 2.2. The parameter that influ-

ences the activation losses is the exchange current density i_0. It depends, among other things, on the catalytic activity of the electrode surfaces and indicates the magnitude of the no-load current resulting from the equilibrium between electrode reactions and back reactions. The greater i_0, the smaller the over-voltage due to activation losses. The activation losses are proportional to $\ln(i/i_0)$. [18, 46]

Ohmic losses are caused by the limited conductivity in the electrolyte but also by contact resistance between cell and contacting and the conductivity of the electrodes [46]. According to $U = R \cdot I = ASR \cdot i$ the ohmic losses are proportional to $i = I/A_{\mathrm{Cell}}$. As already mentioned the conductivity of the electrolyte increases with the temperature. At the same time, the resistance in the current-carrying components, i.e. in the nickel of the anode and the interconnects of a stack or the contacting of a single-cell, increases with temperature.

Concentration losses occur at high current densities when the rate of electrochemical reactions is limited by diffusion of reactants from the gas stream to the active sites. The concentration polarisation is strongly dependent on the structure of the electrodes [47]. If the porosity is too low, insufficient mass transport to the TPB can lead to a drop in cell voltage already below $FU \rightarrow 1$. The maximum achievable current density for a given microstructure is designated by i_{L} and can be determined from the I-V-curve. The concentration polarisation is also influenced by the type of gas since the diffusivity of CO through the pores of the anode is worse than that of H_2 [48]. The concentration losses are proportional to $\ln(1-i/i_{\mathrm{L}})$.

2.2.3 Internal Reforming and CO-Utilisation

Due to the high operating temperature SOFCs can be operated not only on hydrogen but also with gases containing hydrocarbons and carbon monoxide; for example bio-syngas, biogas, mine gas, ethanol, methanol or pre-reformed diesel and kerosene [23]. The majority of current fuel cell applications run on internally or externally reformed natural gas [49]. In addition to the electrochemical oxidation of hydrogen further reactions then take place at the cell which supply hydrogen. At the nickel surface of the anode methane (eq. 2.8) or higher hydrocarbons (eq. 2.9) can be reformed or the water gas shift reaction (WGS) of carbon monoxide can take place (eq. 2.10).

$$CH_4 + H_2O = CO + 3H_2 \qquad \Delta^R h(T_0, p_0) = 206\,\mathrm{kJ/mol} \tag{2.8}$$

$$C_nH_m + nH_2O = nCO + (n + \frac{m}{2})H_2 \qquad \Delta^R h(T_0, p_0) > 0 \tag{2.9}$$

$$CO + H_2O = CO_2 + H_2 \qquad \Delta^R h(T_0, p_0) = -40\,\mathrm{kJ/mol} \tag{2.10}$$

The reaction enthalpy values were taken from [31]. The reforming reactions are endothermic, the CO shift slightly exothermic. The internal reforming of methane is also used to consume part of the heat generated during the operation of a fuel cell stack [20]. This can reduce the airflow to cool the cells which in turn reduces operating and investment costs for air blowers. The consumption of water by steam reforming and WGS shifts the reaction equilibrium of hydrogen oxidation to the reactant side which increases the cell voltage.

The operation of SOFCs on hydrocarbon-containing gases has been described by several authors [17, 31, 50–55]. Depending on reaction equilibrium carbon deposits can form in unfavourable gas compositions. Too high a proportion of CH_4 or CO in relation to water vapour content can lead to irreversible damage of the anode. A summary of the different forms of carbon deposition can be found in [31]. Carbon deposits can occur even though chemical equilibrium considerations predict otherwise [51, 52, 56]. This is especially the case when there are unsaturated or higher hydrocarbons (e.g. tars) in the fuel as these lead to a locally increased C-density which does not correspond to the chemical equilibrium.

As already discussed by Bieber [31] there is disagreement in literature as to whether CO or CH_4 can also be directly electrochemically oxidised. Certainly the way of conversion depends on the anode material used and on the operating conditions. For cells with a nickel-containing anode of sufficient thickness it can be assumed that CH_4 and CO are converted to H_2 before they reach electrochemically active areas [57]. Several authors stated that the electrochemical oxidation of CO on nickel is significantly slower than that of H_2 [48, 54, 58]. This leads to H_2 being consumed preferentially but CO being used when there is no or only little H_2 in the fuel gas. In addition, the diffusivity of CO to the TPB is lower than that of

H_2 [48]. On cerium-containing anodes – in the form of Ni/GDC – at least partial direct oxidation is very likely since cerium is also active as an oxidation catalyst for hydrocarbons [26].

2.3 Tars

Depending on the biomass employed, the type of gasifier and the operation parameters the raw bio-syngas contains various impurities in form of particles, sulphur (e.g. H_2S) and chlorine (e.g. HCl) compounds and tars [9]. Particles have to be removed in order to prevent the plugging of any downstream equipment. As stated by Sasaki et al. [21] even low concentrations in the ppm range of H_2S and HCl lower the performance of the SOFC and therefore have to be removed from the bio-syngas by scrubbing or adsorption. In the following the formation of tars and options for their removal or handling are discussed.

2.3.1 Formation of Tars during Biomass Gasification

The gasification of biomass takes place in several steps, each of which depends on the prevailing temperature [8]. After entering the gasifier the biomass first dries (50 to 200 °C). With further heating the first components are volatilised and lignin structures and hemi-celluloses are broken up by pyrolysis. The actual gasification during which the bio-syngas is produced takes place at temperatures above 650 °C. Depending on the time of their formation during the gasification process tars can be divided into primary, secondary and tertiary tars [59]. Primary tars are oxygen-rich hydrocarbon compounds that are released during the volatilisation or pyrolysis of the biomass, e.g. phenol, cresol and acetic acid. Secondary tars are formed from primary tars by dehydration, decarbonisation and decarboxylation. Examples are toluene, xylene and biphenyl. Tertiary tars, for example naphthalene, pyrene or fluorene, are formed by recombination of existing tars.

In total over 200 tars can be distinguished. With increasing temperature in the gasification zone the proportion of tertiary tars increases and that of primary and secondary tars decreases [59]. At the same time the amount of tar decreases towards

higher operating temperatures. The tar content in the bio-syngas is strongly dependent on the design of the gasifier and the operating conditions and can therefore vary from 0.01 (fixed-bed downdraft gasifier) to 100 g/Nm^3 (fixed-bed updraft gasifier) [60]. The bio-syngas of fluidised-bed gasifiers typically contains 1-15 g/Nm^3 tars.

For a bubbling fluidised-bed gasifier Mayerhofer et al. measured a total tar amount of about 5 to 10 g/Nm^3 with phenol and naphthalene being the most common tars [11]. Kirnbauer et al. [61] also identified naphthalenes (naphthalenes, 2-methylnaphthalenes, 1-methylnaphthalenes) as the prevailing tars in the product gas of a dual fluidised-bed gasifier. They measured an overall tar content of <7 g/Nm^3.

2.3.2 Handling Tars

If the temperature in equipment downstream of the gasifier falls below the dew point of a tar[4], the latter can condense and over time lead to plugging of tubes and filters or fouling in heat exchangers. At temperatures above 400 °C the tars can form solid char deposits [63]. Depending on the concentration of the tars the system design and the use of the product gas a more or less extensive cleaning of the tars from the bio-syngas is necessary. In principle there are three options how to handle the tars in the syngas: cold gas cleaning, hot gas cleaning and internal reforming in the SOFC [63]. Table 2.1 summarises the respective advantages and disadvantages.

In cold gas cleaning processes the bio-syngas is either cooled down to such an extent that high-boiling components condense or they are removed by adsorbers or scrubbers. In the latter tars and other impurities are separated with washing agents [67]. As these processes are state of the art they are less expensive than hot gas cleaning. In the case of very large amounts of tar in the raw gas its recovery from the scrubbing liquid is meaningful, which enables further material use in chemical synthesis processes[5]. Since the raw bio-syngas must first be cooled

[4]Dew points for 1 g/Nm^3: phenol T < 18.7 °C; naphthalene T < 30.1 °C; fluoranthene T < 124.3 °C, perylene T < 216.2 °C [62].

[5]Tar output for a fluidised-bed gasifier with a bio-syngas production of 10 Nm^3/min and tar

Table 2.1: Comparison of methods for handling tars in bio-syngas. [17, 63–66]

Option	Advantages	Disadvantages
Cold gas cleaning (scrubber)	• removal of all condensable/soluble impurities • truly clean gas • state of technology • material use of the tars possible • state-of-the-art SOFCs can be used	• equipment effort • possibly multiple stages for removal of polar and non-polar tars • energetic losses • treatment / disposal of the scrubber liquid • high maintenance effort • additional risk of failure • CH_4 and CO are converted at the cell → T-gradients • tars are not used energetically • gaseous unsaturated hydrocarbons (C_2) remain in gas phase
Hot gas cleaning (external reforming)	• only H_2 and CO as fuel at the cell • can also absorb other impurities → protection of the (more expensive) SOFC • available technology • SOFC can be operated at a higher FU compared to internal reforming • energetic use of H_2 and CO from tar reforming • state-of-the-art SOFCs can be used • heat integration with SOFC possible	• equipment effort, possibly multiple stages • high maintenance effort • additional risk of failure • sulphur and chlorine still must be removed • more cooling air in the SOFC stack necessary
Internal reforming in SOFC	• reduced equipment effort • less complex overall system • energetic use of tars • internal use of electrochemical heat generation in SOFC	• tolerant cells necessary • high T-gradients in the cell due to hydrocarbon reforming • risk of carbon deposits and related damage to the anode • sulphur and chlorine still must be removed • SOFC must be operated at a safe FU

down for cleaning and then be reheated before the SOFC, the overall efficiency of a system is significantly reduced when using cold gas cleaning [65]. In addition, the heating value of the tars is no longer available for conversion in the SOFC and the use of washing liquids and adsorbents produces toxic waste, the disposal of which is associated with effort and costs [63].

Reviews on hot gas cleaning processes for the use of bio-syngas in SOFCs can be found in [63] and [68]. A distinction is made between catalytic and non-catalytic processes. The latter requires temperatures above 1400 °C for complete tar conversion [69]. Tar removal via plasma is also possible. For catalytic removal steam reforming or partial oxidation are used. Tar reforming is mostly done on nickel catalysts which are cheap but prone to deactivation by poisoning, fouling, coking and thermal degradation [63] [66]. For the conservative case that SOFCs can only be operated permanently on quasi-tar-free bio-syngas, Aravind and de Jong have proposed the following hot gas cleaning process for fluidised-bed gasifiers [63]: by using in-bed catalysis the tar content in the raw gas is reduced to 2 g/Nm^3; then catalytic cracking is carried out in a fixed-bed reactor on dolomite at 700-900 °C, whereby the tar content is reduced to a few 100 ppm; in a further reactor the tar concentration is brought down to a few ppm on a nickel catalyst; in order to protect the nickel catalyst H_2S and HCl are separated upstream to the catalytic process steps.

The complete cleaning of the tars requires a high level of equipment and economic expenditure. In addition, with the increasing number of components the risk of failure for the entire system and the maintenance effort increase. It is therefore desirable to be able to reduce the scope of cleaning. By reforming the tars internally at the SOFC equipment for their separation is no longer necessary or can be greatly reduced. The heating value of the tars is then available for power generation at the SOFC, but the risk of premature degradation of the SOFC is also higher. Literature data on the usability or harmful effects of tars are discussed in the next section.

concentration of 5 g/Nm^3: 5 g/Nm^3 · 10 Nm^3/min = 50 g/min = 3 kg/h = 24 t/a.

2.4 SOFCs and Tars

In addition to the flow-mechanical problems due to condensation and coking, tars can have several – positive and negative – effects on the operation of the SOFC [22, 70]:

1. The tars are internally reformed or oxidised at the anode and are thus converted into electricity in the SOFC.
2. The tars are inert and leave the SOFC with the anode exhaust gas.
3. The tars adsorb at the anode of the SOFC and thus impede cell reactions.
4. The tars lead to carbon deposits and impede gas transport to or within the cell.
5. The tars trigger structural changes of the anode, for example by the formation of carbon whiskers and/or metal dusting.

Scenario 1 is the best case, but can only be realised if SOFC materials are tolerant to the tars and show a high performance in reforming of tars. Already for bio-syngas with medium tar content the amount of additional fuel from the reforming of tars is significant: assuming a fuel gas flow of $1\,\mathrm{Nm^3/min}$ and complete reforming $5\,\mathrm{g/Nm^3}$ of tar deliver around $0.022\,\mathrm{Nm^3/min}$ of additional H_2 and accordingly increase the H_2-content in the bio-syngas by around 10 %. Scenario 2 leads to an unaltered SOFC performance, but requires downstream removal of the tars. Effect 3 leads to temporal but reversible decrease of SOFC performance. Scenario 4 and 5 accelerate the degradation of an SOFC or lead to complete cell failure which must be absolutely avoided. Since tar from real bio-syngas contains various species with very different properties, all effects can occur at the same time or even amplify each other.

The following two sections focus on the effects of tars on SOFCs as found in literature. First, laboratory experiments with simulated bio-syngas and model tars are summarised[6], then an overview of experiments on coupling of gasifier and SOFC carried out so far by different authors is given.

[6]Sections of this overview have already been published in [71] and [72].

2.4.1 Tests in Literature with Model Tars in Simulated Syngas

Table 2.2 provides an overview of studies in which SOFCs were tested with model tars in simulated bio-syngas. It becomes evident from the table that there is a lack of comparable experiments. The parameters of operation – cell temperature, gas composition, contaminant choice and concentration, dosing duration and current density – can all have an effect on the resistivity and degradation rate of the cell. Depending on the intended application almost each choice of parameters can make sense. However there are studies in literature in which conditions were established that are not relevant to any applications – such as using hydrogen plus nitrogen as carrier gas for the tar contaminants or operating the cell with no or low electrical load [70, 73, 74].

The suitability of a certain cell design for operation on tar-laden gas cannot be reduced to the choice of anode materials, in this case either Ni/YSZ or Ni/GDC. As with any catalyst material robustness and performance is a complex relationship of material choice and structural parameters such as porosity and particle sizes in the cermet and thickness of anode or substrate layer [51].

The highlights from the effects of tars in the tests found in literature are summarised in the following:

Papurello et al. [75] tested the influence of naphthalene on Ni/YSZ ASCs at $0.33\,A/cm^2$ and 750 °C: in pure H_2 30 ppm of naphthalene ($0.17\,g/Nm^3$) did not affect the performance of the cell negatively whereas 10 ppm ($0.06\,g/Nm^3$) in syngas drastically decreased the cell potential. Additionally using I-V-curves, the authors stated that naphthalene inhibited both electrochemical and reforming reactions. Naphthalene therefore did not only adsorb on the nickel surface at the active sites for reforming, but also at the TPB where electrochemical oxidation takes place. In the worst case the reduction of available fuel by the shortfall of H_2 from reforming could lead to critical fuel utilisation levels and consequently to nickel oxidation at the anode.

Like Papurello et al., Hauth et al. [76] saw the multiple effects of naphthalene for Ni/GDC anodes when adding $11.6\,g/Nm^3$ of it to either hydrogen or syngas at 900 °C. For the first case the authors reported an increase of the OCV whereas it decreased in the second case. The increase in OCV during H_2 operation cannot

be interpreted as a relevantly successful usage of naphthalene: in OCC usually a minimum number of free TPB exists with which the Nernst voltage can be reached and the Nernst voltage is increased by the partial reforming of naphthalene. During operation under load, however, naphthalene poisoning manifested itself for all fuel gas mixtures in an increased over-voltage caused by a reduced amount of free TPB, as discussed in [75]. In addition, during syngas operation Hauth et al. detected an increased concentration of CH_4 in the anode off-gas due to naphthalene poisoning of methane reforming. It is remarkable that naphthalene was able to block CH_4 reforming even at an operation temperature of 900 °C. This phenomenon and a decrease in cell voltage were also observed by Dekker et al. [77] when operating a Ni/GDC ESC at 850 °C on syngas and naphthalene as model tar. They reported analogue effects for phenanthrene and pyrene.

All studies with naphthalene have in common that no carbon deposits or structural changes of the cell were reported. In contrast, benzene and toluene can lead to severe carbon deposits at the cell. Using these two model tars in dry H_2 plus N_2, Mermelstein et al. reported carbon deposits and subsequent metal dusting on Ni/YSZ ESCs at 775 °C [73]. Metal dusting is a type of corrosion which affects different metals – especially iron and nickel – in gases with high carbon activity [78]. Due to carburisation of nickel and the resulting stress on the cermet matrix, disintegration takes place, resulting in metal dust [79].

Nickel is an excellent catalyst for the reforming of hydrocarbons, but it also catalyses the formation of carbon filaments which can damage the anode. To prevent carbon deposits on the anode carbon must be oxidised or reformed faster than it is deposited on nickel [26]. This is the case for Ni/GDC anodes as the carbon is oxidised by cerium (Ce) which leads to the reported higher robustness when operated on carbon-rich fuels. Nevertheless, even in Ni/GDC anodes the reforming of hydrocarbons takes place on nickel since Ce does not crack C-H bonds [80]. If the active Ni sites are for example covered by naphthalene the reforming of CH_4 is inhibited and the performance decreases also for this anode type, as observed by [76, 77].

The rate of reforming reactions and also the adsorption behaviour of tars strongly depend on temperature. The specification of an established tar tolerance is therefore only meaningful in connection with the operating temperature of the SOFC.

For example: for a Ni/YSZ ASC Pumiglia et al. [81] found that at 650 °C just several hundreds mg/Nm^3 of toluene in syngas have a severe influence on the cell as they increased the polarisation resistance and led to cell failure after 150 h of operation; on the other hand for a operation temperature of 800 °C Madi et al. [82] reported a concentration of toluene as high as 14 g/Nm^3 in syngas to be the tolerance limit for safe operation of a Ni/YSZ ASC.

Meaningful studies in which tar tolerance was stated were mostly carried out on Ni/GDC anodes at high temperatures. It is not possible to conclude whether Ni/GDC actually has a higher resistance to tars or whether the promising results were achieved by faster catalytic tar conversion or lower adsorption tendency of the tars at high temperatures. There are few studies in which Ni/YSZ and Ni/GDC cells have been compared at the same temperature. Mermelstein et al. [74] performed tests with both anode types at 765 °C and 15 g/Nm^3 benzene and showed that Ni/GDC was tolerant to the presence of the model tar while Ni/YSZ suffered from carbon deposition and detachment of the anode from the electrolyte. Since the test time was very short (30 min), it is not clear whether the Ni/GDC anode also had a permanent tolerance to benzene.

This is a drawback of most studies in literature: the tolerance of a cell type to a model tar is attested after only a few hours of operation whereas the real SOFC application must run stably over at least 40000 h. At the moment there is no data in literature on the performance of SOFC single-cells during long-term dosing of a contaminant but these data are of enormous importance.

Another main insight from all the different studies is that different tar species lead to very different effects on the SOFC and that there is not one single model tar that could represent all others. Besides this, the lean results from literature suggest that the tar content must be reduced to only few ppm when using Ni/YSZ in B-IGFC systems if the SOFC is to operate permanently at intermediate temperatures without any loss of performance [63]. For this cell type further extensive investigations are necessary to understand the effects of tars in order to develop robust and at the same time high-performance cells.

Table 2.2: Overview on tests in literature for operation of SOFCs on model tars in simulated bio-syngas.

Anode type	Cell type	T, °C	Main gas, vol%						c_{tar}, g/Nm^3	Duration, h	Load, A/cm^2	Result	Source
			H_2	CH_4	CO	CO_2	N_2	H_2O					
Ni/YSZ	ASC	650	25	0	15	14	36	10	0.1 toluene	150	0.4	cell failure, carbon deposits blockage of pores	Pumiglia 2017 [81]
Ni/YSZ	ASC	800	65	0	5	25	0	5	18 toluene	25	0.25	stable operation until 14 g/Nm^3; for 18 g/Nm^3 decline of cell performance, disintegration of nickel contacting, carbon deposits	Madi 2015 [82]
Ni/YSZ	ASC	750	15	2	13	7	36	26	0.02 toluene	2	0.32	irreversible degradation	Papurello 2016a [83]
Ni/YSZ	ASC	750	15	2	13	7	36	26	0.05 naphthalene	2	0.32	increase of ASR	Papurello 2016a [83]
Ni/YSZ	ASC	750	100	0	0	0	0	0	0.17 naphthalene	1	0.33	stable operation	Papurello 2016b [75]
Ni/YSZ	ASC	750	19	2	17	8	47	7	0.06 naphthalene	1	0.33	decline of performance, inhibition of reforming	Papurello 2016b [75]
Ni/YSZ	ASC	750	14	4	16	14	37	13	3 naphthalene	8	0.3	decline of cell voltage below 600 mV	Dekker 2006 [84]
Ni/YSZ	ESC	800	16[d]	2	20[d]	16[d]	47[d]	0-10	6.3 toluene	< 5	< 0.15	decline of cell voltage in dry gas, carbon deposits	Liu 2011 [85]
Ni/YSZ	ESC	775	15	0	0	0	85	0	15 tars[*]	0.5	var	performance loss, metal dusting of anode	Mermelstein 2009 [73]
Ni/YSZ	ESC	765	15	0	0	0	85	var	15 benzene	0.5	var	irreversible damage of anode, influence of current density and steam content	Mermelstein 2010 [74]
Ni/GDC	ESC	765	15	0	0	0	85	var	15 benzene	0.5	var	cell unaffected	Mermelstein 2010 [74]
Ni/GDC	ESC	900	21	6	13	13	bal	27	11.6 naphthalene	0.3	0	decrease of cell voltage, blockage of CH_4 reforming, no carbon deposits	Hauth 2011 [76]
Ni/GDC	ESC	800	wet syngas						< 20 toluene	24	0.1	stable operation, partial reforming of toluene	Liu 2013 [86]
Ni/GDC	ESC	850	14	4	0	30	37	13	0.3-3 naphthalene, 1 phenanthrene, 0.2 pyrene	5	0.14	reversible decrease of cell voltage, blockage of reforming, minor blockage of H_2-oxidation	Dekker 2007 [77]
Ni/GDC	ESC	850	>0	0	0	0	> 0	4	0.63 naphthalene	2	0	increase of OCV, partial reforming of naphthalene	Aravind 2008 [70]
Ni/GDC	ESC	850	7.5	2.5	0	0	43	47	8.6 naphthalene	< 10	0.1	voltage decrease, cell failure	Frank 2010 [64]

[*] mixture of benzene, toluene, naphthalene, phenol and pyrene
[d] dry

2.4.2 Tests in Literature with Tar-Containing Real Bio-Syngas

A drawback of the experiments with model tars is that they may not be representative for operation on real tar-containing bio-syngas. Thus, Lorente et al. found that the dosage of toluene led to more carbon deposition at the SOFC than the same tar amount from a mixture of real tars [22]. In addition to the laboratory experiments, experiments with real bio-syngas are therefore also important, in which the interaction of the different tar components can be investigated.

Table 2.3 summarises the experiments found in literature in which SOFC single cells or stacks were coupled with gasifiers. For all tests listed other contaminants (S, Cl, Particles) were removed from the bio-syngas.

The overview shows that stable, coupled operation is possible with different gasifier types. In short-term experiments no significant degradation or carbon deposits could be detected even with tar concentrations of up to $10\,g/Nm^3$ tar in an otherwise purified biosyngas [87]. Biollaz et al. were even able to demonstrate operation on $5\,g/Nm^3$ tar with a tubular cell over 1200 h with only 1 % performance loss [88]. Unfortunately the anode type of their cell was not specified. Since the operation of gasifier test plants is usually costly and personnel-intensive, there are also no results in literature on long-term system stability over several 1000 or even 10000 h.

Except from the studies by Gadsboll et al. all experiments with tar-containing bio-syngas were carried out at very high SOFC temperatures of up to 950 °C. Similar to the tests with model tars it cannot be said with certainty whether tar tolerance in these experiments was caused by the cell type employed or the high temperatures. As discussed in section 2.2.1, such high operating temperatures are not desirable with respect to cost-effective stacks. They place increased demands on the materials used in the SOFC stack. In ferritic steels such as CroFer 22 APU creep problems occur at higher temperatures which especially reduce the durability of SOFC stack concepts with thin interconnects [89]. Lower operating temperatures, on the other hand, allow a wider choice of materials which are cheaper and easier to process [25] and therefore preferable with regard to the economical operation of SOFC systems.

Table 2.3: Overview on tests in literature for operation of SOFCs on tarry bio-syngas.

Cell type[1]	**T, °C**	**Gasifier type**	**c_{tar}**[2]**, g/Nm^3**	**Duration, h**	**Load, A/cm^2**	**Result**	**Source**
Ni/GDC ESC SC	850	two-stage Viking	0	150	0.26	stable operation, no carbon deposition	Hofmann 2007 [90]
Ni/GDC ESC SC	850	BioHPR	3	7	0.26	stable operation, no carbon deposition	Hofmann 2008 [91]
Ni/GDC ESC SC	850	circulating fluidised-bed	10	<10	0.13	stable operation, no carbon deposition	Hofmann 2009 [87]
Hexis St	?	ECN Pyromat	0	48	?	minor performance decrease, soot formation	Oudhuis 2004 [92]
Hexis St	950	updraft fixed-bed	8	30	0.06	6 % performance loss within 30 h	Nagel 2007 [93]
Hexis St	950	updraft fixed-bed	0	28	?	increase in anode pressure drop	Nagel 2011 [94]
ESC St	850	bubbling fluidised-bed	0	2 x 100	0.124	stable operation	Dekker 2008 [95]
tubular cell	950	updraft fixed-bed	5	1200	0.06	1 % performance loss	Biollaz 2009 [88]
Ni/YSZ ASC St	700	air-blown, two-stage Viking	0.005	62	var	stable operation	Gadsboll 2017 [96]
Ni/YSZ ASC St	700	air-blown, two-stage Viking	< 0.015	<10	var	stable operation	Gadsboll 2019 [97]

[1] SC – single-cell, St – stack

[2] Anode inlet

Chapter 3

Objectives of this Thesis and Methodology

There is disagreement in literature as to whether tars damage the SOFC or whether they can be used as fuel. Moreover, only few meaningful studies can be found in which measurements have been carried out for a sufficiently long time and under realistic conditions – under load, with (simulated) bio-syngas, with large cells.

Relevant measurements on tar tolerance were carried out with electrolyte-supported cells (ESC) with Ni/GDC anode. The higher temperatures at which ESC must be operated (>800 °C) to provide sufficient power could be the main reason for their higher tar tolerance. At the same time, however, the operating temperature of the ESC sets high demands on steels used in SOFC stacks and BOP equipment.

In contrast, ASCs with Ni/YSZ anode exhibit higher performance even at intermediate temperatures < 750 °C. At these temperatures significantly cheaper steels for the SOFC stacks and other equipment can be used. The motivation is therefore to use SOFCs based on these high-performance Ni/YSZ ASC to convert bio-syngas into electricity. In order to minimise the overall costs of the system, the SOFCs should be so robust that the pre-reforming or separation of tars from the bio-syngas is no longer necessary or could be reduced to a minimal extent.

In this context, the scientific questions of this work are as follows:

- Can state-of-the-art Ni/YSZ SOFC be operated on tar-containing syngas at 700 °C?
- Which SOFC components and processes are affected by tar-induced degradation?
- Do different types of tars have different effects on the cells?
- Are the effects reversible?

In order to answer the questions, experiments were carried out on anode-supported SOFCs with simulated bio-syngas to which model tars were added. Phenol (primary tar) and naphthalene (tertiary tar) were selected as model tars as these are two of the most frequent tar components in bio-syngas from fluidised-bed gasifiers [98].

Chapter 4 describes the cell types studied and the test rigs used for the experiments. In addition, the standard measurement conditions are discussed. Cell temperature, current density and gas composition were kept the same in nearly all tests and the type, dosing duration and concentration of tars were varied. Using the impedance measurement available on the single-cell test rig, the changes caused by tars could be examined in detail. The tests on the short stacks were one step closer to application and also provided data on exhaust gas composition.

In the following chapter 5 the measuring method of electrochemical impedance spectroscopy (EIS) is explained in detail. As it significantly expands the information from the cell voltage, EIS is very well suited to investigate the effects of tars. With the help of literature data and reference measurements, the processes visible in the spectra of this work are interpreted in this chapter.

Based on experimental data, in chapters 6 and 7 the effects of naphthalene and phenol on cells with Ni/YSZ and Ni/GDC anode are investigated and compared. Several single-cell experiments with each of the tars were complemented by a short-stack experiment to obtain information about the behaviour in a realistic system.

The two tars showed completely different harmful effects on the cells. For the measurements with naphthalene, the impedance data could be used to explain the process of cell poisoning in more detail. The same applies to the analysis of the anode exhaust gas during the short-stack experiments.

All investigations were carried out within the framework of the DFG-funded project "SynSOFC – Development of improved anodes in oxide ceramic fuel cells (SOFC) for the conversion of synthesis gas from the thermochemical gasification of biomass into electricity". The aim of this project was and is to achieve a higher robustness of the SOFC against biogenic impurities by using alternative materials while maintaining the same cell performance. The focus of the degradation tests was initially on the comparison of the effects of different tars. As the project title suggests, only the anode layer was originally to be changed, but this approach had to be revised after the experiments with phenol. The results of this work show weaknesses of the state-of-the-art cells when exposed to tars and thus provide starting points for the development of optimised SOFCs.

Chapter 4

Test Rigs and Tested Cell Types

The experiments in this thesis were performed on different types of 10x10 cm^2 anode-supported cells with Ni/YSZ substrate. The differences between the types are discussed at the beginning of this chapter. Subsequently, the employed test rigs are described. Two SOFC test rigs were used within the scope of this thesis: the single-cell test rig and the short-stack test rig. The former was already existing at the LES and, in addition to minor modifications such as the retrofit of the cell housing, was extended by the impedance spectroscope. The latter was designed and constructed in the scope of this thesis. It is integrated into the infrastructure of the existing synthetic natural gas (SNG) station at the LES. In addition, the analytics used for the determination of the tar content in the bio-syngas are explained at the end of the chapter.

4.1 Cell Types and Stacks Tested in this Thesis

For the experiments in this thesis four types of SOFCs were used: CTb, CTJb, TypIIIb and CTGDC. The first three types have a Ni/YSZ anode, the fourth a Ni/GDC-anode. In addition, experiments were carried out on short-stacks. All cells and the stack design are described in the following.

4.1.1 ASC with Ni/YSZ Anode

Three similar cell types with Ni/YSZ anode were used for the single-cell tests. TypIIIb cells were developed and manufactured at Forschungszentrum Jülich (FZJ) which has a focus on anode-supported SOFCs [99]. The CTb cells were manufactured by CeramTec (Marktredwitz/Germany) based on licences from FZJ and are a further development of TypIIIb. For the CTJb cells, CeramTec provided only the substrate, while the functional layers were applied by FZJ. The latter were also used in the tested short-stacks. All types are anode-supported cells with a Ni(O)/YSZ substrate, Ni(O)/8YSZ anode, 8YSZ electrolyte, GDC barrier layer and LSCF cathode. The area of the cathode was 9 x 9 cm^2. There are differences between TypIIIb and CTb. TypIIIb has a substrate made of Ni/8YSZ whereas the substrate of CTb is thinner and made of Ni/3YSZ [32, 100]. Moreover, pores and particles in the substrate of CTb are finer. A comparison of the microstructure of the different layers of TypIIIb and CTb cells can be found in [40].

The production of the TypIIIb cells takes place in several steps [101]. The Ni/8YSZ substrate is first foil-cast, dried, cut and then pre-sintered at 1240 °C. Subsequently, the functional layers are applied by screen printing, whereby each layer is first dried and then sintered. The sintering temperatures for Ni/8YSZ anode, 8YSZ electrolyte, GDC barrier layer, and LSCF cathode are 1230, 1400, 1300, and 1080 °C, respectively. After sintering the electrolyte, the cells are laser-cut to the exact size. Compared to electrolyte-supported cells, the manufacturing and sintering effort is increased, but the power density is higher.

4.1.2 ASC with Ni/GDC Anode

In addition to cells with Ni/YSZ anode, Jeong in Jülich also produced cells whose anode layer consisted of Ni/GDC. In this thesis these cells are referred to by the abbreviation CTGDC. The development and manufacturing procedure is described in [32]. As with the CTb and CTJb cells, the substrate is from CeramTec and consists of Ni/3YSZ. Except for the anode, all layers are identical to the Ni/YSZ anode cells. As described in [102], interdiffusion between the anode and the electrolyte occurred in the CTGDC cells. This caused the conductivity of the electrolyte to

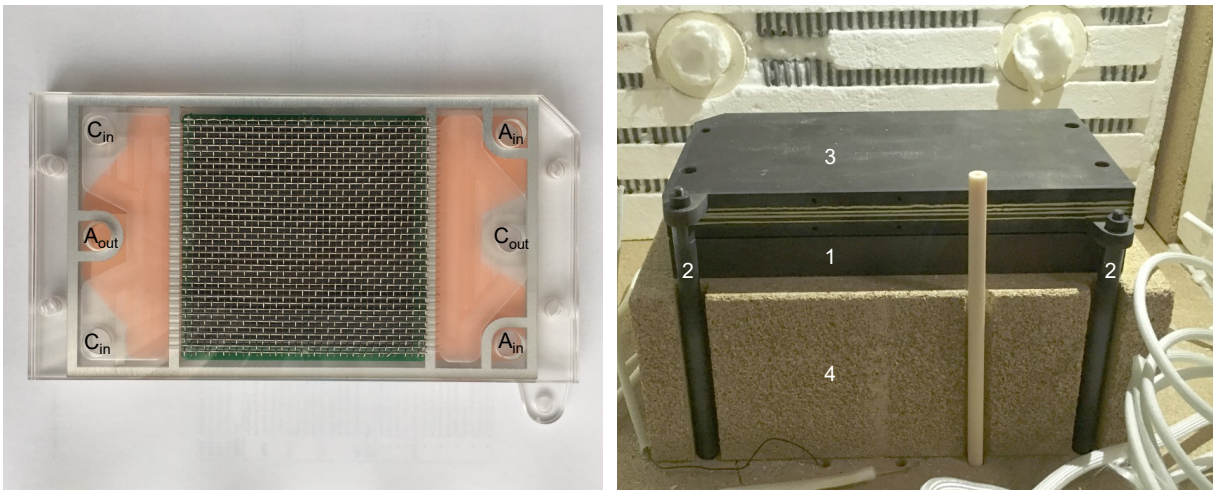

Figure 4.1: Transparent model of the F10 stack design, view at anode side with nickel contact mesh (left). 2-layer F10 short-stack in installed condition (right). A_{in}: Fuel inlet, A_{out}: Fuel outlet, C_{in}: Air inlet, C_{out}: Air outlet, 1: Adapter plate, 2: current collector, 3: stack, 4: furnace insulation.

deteriorate and triple-phase-boundaries were reduced in the anode. The combination of YSZ and GDC therefore had a lower conductivity than the pure components. Interdiffusion increased with the sintering temperature of the electrolyte. In electrolyte-supported cells with Ni/GDC anode this problem does not occur since the electrolyte is sintered at the highest temperature first and then the anode at a lower temperature. The cell type was examined before the tests in this thesis on 5 x 5 cm^2 cells [102]. With hydrogen as fuel gas at 820 °C the cell voltage fell below 0.8 V at a current density of 0.7 A/cm^2, which was only 50 % of the current density from a reference cell with Ni/YSZ anode.

4.1.3 Jülich F10-Stacks

In real applications SOFC single-cells are integrated into stacks. By connecting many cells in series, a voltage level suitable for power generation can be achieved. At the same time, the stack also provides a separate supply of fuel gas and air to the cells. In this work short-stacks in the F10 design of Forschungszentrum Jülich with two or four cells were used, see Figure 4.1. Details on this stack type can be found in [103]. In the stack fuel gas and air flow in counterflow, with both gas

streams being supplied from below by means of an adapter plate. Since the stack does not generate enough waste heat, it must be placed in a furnace to control its temperature. The interconnectors and cell frames of the stack consist of Crofer 22 APU (VDM Metals, Werdohl/German) [104], which up to 900 °C forms a top layer of electrically conductive chromium-manganese oxide with a low chromium evaporation rate [89]. The individual metal layers were sealed with glass sealant (Type 87 ZYBF-2). In order to further reduce chromium evaporation and poisoning of the cathode, a $MnCo_{1.9}Fe_{0.1}O_4$ (MCF) coating is applied via atmospheric plasma spraying (APS) on all exposed parts of the interconnector on the air side [41]. A fine and a coarse nickel mesh are used for contacting at the anode side, and a thick contact layer of $LaMn_{0.45}Co_{0.35}Cu_{0.2}O_3$ (LCC10) coating is applied onto the cathode via screen printing.

The cell type in the stacks is variable. In the short-stacks examined in this thesis, 10 x 10 cm^2 CTJb cells were used, i.e. substrates from CeramTec printed with the functional layers by Jülich. The electrochemically active area in the stack was determined by the size of the cathode and is 80 cm^2 per cell. The end plates and the middle interconnector plate had three drill holes with a depth of 40 mm each, into which thermocouples could be inserted. With these the temperature inside the stack, 10 mm from air and gas inlet[1] and in the middle of the cells, could be measured. Potential wires of platinum welded to the end plates and to each interconnector acted as contact for measurement of all cell voltages.

All stacks were built by ZEA-1 at FZJ. The acceptance test was carried out on the IEK-3 at FZJ, in which the glass seals were joined and the anodes of the cells reduced. In addition, I-V-curves were recorded as reference at different temperatures with moist and dry hydrogen. The stacks lose power each time they are removed from a test stand. In addition, the bottom cell always has a lower cell voltage, which is probably due to the lower temperature caused by heat dissipation through the adapter plate.

[1] Measured from the edge of the cell.

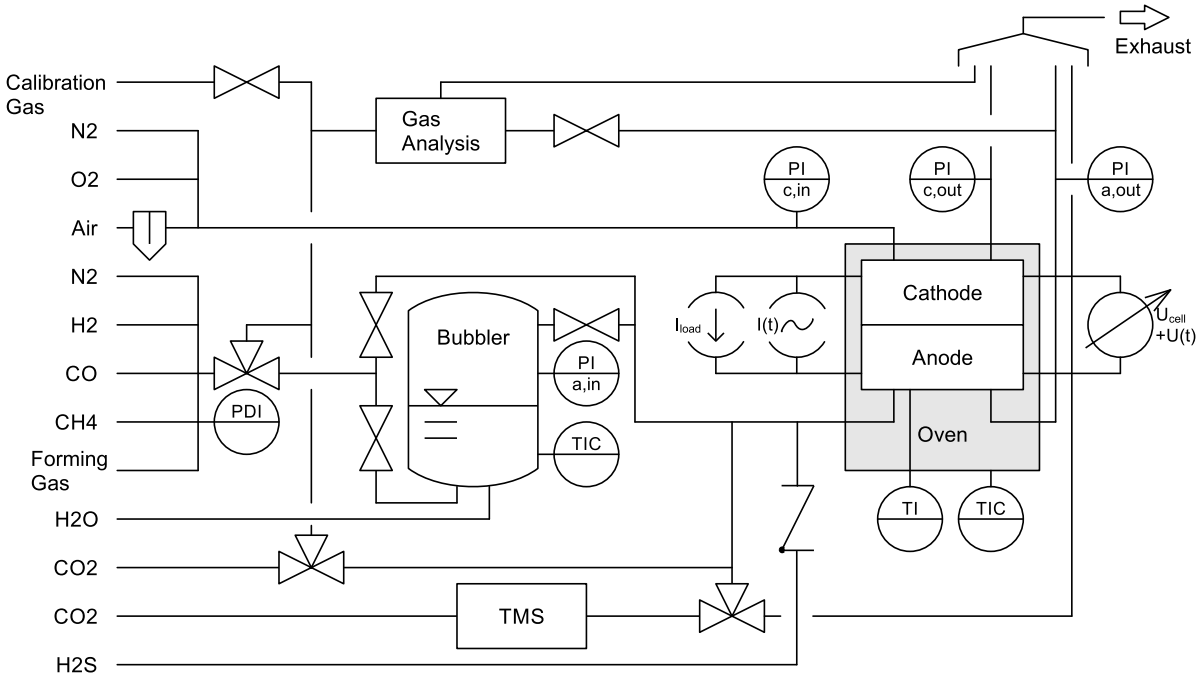

Figure 4.2: Scheme of the single-cell test rig. MFCs for gas dosing are not included in the scheme.

4.2 Single-Cell Test Rig

The single-cell tests were performed using an Evaluator C1000 HT test rig from FuelCon (Magdeburg, Germany) including a TrueData-EIS 100 A/35 V/50 kHz impedance analyser.

4.2.1 Layout

Figure 4.2 shows the P & ID of the FuelCon single-cell test rig including the devices for tar dosing (TMS). Several details of the test rig were modified in the course of this thesis: after cell 22 (C22) the impedance spectroscope was installed; after C25 additional gas pipes for tests with gaseous contaminants like H_2S and a bypass for calibration of off-gas-analytics were installed; from C27 onwards the tests were conducted using a new anode housing with better flow distribution and better electrical contacting, the latter was renewed after C61; commissioning of the new

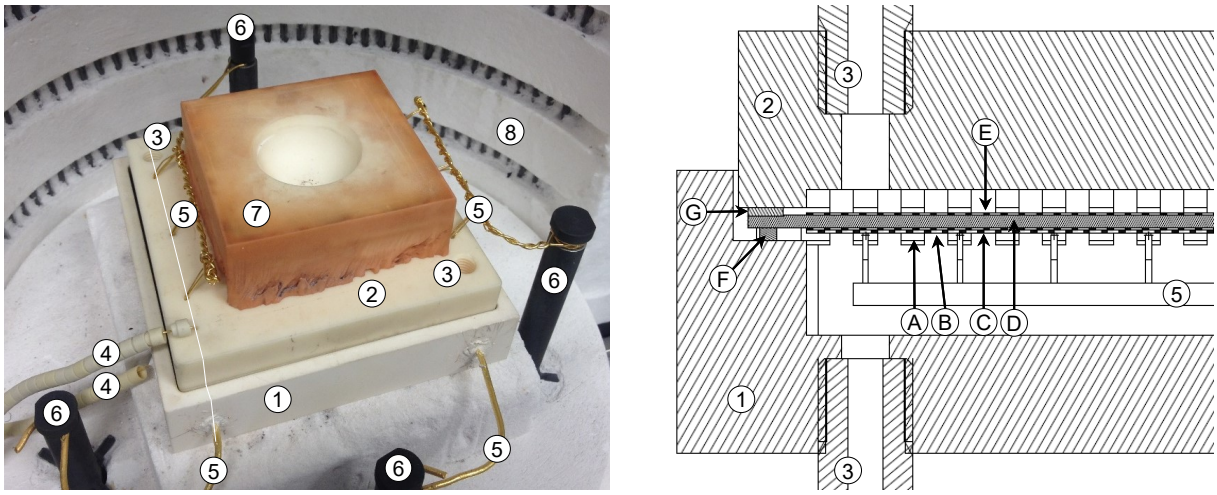

Figure 4.3: Photo of the housing assembly (left) inside the furnace and cross-section through inlet manifold (right). Position of the cross-section is indicated in the photo by the white line. 1) anode ceramic housing, 2) cathode ceramic housing, 3) ceramic tubes for gas and air supply and connections for the tubes, 4) sense wires, 5) current collector wires, 6) current rods, 7) adapter for pneumatic stamp, 8) furnace. A) gas channel, B) bar for contacting, C) two nickel meshes, D) Cell, E) gold grid, F) gold seal, G) Flexitallic seal.

housing was completed by C32, which is also the first cell for which results are discussed in this thesis; from C36 on also mixtures of O_2 and N_2 could be dosed to the cathode side; the former platinum mesh for contacting on the cathode was replaced by a gold grid after cell 39; trace heating of the anode inlet gas flow was improved several times, after the C25, C34 and C43. The different components of the single-cell test rig are described in the following.

Housing, contacting and furnace

The housing for 10 x 10 cm^2 cells is shown in Figure 4.3. It consists of two parts for anode (bottom) and cathode (top) made from Al_2O_3 (Degussit AL24). The housing was placed inside an electric furnace with an inner diameter of 250 and inner length of 375 mm. The maximal continuous temperature is 1050 °C and the maximum heating rate is 20 K/min. One function of the housing is the supply of the cell with fuel and air. On both electrodes the gas enters a manifold perpendicular

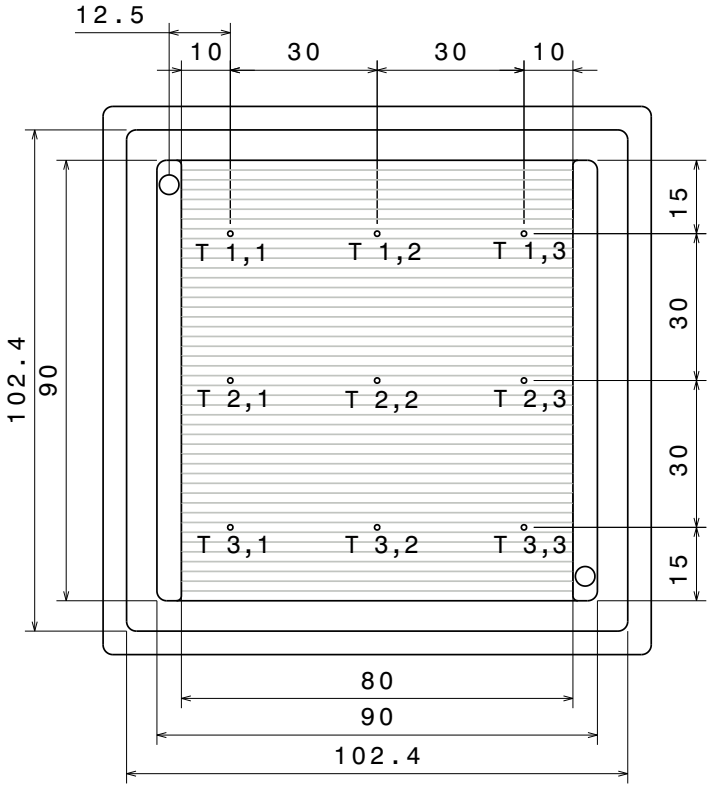

Figure 4.4: Top view at anode-side flow-field which indicates dimensions and positions of thermocouples in mm. Fuel inlet on top left.

to the cell via an Al_2O_3 tube and then flows from there through the channels of the flow-field along the electrodes. At the outlet the gas is collected in another manifold and from there flows through the outlet pipe. See Figure 4.4 for the respective dimensions of the manifold and the flow-field. Fuel and air are fed in counterflow.

The bars of the manifold serve to press the metal meshes, which collect the current generated by the cell, against the electrodes. For contacting at the anode side a nickel mesh[2] from Tedra-Dahmen (Wassenberg/Germany) with fine gold wires welded on it was used. It was renewed after C61. An additional layer of nickel mesh was placed upon the first layer and was changed after every test. Originally a platinum mesh with attached gold wires was used at the cathode, but was re-

[2]Mesh size 0.225 mm, wire diameter 0.1 mm; purity: 99 % Ni, 0.3 % Mn, 0.02 % Si, 0.15 % Mg

placed by a gold-grid from Fiaxell (Lausanne/Switzerland) after C38. The area of electrical contact in the housing, relevant for the calculation of the area-specific electrical load, was 90 x 80 mm^2.

Current collector wires made of fine gold are welded onto the meshes. The housing therefore has feed-throughs at both electrodes for the current conductors and the sense line. The sense line measures the voltage of the cell and is used for the control of the electrical load; it is also welded onto the metal meshes. As a further function the housing prevents the ingress of air on the anode side, which otherwise would lead to oxidation of the anode. On the other hand no fuel gas should emerge from the housing and burn off. Figure 4.3 shows the cross-sectional view and the applied sealing concept. A sealing frame made of fine gold was used at the anode side. The cathode side was sealed with Thermiculite 866 (Flexitallic, Willich/Germany). During operation the housing assembly was loaded with 400 N via a hydraulic ceramic piston[3], which sits in an adapter piece made out of alumina.

Compared to the original version used up to C27, the anode housing has deeper manifolds (depth 8 mm) and shallower channels (depth 1 mm). As the pressure loss in the 23 channels is higher than in the flow-field, a more uniform gas distribution over the entire width of the cell was achieved. The flow velocity of the gas in x-direction is 0.08 m/s in the manifold and 1.3 m/s in the channels with a gas flow of 1 Nl/min; the residence time is in both sections 0.06 s[4].

Gas and Steam Dosing and Trace Heating

For the dosing of gases on the anode side the test rig includes six mass flow controllers (MFCs). H_2, N_2, CO and CH_4 can be mixed by the MFCs, and the combined gas stream flows through a bubbler for dosing of steam. CO_2 does not flow through the bubbler to prevent its dissolution in water. The steam content of the fuel gas is controlled by the temperature of the bubbler which determines the saturation pressure of water. The automatic refilling of the bubbler with cold water led

[3]For safety reasons the piston must be in contact with the housing before the load can be fully applied.

[4]Volume at 700 °C calculated with ideal gas law, cell reactions neglected, volume of gold wires in manifold and channels neglected.

to periodic upward spikes in the cell potential of several mV for few seconds since less steam was produced for a short time and the pressure at the cell was disturbed by the higher pressure of the water conduit. The deionised water for the bubbler comes from a unit in the lab which deionises tab water. For the measurements with gaseous contaminants a separate MFC is installed. It is calibrated for the dosing of H_2S. The gas from this MFC is not led through the bubbler either. The control range of the MFCs for CH_4, N_2, CO, CO_2 and H_2S is 0.01 to 0.5 Nl/min; for H_2 it is 0.02 to 1 Nl/min. All gases came from cylinders. The purity of H_2, CO, CO_2 and CH_4 was 5.0, 3.0, 4.5 and 2.5/4.5 respectively. At the cathode there are two MFCs for N_2 and air with a control range of 0.01 to 0.5 and 0.2 to 10 Nl/min, respectively. In addition, an analogue flow meter for an O_2 stream was installed after C35. This way mixtures with variable partial pressure of oxygen can be dosed to the cathode. After C66 a cascade of filters was installed at the pressurised air supply in order to prevent the contamination of the cathode with silicon oil.

The pressure at the cell can be increased by inlet pressure regulators attached to the exhaust gas lines of air and fuel gas. In practice this can only be achieved if the housing is sufficiently tight. All pipes in which steam or tar flow are equipped with trace heating. The section of the gas piping directly before the furnace was heated to around 170 °C during the experiments. The section coming from the bubbler had a little lower set temperature in order to facilitate smooth temperature control of the downstream section. The connection hose between tar mixing station and test rig was heated to 180 °C.

Electrical Load and Impedance Spectroscope

The electrical load (TrueData-Load, FuelCon) dissipates the current produced by the cell via adjustable resistors. The heat generated in the load is transferred to the environment by fans. The load can be controlled in the four operating modes const. I, const. U, const. R and const. P. The power range is 260 W, where the maximum current is limited to 100 A. The cell voltage can be regulated between 35 and 0 V. Two measuring ranges are available for measuring current and voltage, which are automatically applied. The current ranges are 0-100 and 0-4.5 A, the resolution being +/- 0.05 % FS of the range selected and +/- 0.08 % of the value,

respectively. For the voltage, the ranges go from 0-35 and from 0-2.5 V, where the resolution is +/- 0.03 % FS of the range selected and +/- 0.05 % of the value, respectively. Two Inconel rods for each pole are used to lead the current conduction from below into the furnace to the cell, see Figure 4.3. In the furnace the rods are connected to the contacting meshes on the cell by gold wires. The measurement of the cell voltage and the compensation of the voltage drop in the current rods is carried out via separate thin cables, the sense line, which are also connected to the metal meshes in the housing.

A TrueData-EIS 100 A/35 V/50 kHz impedance analyser was added to the test rig during work on the thesis. It is connected parallel to the electric load. It superimposes an AC-signal with frequencies from 0.01 Hz to 100 kHz to the DC-signal of the electric load which leads to a response of the cell voltage. From this response the phase shift and the amplitude are evaluated in order to determine the impedance, see section 5.1. The amplitude of the excitation current is chosen automatically by the device but can also be set manually. At high frequencies and low impedances, coupling effects may occur between the sense line and the load cables [105]. Too wide distances between the two wires of the sense line are critical because they may act as coils and lead to inductances which overlap in the impedance measurement. Therefore, they were twisted against each other as tightly as possible and care was taken that the load cables did not run parallel to the sense cable. Shielded wires would be preferable to block the influence of electromagnetic fields, but they are costly as they are to withstand the temperatures prevailing in the furnace.

Sensors

At the anode side nine Type N thermocouples (TC, Mönchengladbach/Germany, accuracy 1.5 K or 0.004 · T[K]) arranged in a rectangular raster are used to measure the temperature of the cell, see Figure 4.4. The distance between the tips of the thermocouples and the anode gas is 3 mm; between gas inlet and $T_{i,1}$ it is 12.5 mm in flow direction. From C41 on mantle thermocouples were used since their vertical position was easier and more reliable to adjust. Furthermore, the temperature of the piping is monitored at several spots at the inlet and the out-

let. Pressure sensors were used to monitor the inlet and outlet of fuel gas and air (see $dp_{\mathrm{A,in}}$, $dp_{\mathrm{A,out}}$, $dp_{\mathrm{C,in}}$, $dp_{\mathrm{C,out}}$ in Figure 4.2). A differential pressure sensor monitored the overpressure of the fuel gas inlet with respect to the ambient pressure.

Control Software, Alarming and Auxiliaries

Via the test rig software (FuelCon TestWork 7), all relevant process parameters can be controlled, including gas flow and gas composition on anode and cathode, temperature of the furnace and trace heating, mechanical load on the cell housing and state of valves. Also the impedance spectroscope is controlled by TestWork. All changes of sensor data or set values, called tags, are logged into a database of up to 10 GB. When the maximum file size is reached, a new database is generated. It is possible to operate the test rig via scripts [106]. The language of the code is visual basic script (vbs).

Alarm routines are programmed in a configuration database. This means that they can only be manipulated by FuelCon as manufacturer of the test stand, but not by the user. Red alarms cause the test stand to go into emergency shutdown, turning off load, furnace and all gases. In most cases this means that a measurement is aborted if necessary steps to prevent the cooling of the furnace or the re-oxidation of the anode are not made. Red alarms occur, for example, when the pressure in a gas cylinder falls below 3.5 bar, when deionised water is not available or when the laboratory exhaust fails. Also a too low or too a high pressure of the compressed air supply would trigger an alarm[5].

4.2.2 Equipment for Tar Dosing for Single-Cell Tests

The tar mixing station (TMS) was used to add tars to the simulated bio-syngas in the single-cell experiments. It consists of five tar containers, for fluoranthene, biphenyl, phenol, fluorene and naphthalene. CO_2 is used as carrier gas for the tars which is dosed by separate MFCs, see Figure 4.5. Since the temperature of every

[5]The occurrence of these alarms could be prevented by holding a reserve bottle with compressed air and by a pressure relief valve.

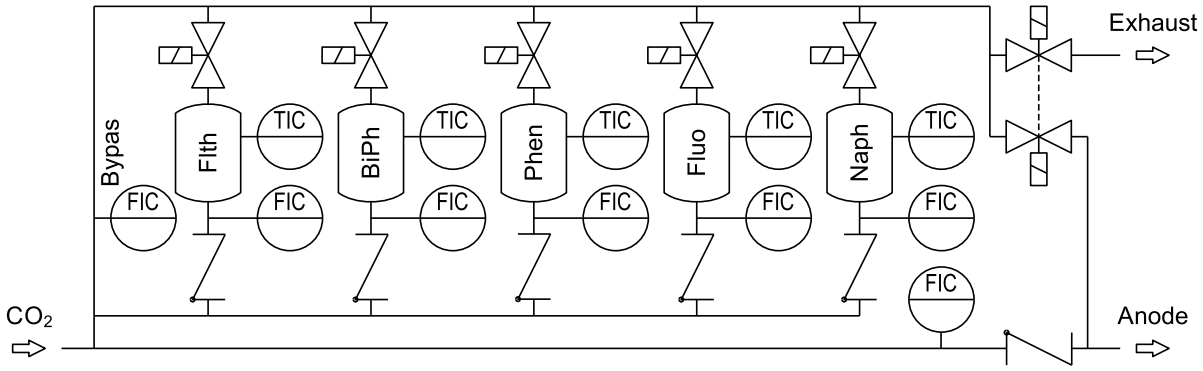

Figure 4.5: Flow diagram of the tar mixing station (TMS) for dosing of fluoranthene (Flth), biphenyl (BiPh), phenol (Phen), fluorene (Fluo) and naphthalene (Naph) using CO_2 as carrier gas.

reservoir can be controlled independently, the CO_2 can carry a defined amount of tar, depending on the saturation pressure of the respective tar species. The resulting mixture of CO_2 and tar flows through heated pipes and is combined with the other syngas components upstream of the housing of the cell. The maximum temperature of the trace heating is limited by the PTFE seal of the magnetic valves and is 184 °C. This also defines the maximum obtainable tar concentrations. For establishing steady tar concentrations before starting the dosing and checking the tar concentration without dosing tar to the cell, the tar-laden gas can be led to the exhaust by a bypass. The pipes of the TMS can be purged after tar dosing by an additional MFC. The MFCs are controlled by a LabView programme [107]. The temperature of the containers and the pipes is adjusted by an analogue heating controller and logged in the database of the test rig.

The amount of tar in the carrier gas depends on its saturation pressure which in turn depends on temperature. The respective constituent equations for phenol and naphthalene are given in appendix A. The actual temperature was measured with a thermocouple that was placed in the gas phase of the containers. With known $p_{\mathrm{sat}}(T)$ the amount of tar in grams per standard cubic meter ($T_0 = 273.15$ K, $p_0 = 1.013$ bar) in the anode gas is:

$$c = \frac{p_{\text{sat}}}{p} \cdot \frac{\dot{V}_{\text{cg}}}{\dot{V}_{\text{anode}}} \cdot \frac{MW_{\text{Tar}}}{V_{\text{mol,ig}}} \cdot 1000 \, \frac{\text{l}}{\text{Nm}^3}.$$

Here $\dot{V}_{\text{cg}}$ is the volume flow of the carrier gas through the tar container, $\dot{V}_{\text{anode}}$ is the total volume flow at the anode. It is assumed that the gas behaves ideally and reaches saturation in the container since the residence time is – depending on the filling level – at least 15 min. $V_{\text{mol,ig}}$ is the volume of 1 mole of an ideal gas.

4.2.3 Standard Test Conditions and Test Sequence

The experimental parameters for the measurements in this thesis were defined at the beginning and retained for all cells. Type, concentration and dosage duration of impurities were varied. With the exception of the impurity phase, the measurement procedure was largely standardised. This standard procedure is described below. Afterwards the test results for a reference cell operated on pure syngas are shown and the initial performance of all cells measured in this work is compared.

Standard testing procedure

The sequence of a measurement was divided into several phases.

- **Preparation**: The cell was first weighed. An additional nickel mesh was placed on the lower nickel mesh to which the gold wires were welded. The gold seal placed between the substrate and the lower ceramic shell was replaced as soon as it was too thin or too wide. The cell was placed on mesh and gold gasket with the cathode facing up. The thickness of the gold seal had to be such that both a sealing of the cell and a good contact between substrate and nickel mesh were achieved. On the cathode side a seal made of Thermiculite 866 was applied placed between the electrolyte and the upper ceramic housing part. The latter was last placed on the cell with the contacting grid facing down. Everything was pressed by the pneumatic stamp with 400 N. The screws on the Inconel current bolts, which clamp the gold wires, were checked for tightness. The oxide layer on the respective contact surfaces

was previously removed. The ceramic adhesive on the feed-throughs of the gold wires from the housing was checked for cracks and replaced if necessary. Finally, the ceramic tubes were screwed into the air side and the furnace was closed.

- **Reduction**: The furnace was heated at 1.5 K/min to 900 °C for reduction of the anode. From 200 °C on the fuel side was purged using 0.5 Nl/min forming gas with 5 vol% hydrogen to prevent oxidation of the nickel mesh. At the same time the trace heating was switched on. The bubbler was open during heating and 2 Nl/min air flowed at the air side. When 900 °C was reached, the fuel gas flow was gradually changed to 0.5 Nl/min H_2 and held for at least 4 h, for reduction of substrate and anode.
- **Reference tests**: The cell was tested for a possible fracture by briefly increasing the pressure of the cathode exhaust gas. If the voltage signal remained unchanged at an increase of 30 mbar, the cell was assumed to be intact. Otherwise, air overflowing from the cathode side would have burned off H_2 and lowered the OCV. In this case the measurement must be stopped. If the test was successful, there were two measurement programmes in which impedance spectra could be used to compare the performance of the cell with other cells. At 0.5 Nl/min H_2 plus 0.074 Nl/min H_2O ($T_{\text{bubbler}} = 50$ °C) and 15.6 A the furnace temperature was first lowered in 40 K-steps to record three impedance spectra in a row at each stage. The standard settings for the spectra were: 51 data points at 51 frequencies, distributed logarithmically between 20 kHz and 0.1 Hz; duration of every data point was either six periods of oscillation for low frequencies or eight seconds for high frequencies in order to reduce noise; the amplitude of the excitation current was 2.5 A. To further reduce noise in the lower frequency arc, the three spectra representing one state of the cell were averaged prior to further data analysis. At 700 °C, a gas composition of 50 vol% H_2O, 25 vol% H_2, 10 vol% CO, 10 vol% CO_2, and 5 vol% N_2 was adjusted. Subsequently, N_2 was gradually replaced in 0.01-steps by CH_4 and impedance spectra were recorded.
- **Syngas operation**: The standard gas composition was 50 vol% H_2O (T_{bubbler}= 82.7 °C), 25 vol% H_2, 10 vol% CO, 10 vol% CO_2 and 5 vol% CH_4, which corresponds to bio-syngas from an allothermal fluidised bed gasifier [98]. The

volume flow of fuel gas and air was 1 and 2 Nl/min, respectively. The electrical load was set to a constant value of 24.3 A[6], the specific cell current was therefore approximately 0.34 A/cm^2. The furnace temperature was set to a value keeping cell temperatures at approx. 700 °C, whereby the temperatures at the gas inlet and outlet were lower than in the middle of the cell. Since the exhaust gases from the housing are drawn off via the exhaust air system, the pressure inside the housing was lower than in the surrounding furnace or laboratory. The pressure at the cell therefore also fluctuated with the atmospheric pressure (0.94-0.98 bar) because the ventilation produced a constant negative pressure difference compared to ambient pressure. After establishing stationary conditions, impedance spectra were recorded at regular intervals.

- **Poisoning**: After a sufficiently long phase with pure syngas tars or other gaseous impurities were added. Type, concentration, dosing duration and repetition were variable. For tar dosing, 0.05 or 0.1 Nl/min of the CO_2 volume flow was passed through a tar container with the aid of the relevant MFC.
- **End of the test**: After the tests the cells were cooled down to room temperature at 1.5 K/min in forming gas atmosphere. The bubbler remained open but was no longer heated. Below 180 °C furnace temperature the forming gas was switched off as were the trace heatings at a later point in time. After cooling down the housing was dismantled and all abnormalities and the condition of the cell and the housing were documented. The cell was weighed and the microstructure was examined if necessary.

Reference test on pure syngas – C33

Before the experiments with tars the influence of pure synthesis gas on the cell was investigated in the reference measurement on C33. For this purpose a cell was operated on simulated bio-syngas for 250 h, see Figure 4.6. As with all other cells in this thesis, the oscillation of the cell voltage during the EIS measurements was removed from the data. The voltage signal showed fluctuations, being 3 mV higher during the day. This could be traced back to the ventilation in the laboratory

[6]In order to prevent damage on the gold wires of the contacting the maximum current was limited to 30 A.

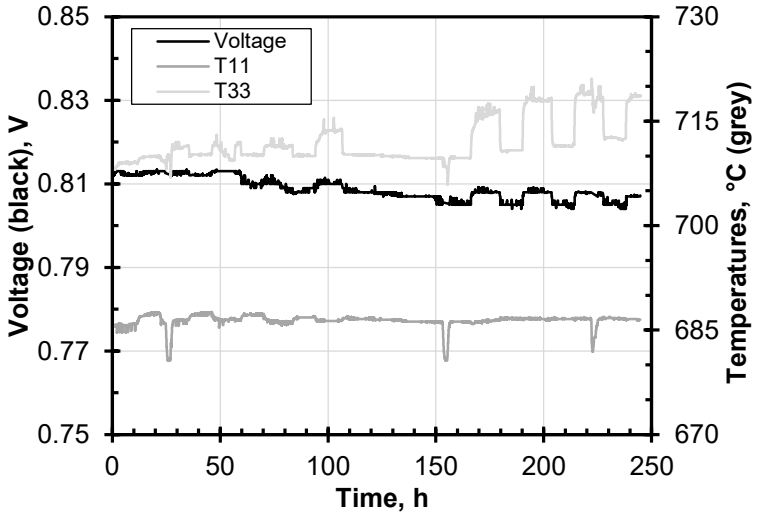

Figure 4.6: Cell potential and temperatures during operation of C33 on clean syngas at 700 °C and 0.34 A/cm^2.

which operated on reduced power at night, thus changing the pressure at the cell and therefore influencing the cell voltage. The outlet temperature showed a very strong response to this cycle, being 8 K lower at night than during the day. The cell, as it turned out after the end of the measurement, was broken at the outlet. This means that the temperature changes could have been related to the combustion of fuel gas with air from the cathode side. The fluctuations in voltage and temperature also occurred with other cells but a systematic relationship between fluctuations and cell breakage could not be established.

Apart from the fracture the cell showed no structural changes. This means that operation on standard conditions did not lead to carbon deposits. This confirms the result of the risk assessment for carbon deposits using the ternary C-O-H diagram shown in Figure 4.7. The composition of the standard syngas (sim. bio-syngas) was plotted in this diagram, together with the equilibrium lines for the formation of solid carbon in the form of graphite at 650 and 700 °C. The 650 °C line has been drawn to estimate the local cooling by methane reforming. The property data for the equilibrium of graphite formation were taken from the software FactSage. The operating point was determined for OCC. If the cell is operated under load, the operating point shifts towards the lower right corner of the diagram due to the

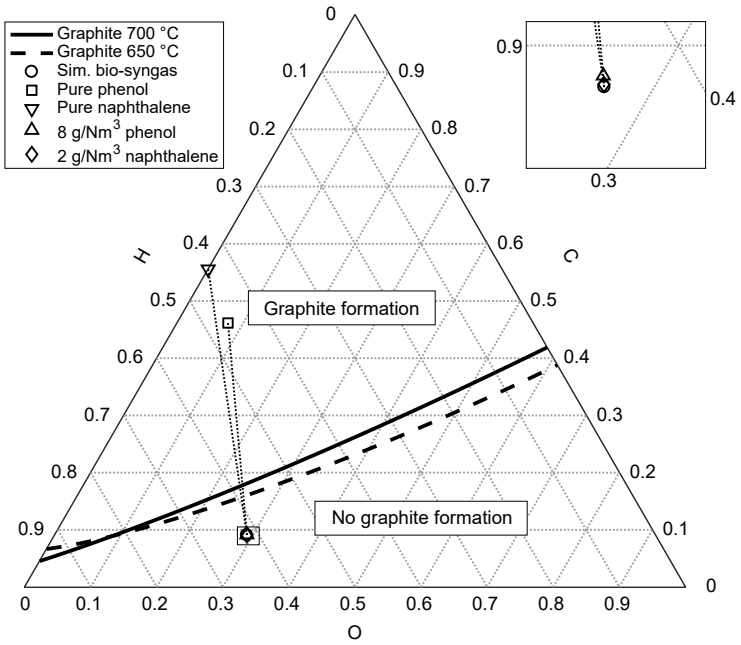

Figure 4.7: Ternary C-O-H diagram with indicated boundaries for graphite formation at 650 and 700 °C and the composition of the simulated bio-syngas. Zoom rectangle shows the change of gas composition when 8 g/Nm^3 phenol or 2 g/Nm^3 naphthalene are added.

supply of oxygen from the cathode. From the diagram it can be seen that the standard syngas of this thesis is not critical with regard to the formation of carbon deposits in the form of graphite.

The OCV at the beginning of the syngas phase was 0.996 V. The calculated OCV with this gas composition at 700 °C was 0.98 V. The value was calculated using an Aspen-Plus simulation for SOFCs, which is described in [108]. Since the OCV is a measure for leakage of the housing [109], it can be stated that the tightness of the housing was satisfying for this test. At 0.34 A/cm^2 the Aspen model predicted a cell voltage of 0.861 V which was 48 mV higher than the measured value at the beginning of the syngas phase. The lower performance might have been caused by an imperfect electric contacting at both anode and cathode side.

As can be seen, operation on synthesis gas resulted in a degradation rate of 3 %V/1000 h. The rate was determined by fitting a linear equation to the data. The rate was more than ten times the general target value of 0.25 %V/1000 h for

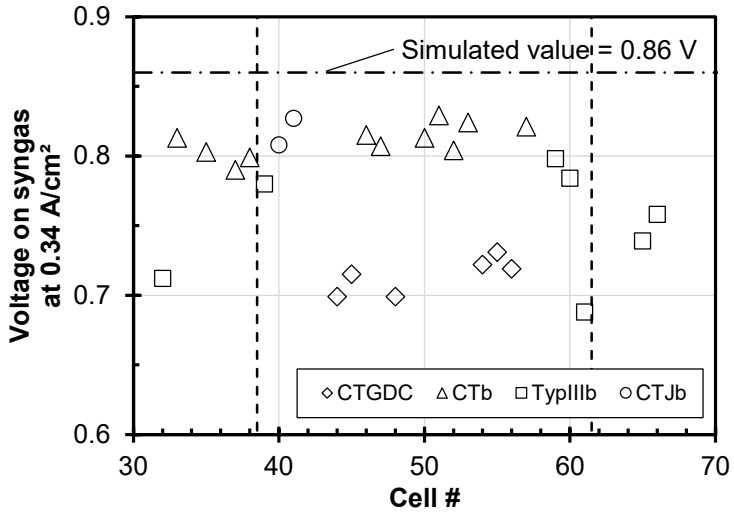

Figure 4.8: Measured cell voltage at 1 Nl/min syngas, 0.34 A/cm^2 and 700 °C for all cells tested in this thesis.

the acceptable degradation of SOFCs [30]. It is assumed that the steady mitigation of the overall performance is caused by a loss of contacting quality in the housing which seems to be common with single-cell tests. It is possible that the degradation rate would have declined during a longer runtime. In literature few examples for medium duration single-cell tests on syngas or carbon rich gases are documented, but some report noticeable initial degradation. Weber et al. [110] tested a Ni/YSZ ESC for 1000 h with dry methane and it showed 11 %V/1000 h voltage degradation during 500 h followed by a recovery over the following 500 h to the initial voltage. Other authors reported doubling of the polarisation resistance during the first 400 h of operation on humidified hydrogen [111]. Due to an incorrect setting of the hardware during the test[7], EIS data for this cell could not be evaluated and therefore could not provide information on the underlying degradation mechanisms.

Comparison of cell voltage during first syngas phase

Figure 4.8 shows the cell voltage of all valid cells tested in this thesis during the first syngas phase at 700 °C and 0.34 A/cm^2. In addition to the initial reference impedance spectra a too low cell voltage at this operation point was used as a decision criterion to abort tests at this early stage. The vertical lines indicate the modifications inside the housing: after C39 the cathode contacting was replaced by a gold grid and after C61 the nickel-mesh with the attached gold wires on the anode side was renewed. CTb cells had mostly uniform voltages above 800 mV, which is lower than the calculated theoretic value for this syngas composition at 700 °C. The performance of the IIIb cells was on the other hand scattered and a little lower. This might be due to the fact that the IIIb cells came from different manufacture batches and the production steps were partly carried out by hand while the CTb cells were industrially manufactured. The two CTJb cells had a performance similar to that of the CTb. Due to intermixing between anode and electrolyte [102], the CTGDC cells had a lower cell voltage between 700 and 740 mV but there were no distinct outliners.

4.2.4 Causes of Failure

As with every scientific experiment, there were also causes of failure for the single-cell measurements. The most frequent problem in this thesis was cell fracture. For most cells a fracture was not detected until after the end of the measurement because it rarely led to abnormal behaviour during operation. Nevertheless, a fracture reduced the full significance of a measurement as it changed for example the temperature distribution or the gas composition. Errors in the contacting also occurred frequently, especially during rebuild phases. A short circuit at the current collectors led to the destruction of several cells. Short circuits at the sense lines prevented the measurement of the cell voltage. If too high a current was adjusted, either consciously or inadvertently, the gold wires of the current collectors melted.

[7] The internal offset-correction was only active until 10 Hz. It could be set to 0.1 Hz by the command *OFR 0.1 by a TCP/IP-connection to the EIS.

Iron-V-carbonyl which had formed in a carbon monoxide steel gas cylinder led for one cell to deposits of iron and carbon dust inside the housing, which blocked the fuel channels.

4.3 Short-Stack Test Rig

The second test rig was the short-stack test rig "StaTe". It was built within the scope of this thesis and is able to operate on bottled gases provided by a gas mixing cart, and on bio-syngas from an allothermal fluidised-bed gasifier. During the operation on real bio-syngas further influences on the degradation of the cells can be investigated, such as a fluctuating gas composition, pressure fluctuations or traces of other impurities than tars. Results of the coupled operation can be found in [112]. The higher contact quality also makes it possible to carry out tests at higher current densities than at the single-cell test rig. A detailed documentation of its setup and commissioning can be found in [113].

4.3.1 Layout

The test rig is designed for measurements on short-stacks of type F10, see section 4.1.3. These are placed in a furnace on an adapter plate. The furnace consists of four 2.1 kW heating elements set up as walls, the bottom and lid are made of Vermilite. Also the distances between the heating elements are closed with Vermilite blocks and under the adapter plate there is a 10 cm high insulation platform. The furnace is mounted on a framework made of item. A controller is used to control both the target temperature and the rate of heating or cooling. The latter was always set to 4 K/min. The base plate is supported on the underside by a stainless steel plate. Both parts are perforated several times for the six gas lines for air and fuel gas, for thermocouples and for the current collectors. The potential wires for the voltage measurement and the thermocouples which measure the temperatures in the stack are led off laterally. To prevent short circuits, these components are sheathed in glass fabric insulation.

The adapter plate made of high temperature steel (1.4742) is used for the supply and removal of gases and must bear the weight of the stack and loading. The latter serves to compress both the layers of the stack itself and the mica seals between the stack and the polished surface of the adapter plate. Four plates made of 1.4828 with a total weight of 50 kg were used as compression weight. Six tubes made of 1.4841 are welded to the adapter plate. Two pipes each are intended for the supply of fuel gas and air and one pipe for the respective exhaust. The fuel pipes are equipped with trace heating to prevent the condensation of tars from the bio-syngas. In order to reach the required temperature of 350 °C, the trace heating was modified several times. The air volume flow on the cathode side is regulated by a float. At the fuel gas side flows forming gas (5 vol% H_2), from 200 °C on during heating and during disturbances. The forming gas is supplied by means of a solenoid valve which is open when no current is applied so that reducing conditions at the anode are ensured even in the event of a power failure. In normal operation the stack receives either mixed fuel gases from the gas mixing cart or bio-syngas from the gasifier. The exhaust gas from the air side is fed into the laboratory ventilation system. After passing through a condenser, some of the fuel gas goes into the flue gas analysis and the rest is burnt in a flare. The pipe to the flare is heated to prevent condensation of residual moisture.

Current collectors made of Inconel are connected to the end plates of the stack which conduct the current of the stack through the bottom plate of the furnace to the electrical load (PLI 2106 from Höcherl & Hackl, Konzell/Germany). Since Inconel forms an electrically insulating oxide layer, the contact surfaces must be polished before each measurement. To control the current and measure the stack voltage, thin silver potential wires are also connected to the load in parallel. The load can be operated stand-alone or with a LabView programme which also controls the gas mixing cart [114]. The rate of current increase during the recording of I-V-curves can also be controlled, the default value being 20 A/min. The single-cell voltages were stored during the first measurements by a data logger (HOBO UX120-006M, Onset, Bourne/USA) and later integrated into the LabView programme via an USB interface (RedLab 1208LS, Meilhaus Electronic, Alling/Germany). When wiring the stack to the interface or the logger, it must be taken into account that

the negative pole is internally connected. In order to avoid short circuits, only the top cell is connected to both poles while the cells below are only connected to the positive pole.

In order to protect the stack in the best possible way in all situations, several safety aspects were taken into account. First, an overflow valve at the fuel gas inlet ensures that the overpressure there cannot exceed the permissible 100 mbar. The under-voltage protection of the load also ensures that the fuel gas utilisation cannot reach critical values after a minimum voltage has been specified. When the emergency stop switch is activated, the load switches to OCC and the solenoid valve for forming gas opens. If the USB interface is correctly configured, the emergency stop can also be triggered and annulled via the LabView programme. The latter also ensures that CH_4 and CO are stopped if no water is added to the fuel gas. Details about the shutdown routines can be found in [114].

4.3.2 Integration in the Existing Infrastructure

The stack test rig was integrated into the existing infrastructure of the synthetic-natural-gas (SNG) test rig, which in turn is coupled to the allothermal fluidised-bed gasifier. For a detailed P & ID of the overall setup see the appendix of [113]. The gasifier and the related equipment are described in [112]. The gas flow through the gas cleaning in the SNG rig can be altered during operation. This way it is possible to bypass one or several reactors for tar cracking, chlorine- or sulphur-removal. When the SOFC is operated on tar-laden syngas, the anode off-gas is led through a separate condenser in order to protect downstream equipment from tar contamination. The gas mixing cart is used for operation on simulated bio-syngas. With its help the anode can be supplied with H_2O, H_2, CH_4, CO, CO_2 and N_2. The gasifier and the SNG line are controlled and monitored by the same system control. All signals for temperature and pressure of the stack test rig have been integrated into this control. Differential pressure sensors monitor the overpressure at the stack and the pressure difference between the fuel gas side and the air side.

During the tests on stacks F1002-189 and F1002-190 the exhaust gas composition after condensation of the water content was measured online using a C700 gas analyser (Sick, Waldkirch/Germany). The gases CH_4, CO and CO_2 are measured

by non-dispersive infra-red absorption (NDIR). For H_2 a thermal conductivity detector (WLD) is used and a paramagnetic sensor for O_2 [115]. The ranges for CH_4, CO, CO_2, H_2 and O_2 are 0-10, 0-70, 0-40, 0-40 and 0-25 vol%, respectively. The nitrogen content results from the difference to one hundred percent. If the concentration of a component leaves the measuring range, the overflow is output as N_2[8]. The gas analyser must be calibrated regularly; a zero point calibration is performed before each measurement.

4.3.3 Tar Dosing during Short-Stack Tests

A single tempered container filled with tar was used for the dosage of tar during stack tests. The construction and design was based on the experience gained with the tar mixing section (TMS) for the single-cell tests. The size of the container was such that the gas could be saturated with tar even at the maximum volume flow of carrier gas. In addition, the amount of tar that can be filled in should be sufficient for one experiment. The exact structure, design calculations and commissioning can be found in [116]. In contrast to the squat containers of the TMS, an elongated shape was chosen to allow more uniform temperature control and to keep the radial temperature differences small. A heating sleeve (Horst, Lorsch/Germany) was used for the heating instead of the winding with heating cords, which ensured significantly more constant and faster temperature control. The selected pipe geometry was placed horizontally in order to achieve the largest possible interface between tar and carrier gas. For easy filling or cleaning the tank was equipped with Tri-Clamp connections. Two thermocouples measured the temperature of the container wall and in the gas outlet. The latter was used to calculate the saturation vapour pressure.

[8] A gasflow of 50 vol% CO and 50 vol% H_2 generates the output 50 vol% CO, 40 vol% H_2 and 10 vol% N_2.

4.4 Tar Detection

The actual amount of tar in simulated syngas or bio-syngas was verified offline by the solid phase adsorption (SPA) method proposed by Brage et al. [117]. Provided that a gas chromatograph is available, this is an easy measure to detect different types and the amounts of tars. For the method 100 ml of gas were sampled from the gas stream and led through a fixed bed in which tars adsorb (Hypersep 100 mg Nh2, ThermoScientific, Rockwood/USA). The captured tars could be eluted afterwards with a solvent, here dichloromethane (DCM SupraSolv, Merck, Darmstadt/Germany) was used. The mixture of solvent and tars was collected in 2 ml glass vials. 1μl of the mixture was injected to the column (19091J-413, Agilent, Santa Clara/USA) of a gas chromatograph (7890 A from Agilent with modifications from Joint Analytical Systems, Moers/Germany). Different tar species desorb from the column when it is heated at a constant rate and lead to peaks in the signal of the downstream flame ionisation detector. Based on reference samples the retention times and integrated peak area give information on tar species and concentration in the sample, respectively. See appendix B for the calibration curves for phenol and naphthalene.

There are four ports for SPA measurements at the single-cell test rig: two at the tar dosing, one upstream of the anode and one downstream. The short-stack test rig has three ports; one at the tar dosing, one upstream and one downstream of the stack. Sampling in the wet anode gas streams was less exact since steam condensed in the sampling volume, which led to an increase of sampled gas volume. This way the tar content in the wet syngas is overestimated. Not all tars are quantitatively detectable by the SPA method. If the vapour pressure is low, for example for toluene, they evaporate from the amino column before being transferred into the solvent. A detailed analysis of the precision of the method can be found in [118].

Chapter 5

Electrochemical Impedance Spectroscopy

If electrochemical degradation of an SOFC occurs, the total resistance increases, which results in visibly decreasing cell voltage. This decrease by itself does not provide any information on how the resistance increased. To get a deeper insight into the processes that take place in fuel cells, or other electrochemical devices, impedance spectroscopy (EIS) is a widely used method [119]. Once all processes are identified, the information about which of them limit the performance can be used to optimise cells. In this context impedance means alternating-current resistance. In contrast to the pure ohmic (or DC-) resistance, the complex value of the impedance also provides information about the phase shift of the measured system [120]. Since the method is non-destructive and has little influence on the performance of the cell, it is well suited to observe minimal temporal deterioration online.

Other than an ASR-value obtained from I-V-curves, EIS allows to separate the overall polarisation resistance of the cell so that the contributions of the different electrochemical processes like adsorption, heterogeneous reactions at interfaces, mass transport on both electrodes in the bulk and at active surfaces or reforming of fuel can be distinguished. The different processes have characteristic excitation frequencies, also called relaxation times. The relaxation times usually cannot be

determined directly from the measured impedance data but require the evaluation of the distribution of relaxation times (DRT)[44], see section 5.4. The identification of the processes that were visible in the EIS data of this thesis is done in section 5.5 for Ni/YSZ Anodes.

In addition to the use of impedance measurements in research, the measurement method is also suitable for monitoring electrochemical systems, such as fuel cells or batteries, during operation. By regularly recording complete spectra, changes in the cell might be observed before the performance of the cell deteriorates. Since the necessary measurement technology is expensive, especially the frequency response analyser (FRA), there is also the alternative of continuously monitoring the impedance at one or a few discrete frequencies at which changes can be expected.

At this point, total harmonic distortion analysis (THDA) should also be mentioned as a monitoring tool [121]. As with conventional impedance measurements, the load current is superimposed with an excitation current and the voltage response is evaluated, or vice versa. Afterwards, the signal is examined for integer multiples of the excitation frequency using discrete Fourier transformation. Inside the linear range of the I-V-curve no such harmonics occur. On the other hand the excitation signal is disturbed outside the linear range. This is the case if the FU at an SOFC becomes too large and concentration limitation occurs. With the help of the THDA defective cells in an SOFC stack can be detected easily after manufacturing, and it enables to operate an SOFC-system at the maximum possible non-critical FU.

5.1 Determination of Impedance

To measure the impedance, a sinusoidal alternating current $i(t) = i_0 sin(\omega t)$ with excitation amplitude i_0 and frequency ω is superimposed on the set constant current i_{load}[1] [44]. As long as the system is linear, the cell voltage U_{cell} responds to this excitation with a sinusoidal voltage signal $U(t) = U_0 sin[\omega t + \phi(\omega)]$ oscillating around the current operating voltage U_{cell}. U_0 is the amplitude, ω the frequency and ϕ the frequency-dependent phase shift of the response. The system becomes

[1] In this thesis i denotes current density whereas j is the imaginary unit.

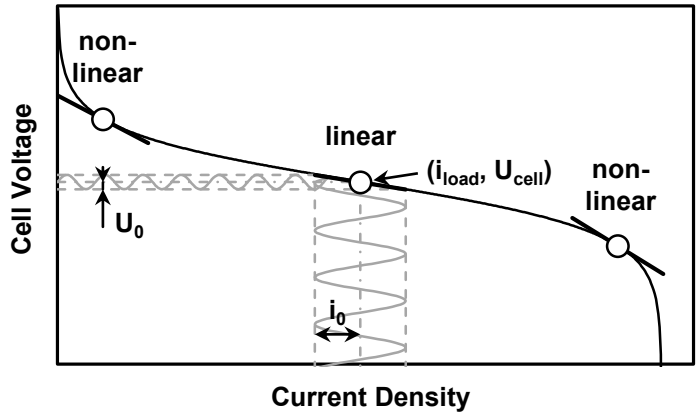

Figure 5.1: Agitation of an H_2-fueled SOFC during EIS measurement and indication of nonlinear behaviour for a fixed i_0.

non-linear for measurements close to $i \to 0$ with too high excitation amplitudes or generally for excitation amplitudes that are too large, as shown in Figure 5.1. Due to this linearity, it is also possible to excite the voltage and evaluate the response in the current signal.

Analogous to Ohm's law and with the help of Euler's formula $exp(j\omega t) = cos(\omega t) + jsin(\omega t)$ the impedance can be calculated from the frequency-dependent current and voltage data:

$$\begin{aligned} Z(\omega) = \frac{U(t)}{i(t)} = \frac{U_0 \sin\left[\omega t + \phi(\omega)\right]}{i_0 \sin \omega t} = \frac{U_0 \exp\left(j(\omega t + \phi)\right)}{i_0 \exp\left(j\omega t\right)} = \\ = \frac{U_0(\omega)}{i_0} \exp\left(j\phi(\omega)\right) = |Z(\omega)| \exp\left(j\phi(\omega)\right). \end{aligned} \tag{5.1}$$

Besides the polar coordinates form in Eq. 5.1, the impedance can also be expressed in rectangular coordinates:

$$Z(\omega) = \mathrm{Re}\left\{Z(\omega)\right\} + j\,\mathrm{Im}\left\{Z(\omega)\right\}. \tag{5.2}$$

The measurement is repeated for a variety of frequencies in the SOFC-relevant range between 0.1 Hz and 100 kHz with about 10 measurement points per decade [109]. Thus, the impedance spectrum is obtained from the frequency-dependent

values for phase shift and impedance amount, or the real and imaginary parts. The spectrum then represents the reaction of the cell to the sinusoidal current changes at a certain operating point.

5.2 Representation of EIS Data in the Nyquist Plot

As can be seen from Eq. 5.2, the impedance data shows real and imaginary components. Accordingly, the representation takes place in the complex plane, i.e. as a Nyquist plot. In this representation the x-axis corresponds to the ohmic resistances, the y-axis to the inductances of the measured system. Usually the y-axis is plotted in the inverted direction since the measured inductance has negative values. If positive imaginary components occur, they can be traced back to inductive disturbances in the measurement setup.

Figure 5.2 shows an exemplary Nyquist plot for a cell that was tested in the course of this thesis. For SOFCs two or more arcs usually appear in the Nyquist plot. Several characteristics can be identified from the graph. The intersection of the spectrum with the x-axis at high frequencies ($\omega \rightarrow \text{inf}$) represents the ohmic resistance. According to [36], SOFCs reach the domain influenced only by ohmic resistance at frequencies above 1 MHz. On the other hand, Ohm's resistance can already be estimated reliably with values recorded at 10^4 Hz since the absolute changes in the real part between 10^4 and 10^6 Hz are usually small [122]. The width of the spectrum corresponds to the polarisation resistance. The maximum x-axis part gives the ASR and is equal to the slope of the I-V-curve at the current operating point.

In addition to the constraint of linearity mentioned above, temporal invariance or stability – the system does not change during the measurement – and the causality – the response signal depends exclusively on the excitation signal – of the measurement must be given so that a spectrum can be valid [119]. For this the interdependence between real and imaginary part can be represented by the Kramers-Kronig-transform integrals (KK). With the help of these integrals the imaginary part of a spectrum can be determined from a measured real part [123].

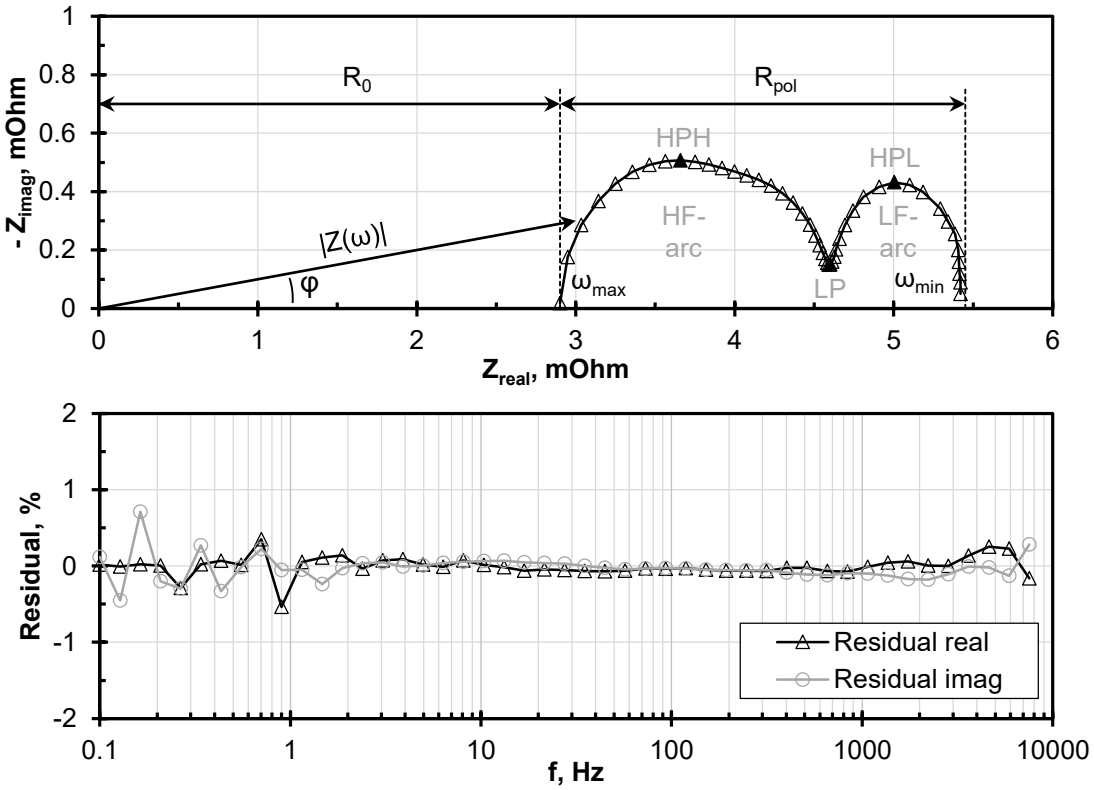

Figure 5.2: Nyquist plot of a typical impedance spectrum of this thesis. HPH: high point of high frequency arc (HF-arc); HPL: high point of low frequency arc (LF-arc); LP: low point between the two arcs. Bottom: According residuals of the Lin-KK-Test for the shown spectrum.

$$Z_{\mathrm{real}}(\omega) = \mathrm{R}_0 + \frac{2}{\pi}\int_0^{\infty} \frac{xZ_{\mathrm{imag}}(x) - \omega Z_{\mathrm{imag}}(\omega)}{x^2 - \omega^2} dx \tag{5.3}$$

$$Z_{\mathrm{imag}}(\omega) = \frac{2\omega}{\pi}\int_0^{\infty} \frac{Z_{\mathrm{real}}(x) - Z_{\mathrm{real}}(\omega)}{x^2 - \omega^2} dx \tag{5.4}$$

If the measured imaginary part does not correspond to the imaginary part determined from the real part, the data must be non-KK transformable and are therefore non-linear or unstable. A tool provided by KIT was used in this thesis to apply the KK-relationships to the measurement data [124]. This tool first approximates

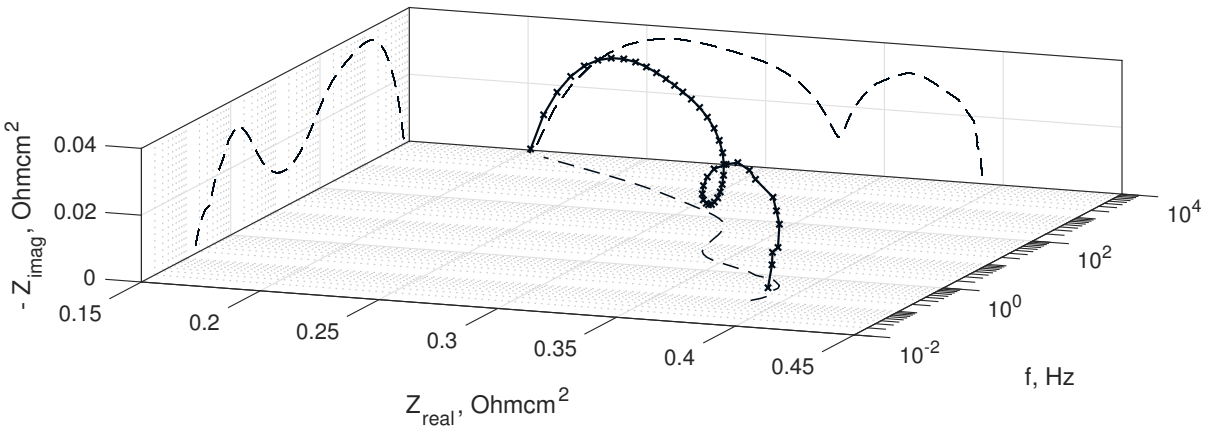

Figure 5.3: Projection of imaginary, real and frequency contribution in impedance data on the coordinate planes.

the measurement data by a sufficiently large number of RC-elements[2] in order to enable the necessary integration. Subsequently the residual between the measured and the imaginary part calculated from the real part is evaluated. For valid measurement data this residual should not be greater than 0.5 % over the entire frequency range, see Figure 5.2 for an example of a valid spectrum. In addition, the residuals should randomly fluctuate over the whole frequency range [123]. In this thesis spectra were only used for further evaluation if the Kramers-Kronig test was valid.

In addition to the Nyquist plot, there are other display options for the impedance data. In Bode diagrams the magnitude and the phase shift of the impedance are plotted over the frequency of the excitation. Depending on the application, one form of representation may be more suitable than another. All two-dimensional representations have in common that never all information contained in the impedance data – frequency, real component, imaginary component, phase shift – can be represented. Figure 5.3 illustrates this by projecting the impedance data onto the coordinate planes.

[2]Parallel connection of a resistor and a capacitor.

5.3 Interpretation of Impedance Data

For the example of a pure ohmic resistance whose impedance is not frequency-dependent, the imaginary part is equal to 0 [120]. In general, a phase shift only occurs if inductive processes are excited in which electrical energy can be stored [119].

To put it in a very simplified way, the fuel cell during impedance measurement can be imagined as a multiple spring pendulum which is oscillated at the upper end and in which each electrochemical process or resistance corresponds to a weight. The first weight corresponds to the ohmic resistance and is rigidly connected to the oscillation source. In contrast to this model, the real electrochemical processes also contain damping elements which lead to additional complexity or non-linearity of the system.

Within this model system there are two limiting cases: 1. Above a certain frequency, apart from the ohmic resistance, no more weight is set into oscillation. The amplitude of the response is then 0 and the measured impedance corresponds to Ohm's resistance. This marks the left end of the impedance spectrum in the Nyquist plot, (see Fig. 5.2). 2. Below a certain frequency all processes are excited and no phase shift occurs, i.e. all weights oscillate in phase with the excitation oscillation. This state corresponds to the right end of the impedance spectrum where no imaginary part is measured and the real part corresponds to the sum of ohmic resistance and all polarisation resistances of the individual electrochemical processes. The total resistance then approaches the value that can be determined from the slope of the I-V-curve for the current operating point of the cell [44].

Starting from the upper limit case more and more electrochemical processes are excited as the excitation frequency decreases. In an ideal system each process has a discrete excitation frequency at which it responds to the excitation signal [125]. In the real system, on the other hand, the response is distributed around an average relaxation time. This is caused by local gradients of gas composition or temperature, for example, that cause processes to run differently well across the cell or by size distribution of grains and pores of the electrodes. By the superposition of the response of the individual processes further resonance states occur which lead to overtones, or states, in which the oscillations can neutralise each other.

The impedance data is often used to develop an equivalent circuit model of the cell (ECM) in which all electrochemical processes are represented [36, 119, 126]. The processes are then modelled with circuits of different elements – resistors, capacitors, inductances – and fitted by adapting the parameters of the elements to the experimental data. The fit-parameters must not only be adapted to individual spectra, but must also fit for all measured reference data. This is associated with very long computing times since up to 500 reference spectra have to be evaluated for a complete ECM [109]. Alternatively, the spectra can first be parametrised to save computing time [127]. Once a meaningful model has been found, degradation mechanisms of the cell can be quantitatively determined if the fit-parameters change. The identification of such an ECM is not trivial since there are multiple processes that affect the impedance and which overlap [125]. On the way to an ECM an analysis of the distribution of the relaxation times is frequently used, see section 5.4, since this provides a statement on the number of processes excited in the impedance analysis – mostly 3 to 6 – and on their excitation frequency [126].

The aim is to create a physically meaningful model in which each element corresponds to an electrochemical process. Ideally, this model can follow all changes in the operating parameters and also offers the possibility of predicting the response of the cell to changes. The pure numerical quality of the model is of secondary importance. Numerical quality can be easily achieved by connecting a sufficiently high number of RC-elements in series, but this does not lead to any added value in the interpretation of the data [128]. Reversely, an ECM with physically meaningful circuit elements can also be used for process identification in the cell by fitting various conceivable elements to the measurement data.

Despite initial activities [129, 130] no satisfactory ECM could be found in this thesis since the EIS data contained too many perturbations. Instead, impedance spectra were interpreted using reference measurements varying operating parameters – temperature, gas composition – and literature data, see section 5.5.

5.4 Distribution of Relaxation Times

Another way to display the impedance data is to calculate the distribution of the relaxation times (DRT) [125]. This delivers a representation of the data where the single electrochemical processes are sorted by their characteristic time constant τ, and thus by the frequency by which they responded to the agitation signal. With the help of DRT, up to three processes per frequency decade can be distinguished. In contrast to the Nyquist or Bode diagrams, the DRT contains both frequency information and information on how much of the total polarisation resistance is accounted for by an electrochemical process.

The first-time application of the DRT on the impedance data of SOFCs and the description of the mathematical basics were done by Schichlein et al. [125]. The relaxation times τ cannot be measured directly because the values from the impedance measurement at a certain frequency ω also contain parts of other relaxation times above and below ω^{-1}. Starting point for the determination of the DRT is a convolution equation based on functional analysis which connects the distribution function with the measured impedance data [131].

$$Z(\omega) = R_0 + Z_{\mathrm{pol}}(\omega) = R_0 + R_{\mathrm{pol}} \int_0^\infty \frac{\gamma(\tau)}{1 + j\omega\tau} d\tau. \tag{5.5}$$

Here $\gamma(\tau)$ is the desired distribution function of the relaxation times, ω is the angular frequency, $Z(\omega)$ is the measured impedance data with the frequency-independent ohmic component R_0 and the polarisation resistance $Z_{\mathrm{pol}}(\omega)$; j is the imaginary unit. The determination of $\gamma(\tau)$ from $Z(\omega)$ cannot be performed analytically since the measurement data is only available in a finite frequency range and therein only at discrete frequencies. To avoid this, Schichlein et al. expressed the frequency-dependent components by a series connection of a finite number of RC-elements [125]:

$$Z_{\mathrm{pol}}(\omega) = \sum_{k=1}^{N} \frac{R_{\mathrm{pol},k}}{1 + j\omega\tau_k} = R_{\mathrm{pol}} \sum_{k=1}^{N} \frac{\gamma_k}{1 + j\omega\tau_k}; \sum_{k=1}^{N} \gamma_k = 1. \tag{5.6}$$

$R_{\mathrm{pol},k} = \gamma_k R_{\mathrm{pol}}$ represents the ohmic resistance and τ_k the relaxation time of the k-th RC element. The sum of all γ_k is equal to 1. The extreme case of a series circuit as in 5.6 with an infinite number of RC elements with relaxation times between 0 and ∞ leads to the equation 5.5. By applying a sufficiently high number of RC elements, a model for the measurement data is obtained which has no physical significance but maps the dynamic behaviour of the system [125].

For the calculation of the DRT either the real or the imaginary part of the measurement data can be evaluated, provided that the correct connection between the measured real and imaginary parts has been checked with the aid of the KK correlations (cf. equations 5.3 and 5.4).

$$Z_{\mathrm{imag}}(\omega) = Z''(\omega) = -R_{\mathrm{pol}} \int_0^\infty \frac{\omega\tau}{1+(\omega\tau)^2}\gamma(\tau)d\tau \tag{5.7}$$

$$Z_{\mathrm{real}}(\omega) = Z'(\omega) = R_0 + R_{\mathrm{pol}} \int_0^\infty \frac{1}{1+(\omega\tau)^2}\gamma(\tau)d\tau \tag{5.8}$$

The solution of one of these convolution products can be done in different ways. Schichlein et al. solved the imaginary components by a Fourier transformation in order to obtain the DRT. For a stable solution during integration the measurement data must be extrapolated beyond the measurement range with an asymptote against $Z'' = Z_{\mathrm{imag}} = 0$. Leonide introduced a solution with the help of Tikhonov regularisation based on the data of the real part [126]. Based on this, a matlab code was developed at LES [132], which solves the numerical problem using the software FTIKREG [133]. The usability and functionality of the Matlab code has been continuously improved in several theses [127, 129, 130, 134]. Central component of this code is the determination of the regularisation parameter λ which decides on the resolution of the DRT [135]. Too fine resolution leads to misinterpretation of noise in the measurement data as electrochemical processes, too coarse resolution leads to existing processes not being mapped, resulting in a too smooth DRT. Meanwhile several commercial or freeware software tools are available for the evaluation of the DRT, e.g. DRTtools [136].

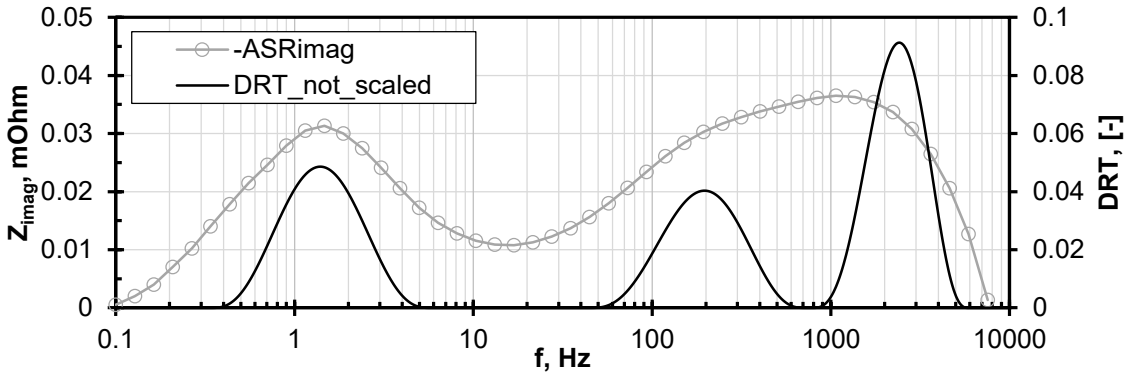

Figure 5.4: DRT for the impedance data shown in Figure 5.2 together with imaginary part.

Figure 5.4 shows the calculated DRT for the impedance data shown in Figure 5.2. In addition, the measured imaginary part of the raw data was plotted. It can be seen that more processes can be identified from the DRT than from the imaginary part alone. Whereas the DRT is calculated for a range of relaxation times τ, on the x-axis of the DRT usually the frequency $f = 1/(2\pi\tau)$ is shown. The DRT can be normalised or non-normalised; the area below the peaks is then either equal to 1 or equal to R_{pol} and the y-axis has accordingly either the unit s or Ohmcm^2. In the first case, the area below a peak indicates the share of a process in the total polarisation resistance, in the second case the absolute ASR caused by a process. In this thesis, normally the non-normalised form is shown. Since the non-normalised DRT is calculated by multiplying the normalised form with R_{pol}, errors in the determination of $R_{\mathrm{pol}} = \max(Z_{\mathrm{real}}) - \min(Z_{\mathrm{real}})$ have a direct influence on the results.

The excitation frequency of an electrochemical process can change with temperature, gas composition and current density. Therefore, the centre frequency, width and area of a peak strongly depend on the set operating conditions [137]. The wider a peak of the DRT, the greater is the non-ideality at its characteristic frequency due to the superposition with fractions of processes with similar relaxation times. Very wide peaks are often influenced by two processes. They can be separated by a systematic change of operating parameters, e.g. the oxygen content at the cathode or the operating temperature.

5.5 Process Identification for Ni/YSZ Anodes

In the following, the processes visible in the EIS data of this work are identified. Literature data is included for this purpose. On the other hand, reference measurements were carried out in which the effect of specific changes of operating parameters on the spectra or on the DRT was investigated. The interpretation is limited to the Ni/YSZ ASCs used in this work with a focus on the CTb cells.

5.5.1 Literature Review on EIS Interpretation

Initially, literature was evaluated in which the impedance data of anode-supported SOFC with Ni/YSZ anode were analysed. Despite the prevalent use of EIS for the characterisation of electrochemical systems, the data available for the exact interpretation of the processes for SOFCs is still sparse. For the Ni/YSZ cells used in this work the selection is even more limited. Therefore, the work of Kromp and Leonide (Karlsruhe Institute of Technology, KIT) is primarily relevant as the measurements were also carried out on Ni/YSZ ASC by Forschungszentrum Jülich [36, 126, 138]. In addition, the most detailed discussion of the DRT method can be found in these papers. Of course, Jülich's cells have continuously been developed further since these publications, which makes the one-to-one transfer of the process interpretations to the measurements in this thesis more difficult[3]. Furthermore, there are relevant papers on Ni/YSZ ASC from the Technical University of Denmark (DTU) and the Politecnico di Torino, for example [139] or [140], which had cells from Risø and SolidPower, respectively.

The DRT was applied to the EIS data by all authors, which is state-of-the-art, in order to interpret the reaction of the different processes to changed operating parameters. Often an ECM was used additionally with which changes of the spectra are converted into quantitative changes of the process variables. In most cases parameters such as cell temperature, fuel utilisation, p_{H_2}/p_{H_2O}, current density and p_{O_2} were varied to interpret the spectra for operation on H_2/H_2O at the anode. For the operation on syngas or reformate further parameters are added with p_{CH_4}, p_{CO} and p_{CO_2} together with further processes like the reforming of CH_4 and the water

[3] I.e. the thickness of the substrate was significantly reduced.

gas shift reaction (WGS) of CO, which influence the electrochemistry indirectly by the production of H_2. The data becomes even more specific when the effects of impurities, such as H_2S [141] or tar [75], are considered.

In the impedance data, processes can be identified which are either directly electrochemical or which cause a polarisation resistance due to their occurrence. For example, the reformation of CH_4 in the anode substrate produces hydrogen, which increases the hydrogen partial pressure at the TPB and promotes electrochemical charge transfer there. In the impedance data however, not the reformation itself is visible, but only the effect on electrochemistry. At the same time only processes for which a resistance has to be overcome are visible in the data. If processes only cause a low resistance at given operating parameters, they do not appear or are covered by more inhibited processes. In order to make them visible a targeted deterioration of the process is necessary. For example, the mass transport at the cathode, which does not occur visibly at the cathode during operation on air as gas, can be distinguished from the processes at the anode by lowering the oxygen partial pressure at the cathode.

For the interpretation of the impedance data or the peaks in the DRT measurements a large variety of parameter sets are therefore necessary until the parameter dependencies of all processes can be recognised or until all processes can be made visible. The characterisation of a new cell type is based on 300 to 500 reference spectra [109]. It has not yet been taken into account that the measurement setup may also have a large influence on the visible processes. For optimal results – apart from the avoidance of inductances – the conditions at the cell have to be as uniformly as possible, which may for example be achieved by a large gas volume flow or small cell sizes. However, if the cells are too small, edge effects can falsify the results.

The results of the interpretation of the impedance data from literature are summarised in the Figure 5.5 and ranked according to the respective excitation frequency or relaxation time. The figure is based on the data in [36, 139, 140, 142]. Depending on the test setup, the cell and the accuracy of the operating parameters, the frequency ranges of the processes are specified more in a wider or narrower way in literature. Consequently, the areas in which a process can occur are kept wide in the diagram. As already mentioned above, there are processes that directly

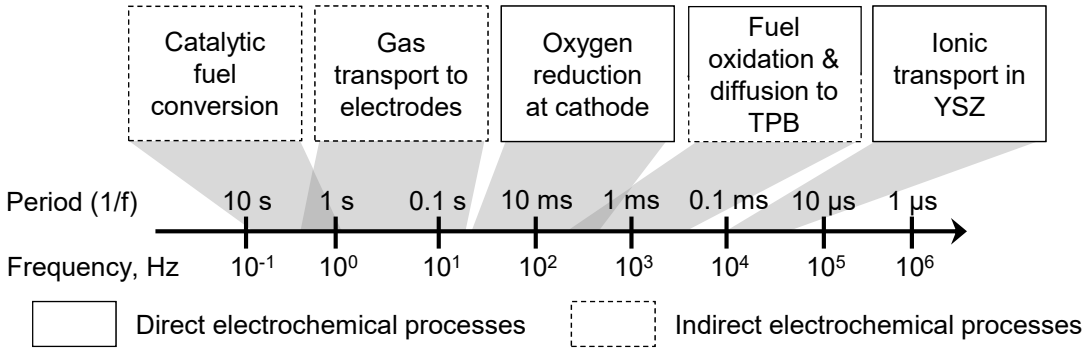

Figure 5.5: Order of the processes identifiable in the impedance data based on the frequency range in which they are excited. [36, 139, 140, 142].

influence electrochemistry – oxygen reduction, fuel gas oxidation, ion transport – and those that only have an indirect influence – fuel conversion reactions, gas transport.

The ohmic resistance in the electrical conductors is not frequency-dependent and is therefore not shown in the figure. The fastest frequency-dependent process in the impedance data is the ion transport of oxygen ions from the cathode through the dense YSZ of the electrolyte to the anode at frequencies >10 kHz. At lower frequencies up to 200 Hz, the processes at the TPB of the anode layer are excited. Several physical processes occur: the O^{2-}-transport into and out of the YSZ of the anode; the charge transfer at the interface Ni/YSZ/gas phase, in which oxygen ions, electrons and H_2/H_2O are involved; the dissociative adsorption of H_2 and the desorption of H_2O [143]; the diffusion of H_2 and H_2O to and away from the TPB. For state-of-the-art cells the thickness of the anode layer is such that gas diffusion in this finely pored layer is not limiting[4]. Since the processes at the TPB are complex and depend on several material and operating parameters, even with EIS they cannot be observed completely separately. In EIS one usually only sees the net response to the excitation frequency, which is characterised by a limiting step. Nevertheless, with the help of DRT it can be estimated that the diffusion processes to the TPB are rather excited at frequencies of several 100 Hz and the other processes at several 1000 Hz.

[4]Cells in this thesis: $d_{\text{anode}} \approx 7\mu m$ [40]

In the frequency range from 2 to 500 Hz the reduction of O_2 and the transition of O^{2-}-ions into the cathode structure take place at the cathode. At rather low frequencies <10 Hz both the mass transport in the cathode and in the anode substrate are excited which overlap in the spectra. During operation on air the transport resistances at the cathode can be neglected [126]. At the fuel gas side the transport strongly depends on the porosity and morphology of the substrate. Both reactant (H_2) and product (H_2O) must be transported to or away from the anode.

The slowest processes are the conversion reactions that take place on the Ni of the anode substrate, i.e. the reforming of CH_4, the water gas shift of CO and also the cracking of tars and other higher hydrocarbons. The excitation frequency depends on the respective reaction kinetics. Due to the production of H_2 and the consumption of H_2O, the conversion reactions also influence the processes at the triple phase boundaries.

For completeness it should be mentioned at this point that also mass transport outside the cell can appear in impedance data. Thus Sonn et al. [137] assigned processes at 10 and 200 Hz to gas transport in the flow-field and in the contact grids, respectively. In their work symmetrical cells with thin Ni/YSZ anodes on an electrolyte were used as support in which the anode is in direct contact with the gas flow. In contrast, in anode-supported cells the anode substrate separates the anode and the convective gas flow in the channels or contact network. As a result, an oscillating consumption of hydrogen due to the excitation current of the EIS measurement is dampened by the 10 times slower mass transport through the substrate and is not directly dependent on the gas flow in the channel.

5.5.2 Reference Spectra

In the following section reference spectra are used to interpret the processes identifiable in the impedance data of this work. Due to cell size the set conditions are not constant over the whole cell. The already existing coupling of several processes at the SOFC therefore becomes even more complex through the superposition of gradients in temperature and gas composition. Consequently, the effect of manip-

ulation of one operating parameter cannot always be clearly delimited since for example a higher current density affects the gas composition and at the same time the temperatures at the cell change to different degrees. Although it was possible to compensate for the global temperature fluctuation in the existing measurement setup by adjusting the furnace temperature, altered temperature gradients could not be compensated in this way. A definite assignment of the observed peaks is avoided in this work since the processes visible in the data always resulted from the superposition of several different and/or locally distributed processes. Since the same phenomena also occur during impedance measurements in SOFC stacks, the measurements of this work are an important step towards characterisation during real operation.

Although it has been said above that the DRT has the advantage of combining polarisation resistance and frequency dependency, the following interpretation is also based on the Bode diagrams and the evolution of the shape of the spectra using the characteristic points drawn in the schematic Nyquist plot (Figure 5.2). Otherwise more extensive pre-processing of the impedance data would have been necessary to prevent noise in the measurement data from being interpreted as additional DRT peaks. Nevertheless, the DRT was basically used to limit the number and frequency range of existing processes.

The reference spectra shown were recorded on CTb cells as these were characterised by a very high reproducibility due to their industrial production. Only the study *CO* was performed on a TypIIIb cell. Most of the spectra were recorded in the course of students' theses and partly evaluated [127, 129, 130, 134]. In almost all spectra three peaks were visible, which were approximately at 1-2 Hz, 100-200 Hz and 1-2 kHz. Due to the strong inductances under load above 9.6 kHz, the fastest processes, especially ion transport, could not be visualised and, as already mentioned, for the same reason the smallest real part did not correspond exactly to the ohmic resistance of the cells.

Table 5.1 gives an overview of the studies carried out. The parameters furnace temperature, methane and carbon monoxide content in the syngas, H_2O content in H_2/H_2O mixtures and oxygen content at the cathode were varied. The Figures 5.6 and 5.7 show the impedance data during the study *Temp1*, the variation of the furnace temperature between 680 and 730 °C. The cell was operated on syngas un-

Table 5.1: List of studies conducted for process identification.

	Temp1	**Temp2***	**CH4***	**CO**	**Steam**	**O2_H2**	**O2_Syn**
H_2, Nl/min	0.25	0.5	0.25	0.25	**1-0.43**	1	0.25
CO, Nl/min	0.1	0	0.1	**0-0.1**	0	0	0.1
CO_2, Nl/min	0.1	0	0.1	0.1	0	0	0.1
CH_4, Nl/min	0.05	0	**0-0.05**	0.05	0	0	0.05
H_2O, Nl/min	0.5	0.074	0.5	0.5	**0.053-0.986**	0.078	0.5
N_2, Nl/min	0	0	**0.05-0**	**0.1-0**	0	0	0
$O_{2\ C}$, Nl/min	0.42	0.42	0.42	0.42	1	**1/0.75/0.5/0.1**	**1.00/0.4**2
$N_{2\ C}$, Nl/min	1.58	1.58	1.58	1.58	0	**0/0.25/0.5/0**	**0/1.58**
Current, A	24.3	15.6	15.6	24.3	0	0	24.3
Furnace, °C	**680-730**	**900-700**	700	700	900	700	700
Cell	C52	C57	C51	C65"	C47	C47	C47

" TypIIIb

* Part of general start-up procedure

der load. The constant parameters are shown in Table 5.1. For the other reference spectra the corresponding figures can be found in appendix C. Before the visible effects are discussed, the types of representation are going to be described.

Figure 5.6 a shows the EIS data of *Temp1* in the complex plane, i.e. the Nyquist plot. In 5.6 b the imaginary part (Z_{imag}) of the characteristic points of the spectra as shown in Figure 5.2 is plotted over the furnace temperature. This corresponds to the projection of the Nyquist plots on the imaginary axis, which is also illustrated by the arrangement of the diagrams. In 5.6 c the real part (Z_{real}) of HPL, LP and HPH as well as R_0 and R_{pol} are plotted analogously, which corresponds to the projection on the real axis. In the same plot the cell voltage at the beginning of the respective EIS measurement is included. In 5.6 d the DRT and the imaginary part plotted over the excitation frequency are compared for the first and last measuring point, as already shown in Figure 5.4. The left plots of Figure 5.7 show the development of total impedance (5.7 a), imaginary part (5.7 c) and DRT (5.7 e) during parameter change. Total impedance and imaginary part are plotted over the excitation frequency, which corresponds to the Bode plots. In the right plots 5.7 b, d and e the difference to a reference measuring point was formed, usually the first or last point of a study. This allows to clearly identify the frequency ranges in which the impedance data had changed the most.

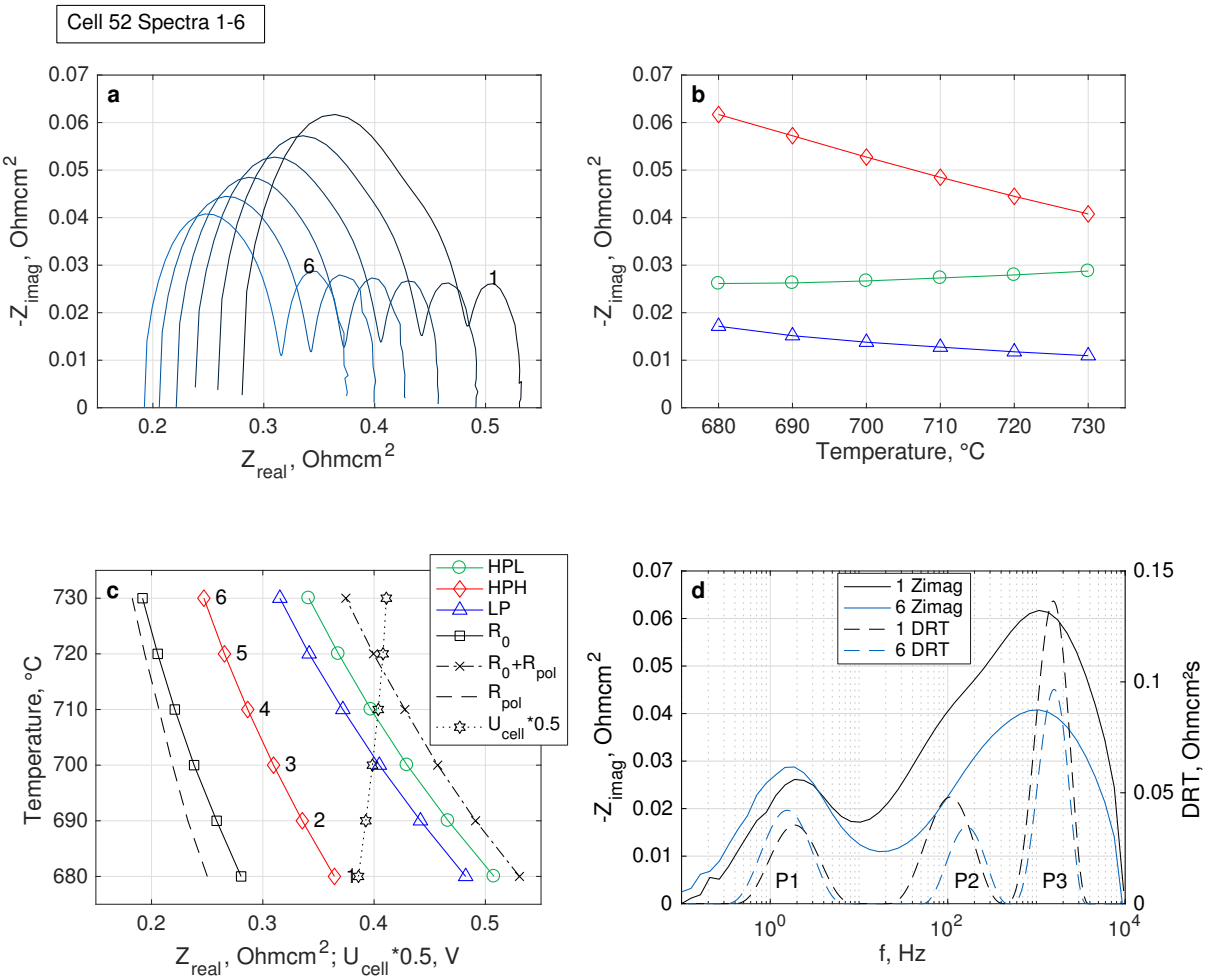

Figure 5.6: Impedance data for variation of furnace temperature at syngas operation (Study *Temp1*). 1: 680, 2: 690, 3: 700, 4: 710, 5: 720, 6: 730 °C. Other operation conditions see Table 5.1. C52.

Effect of small temperature changes (Study *Temp1*)

Even in a relatively small interval of 680 to 730 °C, the temperature had a strong influence on the processes at the SOFC. First, it can be clearly seen that both the ohmic resistance and the polarisation resistance decreased in this range with increasing temperature (Figure 5.6 c). The development of R_{pol} can be analysed even more precisely. Both the height and the width of the HF-arc decreased significantly with increasing temperature, see the trend of HPH in Figure 5.6 b and of LP in Figure 5.6 c, respectively.

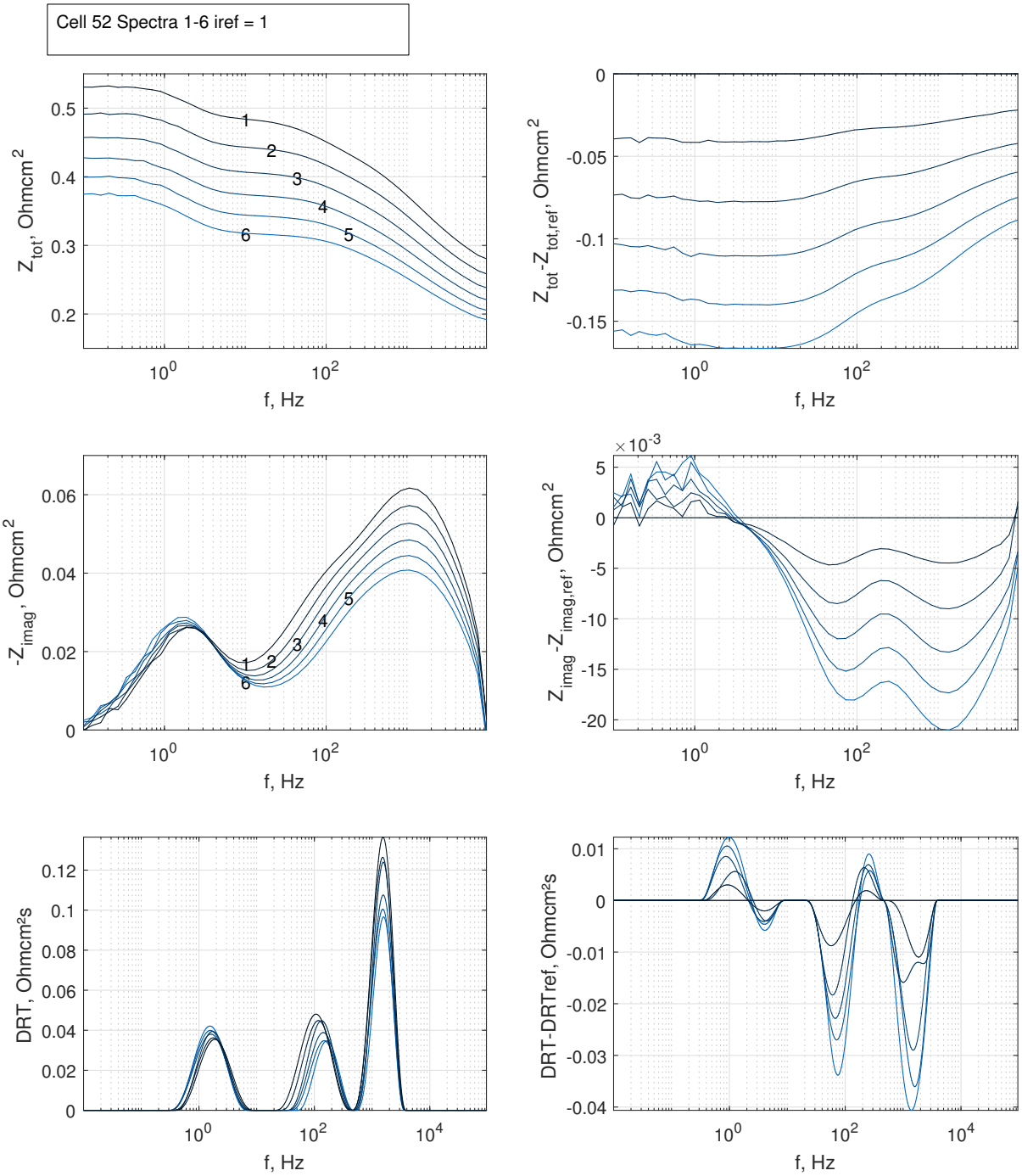

Figure 5.7: Bode-plots and DRT for variation of furnace temperature at syngas operation (Study *Temp1*). 1: 680, 2: 690, 3: 700, 4: 710, 5: 720, 6: 730 °C. Other operation conditions see Table 5.1. C52.

The LF-arc, on the other hand, grew slightly with temperature and was otherwise shifted horizontally by the HF-arc. The same can be seen in the DRT (5.7 e), where the two peaks at high frequencies (P2 at 100-200 Hz and P3 at 1-2 kHz) decreased with increasing temperature while P1 remained approximately constant. P2 shifted to higher frequencies. Figure 5.7 d also shows clearly that with increasing temperature the imaginary part of the higher frequencies decreased. It becomes clear again that the higher frequencies were characterised by two processes. In this respect processes with low or pronounced temperature dependence can be identified. The electrochemical electrode reactions at the TPB, for which activation energy has to be applied as for any other chemical reaction, are strongly temperature-dependent, whereas the mass transport is less influenced by temperature [144]. Consequently, it can be concluded from this study that the HF-arc (P2 and P3) maps processes at the TPB, while the LF-arc (P1) is characterised by mass transport phenomena.

The analysis of this temperature variation is important because it shows that even a relatively small change in temperature around 700 °C has a large influence on the impedance data. When the type of gas is changed or the current is increased, the cell temperature can change by several K at constant furnace temperature. This means that the temperature influence is always superimposed on the actual parameter change. It was not ensured for all reference measurements that the temperature of the cell remained constant. And even if this was the case, only the mean temperature could be adjusted while the temperature distribution was always subject to slight changes.

Effect of temperature increase from 700 to 900 °C (Study *Temp2*)

The Figures C.1 and C.2 in appendix C show the result of the study *Temp2*, in which the furnace temperature was varied between 700 and 900 °C in 40 K steps. The cell was operated at 15.6 A with 0.5 Nl/min H_2 plus 0.074 Nl/min, i.e. 13 vol% steam, at the anode and 2 Nl/min air at the cathode. Despite the different fuel gas composition, the same trends were observed for the shape of the spectra as for study *Temp1*. The Z_{real} curves did not continue linearly in the large temperature range, but inverse-exponentially (Fig. C.1 c). The same applied to the height of the HF-arc, which confirms that it is characterised by thermally activated processes. On

the other hand, polarisation resistance in the LF-arc increased steadily (Fig. C.1 b and c). The assumption that the LF-arc is characterised by mass transport through the anode substrate can explain this behaviour: while the fuel diffusion through the substrate is only slightly improved with increasing temperature [126], the gas density in the channels of the flow-field decreases reciprocally to the temperature. Due to the reduced density, the concentration gradient between channel and anode layer decreases, which reduces the overall mass transport.

From 820 to 900 °C R_{pol} did not decrease further in contrast to R_0 because the decrease of the HF-arc was compensated by the increase of the LF-arc. The overpotential of the cell, defined by the difference between calculated OCV(T) and actual cell voltage, behaved proportionally to R_{tot} respectively to the ASR, see Fig. C.1 c.

In the spectra at 860 and 900 °C it is noticeable that a plateau had formed between the HF- and LF-arcs (Fig. C.1 a). As can be seen from the DRT, P2 split into several smaller peaks at high temperatures; P3 was not divided. That way additional processes had became visible at the higher frequencies at high temperatures. At 700 °C the processes behind P2 and P3 limited cell performance. This led to only two large peaks which covered other processes. At higher temperatures the processes behind P2 and P3 were ameliorated so that also other processes became visible in the data. Since the aim of the investigations presented here was to identify the processes that occur at the operating point of the experiments in the following chapters at 700 °C, the effects at high temperatures are not discussed in more detail.

Effect of methane concentration (Study *CH4*)

The presence of CH_4 in the fuel gas has several effects on the processes in the cell: by reforming on Ni of the anode substrate more H_2 is available; the reforming requires heat and therefore lowers the local temperature at the cell depending on the reaction rate; the reforming consumes water and thereby lowers $p_{\mathrm{H_2O}}$. In the *CH4* study the methane volume flow in syngas operation at 15.6 A and 700 °C was

increased from 0 to 0.05 Nl/min in 0.01 steps, see Figures C.3 and C.4. The total volume flow of 1 Nl/min was kept constant with nitrogen. The inlet temperature had decreased by 8 K, the temperature in the middle of the cell by 3 K since the methane was almost completely converted into CO_2, CO and H_2. The cell voltage increased by 25 mV in response to the higher H_2 concentration.

In the impedance data the increase of CH_4 was expressed by a reduction of the LF-arc. Accordingly, P1 (1-2 Hz) became smaller in the DRT. The explanation is that with more CH_4 more H_2 was formed in the substrate by reforming, which improved the mass transport of H_2 to the anode layer. This corresponds to the frequency range of this process given in literature while the gas reactions only become visible at lower frequencies, see Figure 5.5. R_{pol} remained nearly constant during the increase of the methane fraction, R_0 tended to increase. The HF-arc increased slightly, see Fig. C.4 d. This may be related to the superimposed local temperature reduction and the reduced water content due to reforming, see results from the study *Steam*. The fact that the higher hydrogen concentration due to CH_4 reforming had no stronger effects on P2 and P3 (Fig. C.4 e) corresponds well with the assumption described above that these peaks are processes at the TPB which are thermally activated. This means that at the selected operating point the temperature had a limiting effect on these processes and a higher hydrogen concentration could not improve them.

Effect of carbon monoxide concentration (Study *CO*)

For methane there is agreement in literature that it is reformed first and that only the resulting hydrogen is oxidised. For carbon monoxide there are different statements to be found. However, it can be assumed that at the studies operating point CO at first forms H_2 with H_2O, which is converted into electricity, and that CO is not directly oxidised electrochemically, see section 2.2.3. It should be noted that the electrochemical reaction of H_2 is significantly faster than that of CO [58] and CO is therefore hardly converted as long as H_2 is present in the fuel gas [54]. An evaluation of the reaction equilibrium in Aspen Plus for the standard syngas composition at 700 °C showed that at OCC almost as much CO leaves the cell as is supplied to it. Under load approximately 1/3 of it is converted because the

reaction product H_2 is consumed and water is formed during power generation. In order to obtain a reliable statement on the visible processes in the EIS data, these must be linked to the results of an analysis of the anode exhaust gas and both CO content and current density must be varied.

Overall, the variation of the CO content (study *CO*) showed a similar behaviour as the variation of the methane content. The CO content in the syngas at 24.3 A was increased from 0 to 0.1 Nl/min in 0.02 steps, see Figures C.5 and C.6. The total volume flow of 1 Nl/min was kept constant with nitrogen. The cell type here was TypIIIb. The cell temperatures were approximately constant at a furnace temperature of 700 °C. Between the first and last measuring point the cell voltage increased by 14 mV. The offset between spectrum 27 and 28 probably resulted from the change of the laboratory ventilation to night operation even if this change was not visible in cell temperature or pressure data. From the third measuring point onwards the DRT had four peaks, which is why these data are not evaluated. As with the methane variation, the LF-arc mainly changed; it became smaller with increasing CO volume flow, see Figure C.6 b and c. As with CH_4 this decrease is attributed to H_2 formation in the substrate, which improved mass transport with increasing CO content. A substitution of CO by H_2 not shown here had no influence on impedance data or on cell voltage in another study not shown here.

Variation of H_2/H_2O ratio (Study *Steam*)

In the study *Steam* the effect of a varying water content in the fuel gas was investigated, see Figure 5.8. The measurements were carried out at 900 °C and OCC. The steam content was varied between 5.3 and 69.6 vol% H_2O. According to the OCV measured at the first set point, there were additional 1.6 percentage points of water vapour in the fuel gas, which was caused by leakage from the combustion of H_2 with O_2 (cell voltage U=1.042 V). Due to a faulty test procedure, not only the steam content but also the total volume flow at the anode changed. Nonetheless, this data is discussed for the purpose of completeness.

A priori it could be assumed that an increase in water content, i.e. a higher concentration of the product of the electrochemical oxidation reaction, leads to

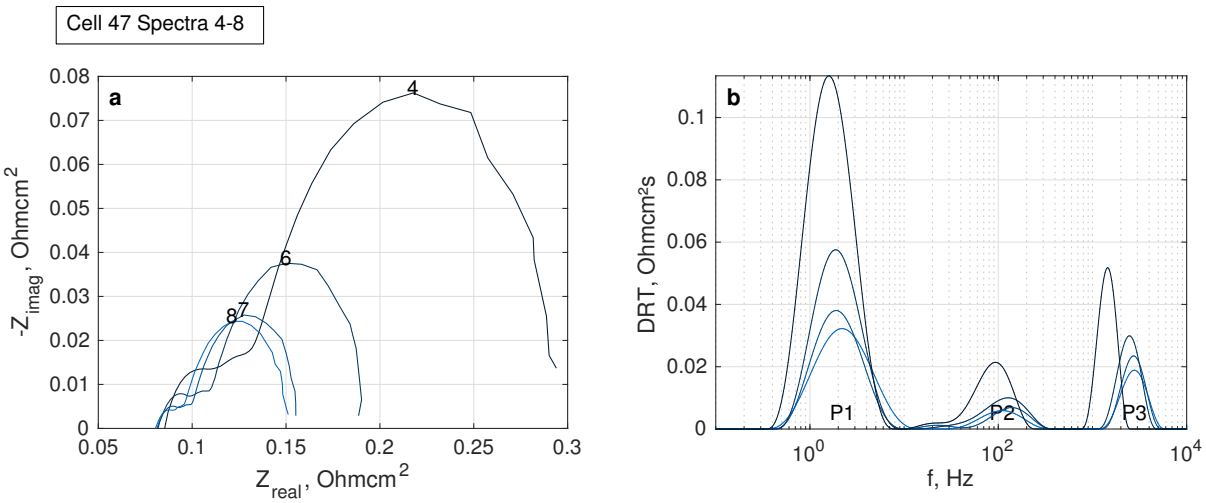

Figure 5.8: Nyquist plot and DRT resulting from variation of steam contents at 900 °C and OCC (Study *Steam*). 4: 5.3, 6: 16.4, 7: 37.5, 8: 69.6 vol% H_2O. Other operation conditions see Table 5.1. C47.

an increase in the polarisation resistance for the relative processes. However, as can be seen from the Nyquist plot, the opposite was the case. At approximately constant R_0 the width and height of the spectra and the height of all peaks in the DRT decreased significantly. These observations are consistent with those of Leonide [126], who varied the vapour content at 757 °C and OCC. The behaviour can be explained by the Nernst voltage as a function of the proportion of water vapour in the fuel gas:

The maximum measured real part of the impedance data R_{tot} corresponds to the ASR which in turn equals the slope or derivative of the I-V-curve. Starting from $y_{H_2O} = 0$, the Nernst voltage decreases with decreasing slope when water vapour content is increased, which leads to its initially left-curved progression. In addition, at open circuit conditions there is an equilibrium between the forward and backward reaction of the electrochemical H_2 oxidation [18]. If a high amount of H_2O is supplied to the anode, the equilibrium shifts to the product side causing the cell voltage to decrease. This leads to the formation of H_2 and O^{2-} from water, which no longer have to be transported from the gas phase but can accumulate at the triple phase boundaries and thus reduce the polarisation resistance. If, on the

other hand, no water is supplied via the gas phase, no back reaction can take place and the area specific resistance is increased. This is consistent with the theoretical considerations of Kim et al [144] who stated that the drier the gas the higher the resulting polarisation resistance[5] at $i = 0$.

This also explains why the LF-arc became smaller. Its width and height were reduced by half from 5.3 to 16.4 vol% steam content, which contributed significantly to the reduction of the polarisation resistance. Due to the accumulation of reactants at the TPB with increasing water content, transport through the substrate loses importance. The same applies to the supply of oxygen at the cathode, which is excited at similar frequencies, see following section.

The study was conducted at OCC. If the current was increased, according to the course of the I-V-curve the polarisation resistance would also initially decrease if the steam content was low. It is to be expected that the polarisation resistance at higher current densities will no longer decrease with the increase in water content but will then be limited by concentration polarisation, resulting in an increase in ASR. This occurs when electrochemical oxidation is limited by too slow a removal of water or too slow a supply of hydrogen.

Variation of cathode oxygen supply (Studies *O2_H2* and *O2_Syn*)

While the focus has been on processes at the anode so far, the oxygen content at the cathode has been varied in two further studies. For the measurements the air supply of the test stand had to be adapted in order to be able to dose mixtures of N_2 and O_2 or pure O_2 at the cathode. The O_2 volume flow was regulated with an analogue flow regulator, which is why the values were less accurate than those of the other volume flows and were not logged automatically.

In the study *O2_H2* the oxygen content was first reduced from 100 to 50 vol% at 700 °C and OCC at a total volume flow of 1 Nl/min with nitrogen as balance. At the last set point 0.1 Nl/min of pure O_2 flowed at the cathode. Fuel gas flow at the anode was 1 Nl/min humidified hydrogen during the whole study. The results are shown in the Figures C.7 and C.8. The LF-arc was most strongly affected and

[5] Identified by the authors as concentration polarisation, which for anode-supported cells also occurs at OCC.

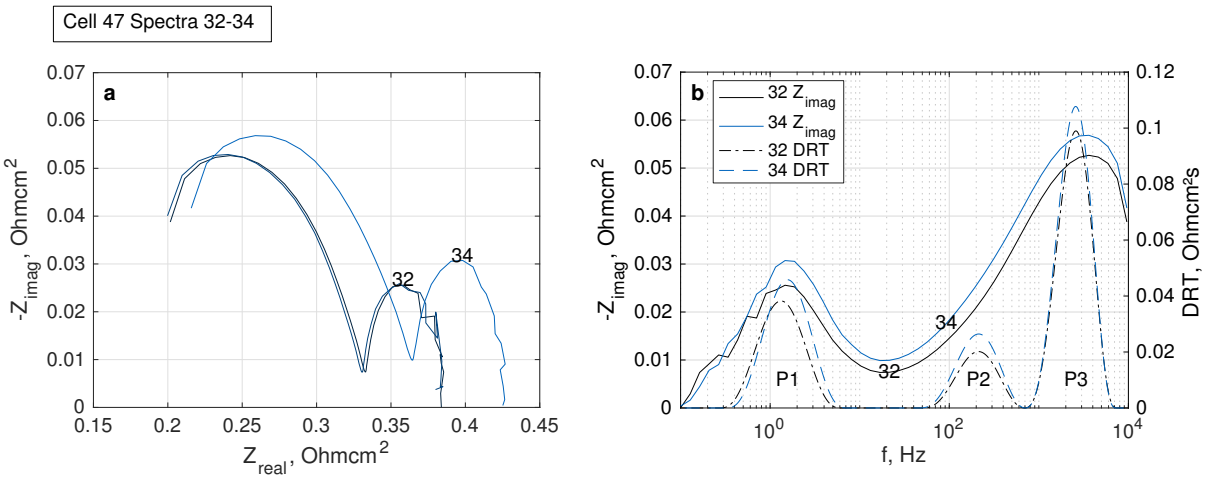

Figure 5.9: Nyquist plot (left), Bode-plot and DRT (right) resulting from variation of cathode gas composition at syngas operation (Study *O2_Syn*). 32& 33: 1 Nl/min O_2, 34: 2 Nl/min air. Other operation conditions see Table 5.1. C47.

grew with the decrease of O_2 content. This corresponds to the assumption that in this frequency range, as at the anode, the mass transport is stimulated. Since no substrate layer has to be overcome at the cathode, the visible process was probably the transport of O_2 from the gas phase to the cathode layer.

Since $Z_{\text{imag}}(f_{\text{max}}) < 0$ and the HF-arc therefore was still wide open, the validity of R_0 and R_{pol} is weakened. This also affects the quality of the DRT results which are directly related to the value of R_{pol}. Disregarding this inaccuracy P1 decreased the most with more oxygen at the cathode, analogous to the LF-arc. P2 and P3 also decreased slightly, but P2 decreased more than P3. P3 was probably hardly affected again because no current was drawn during the study.

A change of the cathode gas flow from 1 Nl/min O_2 to 2 Nl/min air (study *O2_Syn*) led to the alterations in the EIS data shown in Figure 5.9. The fact that the spectrum with air at the cathode was shifted to higher real parts is presumably a consequence of the superimposed decrease of the cell temperature by 8 K. The same explanation applies to the increased imaginary parts at high frequencies. The increase of the low-frequency contributions, on the other hand, is associated with the extenuated mass transport due to the lower oxygen supply since this process is not thermally activated. Nevertheless, the increase of the LF-arc was only small,

which means that the mass transport during air operation is not limiting for the cell performance and consequently does not cause a large part of the polarisation resistance [126]. This is not surprising as the structure and porosity of the LSCF cathode have been designed for operation on air at the cathode.

5.5.3 Resumé

Based on literature data in section 5.5.1 and the observations on the reference spectra shown in section 5.5.2, the following interpretation is proposed for the impedance data of this thesis regarding the processes at the anode:

- Process/Peak 1 at approximately 1 to 2 Hz represents the resistance caused by **gas diffusion through the anode support** from the flow-field to the anode layer.
- Process/Peak 2 at approximately 200 Hz represents the resistance caused by **fuel diffusion in the anode layer** in close proximity to the TPB.
- Process/Peak 3 at approximately 1 to 2 kHz represents the **charge transfer reactions at the TPB** of the anode.

Due to the limitation of the measuring range, the ion transport is not shown in the data. It should become visible at frequencies above 10 kHz. The processes of peak 2 and 3 are closely linked. The HF-arc in the Nyquist plot is therefore shaped by both together, while the LF-arc depends on the process at 1 to 2 Hz. The following points should be noted about the reference measurements and their interpretation:

- The interpretation is only valid for the Ni/YSZ ASCs measured in this thesis.
- The interpretation is valid for operating temperatures around 700 °C. It has not been discussed which other processes become visible at 900 °C when the polarisation resistance of the HF-contributions decreased.
- Due to the concentration and temperature gradients at the cell, only net effects are visible in the EIS data caused by the superposition of locally different process conditions.
- For a more precise identification of the processes measurements on smaller

cells, e.g. 5x5 cm^2, where the gradients are less pronounced, are advisable.

- In contrast to spectra in literature, almost always only three processes were visible in the data of this work. In order to be able to resolve more processes, operating parameters would have to be set at which the above-mentioned processes behind P1, P2 and P3 cause less resistance.
- In addition, the parameters for reference measurements would have to be varied in smaller steps in order to resolve the dependencies more precisely and to be able to compensate for faulty measurements.
- The following additional reference measurements are useful if new CTb cells are available: Variation of the water vapour content at 700 °C and in syngas operation and under load; measurements with virtually pre-reformed syngas; replacement of CH_4 by equivalent amount of H_2.
- The reference measurements are integral components of impedance spectroscopy and must therefore be systematically planned and performed. It is also necessary to repeat the measurements on different cells of the same or different type.
- The application of a physically meaningful ECM to the measurement data is not advised due to the described uncertainties. However, a pseudo ECM for the purpose of parameterising the impedance data for automated evaluation is possible.
- In SOFC-stacks uneven conditions exist not only at cell level, but also along the height of the stack, which further reduces the accuracy of EIS data. The results shown here are realistic and therefore relevant for the application of EIS in stacks.

For the investigation of the effects of model tars on cell performance the evaluation of the impedance data provided a valuable source of information as a supplement to the other static measurements. EIS spectra were regularly recorded during operation with or without tars to detect changes in electrochemical processes. On the other hand, each cell was characterised with the help of the two studies *Temp2* and *CH4* in the beginning in order to be able to stop measurements on malfunctioning cells at an early stage. In the next two chapters the results of the investigations

with naphthalene and phenol as model tars are shown, whereby in particular the influence of naphthalene on electrochemistry could be mapped very well with EIS.

Chapter 6

Effects of Naphthalene as Model Tar

In the following chapter results from single-cell and a short-stack tests with naphthalene as model tar are presented. Parts of the single-cell tests were already published in [72]. Naphthalene was chosen as a model tar because, like phenol, it is one of the most frequent tar components in bio-syngas [98]. Naphthalene ($C_{10}H_8$) consists of two condensed benzene rings and is a tertiary tar [59]. The molecule is very stable and is formed in the gasifier at high temperatures by recombination of secondary tars. The odour of naphthalene is known from its use in mothballs although it has no insecticidal effect. Furthermore, it is carcinogenic and dangerous for the environment [145]. For all tests naphthalene of a purity of >99 % was used (Naphthalene 99+%, Alfa Aesar).

6.1 Single-Cell Tests with Naphthalene

In the following the single-cell investigations with the model tar naphthalene on CTb and IIIb Ni/YSZ ASC but also on cells with GDC-anode are presented. The single-cell test rig described in section 4.2 was used for the tests. All measurements were done at standard test conditions, see Table 6.1. The presence of naphthalene in the fuel gas was checked by the SPA method [117], which always showed positive results of the appropriate magnitude.

All in all the results for six cells that were tested with different naphthalene concentrations and dosing times are shown. At C50 0.4 g/Nm^3 of naphthalene were dosed twice, at C60 the dosage took place with the same concentration but for a

Table 6.1: Standard test conditions for the tests with naphthalene as model tar.

Parameter	Value
Cell size	10 x 10 cm^2
Contacted area	72 cm^2
Reduction conditions	900 °C, 0.5 Nl/min H_2, min. 4 h
Operation temperature	700 °C
Fuel gas (syngas), vol%	50 H_2O, 25 H_2, 10 CO, 10 CO_2, 5 CH_4
Flow anode	1 Nl/min
Flow cathode	2 Nl/min (compressed air)
Pressure	0.94-0.98 bara
Electrical load	24.3 A = 0.34 A/cm^2
Load on cell housing	400 N

longer time. In addition an active regeneration of the cell was carried out at C60 by increasing the furnace temperature. At C54 and C55 the naphthalene concentration was also 0.4 g/Nm^3, but due to their GDC anode they behaved significantly different than the cells with YSZ anode (C50, C51, C60, C61). C51 was exposed to 2.5 g/Nm^3 naphthalene and at C61 also 0.5 g/Nm^3 phenol was dosed in addition to 0.1 g/Nm^3 naphthalene.

6.1.1 Repeated Dosing of 0.4 g/Nm^3 Naphthalene

In the following the procedure and the test results of a repeated dosage of 0.4 g/Nm^3 naphthalene are described. The tested cell was C50, a CTb-cell.

After the standardised initial phase, during which the reduction of the anode and the recording of reference impedance spectra took place, and after 64 hours of operation on clean syngas, 50 ml of the CO_2 volume flow was passed through the heated naphthalene container. At an average container temperature of 54.4 °C (+/- 1 K), 0.42 g/Nm^3 (+/- 0.03 g/Nm^3) of naphthalene was added to the syngas, corresponding to approximately 75 ppm.

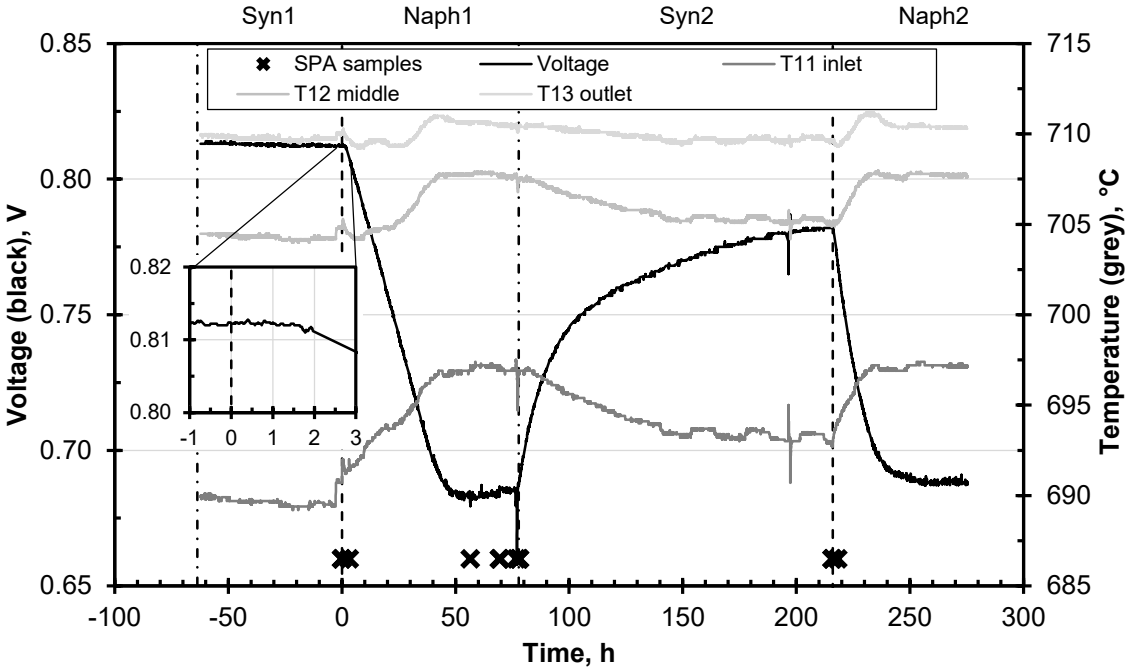

Figure 6.1: Cell potential and temperatures during operation on clean syngas (Syn1 and Syn2) and syngas plus 0.4 g/Nm^3 naphthalene (Naph1 and Naph2). C50, CTb. Operation conditions see Table 6.1.

Interestingly the voltage signal only reacted to the presence of naphthalene with a delay of 1.5 h, see Figure 6.1, whereas the theoretical residence time in the tubing between tar container and cell was < 1 min[1]. The voltage then dropped at a constant rate until it settled on a plateau approximately 130 mV below the initial voltage. Similar behaviour was observed for naphthalene by Dekker et al. or Hauth et al. [77, 146]. Poisoning with H_2S also leads to an analogous voltage curve [54, 139]. Reaching the plateau the voltage signal became more and more noisy. This was probably due to the fact that naphthalene constantly blocked TPBs and then these were cleared by reforming the naphthalene again. After the cell voltage was in this stationary state for about 24 h, the naphthalene supply was switched off. As a result the voltage recovered immediately but at a decreasing rate[2]. The progression of the signal suggests that it would not have reached its

[1]So in a real system no effect on performance would be visible in the case of a short-term failure of tar removal.

[2]A function of the form $U_{\mathrm{fit}} = 1/((t - b_{\mathrm{a}})^{b_{\mathrm{b}}}) + b_{\mathrm{c}}$ can be fitted to the voltage data, see next

original level within a reasonable time span. After a regeneration phase of 138 h on pure syngas naphthalene was dosed again which made the voltage drop – this time without delay – and stabilise again on a similar level. However, unlike the first dosing, it took longer for the voltage to become stationary and the maximum rate of voltage decrease was higher.

In parallel with the decreasing voltage rising temperatures were recorded with all nine thermocouples (TC) placed on the cell. The trends of the temperature at the fuel inlet, mid of cell, and fuel outlet are shown as darker to lighter grey curves, respectively, in Figure 6.1. The temperatures at the entry of the cell (distance in flow direction between the entry tube and $TC_{i,1}$ was 12.5 mm, positions see Fig. 4.4) increased instantaneously at a constant rate and became stationary at the same time as the cell voltage. The temperatures at the outlet (distance in flow direction between $TC_{i,3}$ and outlet pipe was 12.5 mm) first decreased slightly and then also increased after half of the period of constant voltage decrease.

This behaviour, which was also observed by Hauth et al. [76], stems from the competition between methane and naphthalene reforming in the anode substrate. The latter is slower and therefore inhibits the conversion of methane [64, 147]. Due to the reduced reforming rate less heat was consumed compared to operation on clean gas, which caused the temperature rise. Furthermore, according to the reduced cell voltage, an increased share of the available chemical exergy of the fuel is converted into heat. The fact that the temperatures at the outlet first dropped and then rose indicates a methane reforming inhibition front migrating across the cell. This front was driven by the condition that more and more of the cell surface was poisoned by naphthalene and less methane could be converted in these areas. In the areas further downstream where more methane reforming could then take place, the temperature dropped briefly due to the endothermic character of the reaction only to rise again as soon as naphthalene arrived there. The increase at the thermocouples at the outlet was less pronounced than that at the inlet. This is due to the fact that during normal operation the greater part of methane was reformed at the inlet and therefore the temperatures there could rise more strongly and that the methane was converted by the progressive poisoning on a larger area. The increase of temperatures at the outlet due to naphthalene

section 6.1.2

poisoning could either indicate that CH_4 was also converted at the cell outlet during normal operation. Or it might be caused by less cooling of the anode gas in the upstream cell areas due to less reforming or by the stronger generation of waste heat, when the cell potential decreased above or a combination of both.

Cell temperatures fell again when naphthalene was stopped. The inlet temperatures, like the cell voltage, did not reach the original values, which may indicate a persistent blockage of the methane reforming. During the second dosing the temperatures rose to the same levels as the first time. However, this time the increase occurred only at the outlet with a delay of 2 h after a minimal drop while the other cell temperatures rose immediately.

Variation of Methane Content

In order to test the remaining activity of methane reforming, the CH_4 volume flow (0.05 Nl/min) was temporarily replaced by N_2. Shortly before the end of the first naphthalene phase ($t = 77$ h) this had only a minor effect: the inlet temperatures increased by approx. 0.5 K and the cell voltage decreased by 5 mV. Estimations using an AspenPlus Model of the SOFC [108] showed that the absence of methane would result in a voltage drop of about 30 mV which was also confirmed during the reference measurements in 5.5.2. This is a further indication that the conversion of CH_4 was strongly inhibited by naphthalene and that CH_4, like N_2, flowed along the cell almost as inert compound. The remaining voltage response can either be an indication that a residual reforming activity was still present, or could be due to the different properties of N_2 (heat capacity, viscosity, ...). For the partially recovered cell ($t = 196$ h) a more pronounced increase in the inlet temperatures (2 K in 4 min) and a reduced cell voltage (- 20 mV) could be observed accordingly.

SPA Results

With the aid of the SPA samples naphthalene was always detected in the gas supplied to the cell, even immediately after starting the dosing. Shortly before the end of the first naphthalene phase a very low concentration was measured at the cell exit, which, however, could not be evaluated quantitatively. This is a further

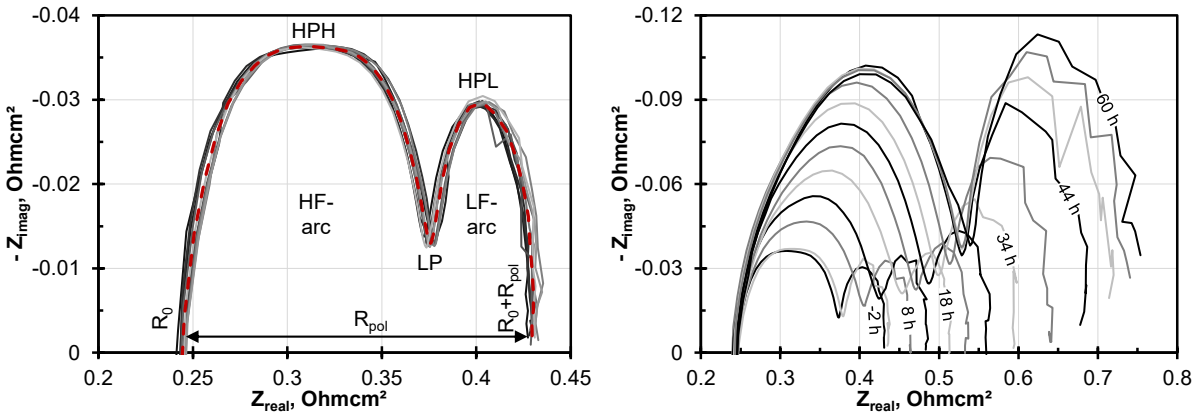

Figure 6.2: Nyquist plots of the EI-spectra during Syn1 (left) and during dosing of 0.4 g/Nm^3 naphthalene (right). Numbers on spectra indicate elapsed time since start of dosing of naphthalene. Characteristic points of the spectra are indicated in the left figure. HPH: high point of high frequency arc (HF-arc); HPL: high point of low frequency arc (LF-arc); LP: low point between the two arcs. Operation conditions see Table 6.1.

indication that in the stationary phase of poisoning naphthalene was either mostly converted by reforming, or that the anode substrate was not yet saturated with naphthalene.

EIS Results

During the experiments impedance spectra were recorded at regular intervals with the parameters specified in section 4.2.3. Only the values between 9.6 kHz and 0.1 Hz could be used due to inductances in the wiring and the measuring points at low frequencies were noisy due to the unstable steam dosing via the bubbler. All spectra were valid for further evaluation according to the Kramers-Kronig Test [124].

Figure 6.2 shows the impedance spectra recorded during the initial syngas phase (left) and the first naphthalene dosing (right). In contrast to the analogue diagrams of the measurements with phenol as model tar, naphthalene had a significant influence on the spectra. As the voltage signal became more noisy reaching the plateau,

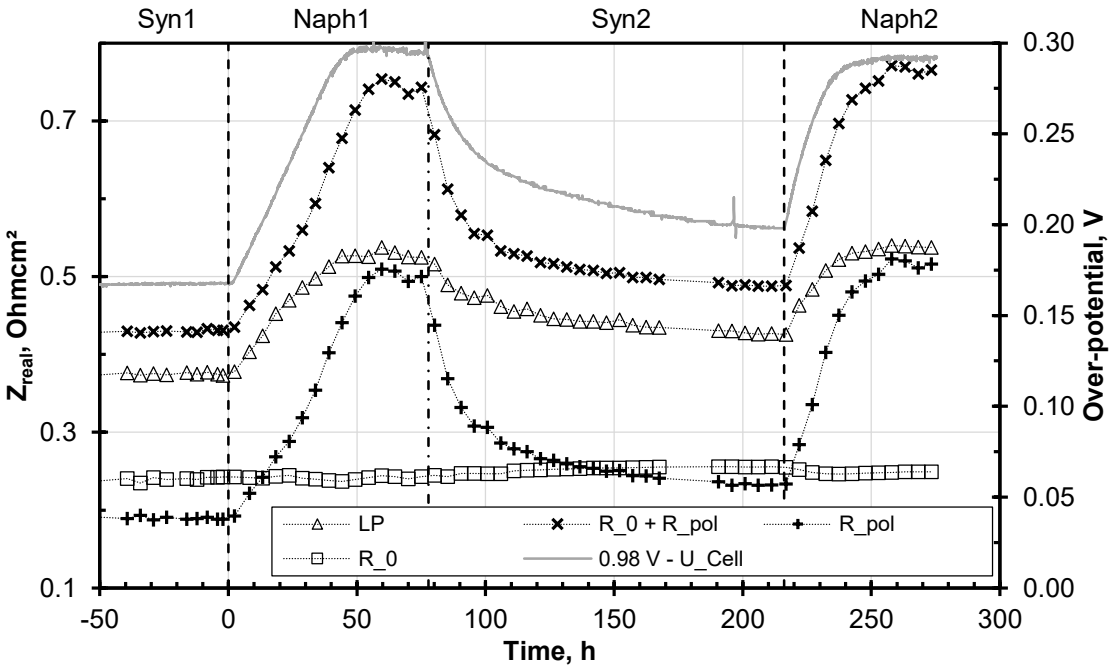

Figure 6.3: Alteration of the real ASR of the EI-spectra during dosing of naphthalene and the recovery together with the over-potential $OCV_{\text{syngas}} - U_{\text{cell}}$. Operation conditions see Table 6.1.

the LF-arc got more wrinkled with longer runtime on naphthalene. Whereas the variance of the spectra was low during Syn1, both arcs grew strongly during Naph1 and the polarisation resistance more than doubled.

Figure 6.3 provides a clearer representation of the EIS data. This type of plot was already introduced for the evaluation of the reference spectra in section 5.5.2. The temporal evolution of the real part (Z_{real}) of characteristic points (as indicated in Figure 6.2) of the spectra are plotted: the ASR at the low-point between the two arcs LP, the polarisation resistance R_{pol}, the minimum real part R_0 and the maximum real part $R_{\text{tot}} = R_0 + R_{\text{pol}}$. The diagram thus shows the view at the spectra from the y-imaginary-direction. In addition the over-potential calculated from $OCV_{\text{syngas}} - U_{\text{cell}}$ is plotted on the right y-axis.

While the parameters of the spectra in syngas operation were nearly constant, the polarisation resistance in the HF-arc – the distance between R_0 and LP – began to grow constantly from the start of naphthalene dosing. On the other hand, the

polarisation resistance of the LF-arc – the distance between LP and R_{tot} initially remained approximately constant and then increased sharply. It is noticeable that the beginning of this increase coincided with the rise in the outlet temperature. The growth of the HF-contributions ended at the time when the over-voltage no longer increased at a constant rate. The polarisation resistance at the lower frequencies, on the other hand, did become constant later, at the same time as the cell voltage became stationary.

The recovery of the cell took place faster – reversed to poisoning – in the LF-parts, which after 20 h showed again approximately the same values as before the poisoning. The HF-arc only narrowed again very slowly and was still noticeably wider before the start of Naph2 than in the un-poisoned state. On the other hand, the recovery was symmetrical: by the time Naph2 was started ($t = 215\,\mathrm{h}$), the Z_{real}-values of the spectra were almost identical to the time during Naph1 when the cell-voltage had the same value ($t = 12\,\mathrm{h}$). Just as all cell temperatures immediately increased at the second dosing, both HF- and LF-contributions also changed instantaneously in Naph2. Here too, the parameters reached very similar plateau values.

Figure 6.4 shows analogously the course of the characteristic points in the imaginary part, i.e. not the width of the arcs of the spectra but their height and the position of the low point between them. The representation shows the view from x-real-direction to the spectra. Here too, it can be seen clearly that the HF-arc increased constantly immediately after switching. However, it also becomes visible that the height of the LF-arc – in contrast to its width – began to rise immediately in an s-shaped curve. As in the real components first the HF-arc reached its maximum and only later the LF-arc. During regeneration the LF-arc returned approximately to its original height, but did so more slowly than its width. The maximum of the HF-arc was still significantly increased even after 138 h of regeneration.

So far only the behaviour of HF- and LF-arcs has been considered. The affected processes could be subdivided with the help of further evaluations. Figure 6.5 a shows the development of the DRT during Naph1; the later the curves are recorded the more blue they are coloured. In Figure 6.5 b the development of the height of the DRT peaks over time is plotted. Since noise in the measurement data

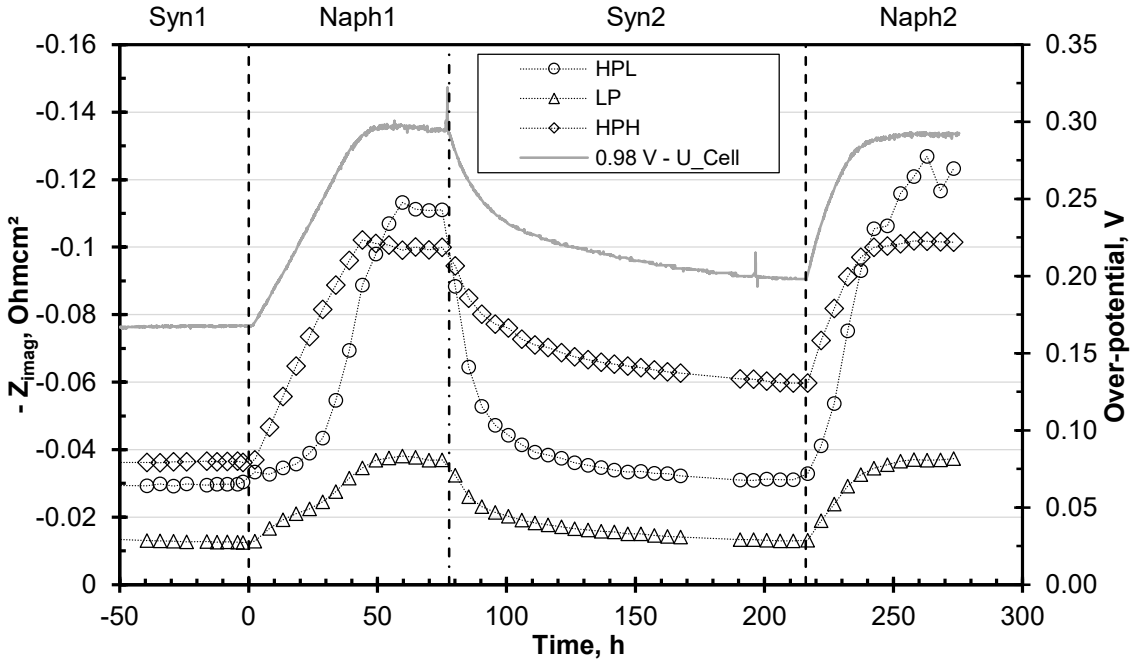

Figure 6.4: Alteration of the imaginary ASR of the EI-spectra during dosing of naphthalene and the recovery together with the cell voltage. HPL: ASR at maximum of low-frequency arc; HPH: ASR at maximum of high-frequency arc; LP: ASR at low point between the two arcs. Operation conditions see 6.1.

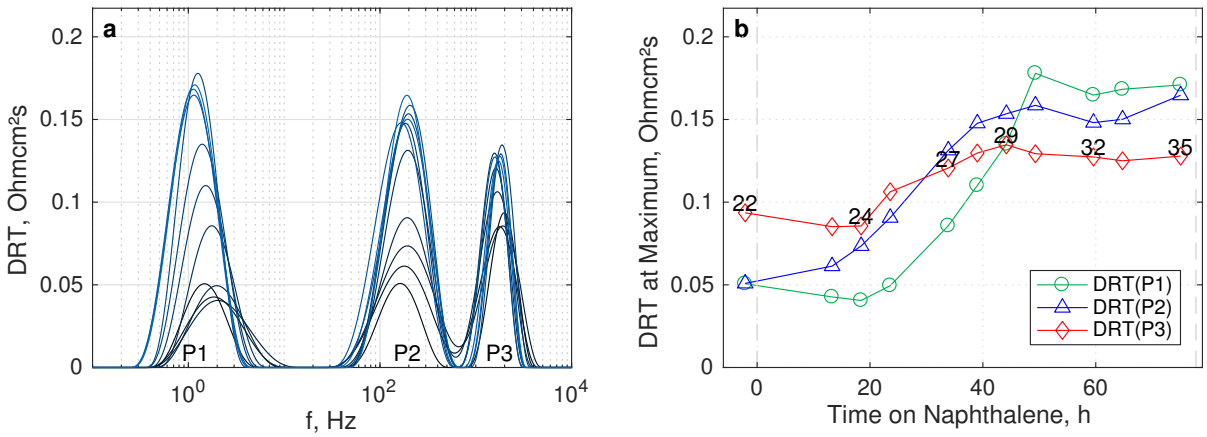

Figure 6.5: a) DRTs during Naph1, chronologically ordered from black to blue, b) trends of the peak center height. 22: last spectrum in Syn1. Operation conditions see Table 6.1.

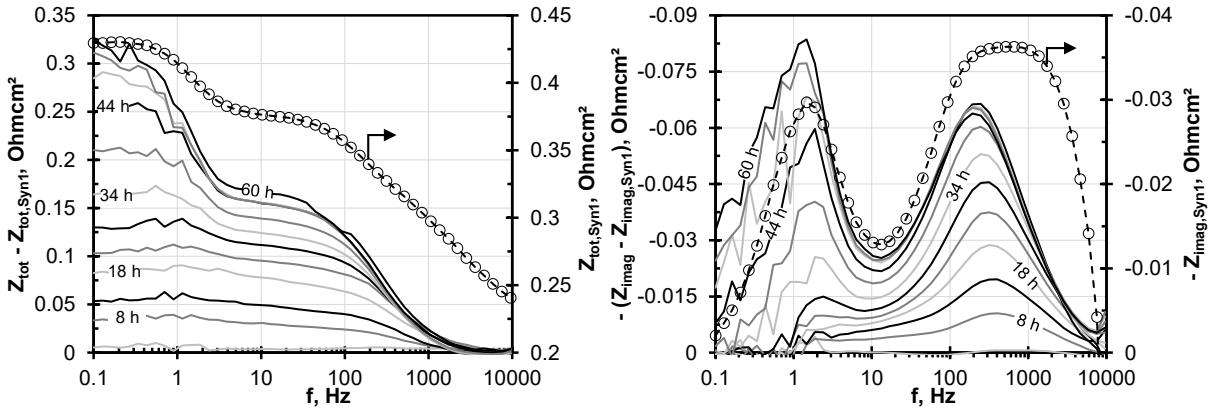

Figure 6.6: Alteration of the absolute value of the impedance (left) and the imaginary part (right) referred to the data during Syn1, plotted over the excitation frequency. Dotted lines represent data during Syn1. Operation conditions see Table 6.1.

had a direct effect on the DRT results and some of the curves were distorted as a result, not all calculated DRTs are shown in the diagrams. The DRT data shows, as usual, three main peaks, with P1 characterising the LF-arc and P2 and P3 together characterising the HF-arc. It becomes clear now that the observed instantaneous growth of the HF-arc was mainly caused by an increase in polarisation resistance at 200 Hz. The peak at 2 kHz, on the other hand, grew relatively little. P1 began to grow after the spectrum at 18 h, analogous to the results shown above.

In addition to the evaluation of the DRT, the differential Bode-plots give a similar picture of the poisoning progress, but this data is less susceptible to numerical errors, see Figure 6.6. In the left figure the absolute value of the impedance ($Z_{\mathrm{tot}} = |Z|$) for the mean spectrum of Syn1 is plotted on the right y-axis and over the excitation frequency. The curves plotted over the left y-axis (solid lines) represent the evolution of the difference in Z_{tot} to the Syn1-spectrum. The right figure was generated analogously with the imaginary part of the spectra. In addition to the Figures 6.3 and 6.4 it becomes apparent that during the poisoning the spectra at first changed at frequencies above 5 Hz. As already observed in the DRT, the impedance of the lower frequencies began to increase only after 18 h. The imaginary part of the high-frequency arc had not only increased but its maximum had also shifted to lower frequencies.

Conclusions From This Test

From the results shown so far it is clear that naphthalene had a strong influence on the performance of the cell. The main finding is that naphthalene not only blocked the conversion of CH_4 and CO but also the processes in the anode layer and at the TPB. Analogous to the interpretation given in section 5.5.3, it can be deduced from impedance data that naphthalene initially only inhibited fuel diffusion in the anode layer and thus caused the HF-arc to grow at 200 Hz. The charge transfer reactions at the TPB (around 2 kHz) were also inhibited but only to a lesser extent. From the height of P3 in the DRT it can be concluded that the charge transfer reactions already had a limiting effect on cell performance during operation on clean syngas due to the relatively low temperature. Due to the obstruction of fuel diffusion caused by naphthalene, P2 replaced P3 as the main limiting effect. Thus hydrogen which arrived at a TPB despite increased diffusion resistance was converted almost as rapidly as before. On the other hand, gas diffusion through the anode support only became a limiting effect when the H_2-utilisation became too large due to the inhibited conversion of CH_4 and CO. The corresponding polarisation resistance peaked when methane reforming and WGS were inhibited throughout the cell. From the behaviour of the cell during Syn2 this limitation can be very well interpreted: during recovery the LF-arc quickly returned to its original size. This means that a condition occurred in which the gas transport through the substrate was no longer limiting. At the same time the cell temperatures were still higher compared to the unpoisoned state. This leads to the conclusion that not the entire CH_4 was converted again at this point in time, but enough of it so that the process of transporting fuel gas through the substrate was no longer limiting the cell performance.

6.1.2 Prolonged Dosing and Active Regeneration

The results of the measurements on C60 are shown below. Like C50 this was subjected to 0.4 g/Nm^3 of naphthalene. In contrast to C50, the dosage was continued after the end of the constant voltage decrease in order to find out whether the cell

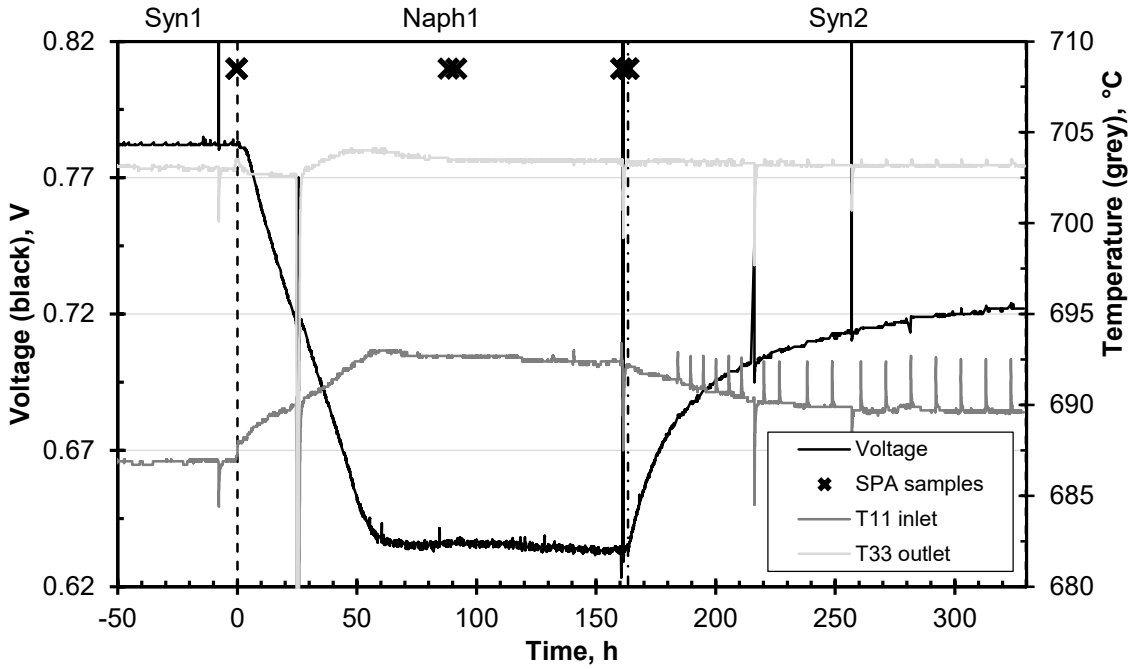

Figure 6.7: Cell potential and temperatures during operation on clean syngas plus 0.4 g/Nm^3 naphthalene. C60, TypIIIb. Operation at standard conditions, see Table 6.1.

performance would deteriorate even further from this state. After the cell voltage at C50 had recovered only incompletely after switching off naphthalene, for C60 it was attempted for restoring the performance by increasing the operating temperature.

Initial Poisoning

After 72 h on pure syngas 0.4 g/Nm^3 naphthalene were dosed at C60 like C50, see phase Naph1 in Figure 6.7. In contrast to C50, C60 was a TypIIIb cell. After about 3 h, i.e. 1.5 h later than at C50, the constant decrease in cell voltage began which is due to the thicker substrate of the TypIIIb cell. The dosage was interrupted at hour 25 for 1.3 h due to a failure of the laboratory ventilation and a resulting emergency stop of the test stand. After 60 h cell voltage and temperatures reached a stationary level. Impedance data during poisoning evolved completely analogous to C50.

In the following 100 h there was no further decrease in cell performance and impedance data showed no more changes, apart from minor fluctuations[3]. This indicates that a stationary state between the adsorption of naphthalene and its reforming or desorption must have occurred already at the time of reaching the plateau. Since no naphthalene was measured in the SPA samples at the cell outlet, adsorption seemed to be mainly counteracted by reforming. The fact that, in contrast to C50, no naphthalene was detected in the exhaust gas is probably due to the larger substrate volume of C60 and the resulting higher conversion rate.

For C50 the hypothesis was proposed that the substrate might not have been saturated with naphthalene in this state and that the voltage could have decreased further as soon as reaching saturation. This possibility is excluded by the measurement at C60. If the substrate were not saturated after 162 h naphthalene dosage, it would have been loaded with about 4 $g_{Naph}/24\,g_{Substr} = 0.17\ g_{Naph}/g_{Sustr}$, neglecting reforming and desorption. For comparison: the adsorption capacity of activated carbon is up to 0.3 g/g [148] depending on the conditions. However, activated carbon disposes of a 100 times higher inner surface [40]. So it seems unrealistic that at the end of Naph1 saturation was not reached yet and it can be assumed that the voltage would not have fallen further under the given operating conditions.

After 162 h naphthalene dosage the supply was switched off, whereupon the cell recovered in syngas again with decreasing rate (Syn2). The two voltage peaks were triggered by two restarts of the control PC and the resulting shutdown of the electrical load. After 167 h the cell voltage had reached 92% of the value of Syn1. The spikes in the course of T11 and T33 are a consequence of the replacement of the methane volume flow in the syngas by nitrogen, as had already been done at C50[4]. The first two variations were made at the end of Naph1 at 141 and 160 h without causing a reaction in the temperature signal, while the voltage decreased by 10 mV.

[3] A long-term degradation due to local Ni-oxidation by fuel gas depletion, as observed by Hauch et al. for poisoning with H_2S [139], therefore did not occur. However, it is possible that a significant increase in current density for C60 could also have led to the degradation mechanisms shown by Hauch et al. if fuel gas utilisation reached critical levels due to naphthalene inhibition.

[4] As it was done with the voltage oscillation during EIS measurements the resulting voltage decrease was filtered out of the voltage curve shown.

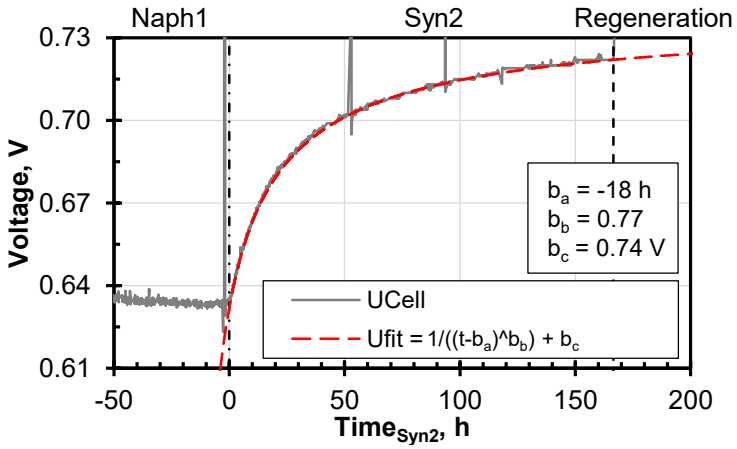

Figure 6.8: Fit-result of a hyperbolic function to the voltage signal during Syn2. Time axis starts when naphthalene supply was switched off. C60, TypIIIb. Operation at standard conditions, see Table 6.1.

From hour 184 the methane variation was carried out after every second impedance measurement, and analogous to the recovery of the cell the resulting temperature increase was more and more pronounced, which led to the spikes visible in the course.

As shown in Figure 6.8 the voltage increase after switching off naphthalene can be described very well with a hyperbolic function. The slow or rather incomplete recovery might be explained by the fact that naphthalene was also adsorbed on YSZ, on catalytically inactive nickel or on other components of the housing where it was not initially reformed. Only with decreasing local naphthalene partial pressure it could desorb from there and reach catalytically active sites of Ni where it was reformed.

Active Regeneration

According to Jess et al. the conversion of naphthalene on nickel catalysts is only complete at temperatures above 800 °C [147]. In order to accelerate desorption and improve reforming activity for a short time, after Syn2 the furnace temperature was therefore increased four times for several hours, once to 850 °C and three times to 900 °C. Table 6.2 shows the sequence of this active regeneration and Figure 6.9

Table 6.2: Overview of measurement procedure on C60 and measured values for cell voltage, voltage drop and inlet temperature.

Reading point	**Time, h**	**U_{Cell}, V**	**U_{Cell}/ $U_{Cell,Syn1}$**	**T11, °C**	**Duration high temp, h**
End of Syn1	0	0.783	1.00	686.9	
End of Naph1	162	0.633	0.81	692.2	
End of Syn2	328	0.722	0.92	689.6	
After 850 °C-step	341	0.733	0.94	689.4	4
After 1. 900 °C-step	366	0.748	0.96	688.6	4
After 2. 900 °C-step	407	0.770	0.98	685.9	23
After 3. 900 °C-step	433	0.774	0.99	685.6	18
End of Syn3	494	0.768	0.98	685.6	

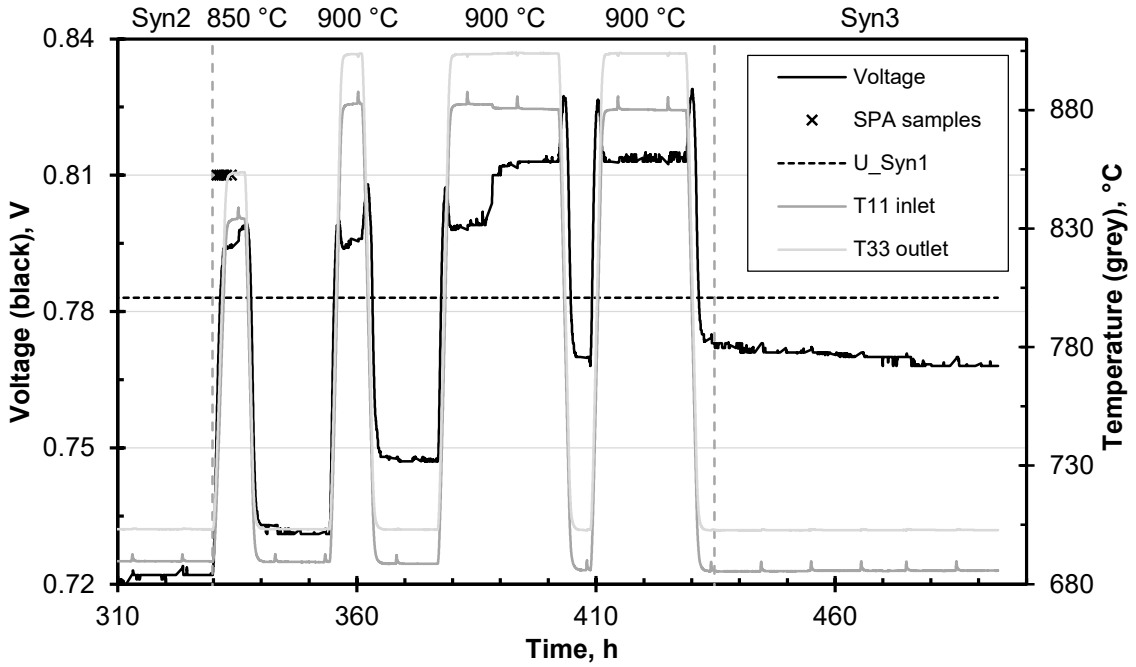

Figure 6.9: Cell potential and temperatures during regeneration in follow up to Syn2 from 6.7. Operation on clean syngas, conditions see Table 6.1. Furnace temperature other than 700 °C is indicated above the plot. C60, TypIIIb.

shows the resulting voltage and temperature signals. The maxima in the voltage curve during heating to 900 °C resulted from the opposite trends of Nernst voltage and electrolyte resistance; the latter decreases with increasing temperature causing the cell voltage to increase while the former decreases, causing the cell voltage to decrease.

It is noticeable that the cell voltage could be increased with each heating phase. After the last 900 °C step it returned to 99 % of the value of Syn1. Parallel to the cell voltage the inlet temperature T11 fell with each heating step, see Table 6.2, which may be related to the restoration of methane reforming activity. The temperature peaks caused by methane variation were also much more pronounced than before active regeneration. During the first heating process to 850 °C SPA samples were taken from the anode exhaust gas at regular intervals. Naphthalene was not present in any of the samples. No evidence of benzene or other possible naphthalene degradation products could be found[5]. This confirms the above mentioned assumption that naphthalene in the substrate and in the anode was only decomposed by reforming and did not desorb as molecule.

The step-shaped voltage increase during the second 900 °C phase at t=388 h is noticeable. The voltage increased by 12 mV, accompanied by a decrease of T11 by 1.5 K. At the next 900 °C phase the voltage reached the same high value. The jump therefore probably represented the time of a largely achieved regeneration. Why this happened abruptly and not continuously like the poisoning cannot be explained at this point. Unfortunately, there is no SPA data available for the time of this voltage rise at t=388 h which could have been helpful in explaining the phenomenon.

After the fourth temperature increase the cell voltage had almost reached the initial level from Syn1 and regeneration could therefore be regarded as successful in principle. However, it should be noted that the impedance data of Syn1 and Syn3 was not the same. The values and the distribution of the cell temperatures were also different but these changes were, in contrast to the impedance data, in the range of the normal drifts occurring during a measurement time of almost 500 h. As shown in Figure 6.10 the HF-arc was still significantly larger after regenera-

[5]The author is aware that the detection of the latter is not fully reliable with the measurement procedure used.

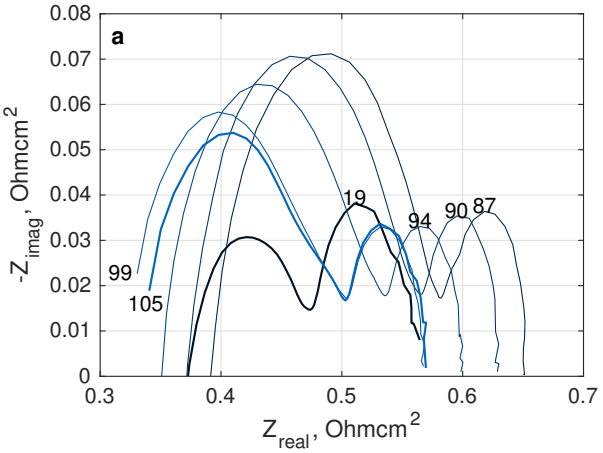

Figure 6.10: Impedance spectra and DRT before, during and after regeneration. 19: Syn1, 87: end of Syn2, 90: after first 850 °C-step, 94: after first 900 °C-step, 99: after second 900 °C-step, 105: Syn3. Operation on clean syngas, conditions see Table 6.1. C60, TypIIIb.

tion (105) compared to the data of Syn1 (19). The LF-arc on the other hand was smaller after regeneration whereas it had reached the initial size already after Syn2 (87). R_0 was significantly lower after regeneration but R_{pol} was larger due to the increased HF-arc. The decrease in R_0 compensated the growth of R_{pol} so that the overall ASR R_{tot} after regeneration was very similar to the value of Syn1 which explains the similar cell voltage. The respective DRT data not shown here indicated that the height of P3 had not changed significantly from the end of Syn2 to Syn3 whereas P2 almost reached the initial height after regeneration. This would indicate that the resistance for electrochemical oxidation at the TPB was still increased and that the regeneration of cell performance was not fully achieved. On the other hand it is also possible that the positive effects of the increased temperature were compensated by other deteriorating effects. Whether the first or the second explanation is valid and what caused the variation of R_0 cannot be conclusively determined from this single measurement but should be investigated in future tests.

In the 60 h after the last temperature increase (Syn3) the cell voltage decreased with a clearly increased rate of -9.5 %/1000 h so that it was only 98 % of the Syn1 voltage at the end of the test. One assumption was that the methane variation further

increased the already large temperature differences between the non-contacted cell surface in the manifold (cooled by the methane reforming) and the contacted cell surface in the flow-field (heated by the electrochemical oxidation). This might have led to microscopic but increasingly larger cracks in the electrolyte where fuel gas could burn off. In the follow-up investigation no cracks were found at the cell entrance, see section 6.1.5. In addition, the voltage decrease did not correlate with the times of methane variation. In the impedance data of Syn3 a steady increase of the ohmic resistance could be observed which shifted the spectra to the right at constant imaginary contributions. This indicates a decreasing quality of the contact between the metal mesh and the cell, which could have been caused either by the changes between 700 and 900 °C or by the methane variation.

6.1.3 Simultaneous Dosing of Naphthalene and Phenol

In literature there is only few data on laboratory experiments in which several tars were dosed simultaneously to the fuel gas. The number, selection and concentration of tars and the exposure duration represent additional degrees of freedom to the remaining operating parameters, which impairs the comparability of literature data. Frank investigated the effect of combinations with 8.6 g/Nm^3 naphthalene, 10.5 g/Nm^3 phenol and 16.4 g/Nm^3 toluene in simulated biosyngas at Ni/GDC ESC [64]. She found that naphthalene inhibited the reforming of methane and toluene but not that of phenol since the latter is thermally cracked and does not depend on free active sites on Ni. Lorente et al. collected tars from real bio-syngas (no information on composition) and compared their influence on powdered Ni/YSZ with the influence of pure toluene as model tar [22]. They noticed that in humidified hydrogen as main gas toluene alone led to stronger carbon deposits than the tar mixture. Since no electrochemical investigation was possible on the powders, the harmful influence of heavy tars such as naphthalene on cell performance was ignored. Similar observations were made by Mermelstein et al. [73]. At Ni/YSZ ESC a mixture of pyrene, phenol, naphthalene and benzene led to less carbon deposition than pure benzene. Since the experiments were performed with mixtures of H_2 and N_2 as main gas, the inhibition of CH_4 reforming by naphthalene and pyrene was not investigated.

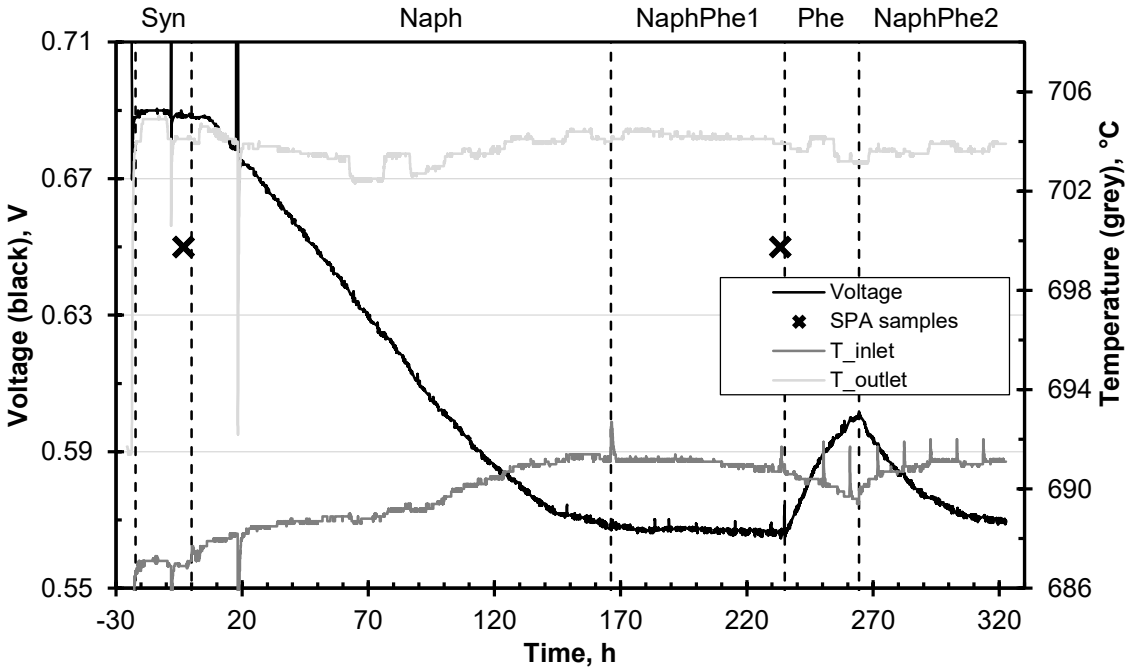

Figure 6.11: Cell potential and temperatures during operation on clean syngas plus 0.1 g/Nm^3 naphthalene plus 0.5 g/Nm^3 phenol in varying combinations. C61, TypIIIb. Operation on standard conditions, see Table 6.1.

Figure 6.11 shows the trends of cell voltage, T11 and T33 of C61. After an initial syngas phase, 0.1 g/Nm^3 naphthalene were added for 166 h (Naph1). Due to the low tar concentration, the voltage dropped with a delay of 6-7 h. Subsequently, an additional 0.5 g/Nm^3 phenol were added (NaphPhe1). As can be seen in Figure 6.11, the voltage drop caused by naphthalene was probably not over at the beginning of the phenol dosage. The voltage decrease took place over several days due to the low naphthalene concentration, which made it difficult to estimate whether the cell had already reached the stationary state. After 69 h of the combined dosage naphthalene was switched off. In the 29 h in which only phenol was dosed as model tar (Phe1) the cell voltage recovered significantly. When the naphthalene supply (NaphPhe2) was resumed, the voltage approached the plateau level again within the 60 h until the end of the test.

The cell temperatures changed analogously to the cell voltage and the progress of naphthalene poisoning. The course of T33 was mostly superimposed by the day-night cycle of laboratory ventilation. In the EIS data during NaphPhe1 no influence of the additional phenol was visible. The imaginary parts of the impedance were constant, the real parts fluctuated due to the noise of the cell voltage. The DRT data could not be evaluated for the latter reason.

Overall, the cell behaved as if only naphthalene had been dosed. However, the cell showed carbon deposits at the cell entrance after the test, see section 6.1.5, which can be traced back to the presence of phenol. The characteristic of phenol as model tar will be discussed in detail in the next chapter.

The basis for the preparation of this experiment was the hypothesis that the cell voltage could increase during NaphPhe1 if naphthalene adsorbed or cracked on the carbon deposits caused by phenol. This assumption was based on the results of coupling the short-stack F1004-89 with a fluidised bed gasifier without using tar-removal. The tests are described in [112]. There it was conspicuous that the stack voltage had not constantly decreased although 0.2 to 0.3 g/Nm^3 of naphthalene had been present in the real bio-syngas in addition to the other main tars benzene, toluene, cresol and phenol. Strong carbon deposits had simultaneously formed in the stack, see the results from post-test analysis in [149]. It was assumed that all tars had contributed to their growth and had not arrived at the anode layer to influence electrochemistry. It is possible that the phenol concentration at C61 was too low to cause "sufficient" carbon deposits to reproduce the conditions in the stack test. However, it is possible as well that the cell voltage had also decreased in the stack, but this was not apparent from the voltage fluctuation caused by the gasifier operation and the increasing blockage of the flow-field.

It would also be interesting to observe the behaviour of the cell if first phenol and then naphthalene were dosed. The data shown here is only one of many conceivable experimental constellations. Altogether the interactions of different tars and also of tars and other impurities must be examined more exactly. However, this takes a considerable amount of time and therefore cannot be done only by electrochemical investigations on entire single-cells but also relies on complementary chemical material studies.

Table 6.3: Comparison of parameters and results of the first dosing of naphthalene for selected cells.

Cell	Type	$c_{Naph,mean}$, g/Nm³	$c_{Naph,mean}$, ppm	Dosing time,h	Voltage Syn1, V	Voltage drop, mV	Time until plateau, h
C50	CTb	0.42	74	78	0.813	130	50
C51	CTb	2.52	441	27	0.829	155	*
C54	GDC	0.44	77	48	0.722	232	33
C55	GDC	0.42	74	52	0.731	229	50
C60	IIIb	0.43	75	162	0.784	147	60
C61	IIIb	0.12	21	**	0.688	**	180**

* Later rise in voltage, no proper plateau

** Addition of 0.5 g/Nm³ of phenol after 166 h

6.1.4 Comparison of Different Cell Types and Concentrations of Naphthalene

In the context of this thesis several measurements with different naphthalene concentrations were performed on three cell types. Table 6.3 gives an overview of the measurements with naphthalene as model tar. Two further measurements each with 1 g/Nm³ naphthalene were not evaluable. The differences between the cell types have already been described in section 4.1: CTb were commercial cells from CeramTec, IIIb were produced completely in Jülich and GDC were cells with Ni/GDC anode which were printed together with the other functional layers on purchased substrates from CeramTec. Main differences between IIIb and CTb substrate were the thickness of the support, its micro structure and the form of YSZ, which was discussed in detail in [32]. These optimised parameters led to a higher performance of the CTb cells. As they were machine-made the tests on CTb moreover showed higher reproducibility.

Figure 6.12 shows the voltage curve during the first naphthalene dosage for the six cells, plotted over time, starting with the start of the naphthalene dosage. For better comparability the cell voltage is related to the voltage during Syn1. Due to emergency stop situations the naphthalene supply was interrupted for a short time at C60 and C61, which led to a brief increase of the voltage at C60. The spike

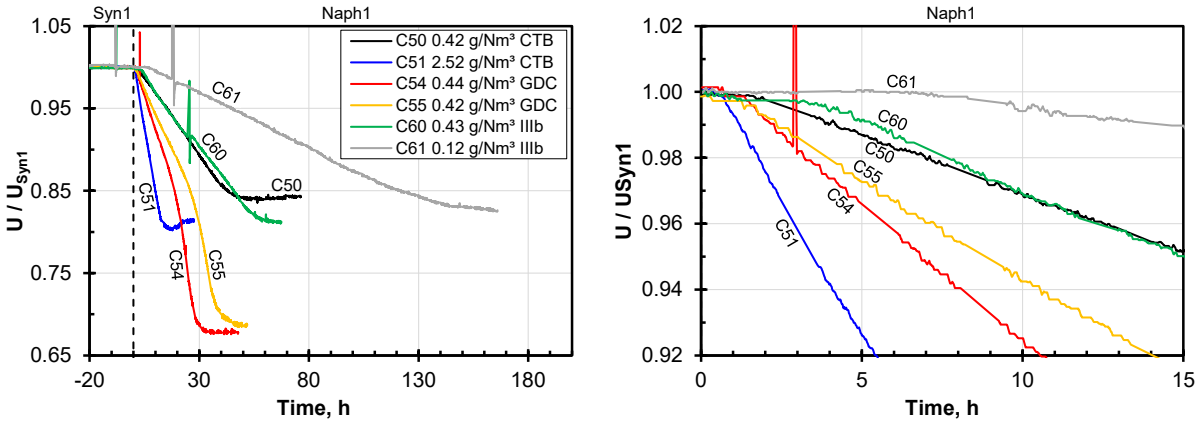

Figure 6.12: Relative voltage drop during Naph1 for different cell types and naphthalene concentrations. Right figure shows close-up on initial 15 h of dosing. Operation conditions see Table 6.1.

in the data of C54 was caused by an error in the test run script. For all cells the voltage decrease resulted in the plateau described above, where an equilibrium of adsorption and reforming of naphthalene had been established.

Even at a low naphthalene concentration of 0.12 g/Nm^3 (C61) there was a significant decrease in cell performance similar to the one at higher concentrations. The comparison of the courses of C50 and C51 or C60 and C61 shows that the greater the naphthalene concentration the faster the voltage decrease. The amount of voltage decrease also correlated with the concentration. The concentration had a stronger effect on the rate of voltage decrease than on its magnitude. The lower the naphthalene concentration the greater the delay of the voltage decrease. A comparison of C50 and C60, i.e. between CTb and IIIb, shows that the delay of the voltage decrease at IIIb occurred later. This can be explained by the thicker substrate of IIIb. In this substrate a larger amount of naphthalene could adsorb before the anode layer was affected by naphthalene poisoning. The rate of voltage decrease was nevertheless very similar for both cell types whereas the magnitude of voltage decrease was greater for IIIb.

As shown in Figure 6.12 the voltage of the GDC cells (C54 and C55) did not only decrease faster compared to the other cell types but also dropped to a significantly lower level. It is also noticeable that the voltage of these cells fell at two different rates, first slower to about 0.6 V and then faster until the plateau was reached. The

transition to the larger slope coincided with the increase in the outlet temperature. Since the voltage curve at C54 made the quality of the measurement doubtful, the measurement was repeated at C55. The behaviour, however, was reproducible; the curves can be superimposed by adjusting the stretching in the t-direction. The different rate of voltage decrease may have correlated with the slightly lower naphthalene concentration at C55 due to a 0.5 K lower tar tank temperature. However, since the difference in concentration was very small, different thickness of the anode layer or other variations in manufacturing conditions may have led to a faster voltage drop at C55. The exact reason for the buckling in the voltage curve of the cells with Ni/GDC anode could not be clarified conclusively. It may have been due to the fact that the voltage fell below a threshold value below which other degradation mechanisms superimposed on naphthalene poisoning; or it might stem from the subsequent poisoning of Ni/YSZ in the substrate and Ni/GDC in the anode layer. Owing to a large LF-arc which will be discussed in the phenol chapter, the EIS data could not contribute to the clarification of the processes.

According to literature Ni/GDC anodes should actually have a higher tolerance to naphthalene because of the mixed-ionic-electronic-conductivity property of GDC not only TPB but triple-phase layers (TPL) are present. However, the performance of the measured Ni/GDC cells was reduced by interdiffusion during the manufacturing process between electrolyte and anode layer [102]. This led to a lower cell voltage and reduced electrochemical activity due to reduced ionic conductivity. With a lower number of active sites for electrochemical oxidation a lower amount of naphthalene is sufficient to inhibit the reactions. This might explain why the cells with GDC anode were more affected by naphthalene since they had less TPB from the beginning which facilitated the inhibition of the electrochemical oxidation at the remaining active sites.

Cell voltage over accumulated amount of naphthalene

As can be seen from the curves in Figure 6.12, the rate of voltage decrease correlated with naphthalene concentration. In the plots of Figure 6.13 the voltage curves are plotted over the supplied amount of naphthalene accumulated. To determine the naphthalene concentration, the measured temperature in the naphthalene container

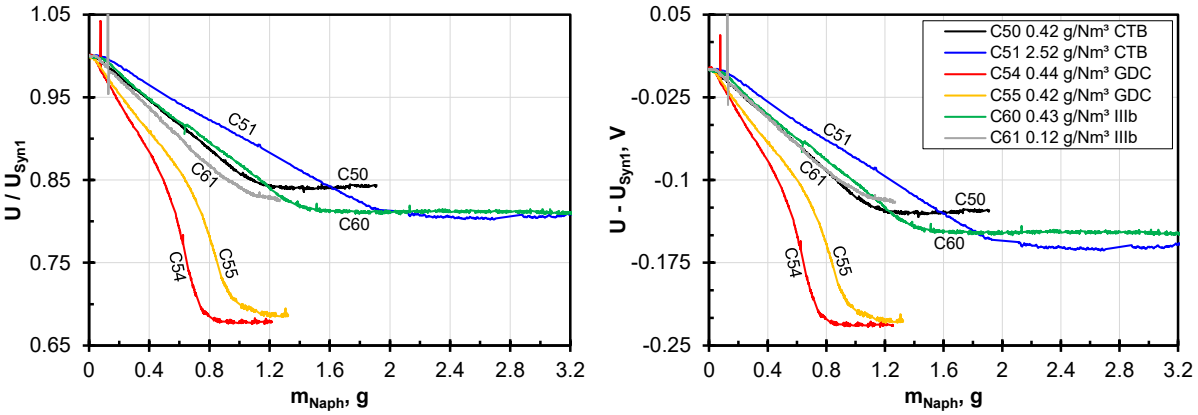

Figure 6.13: Relative (left) and absolute (right) decrease of cell voltage during Naph1 for different cell types and naphthalene concentrations plotted over supplied amount of naphthalene. Operation conditions see Table 6.1.

was used to calculate the saturation pressure, see appendix A for the relevant equation, and the per-minute resolved values were added up. It should be noted that the temperature of the tar container measured at one point does not exactly represent the distribution of the temperature in the container, which can have another profile at different set temperatures.

It can be seen that the rate of voltage decrease over naphthalene amount was very similar for C50, C51, C60 and C61. The cells with Ni/YSZ anode incorporated between 1.2 and 1.6 g of naphthalene before the plateau in the cell voltage was established. C60 took up about 0.3 g more naphthalene than C50 due to the thicker substrate. Both the absolute and the relative voltage decrease were slower for C51 with 2.5 g/Nm^3 than for all other cells. It is conceivable that at this concentration naphthalene was partially condensed at too cold sites in the piping, which would have reduced the amount of naphthalene actually supplied to the cell. It is also possible that not all the naphthalene from the gas phase adsorbed in the cell. What is consistent with these findings is that a minimal amount of naphthalene was measured at the cell outlet at the end of Naph1 for C51. The curves of C54 and C55 were still differing even after compensation of the slightly divergent naphthalene concentration, which makes the explanation given above – variations owing to cell production – appear meaningful. Due to incomplete or slow reforming, naphthalene accumulated in substrate and anode. The comparison between C61, C60 and C51

shows that the absolute voltage decrease just as the amount of naphthalene in saturation was smaller when the concentration of naphthalene in the gas phase was lower. In other words, at higher concentrations in the gas phase a higher degree of coverage of substrate and anode was achieved.

For C50, C60 and C61 the rate of voltage decrease in the linear range was approx. 120 mV/gNaph. As long as the plateau is not reached, an SOFC could be used as a measuring element where the amount of naphthalene supplied can be determined from the voltage drop. However, an ESC would be better suited for such a measuring cell since the anode is in direct contact with the gas phase and cell voltage would therefore immediately respond to poisoning.

6.1.5 Post-Mortem Analysis

C50 and C60 were investigated by post-mortem Forschungszentrum Jülich by Jeong. The evaluation for C50 can be found in [32] and included SEM, EDX and Raman spectroscopy. C60 was investigated with SEM, XRD and Raman, whereby mainly structural changes after regeneration were of interest[6]. None of the naphthalene cells showed carbon deposits in the housing after the measurement. Metal dusting never occurred either. The exception is C61, where phenol was dosed in addition to naphthalene and where the carbon deposits characteristic of phenol occurred.

C50

Besides a crack in the middle of the cell in parallel to the manifold which presumably occurred during shut down, C50 (CTb) did not show macroscopic changes of the structure after 137 h of dosing of 0.4 g/Nm^3 of naphthalene. This was a clear contrast to comparable experiments with phenol as model tar, which showed dissolution of the bond between nickel and YSZ in the anode substrate, see chapter 7. Jeong observed C50 using SEM and found nano-scaled particles in the pores of substrate and anode [32]. Applying Raman spectroscopy he detected small bands of amorphous carbon species, graphene structures – graphite, carbon nano tubes,

[6]Many thanks to Sandra Lobe from Forschungszentrum Jülich for the analysis.

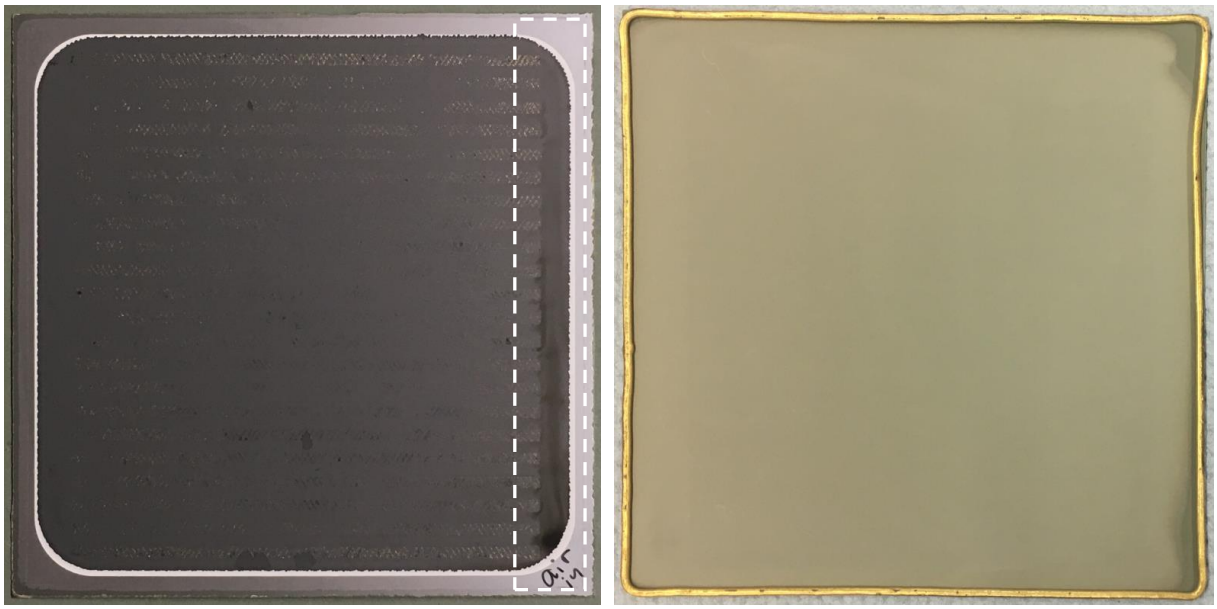

Figure 6.14: Photos of C60 after the test. Left: Cathode electrode side; air inlet in lower right corner; dark area at air inlet manifold indicated. Right: Anode electrode side; fuel inlet in lower left corner.

carbon fibres – and some nano-crystalline graphite in the substrate. He therefore assumed that the detected particles in the SEM consisted of carbon although their shape was different to the carbon particles found after the tests with phenol. There is no quantitative comparison for the amount of carbon after phenol or naphthalene dosing. Whereas the carbon in the tested phenol cell C32 was also found in the middle of the substrate, it was only detected in the area close to the gas phase in the substrate of C50.

The microstructure of C60 – 163 h dosing of 0.4 g/Nm^3 naphthalene, TypIIIb – was investigated after regeneration and shutdown. Like C50 the cell did not show macroscopic changes of the structure, see Figure 6.14. No changes in micro structure due to naphthalene or the repeated regeneration at 900 °C could be observed in the scale of the SEM images, see Figure 6.15 which shows cross sections of the anode inlet area. On other positions, the structure was also not altered. At the air inlet some microscopic cracks could be found but not at the anode inlet. The cracks had been considered as an explanation for the rapidly declining performance

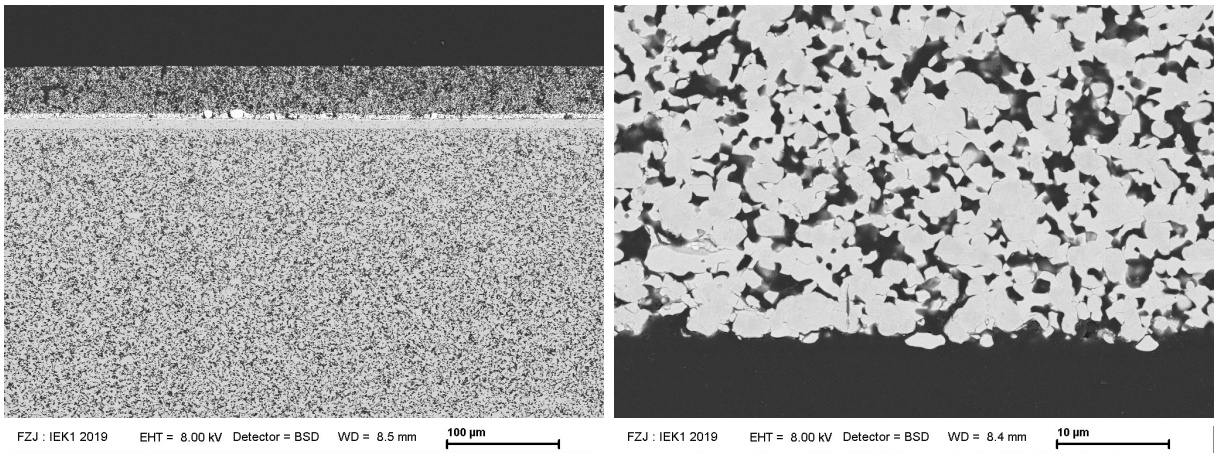

Figure 6.15: SEM images of C60. Cross-section of anode inlet (left) and zoom on interface of anode substrate to gas phase (right).

during the methane cycles at the end of the measurement. A preliminary analysis using Raman spectroscopy did not show carbon in the anode substrate as it was the case for C50. Therefore, no further more detailed studies with Raman were carried out.

After the phenomenon of the dark coloured areas at the cathode had been observed for several cells, they were analysed for the first time at C60. In this cell a black color gradient could be seen along the manifold starting from the air inlet, see indicated area in Figure 6.14. In EDX measurements in this area, besides the cathode materials La, Sr, Co, Fe and O, minimal amounts of Si were found. Reference measurements from the non-black adjacent area did not show silicon. It is assumed that this contamination was transported to the cell via the compressed air supply that may carry both silicone oil mist and gaseous silicone oil. The possible contamination with silicone was already mentioned by Mogensen et al. [150]. Silicone can block TPB at the cathode and reduce the power of the cell if it reaches the cell via the laboratory air. Here the contamination is locally limited though; proximal areas didn't show silicone in the EDX, but the longer the operation of the cell the more area would be affected by it. A fluctuating charge of the compressed air with silicone oil could be one reason for the relatively high basic degradation which had always been observed for previous single-cell tests. On the other hand, the impact is mainly on areas which correspond to the fuel outlet where 1) the electrochemical

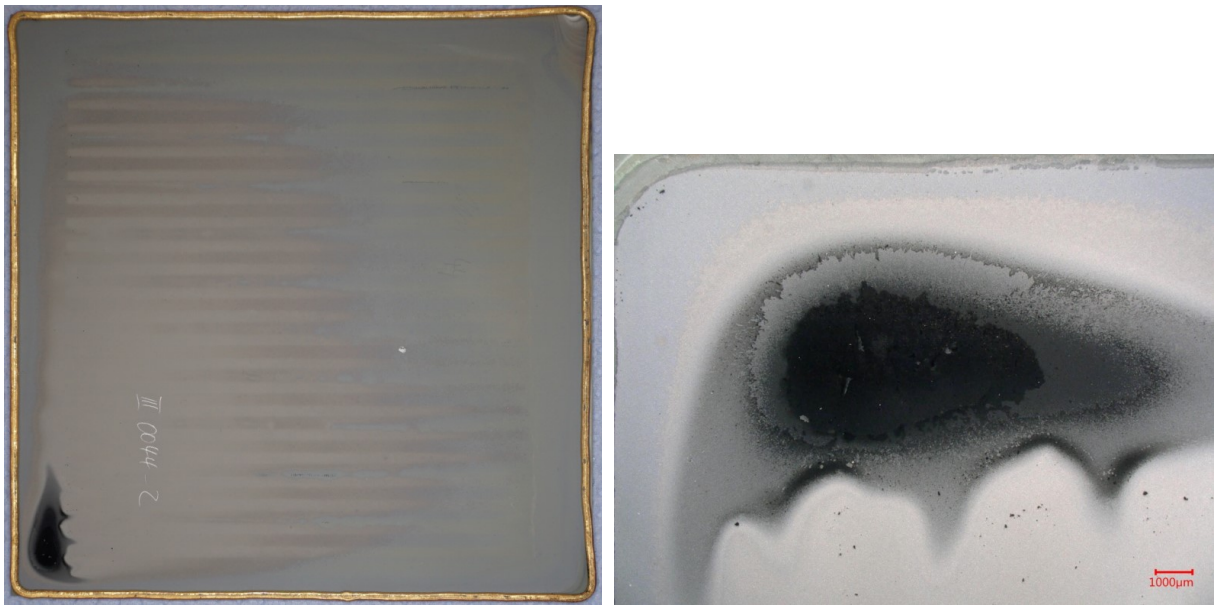

Figure 6.16: Photos of C61 after the test. Left: Photo of the anode after the test; fuel inlet in lower left corner. Right: Close-up on fuel inlet area.

activity is already very low and 2) the electrodes are not connected to the metal meshes for contacting. So even a complete inertisation of the cathode TPB in the air inlet area should not affect the cell performance to a big extent. In order to eliminate the possibly harmful effect of silicone oil, a 0.01 μm filter and an activated charcoal filter were installed upstream to the cathode after the tests for this thesis were completed. The two filters are to remove oil mist and gaseous oil respectively, but the future occurrence of dark areas at the cathode must be taken care of.

C61

While C50 and C60 were completely free of macroscopic carbon deposits after the end of the measurement, phenomena typical of phenol occurred in C61, see Figure 6.16 on the left. As a result of the dosage of 0.5 g/Nm^3 phenol over 158 h, a carbon spot had formed above the gas inlet, which showed different gradations, see 6.16 right. It is suspected that initial dusting exists on the substrate below the carbon deposition, but the cell was not examined more closely with SEM. The size of the affected area at the entrance was similar in size to C47 where 0.5 g/Nm^3 of phenol

were dosed for a similar time of 144 h. However, there was less carbon deposition on C47, probably due to higher leakage past the gold seal and the resulting oxidation of carbon.

As for measurements with pure phenol, carbon deposits also formed on the components of the housing. Especially the inlet manifold had a dense carbon coating. In channels of the flow-field with gold wires the carbon deposits were stronger than in channels without gold wires. In addition the edge of the nickel mesh was covered with soot. The chemical interactions between the metallic components, the anode substrate and phenol need to be further investigated in separate tests in future.

Conclusion from Post-Mortem Analysis

The findings of the post-mortem analysis of C50 and C60 confirm the assumption that naphthalene only adsorbs at the anode structure but does not lead to measurable irreversible degradation within the duration of the experiments. Other than phenol, this adsorption drastically reduces the electrochemical performance of the cell. For further development of the cells it is of great significance to find out at which sites naphthalene binds and at which sites it is reformed. However, this could not be investigated with the measurement setups and methods applied in this thesis but requires dedicated experimental techniques or (molecular) modelling and simulation.

6.1.6 Conclusions after Single-Cell Tests with Naphthalene

The single-cell tests showed that state-of-the-art Ni/YSZ ASC are not tolerant to naphthalene at 700 °C but are affected by considerable performance losses. The tests in section 6.1.4 have shown that even 0.12 g/Nm^3 naphthalene have a serious impact on cell performance but also that the rate of voltage decrease correlates with the amount of naphthalene supplied to the cell. For all cells shown, naphthalene caused the cell voltage to drop by 120 to 160 mV within 15 to 160 h, depending on the concentration of naphthalene. This drop can partly be linked to the inhibited conversion of CH_4 and CO and the associated reduced available amount of fuel. However, the previous reference measurements, see sections 5.5.2 and 5.5.2, have

shown that for the given operating conditions CH_4 and CO add 25 mV and 15 mV to the cell voltage, respectively. The observed voltage drop was much larger. This could be explained by interpreting the individual contributions in the EIS data. Naphthalene had an impact on all three visible physiochemical processes:

The process at 1-2 Hz, which shapes the LF-arc, was assigned to gas transport in the substrate to the anode layer[7]. As already mentioned, initially its contribution to impedance increased only gradually. However, it grew strongly from the point at which it could be assumed from the cell temperatures that methane reforming was inhibited on the entire cell. The H_2 generation from the shift of CO also affected the LF-arc. It was therefore not possible to determine whether the conversion of CO was affected in the same way as that of CH_4. Nevertheless, H_2 formation in the substrate was reduced by the more favoured but very slow reforming of naphthalene which increased the contribution of fuel transport resistances to overall polarisation.

The process at 1-2 kHz was connected to the charge transfer reactions at the TPB and is part of the HF-arc. At the TPB the reaction between oxygen ions and hydrogen takes place. It is plausible that naphthalene has penetrated to this sensitive interface and blocked active sites for electrochemical oxidation by adsorption before being reformed. However in the EIS data shown, the polarisation resistance of this process only increased to a minor extent. As already discussed, this can be explained by the fact that under the prevailing operating conditions it was not the rate of the oxidation reaction at the TPB that limited cell performance but the mass transport to the TPB. The latter was connected to the process at approx. 200 Hz which increased immediately after the start of naphthalene. At similar frequencies also processes at the cathode take place; since the conditions there were kept constant, they did not lead to changes in the impedance data. It could be stated accordingly that the HF-arc mainly changed because the diffusion resistances of fuel to the TPB in the anode layer increased. Because of the reduced availability of active sites fuel had to overcome a higher diffusion resistance before being oxidised. As already mentioned the behaviour might be different at higher current densities where fuel oxidation could become the limiting effect.

[7] In a previous publication [72] it was mistakenly assigned directly to reforming activity.

Due to the omission of CO and CH_4 as fuels, the fuel utilisation at the anode increased significantly: in normal operation at 24.3 A it is 34 %; if CH_4 is assumed to be inert, it increases to 48 %; if even CO is inert, 68 % of H_2 must be converted as the only fuel in order to maintain the current density. As CO and CH_4 no longer supplied the maximum amount of hydrogen, the amount of available fuel decreased. Since water was no longer used for reforming and shifting CH_4 and CO, the water vapour partial pressure at the anode also increased. Both influences reduced the local Nernst voltage at the anode (2 kHz process) and increased the diffusion resistance for the remaining hydrogen (200 Hz process).

Which physical processes were actually affected by the poisoning cannot be precisely defined in the given experimental setup: due to the large cell size and the associated concentration and temperature gradients, varying conditions prevail along the cell. In addition the gradients are not constant but can shift locally over time. Since all processes result in only one measured impedance signal, the exact identification of all occurring loss mechanisms cannot easily be achieved. It also remains questionable whether naphthalene poisoning should not lead to an increase in ohmic resistance, as Hauch et al. [139] had observed for H_2S in Ni/YSZ ASC: if the active TPB is reduced by adsorbed H_2S, the oxygen ions must be transported from the electrolyte into the anode over a longer distance. Since the ionic conduction in YSZ is connected to a high resistance, in this case the ohmic resistance rises, i.e. the entire spectrum is shifted to the right. This was not observed in the present work. Either the increase in ohmic resistance could not be measured due to the inductances or it does not occur with naphthalene. It should be noted that under normal SOFC operating conditions adsorbed H_2S does probably not undergo any further reaction. In contrast to this naphthalene is slowly converted by reforming. This could allow a repeatedly availability of active sites where hydrogen can react with oxygen even at a completely naphthalene-covered anode. This could also explain the increasing fluctuations in the voltage signal as naphthalene poisoning progresses. With sufficiently low current density and low naphthalene concentration in the fuel gas this could be sufficient to prevent an expansion of the reaction volume and thus an increase in ohmic resistance. Further degradation could occur at higher current density and thus a higher fuel utilisation if no H_2 arrives at the anode causing the anode to oxidise locally. This could then lead to delamination

due to increased volume of NiO compared to Ni. This phenomenon did not occur as could be shown by post-test analysis in section 6.1.5. Post-test analysis also proved that naphthalene had no permanent influence on the structure of the anode and that in contrast to phenol, naphthalene did not cause macroscopic carbon deposition on the cell or in the housing.

After switching off naphthalene the cell voltage only recovered very slowly. The reason for this was probably the slow removal of naphthalene, which could also be adsorbed on YSZ or other surfaces and only gradually detached from there with decreasing local naphthalene partial pressure. Through the regeneration experiment, see section 6.1.2, it could also be shown that the cell voltage could be raised back to 99 % of its original level by applying several heating periods to 900 °C. It is assumed that the elevated temperatures led to a complete reforming of naphthalene since it was not detected at the cell outlet during heating. In real systems heating to such high temperatures is not feasible due to the materials used in SOFC stacks[8].

Since Naphthalene blocked the conversion of CH_4 and CO and inhibited electrochemistry, materials for anode and support must be applied which ensure faster catalytic conversion of naphthalene already at intermediate temperature. At the same time the great performance of Ni/YSZ anodes has to be preserved. Nevertheless, sufficient naphthalene tolerance, as reported by other research groups for materials such as Ni/GDC, might probably only exist at elevated operating temperatures where reforming can occur more rapidly and adsorption is less pronounced. Further investigations are necessary to enable material scientists to find more suitable anode materials since higher operation temperatures are not favoured. These investigations must clarify the influence of tars and other biogenic impurities on the anode. Until more robust cells become available, naphthalene must be removed from the bio-syngas – ideally by pre-reforming as the hydrogen produced can be converted into electricity in the SOFC. The costs for this pre-treatment could be compensated by the use of less expensive materials for stack and anode and by a longer lifetime of the SOFC.

[8]The maximum temperature of continuous operation for Jülich's F10-Stacks is 810 °C.

6.2 Short-Stack Test with Naphthalene

In addition to the single-cell experiments shown, a test was carried out on the two-level stack F1002-190 for investigation under application-oriented conditions. The cells used in the stack were CTJb type, i.e. half cells from CeramTec, which were printed with the barrier layer and the cathode in Jülich. The test rig described in section 4.3 was used for this purpose. Gas composition and quantity were adjusted by means of the connected gas mixing station. The amount of tar was set to $2\,\mathrm{g/Nm^3}$, comparable to C51, at which $2.5\,\mathrm{g/Nm^3}$ were dosed in order to achieve a rapid and pronounced effect of naphthalene. The gas analysis available at the stack test stand made it possible to follow the evolution of naphthalene poisoning by means of the composition of the anode exhaust gas, which was a good supplement to the EIS results from the single-cell measurements. In addition more realistic conditions are obtained in the stack test since potentially more reactions can take place at the metallic housing made of Crofer 22 APU of the stack than at the ceramic housing of the single-cell test rig.

6.2.1 Procedure of the Experiment

After installing the stack, it was heated to 700 °C at 4 K/min (furnace set temperature 708 °C). At the same time, 0.5 Nl/min/cell forming gas were flowing through the fuel gas side to prevent the anode pre-reduced in Jülich from re-oxidising. The air side flow was 2 Nl/min/cell for the entire duration of the test from the start of heating.

Subsequently, as with all stacks, a basic characterisation was performed in the form of several I-V-curves with pure hydrogen (1.125 Nl/min/cell H_2), a H_2/H_2O mixture (1.1 Nl/min/cell H_2 and 0.275 Nl/min/cell H_2O = 0.221 mg/min/cell H_2O) and a H_2/N_2 mixture (0.5 Nl/min/cell H_2, 0.61 Nl/min/cell N_2). Using the H_2/N_2 reference curves, the performance of F1002-190 could be compared with the other stacks, see Figure 6.17. It can be seen that the performance was slightly lower but still in accordance to the other stacks. Since the preheating of the cathode air was optimised before the test on F1002-190, its two cells showed only a very small deviation from each other in contrast to the other stacks.

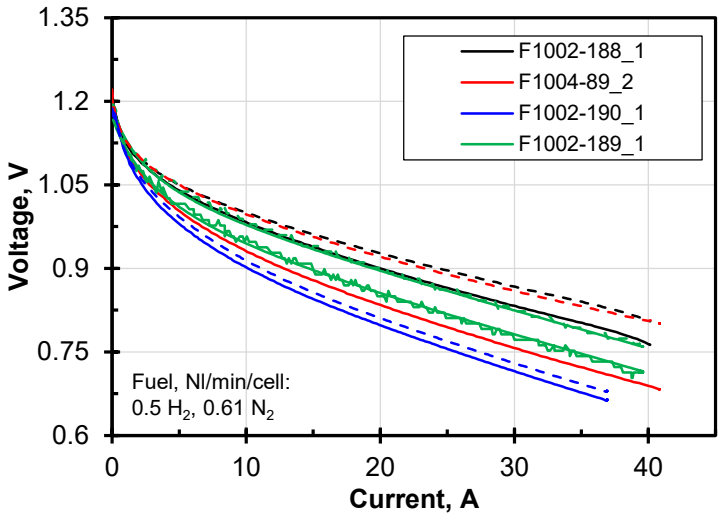

Figure 6.17: Initial I-V-curve at 0.5 Nl/min/cell H_2 and 0.61 Nl/min/cell N_2 of F1002-190 compared to other stacks measured in this thesis. Solid line bottom layer (Cell 1), dashed line top layer (Cell# $\geq$ 2). $T_{\text{stack}} = 700\,°\text{C}$. Noisy data from F1002-189 was fitted with a hyperbolic plus linear term for better visibility.

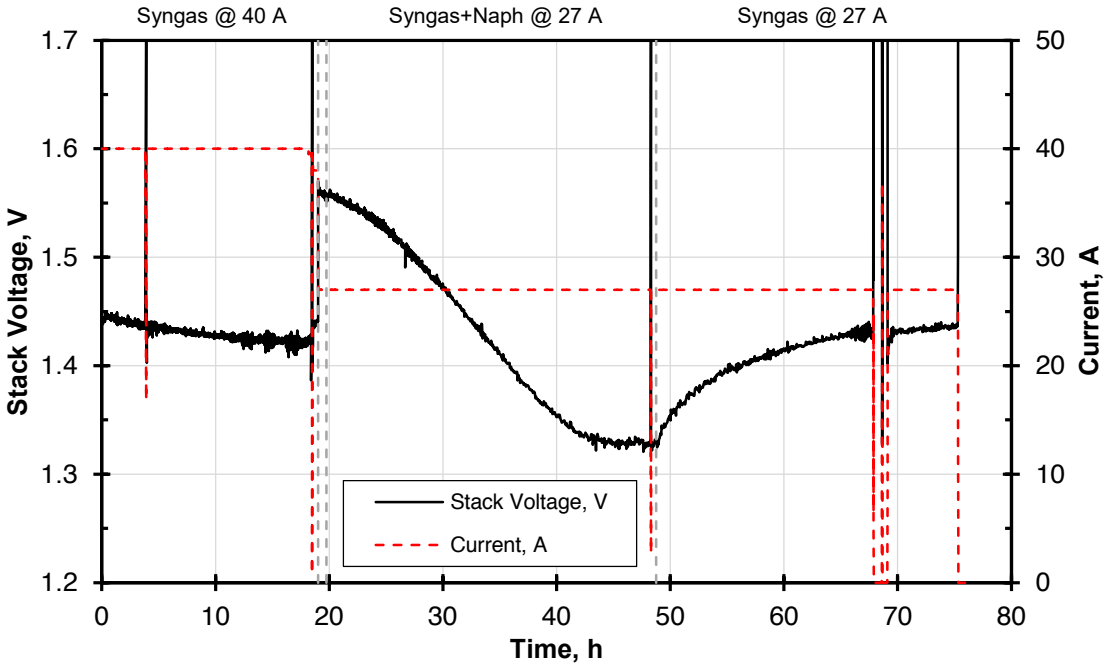

Figure 6.18: Course of stack voltage and applied current. Syngas as main gas, naphthalene concentration 2 g/Nm^3. $T_{\text{stack}} = 700\,°\text{C}$.

Figure 6.18 shows the time response of the stack voltage and the current from the start of operation of the stack on syngas [9]. One can see a clear drop of the voltage within the first 19 h, which can be evaluated as running-in behaviour. At the end of this running-in process the current had to be reduced from 40 to 38 A. The reason for this was a non-ideal contacting between the electrical load and the stack. This caused the voltage drop to be too high, causing the voltage applied to the current collectors to drop below the operating range of the electrical load. To prevent further corrections to the current set point, the current was then set to a significantly lower value of 27 A which led to the increase of voltage before the start of dosing of naphthalene.

As a result, the stack was not operated at a current density of 0.5 but at 0.34 A/cm^2, which corresponded to the value in the previous single-cell measurements. As with the reference curves, the stack performance on syngas was lower compared to other tests: at 0.5 A/cm^2 the top cell voltage was 0.72 V compared to 0.76 V at F1004-89; at 0.34 A/cm^2 the top cell voltage was 0.787 V, whereas in most single-cell measurements more than 0.8 V was measured. The cells in the stacks were contacted at 80 cm^2, but only at 72 cm^2 in the single-cell test rig. The larger active area led to a higher fuel gas utilisation in the stacks at the same current density, i.e. the cell voltage had to be lower.

After approximately one hour of operation on syngas and 27 A, 2 g/Nm^3 naphthalene were added to the fuel gas. For this purpose the tar saturator described in 4.3.3 was used, which was filled with naphthalene and heated to the temperature necessary for the desired tar content. The reference temperature for the calculation of the tar concentration was the temperature in the gas outlet of the container, which was 81 °C. The tar saturator was supplied with 67 ml/min CO_2 via a separate MFC, whereas the volume flow of pure CO_2 was reduced to 133 ml/min. Complete reforming of the naphthalene added to the stack would theoretically result in additional 0.008 Nl/min/cell H_2 and 0.0035 Nl/min/cell CO_2 ($C_{10}H_8 + 20H_2O \longleftrightarrow 10CO_2 + 24H_2$).

As already observed in the single-cell experiments, the voltage dropped steadily from the start of dosing and after approx. 25 hours reached a plateau which was

[9] Volume flows in Nl/min/cell: 0.5 H_2O, 0.25 H_2, 0.1 CO, 0.1 CO_2, 0.05 CH_4.

approx. 110 mV below the voltage last measured with pure syngas for both cells. In contrast to the single-cell measurements with naphthalene, the voltage decrease and the transition to the plateau were smoother. However, a delay of approx. 1 h occurred until the voltage signal decreased; for C51 this was 0.5 h.

The presence of naphthalene in the fuel gas was regularly tested using SPA samples. The port for the measurement was approx. 3.3 m upstream of the stack, the total distance between tar saturator and stack was approx. 9.3 m. Naphthalene was found in all samples upstream of the stack. Due to the condensation of water vapour from the syngas in the syringe, an average of 2.5 g/Nm^3 was measured, i.e. 25 % more than the target value of 2 g/Nm^3. Only in the first sample, which was taken 3.5 hours after the start of dosing, only 1.8 g/Nm^3 were measured. This could – apart from the methodological inaccuracies of the SPA method – explain why the voltage during the experiment fell only gradually and not as abruptly as in the single-cell experiments: the piping to the stack was significantly longer than on the single-cell test rig – 930 cm vs. 230 cm – and accordingly the risk was greater that a section was not sufficiently heated and could initially saturate with naphthalene. In particular, the connection between the tar tank and the gas mixing station might have been critical here as it consisted of a PTFE hose heated with a heating cord. Due to the significantly poorer thermal conductivity of PTFE compared to stainless steel, cold zones might have formed in the latter. This assumption is also supported by the fact that 0.05 g/Nm^3 were still detected in an SPA sample from the supply pipe 1.5 hours after switching off naphthalene. After the test, however, the PTFE hose was rinsed with dichloromethane and no significant amount of condensed naphthalene was detected. In GC spectra of the SPA samples of the anode exhaust gas there was always a small peak at the retention time of naphthalene, but it could not be integrated by the software of the GC, which means that, as with C51, only a small fraction of the supplied naphthalene left the stack and the balance was adsorbed and slowly reformed.

Figure 6.19 shows the plot of the cell voltages over the calculated amount of naphthalene supplied. The voltage decrease measured for F1002-190 was again slower than for C51. The slower transition into the stage of constant voltage decrease can

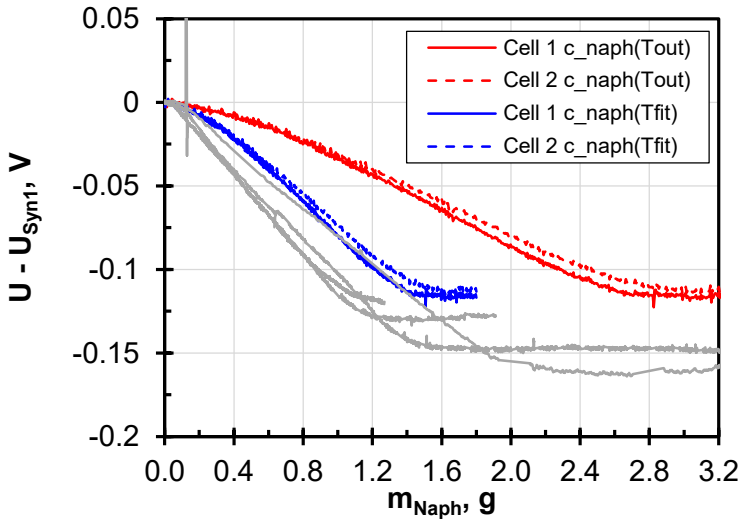

Figure 6.19: Decrease of cell voltage for F1002-190 plotted over supplied amount of naphthalene and compared to single-cell tests (grey curves). Red curves: Tar concentration determined with tar container outlet temperature ($T_{\text{out}} = 81\,°\text{C}$). Blue curve: Temperature adjusted so that the rate of decrease matches the single-cell measurements ($T_{\text{fit}} = 72\,°\text{C}$). Celltype CTJb. Fuel: syngas. $T_{\text{stack}} = 700\,°\text{C}$.

be explained by the above mentioned longer piping and the possibility that it had to saturate with naphthalene first. In addition naphthalene might adsorb better on the Crofer and nickel surfaces of the stack than on the alumina oxide of the single-cell housing, which could also have led to a delay.

It is possible that T_{out} was not representative for calculating the saturation vapour pressure inside the tar container. To obtain a similar rate of voltage decrease as in the single-cell tests one would have to base the calculation of the naphthalene concentration on a temperature of T_{fit}=72 °C, see the blue curve in Figure 6.19. This would correspond to a naphthalene concentration of $1.2\,\text{g/Nm}^3$. At the same time it is possible that the thermocouple inside the naphthalene container of the tar mixing station of the single-cell test rig could also indicate a too low or too high a value; so this cannot serve as a fixed reference. But even if the determination of the actual naphthalene concentration is not fully correct, its exact value is not decisive at this point.

After 29 hours of naphthalene dosage the switch back to pure syngas was carried out, which resulted in the already observed hyperbolic recovery of voltage. Com-

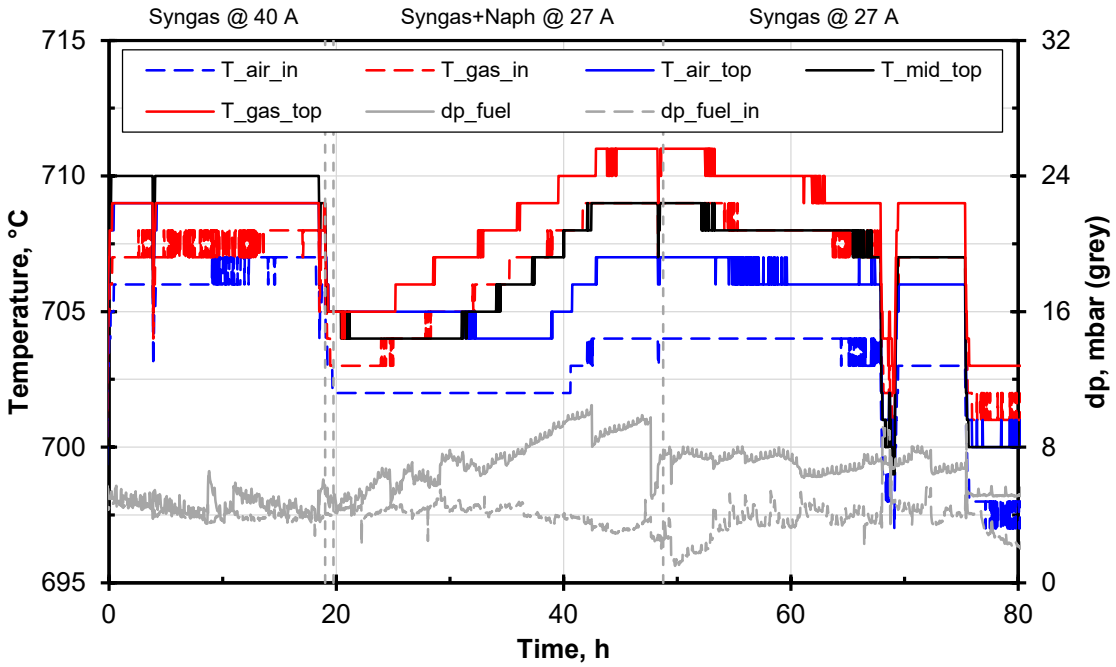

Figure 6.20: Trends of pressure drop at fuel side dp_{fuel}, over-pressure at fuel inlet $dp_{\text{fuel,in}}$ and temperatures on fuel and air side for F1002-190. Solid lines top layer, dashed lines bottom layer. $T_{\text{stack}} = 700\,°\text{C}$; $A_{\text{active}} = 80\,\text{cm}^2$.

pared to C51 the recovery rate decreased faster. After 26 h on syngas – interrupted by a phase with H_2/N_2 as fuel gas for a reference curve – the gas supply was switched to forming gas. The voltage had reached 93 % of its original value until the switch to forming gas.

As in the single-cell tests, see section 6.1.1, the voltage drop was accompanied by an increase in temperature due to inhibition of endothermic reforming, see Figure 6.20. The trends of the thermocouples in the bottom and in the top cell layer behaved parallel to each other, which together with the parallel cell voltages indicated an uniform effect on both cells. The magnitude of the temperature increase was similar to the one observed at C51. The progress of the temperature rise differed due to the different thermal conductivity properties – steel instead of ceramic – in the stack and the different positions of the thermocouples. However, it could also be observed that the temperature initially increased at the inlet (red curves) and only with a delay at the outlet (blue curves), which again showed the

progressing naphthalene front. This was also confirmed by a increasing amount of non-converted methane in the anode offgas. The trends of the offgas analysis will be discussed in 6.2.3. The pressure drop across the stack was nearly constant during the experiment which was interpreted as an indication that the flow in the layers had not changed. In contrast to the experiments with phenol, no carbon deposits were to be expected, which would have increased the pressure drop in the stack.

6.2.2 I-V-Curves

After the first part of the test the stack was "parked" for 66 h with a sufficiently low forming gas flow at the fuel gas side and without drawing current. It was noticed that the stack voltage did not increase further in this phase. Two hypotheses could explain this behaviour: first, the recovery at OCC was not visible because enough TPB were free to deliver the open cell potential; second, naphthalene could probably only be removed from the anode by reforming, which would have required water vapour. When resuming the operation on syngas under load (27 A), the stack voltage was at the same level as before the forming gas phase, which suggests that no further regeneration had taken place simply by flushing with forming gas.

The comparison of the I-V-curves for syngas and H_2/N_2 in Figure 6.21 also shows that the influence of naphthalene poisoning on the OCV was only present in syngas[10]. There are two influences which explain the reduced OCV in syngas: first, the H_2 partial pressure was reduced by unconverted CH_4 and CO and second, less additional H_2 from the conversion of CH_4 and CO was available. Both had an effect on the reactant term in the Nernst equation, resulting in lower cell voltage. Under load both gas compositions had an increased ASR due to naphthalene poisoning. This again shows that naphthalene did not only block reforming reactions but also directly did inhibit electrochemical oxidation of hydrogen or fuel gas diffusion to

[10]The noise in the last curves is due to changes in the measurement setup and cannot be attributed to the state of the cell: smooth curves were measured using the HOBO logger, noisy curves over the Meilhaus interface.

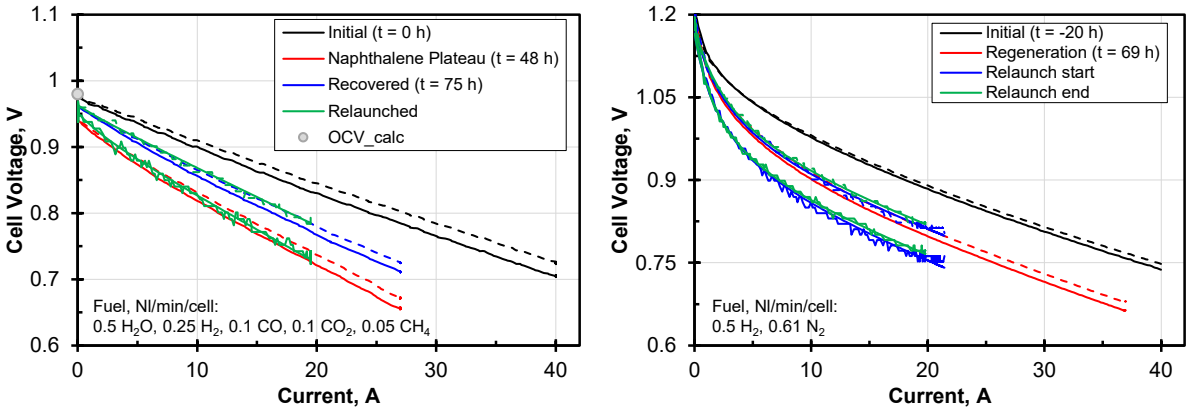

Figure 6.21: Left: I-V-curves of F1002-190 on syngas at indicated instants together with calculated OCV(700 °C). Right: I-V-Curves on H_2/N_2 mixture at indicated instants. Solid lines represent voltage of bottom cell. $T_{\text{stack}} = 700\,°\text{C}$; $A_{\text{active}} = 80\,\text{cm}^2$. Noisy data was fitted with a hyperbolic plus linear term for better visibility.

the TPB, as observed by Papurello et al. [75]. Due to the already mentioned high voltage drop in the current collectors, it was not possible to set a sufficiently high current during the I-V-curves to visualise the mass transport limitation. Together with the ASR, this maximum current density would have provided further data for the interpretation of the poisoning.

Up to the switching to forming gas the cells had clearly recovered, as can be seen from the blue line in the left plot of Figure 6.21. However, the performance was still far from its original state. In order to investigate the influence of the fuel gas composition on recovery, the stack was operated once again. The stack was then operated at 0.5 Nl/min/cell H_2 and 0.5 Nl/min/cell H_2O at the fuel gas side to force the reforming of naphthalene at the anode, intermitted by phases on H_2/N_2 and syngas for I-V-curves. When switching back to syngas, however, 3 vol% CH_4 were still present in the exhaust gas, which was interpreted as a clear sign of persistent poisoning.

As can be seen from the I-V-curves relaunched (green curves) in Figure 6.21 right, the performance could not be further increased. All I-V-curves of syngas and H_2/N_2 recorded in the second run were superimposed. However, the overlaying problem was that the stack had lost performance due to removal and installation and that the air preheater was defective during the second run, which further reduced the

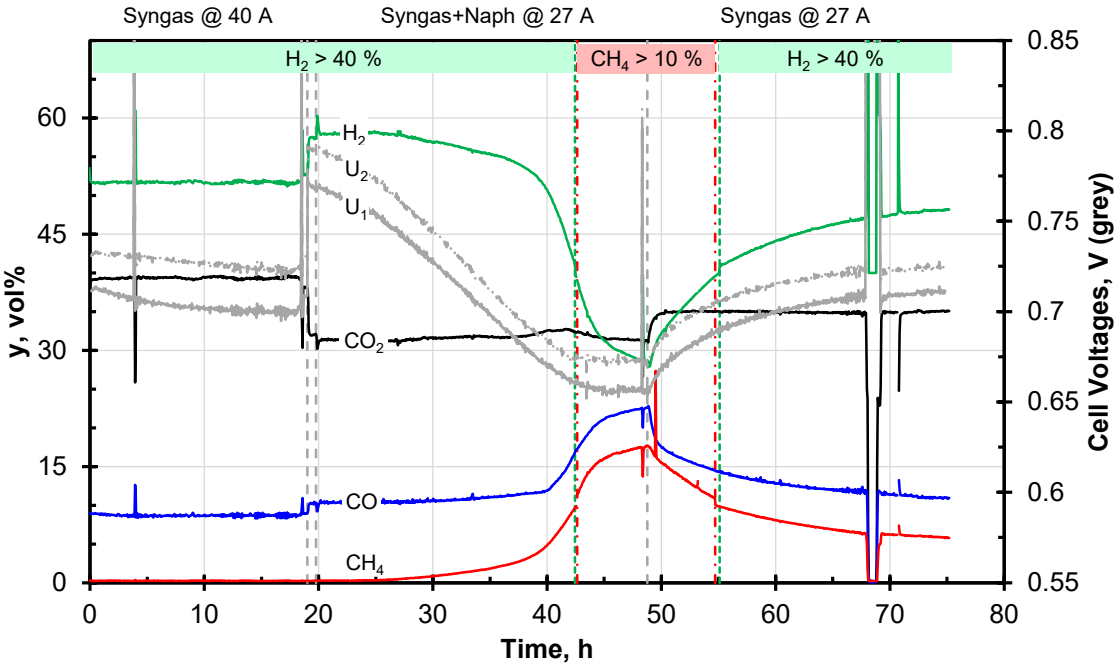

Figure 6.22: Progression of the concentration of main gas components CO, CO_2, CH_4 und H_2 in the exhaust gas during the test on F1002-190. $T_{\text{stack}} = 700\,°\text{C}$.

voltage of the bottom cell. In Figure 6.21 this can be clearly seen from the lower I-V-curves of the bottom cell. It is therefore possible that a successful regeneration was counterbalanced by a degradation of the stack. In this case, however, a decrease in the CH_4 concentration in the exhaust gas would have been observed. Consequently, the stack could not be regenerated by other gas compositions at a temperature of 700 °C.

6.2.3 Off-Gas Analysis

In addition to voltage, temperature and pressure drop, the exhaust gas composition could also be measured during the stack tests. The moisture value of the anode exhaust gas could not be evaluated during this measurement as the gas was already fed into a separate condensate separator upstream of the moisture sensor in order to protect the downstream plant components from any residual tar content.

Figure 6.22 shows the trend of the concentration of the main gas components CO,

CO_2, CH_4 and H_2. For comparison, the curves of the cell voltages were plotted in grey in the same diagram. The value of O_2 recorded at the same time was always below 0.1 vol% and therefore was not evaluated further. The vertical coloured lines indicate the intervals in which the CH_4- or H_2-concentration was outside of the detection limit of the respective sensor, i.e. when CH_4 >10 vol% or H_2 >40 vol%. In this case the excess fraction in the gas analysis was displayed as N_2 value, which in turn was added to the H_2 or CH_4 value in the evaluation. Only one type of gas was at the limit in accordance with the measuring ranges. However, as can be seen for CH_4, the addition resulted in slight discontinuities in the curves.

Without naphthalene and at the beginning of the dosing no methane was measured in the exhaust gas, which corresponds to the reaction equilibrium for the adjusted syngas composition at 700 °C. However, the increasing proportion of CH_4 in the exhaust gas confirms that the presence of naphthalene blocked the conversion of CH_4 at the anode. Even at the end of syngas operation after the naphthalene phase the poisoning was still pronounced, as can be clearly seen from the increased CH_4 content, analogous to the unrestored stack voltage. The CO conversion was also inhibited but at a later point in time than the CH_4 reforming. Since both effects produced less H_2 at the anode and the H_2 utilisation had to increase to maintain the current level, the H_2 concentration in the exhaust gas decreased. As no further decrease in cell voltage was observed in the single-cell measurements over several days after reaching the plateau, the dosing of naphthalene was stopped as soon as the stack voltages were constant.

The qualitative values of the exhaust gas analysis can be converted into volume flows. Via a carbon balance[11]

$$\dot{V}_{\mathrm{C,in}} = \dot{V}_{\mathrm{CH_4}} + \dot{V}_{\mathrm{CO}} + \dot{V}_{\mathrm{CO_2}} \tag{6.1}$$

the volume flows for CO, CO_2 and CH_4 in the outlet can be calculated from their volume proportions. Using the example of CH_4:

[11] Ideal gas, volume flow corresponds to flow of matter. $\dot{V}_{\mathrm{CH_4}} = 0.1\,\mathrm{Nl/min}$, $\dot{V}_{\mathrm{CO}} = 0.2\,\mathrm{Nl/min}$, $\dot{V}_{\mathrm{CO_2}} = 0.2\,\mathrm{Nl/min}$.

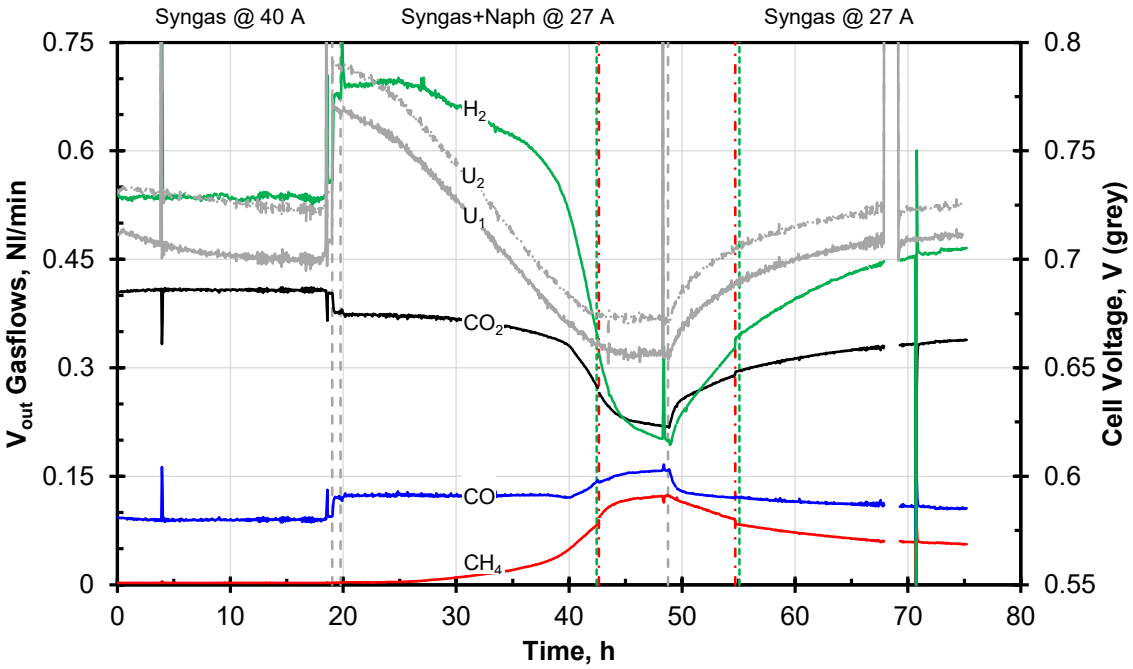

Figure 6.23: Flow rate of main gas components CO, CO_2, CH_4 and H_2 in the anode exhaust gas during measurement at F1002-190. $T_{\text{stack}} = 700\,°\text{C}$.

$$\dot{V}_{\text{CH}_4,\text{out}} = \dot{V}_{\text{C,in}} \frac{y_{\text{CH}_4}}{y_{\text{CH}_4} + y_{\text{CO}} + y_{\text{CO}_2}}. \tag{6.2}$$

From this the total dry volume flow at the outlet

$$\dot{V}_{\text{dry,out}} = \frac{1}{y_{\text{CH}_4} + y_{\text{CO}} + y_{\text{CO}_2}} \dot{V}_{\text{C,in}} \tag{6.3}$$

can be determined. Since apart from CO, CO_2 and CH_4 only H_2 was present in the flue gas, the H_2 volume flow can be calculated with the known total dry volume flow:

$$\dot{V}_{\text{H}_2,\text{out}} = \dot{V}_{\text{dry,out}} - \dot{V}_{\text{C,in}}. \tag{6.4}$$

The results of the dry gas volume flow calculations at the stack outlet are shown in

Figure 6.23. It is clearly visible how the reduction of the current density reduced the conversion of H_2 and CO. While the volume fraction of CO_2 had remained approximately constant over the duration of the measurement, it can now be seen that the CO_2 volume flow decreased significantly in line with the decreasing CO and CH_4 conversion when naphthalene poisoning progressed. The CO conversion on the other hand decreased less strongly than the raw values of the exhaust gas composition had suggested and was very constant initially. It is also noticeable that, in contrast to CH_4, the CO exhaust gas flow very quickly returned to its original level after the switchover.

According to the calculation, more CH_4 left the stack at the end of the naphthalene dosing than was fed to it. As already mentioned, equilibrium calculations in Aspen Plus(R) show that no CH_4 could be formed under the prevailing conditions. The present overestimation of 20 % (0.12 instead of 0.1 Nl/min) was therefore due to errors in gas dosing and analysis. A deviation of the CO-, CO_2- or CH_4-MFC from the target value had a direct influence on the calculated CH_4 volume flow in the anode exhaust gas via the carbon balance. The mean calculated deviations for the dosing of CO, CO_2 and CH_4 were 0.015 Nl/min [151] for the adjusted set points. In addition, the CO_2-MFC was running at the lower end of its operating range during naphthalene dosing where more pronounced deviations from the set point can occur. For periods in which CH_4 was beyond its detection limit the measurement errors of the gas analysis result in a possible tolerance range of dV_{CH_4} = 5.7 ml/min, which corresponds to 4.75 % of the determined volume flow.

In section 6.1.6 it was assumed, based on the EIS data, that the presence of naphthalene led directly to the inhibition of fuel diffusion to and reaction at the TPB. The impairment of reforming activity was observed in the EIS at a later stage. This is now also evident in the stack exhaust gas: the volume flows of CO, CO_2 and H_2 were approximately constant during the first five hours of naphthalene dosing while the voltages of the cells had already dropped by approx. 25 mV. Even the absolute value of CH_4 only rose imperceptibly during this period, but the beginning of its subsequently increasing presence in the exhaust gas can be guessed. During this initial phase naphthalene blocked an increasing number of active centres for electrochemical reactions at the anode. As a result, losses due to diffusion resistances increased and cell voltages dropped accordingly while gas conversion across the cell

was still constant.

As discussed in the section 6.1.6, the omission of CH_4 and CO as fuel led to an increase of FU: in normal operation it was 34 % for the stack due to the larger area contacted; without CH_4 54 %; without CH_4 and CO 75 %, which then represented the hydrogen utilisation. The last H_2 volume flow determined during naphthalene dosing was 0.2 Nl/min, corresponding to an FU_{H_2} of 60 %. For a hydrogen utilisation of 75 % the H_2 volume flow would have had to decrease to 0.125 Nl/min. So reforming and WGS were not completely inhibited at the time of change back to pure syngas, which was also indicated by the fact that the gas analysis values were not yet stationary. The further omission of CO and CH_4 did not lead to a further voltage decrease from a certain point in time. It is possible that then it was no longer the amount of available fuel that was limiting for the cell potential but its diffusion to the anode and the rate of the electrochemical reaction at the TPB.

It is also interesting to know why the inhibition of CH_4 conversion started much earlier and was much more pronounced than the one of CO. One possible explanation is that the reaction kinetics of the endothermic reforming of CH_4 at 700 °C could be slower than the exothermic WGS of CO. This would mean that compared to CH_4, CO would require less non-poisoned cell area to be converted. The fact that CO is formed during the reforming of CH_4 and CO can be used directly by the SOFC under certain conditions [50, 54] leads to a complex relationship that cannot be clarified on the basis of the collected data alone.

6.2.4 Post-Mortem Analysis of F1002-190

After the end of the measurement, the stack was dissected at Forschungszentrum Jülich. There was no macroscopically visible carbon deposition inside the stack. The structure of the cells as well as the surfaces inside the stack did not show visible abnormalities. Detailed investigation on possible microscopic changes via SEM and the detection of microscopic carbon deposits via Raman spectroscopy is pending. It is expected that the results will be comparable to the post-test examination of single-cells tested with naphthalene as model tar [32].

6.2.5 Conclusions after Short-Stack Test with Naphthalene

The behaviour of the short-stack during poisoning by $2\,g/Nm^3$ naphthalene was very similar to the one of the single-cells. The cell voltages reached a plateau after a steady voltage drop after about one day. The rate of voltage decrease and the absolute voltage decrease were lower than in comparable single-cell experiments. This was probably due to the different tar dosing and the longer piping. As in the single-cell experiments, the increase in outlet temperatures marked the presence of naphthalene on the entire cell.

Based on the findings described in the conclusion of the naphthalene single-cell experiments, section 6.1.6, these further findings on naphthalene poisoning can be recorded after the short-stack experiment:

- The poisoning of the cells became very visible in the values of the exhaust gas analysis: reforming of CH_4 was blocked; the CO shift was also inhibited; the increasing loss of CH_4 and CO as fuel was compensated by a significantly increased hydrogen consumption.
- The cell voltages dropped at the beginning of naphthalene dosing without changing the gas composition. Furthermore, the gas composition changed when the voltage was already constant.
- The I-V-curves recorded confirmed that naphthalene in syngas operation reduced both the OCV and the operating voltage under load. With H_2/N_2 as fuel gas an over-potential could also be found with persistent naphthalene poisoning, but the OCV was unaffected. This shows that naphthalene not only did inhibit reforming and CO shift, reducing H_2 partial pressure, but also did block H_2 reactions and mass transfer to TPB.
- No further voltage increase of the stack could be achieved by hydrogen and water vapour rich gas compositions after incomplete regeneration in syngas – or at least regeneration was less than the remaining degradation of the stack.

Chapter 7

Effects of Phenol as Model Tar

In the following chapter results from single-cell and a short-stack test with phenol as model tar are presented. Overall eight single-cells were exposed to phenol. Most of the results were already published in a journal paper [71] and a conference paper [152] so these are only summarised at this point. In addition a single-cell test with repeated dosing of 0.5 g/Nm^3 phenol and the test of a two-layer short-stack with increasing concentration of phenol are discussed in this chapter. Furthermore, a brief comparison of the behaviour of cells with Ni/YSZ and Ni/GDC anode is made. Most of these results are already described in [32].

Phenol (C_6H_5OH) was chosen as a model tar since it is one of the most frequent tar components in bio-syngas from fluidised-bed gasifiers [98]. It is hetero-cyclic and consists of a hydroxy group (-OH) that is bound to a phenyl group (-C6H5). It is a primary tar and originates from the pyrolysis of lignin [59]. It is toxic if swallowed or inhaled, is suspected of causing genetic defects and is toxic to aquatic life with long lasting effects [153]. For all tests phenol of a purity of >99.9 % was used (AnalaR NORMAPUR Phenol, VWR Chemicals).

7.1 Repeated Dosing of Phenol on Single-Cells

The results of the single-cell tests with phenol are presented in the following section. The single-cell test rig described in 4.2 was used for the tests. All four types of anode-supported cells described in 4.1 were tested: the state-of-the-art cells CTb and IIIb with Ni/YSZ anode, CTJb with Ni/YSZ anode printed on Ce-

Table 7.1: Overview of single-cells that were tested with phenol as model tar.

Cell	Type	c_{Phenol}, g/Nm³	Dosed phenol, g	Exposure time, h	Discussion of results
C32	IIIb	1, 2, 4, 8	54.7	216	[32, 71, 100]
C35	CTb	2, 2, 2, 2, 2	25.9	216	[32, 71, 100]
C37	CTb	1.5, 1.5, 1.5, 1.5, 1.5"	28.1	312	[32, 71, 100]
C40	CTJb	2, 4, 4	20.6	98	
C41*	CTJb	2, 2, 2	30.8	256	[152]
C45	CTGDC	2, 2, 2, 2	20.3	169	[32] and 7.1.2
C46	CTb	0.5, 0.5, 0.5	4.3	144	7.1.1
C56	CTGDC	1, 2, 4, 8	54.6	215	[32] and 7.1.2

" last phenol phase for 216 h

* load variied from 0.5 to 0 A/cm²

ramtec substrates combined with a smaller cathode area and CTGDC cells with Ni/GDC anode. The standard test conditions were the same as for the tests with naphthalene, see Table 6.1, so all tests were conducted at 700 °C, with simulated syngas[1] and in galvanostatic mode at 0.34 A/cm². After an initial phase on pure syngas phenol was usually dosed for 48 h, followed by again 48 h on syngas. These 96 h blocks were repeated several times, either with constant (C35, C37, C45, C46) or increasing concentration (C32, C56) of phenol. Only for C41 also the current density was altered. Besides the monitoring of cell voltage, pressure and temperatures, EIS measurements were carried out and evaluated regularly. The presence of phenol in the fuel gas was checked by the SPA method [117], which always showed positive results of the appropriate magnitude.

The cells and their respective test programmes are listed in Table 7.1. For all cell types phenol attacked the Ni/YSZ substrate which led to metal dusting. When phenol was present in the syngas, carbon deposition at the alumina housing oc-

[1]Volume flow in Nl/min: 0.5 H_2O, 0.25 H_2, 0.1 CO, 0.1 CO_2, 0.05 CH_4

curred in the form of a hard-to-remove soot-like layer. At the gold wires agglomerates of carbon formed, which detached during opening of the housing. Detailed post-mortem microstructure analysis was performed on all cells. The results of the latter are discussed in [32, 100].

7.1.1 Ni/YSZ Anodes

The findings already described in [71, 152] for the cells with Ni/YSZ anode (C32, C35, C37, C41) are summarised first. In addition an experiment with 0.5 g/Nm^3 phenol was performed on C46, the operating data of which is discussed below.

Summary of Tests with Phenol on C32, C35, C37, C41

The tests on C32, C35, C37, C41 led to the following observations:

- For cells with Ni/YSZ anode the data showed only minor effects of up to 2 g/Nm^3 of phenol on electrochemistry during operation. The degradation rate was mostly similar to the one of the reference cell.
- When phenol was present in the fuel gas, the voltage signal showed oscillations which intensified with increasing concentration of the model tar. The phenomenon of the oscillating cell voltage was also observed by Chen et al., when the cells were operated on syngas compositions that were meant to lead to the formation of solid carbon [154].
- For every concentration phenol led to carbon deposits on the cell, the housing and the metal surfaces of the contacting. Their occurrence could not be predicted by evaluation of the equilibrium of formation of solid carbon, see Figure 4.7.
- With 4 g/Nm^3 phenol (C32 Phe3) the operation started to get unstable, which was indicated by an erratic voltage signal. At 8 g/Nm^3 occurred a significant decrease in voltage and an increase in the inlet temperature. At the same time the pressure at the cell inlet increased which suggests that strong carbon deposits or material detachment had led to blockage of the gas flow.

- No regeneration of the cell took place during the operation on pure syngas after the voltage had slightly decreased after dosing 4 or 8 g/Nm^3 of phenol.
- The inlet temperature increased with prolonged dosing of phenol and for some cells the thermocouple at the inlet showed downward spiking.
- No phenol was found in SPA samples of the anode outlet gas which indicates that it was fully converted by reforming or more probably by thermal cracking [64] at the given operation conditions.
- From the EIS data a small but steady increase of polarisation resistance at a constant R_0 could be observed for all cells. This was mainly due to an expansion of the high-frequency arc. According to literature, this result could indicate carbon deposition in the anode layer [52, 56, 154]. On the other hand polarisation resistance increased linearly for all cells irrespective of the presence of phenol. It is therefore possible that neither the increase in ASR nor the decrease in cell voltage was not influenced by phenol but caused by superimposed influences of the test setup.
- All cells showed severe disintegration of the support material after the test in form of metal dusting near the fuel inlet. Since the affected area was mostly outside of the electrochemically active area, this deterioration could not be seen during operation. An analysis of the formed dust showed that both nickel and YSZ were attacked by the delamination. The results of the post-mortem analysis are discussed further in section 7.1.3.
- It is therefore important that tests with phenol, as with other impurities, are carried out for a sufficiently long time and that the absence of a response of the cell voltage during a short measurement is not interpreted as an indication for the tolerance of the cell to the respective impurity.

Influence of 0.5 g/Nm^3 of Phenol – C46

Figure 7.1 shows the trend of the cell voltage over time as well as the temperatures at the inlet (T11), outlet (T33) and in the middle (T22) of the cell during the measurement at C46. Phenol was dosed three times for 48 h with 0.5 g/Nm^3 each. As with previous measurements with phenol the cell voltage did not react to its

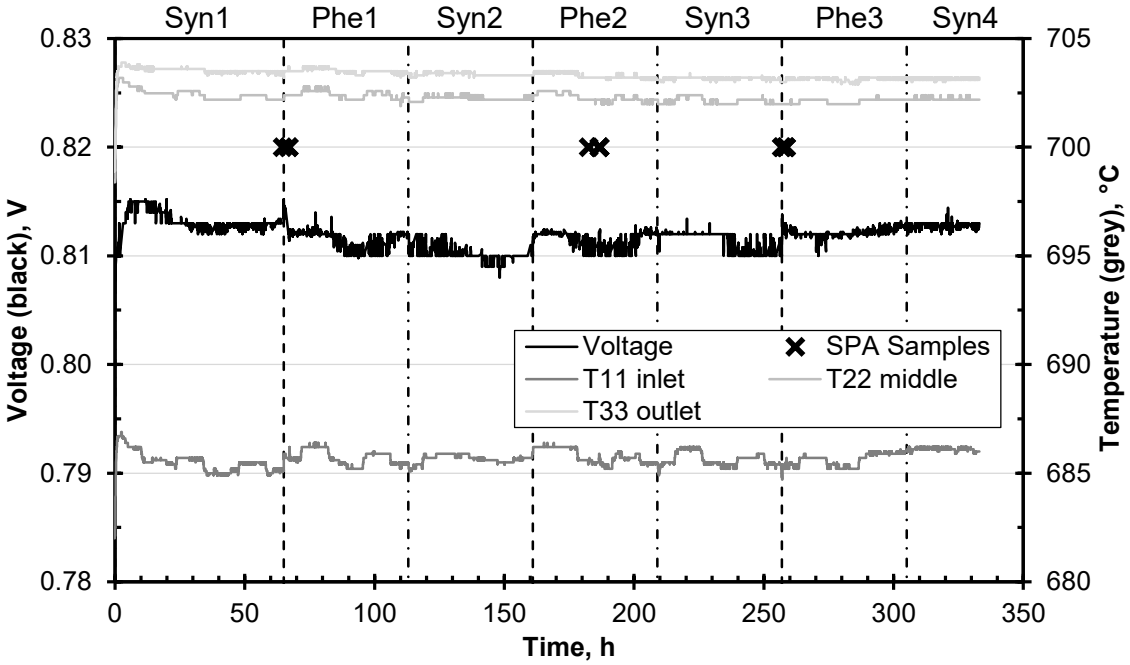

Figure 7.1: Trends of cell voltage and cell temperatures during the test with 0.5 g/Nm^3 of phenol. Dashed lines indicate beginning of dosing of phenol, chain lines the return to pure syngas. C46, CTb. Operation conditions see Tab. 6.1.

presence in the fuel gas. Although the voltage changed with each switching between test phases, there was no uniform trend regarding a positive or negative influence of phenol. A positive effect would be the provision of additional hydrogen by reforming of phenol, a negative one the obstruction of the gas flow in the housing or the mass transport in the cell by carbon deposits. The temperatures at the cell were approximately constant, an increase of the inlet temperature as it had been observed with higher phenol concentrations did not occur. Due to the mentioned day-night cycle of the ventilation system in the laboratory, T11 and also to a small extent T22 showed periodic oscillations during the run.

Nor did the presence or absence of phenol show any influence in the impedance data, see Figure 7.2. The presentation of the data was explained in section 5.5.2 and shows the Nyquist plot (a), the trend of Z_{imag} of the HPL, HPH and LP (b), the trend of Z_{real} of HPL, HPH and LP together with R_{pol} and R_0 (c) and the comparison of the DRT and the imaginary part for the first and the last spectrum

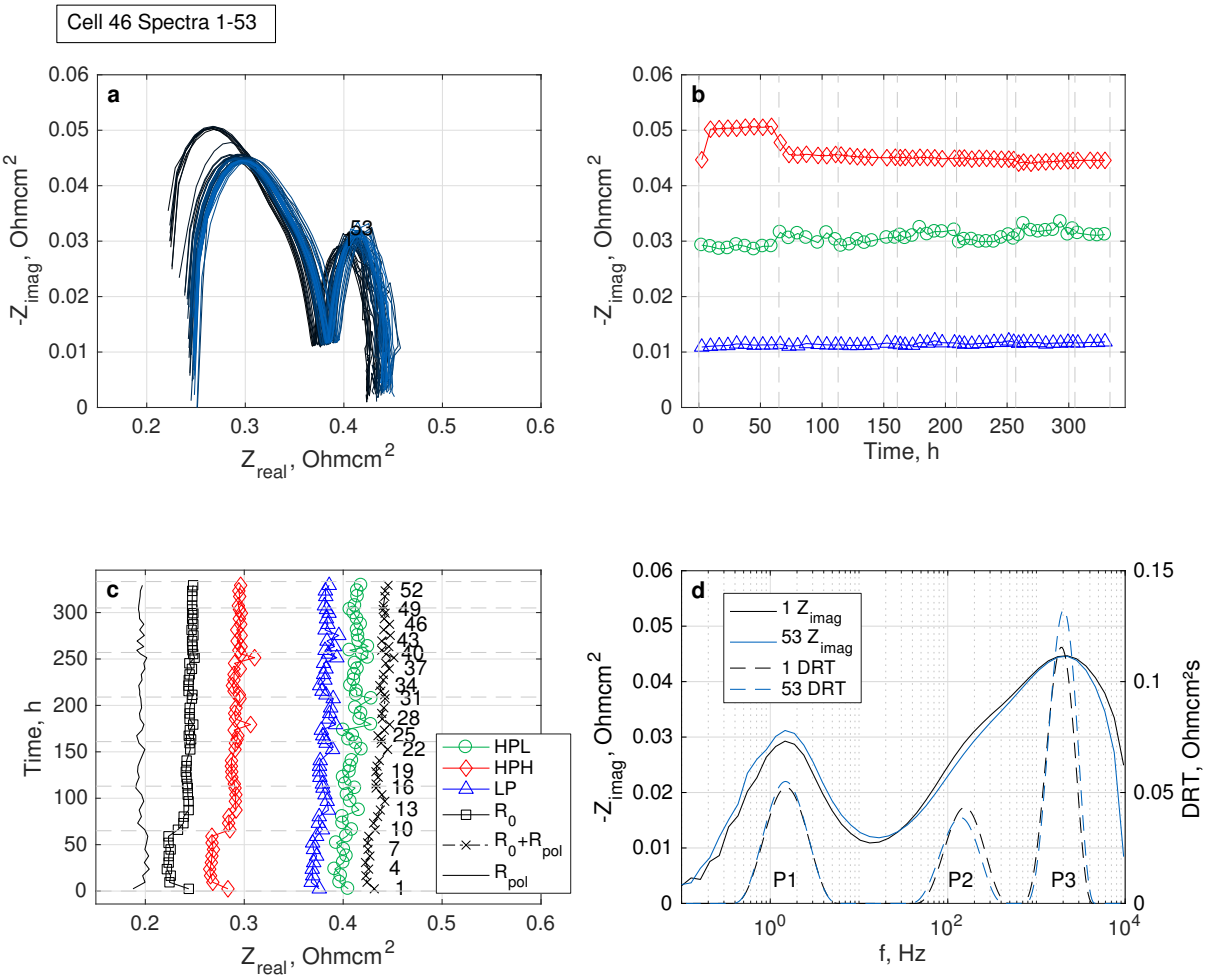

Figure 7.2: Impedance data for C46 starting with Syn1. HPL: ASR at maximum of low-frequency arc; HPH: ASR at maximum of high-frequency arc; LP: ASR at low point between the two arcs. a: Nyquist plot; b: trend of Z_{imag} of the HPL, HPH and LP; c: trend of Z_{real} of HPL, HPH and LP together with R_{pol} and R_0; d: comparison of the DRT and the imaginary part for the first and the last spectrum. Operation conditions see 6.1.

of the test (d). It is unclear why in spectra 2-9 during Syn1 the imaginary part of HPH was increased at constant LF-arc and why R_0 was lower. At the same time cell voltage at the beginning of Syn1 had increased before returning to the original level by spectrum 5. From spectrum 10 onwards the values were again as for spectrum 1. Although this decrease coincided with the beginning of Phe1, it is assumed that this was an anomaly and was not related to the presence of phenol.

Similar to the other phenol cells a systematic increase of polarisation resistance in the HF-arc occurred, see Figure 7.2 c. As shown in Figure 7.2 d, the imaginary part had hardly changed from the first to the last spectrum except for a small increase at low frequencies. In the DRT, between the first and last spectrum in Figure 7.2 d, a slight increase was seen at P3, which corresponds to the wider HF-arc and would indicate a deterioration of electrochemical oxidation at the TPB. However, due to the sensitivity of the DRT to perturbations this observation is debatable. It is also possible that the systematic drifts in the impedance data were caused by cathode degradation. At the end of the measurement it showed the dark areas described in section 6.1.5. These were probably caused by a contamination of the air flow with silicone oil, which can inhibit the catalytic processes at the cathode. At the same time, according to [44], the processes at the cathode are excited below 500 Hz, which would not explain why process P3 at 2 kHz had deteriorated.

On the basis of the data shown it could be assumed that 0.5 g/Nm^3 had no effect on the cell. As with the previous cells, however, metal dusting also occurred in C46 at the anode supports at the fuel gas inlet, see section 7.1.3, which was hardly detectable in the electrochemical performance.

7.1.2 Ni/GDC Anodes

In addition to the cells with Ni/YSZ anode, the effects of phenol were also investigated for the CTGDC cells. In the following, the two cells C45 and C56 will be discussed. C56 was the repetition of C32 at which phenol was dosed in increasing concentrations of 1, 2, 4 and 8 g/Nm^3. C45 was the repetition of C35 at which 2 g/Nm^3 was dosed several times.

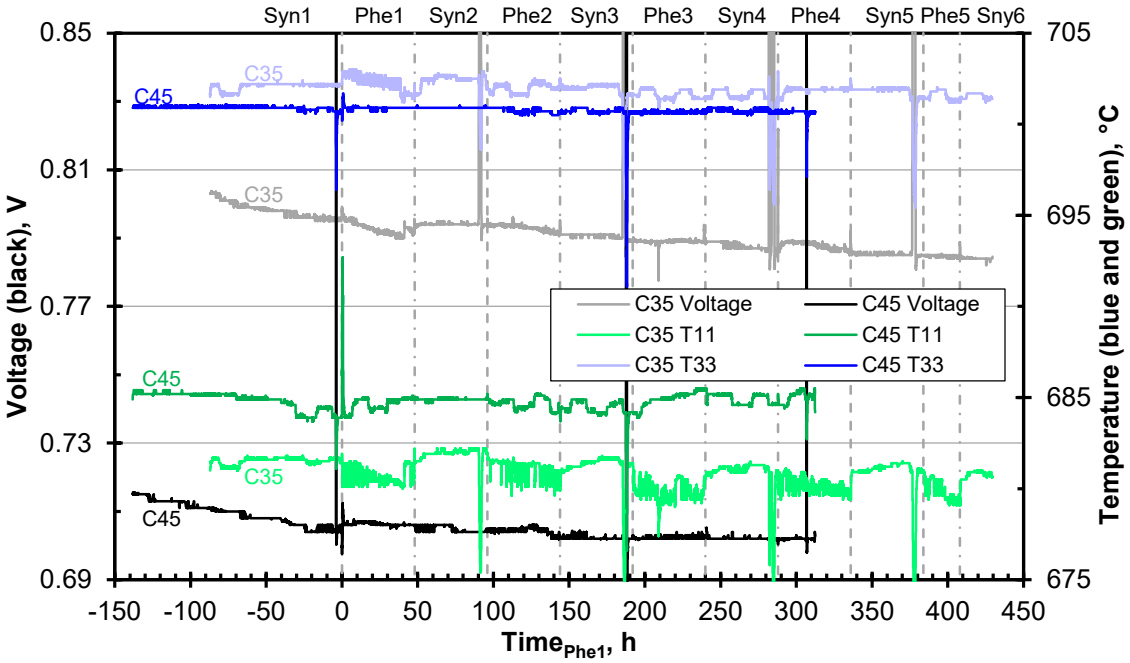

Figure 7.3: Trends of cell voltage and cell temperatures during the tests on C35 (CTb) and C45 (CTGDC). Dashed lines indicate beginning of dosing of phenol, chain lines the return to pure syngas. Time starts with the first dosing of phenol. Operation conditions see 6.1.

C45 – Repetition of C35

Figure 7.3 shows the cell voltage and temperature curves for C35 and C45. The time axis starts with Phe1. C35 was of type CTb so it had the same substrate as C45. For both cells 2 g/Nm^3 phenol were dosed several times after the initial syngas phase. Due to the intermixing between GDC anode and YSZ substrate related to the production process and described in [102], the CTGDC cell C45 had a lower performance than the CTb cell C35. On the other hand, the degradation rate of C35 was higher. Both cells showed a strong decrease in cell voltage during Syn1 which stopped at C45 before Phe1. In addition, C45 did hardly degrade after Syn3. Overall, the effects of external disturbances were greater than the influence of phenol for both cells.

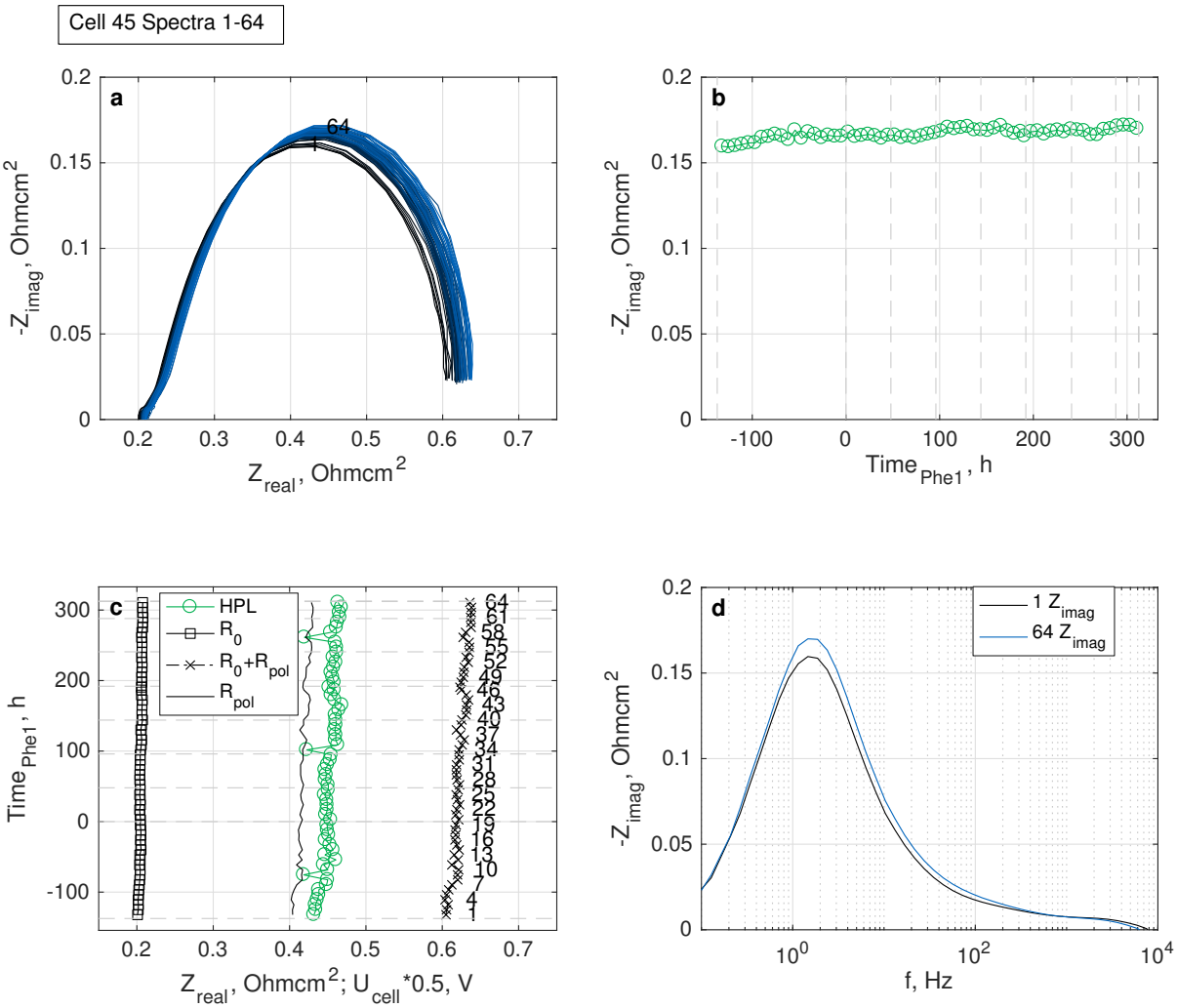

Figure 7.4: Impedance data for C45. HPL: ASR at maximum of low-frequency arc. a: Nyquist plot; b: trend of Z_{imag} of HPL; c: trend of Z_{real} of HPL together with R_{pol} and R_0; d: imaginary part of first and last spectrum. Operation conditions see 6.1.

In contrast to the cells with YSZ anode, only a single large arc occurred in the impedance data of the CTGDC cells, see Figure 7.4 a. It had its maximum at 1-2 Hz, see Figure 7.4 d. If the frequency ranges of the dominant processes[2] were the same for both anode types, this would mean that the mass transport through the

[2]See interpretation in section 5.5.3: 1-2 Hz gas diffusion through the anode support; approx. 200 Hz fuel diffusion in the anode layer; approx. 1-2 kHz charge transfer reactions at the TPB of the anode.

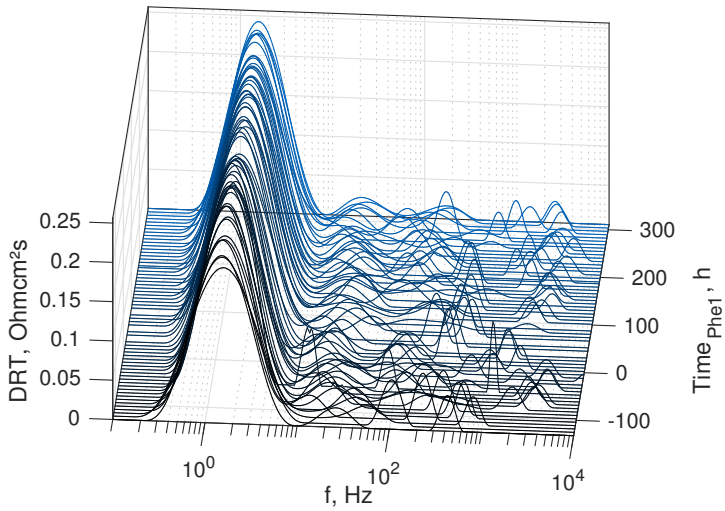

Figure 7.5: Chronological trend of the DRT of C45. Operation conditions see 6.1.

substrate was strongly inhibited in the CTGDC cells. However, since the substrate was not changed, it is unclear what caused the high polarisation resistance at the low frequencies. The intermixing at the interface between anode and electrolyte should rather inhibit the processes at the higher frequencies. This question was not further investigated in the context of this thesis since for this type of anode the problems of cell production must be solved first.

As can be seen in Figure 7.4 c, a constant increase of the polarisation resistance also occurred at C45, independent of the presence or absence of phenol. In contrast to the cells with YSZ anodes this was caused by an increase in the low-frequency range. The superposition of all DRTs from Syn1 to Phe4 in Figure 7.5 shows that the DRT was almost entirely characterised by a process at low frequencies. At the higher frequencies several small peaks occurred for all spectra. These did not follow a uniform trend which made their assignment to physical processes impossible.

C56 – Repetition of C32

At C56 the experimental programme of C32 was repeated, i.e. the dosage of 1, 2, 4 and 8 g/Nm^3 phenol. Figure 7.6 compares the two measurements. C32 was a TypIIIb cell so it had a thicker substrate than C56. Apart from the discontinuities

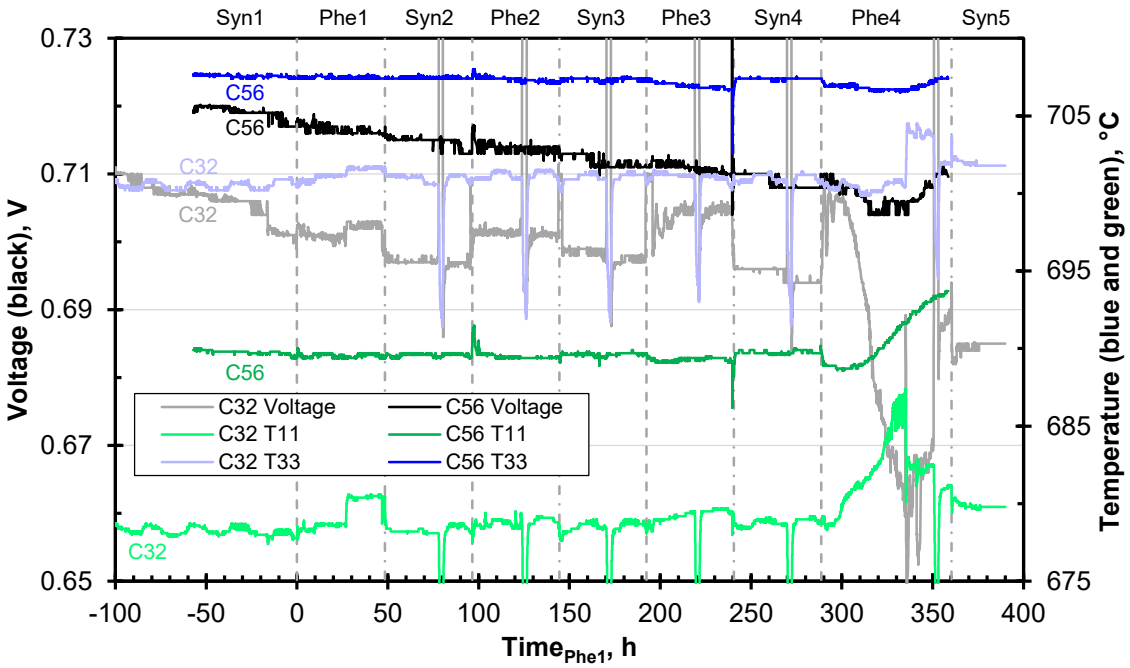

Figure 7.6: Trends of cell voltage and cell temperatures during the tests on C32 (IIIb) and C56 (CTGDC). Dashed lines indicate beginning of dosing of phenol, chain lines the return to pure syngas. Time starts with the first dosing of phenol. Operation conditions see 6.1.

in the voltage signal of C32 the degradation rate up to Phe4 was very similar for both cells. While C32 showed a voltage increase during Phe3, C56 did not react to 4 g/Nm^3 phenol.

The Phe4 phase during which 8 g/Nm^3 were added to the simulated syngas is particularly notable. In these 72 h the behavior of both cells was strongly unsteady in contrast to the phases before. Several changes took place in the cell, presumably due to the strong formation of soot by thermal cracking of phenol and the associated dusting of the anode substrate. For C32 the cell voltage initially decreased by 46 mV and then increased again by 28 mV. The turning point was the SPA sample at hour 336. For C56 the voltage only decreased moderately by 5 mV and then returned to its original level. Parallel to the voltage drop the inlet temperature T11 at C32 rose by 9 K until the rise was stopped by the SPA sample. At C56 T11 first fell slightly and then rose by a total of 4.5 K until the end of Phe4.

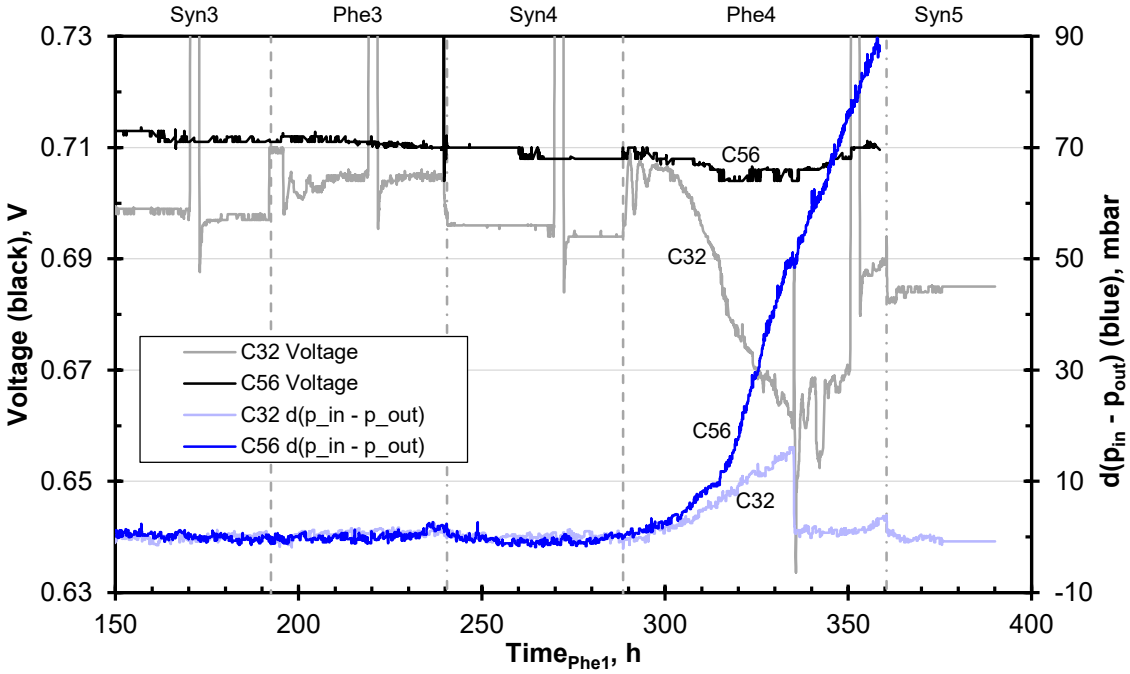

Figure 7.7: Trends of cell voltage and change in pressure drop across the cell during the tests on C32 (IIIb) and C56 (CTGDC). Dashed lines indicate beginning of dosing of phenol, chain lines the return to pure syngas. Time starts with the first dosing of phenol. Operation conditions see 6.1.

During Phe4 an increased pressure drop was noticeable in both cells. In Figure 7.7 it is represented as the change of the difference between p_{in} and p_{out} referred to the average difference between p_{in} and p_{out} before Phe4. The pressure drop increased by 15 mbar for C32 up to the SPA sample and by 88 mbar for C56 up to the end of phenol dosing. An analogous behaviour was observed when operating the short-stack F1004-89 with tar-containing bio-syngas from a fluidised-bed gasifier [112, 149]: due to carbon deposits on the nickel meshes and the flow-field of the stack, the pressure loss had increased so much that the stack could no longer be operated safely. It can be assumed that in C32 and C56 carbon deposits of thermally cracked phenol and dusted substrate material also caused the increasing blockage of the fuel gas flow. During an SPA sample at hour 336 probably oxygen reached C32 causing some of the carbon to burn off, which in turn reduced the pressure drop. The question is, however, why the pressure drop did not increase again after this decrease but remained at the original level. The exact processes

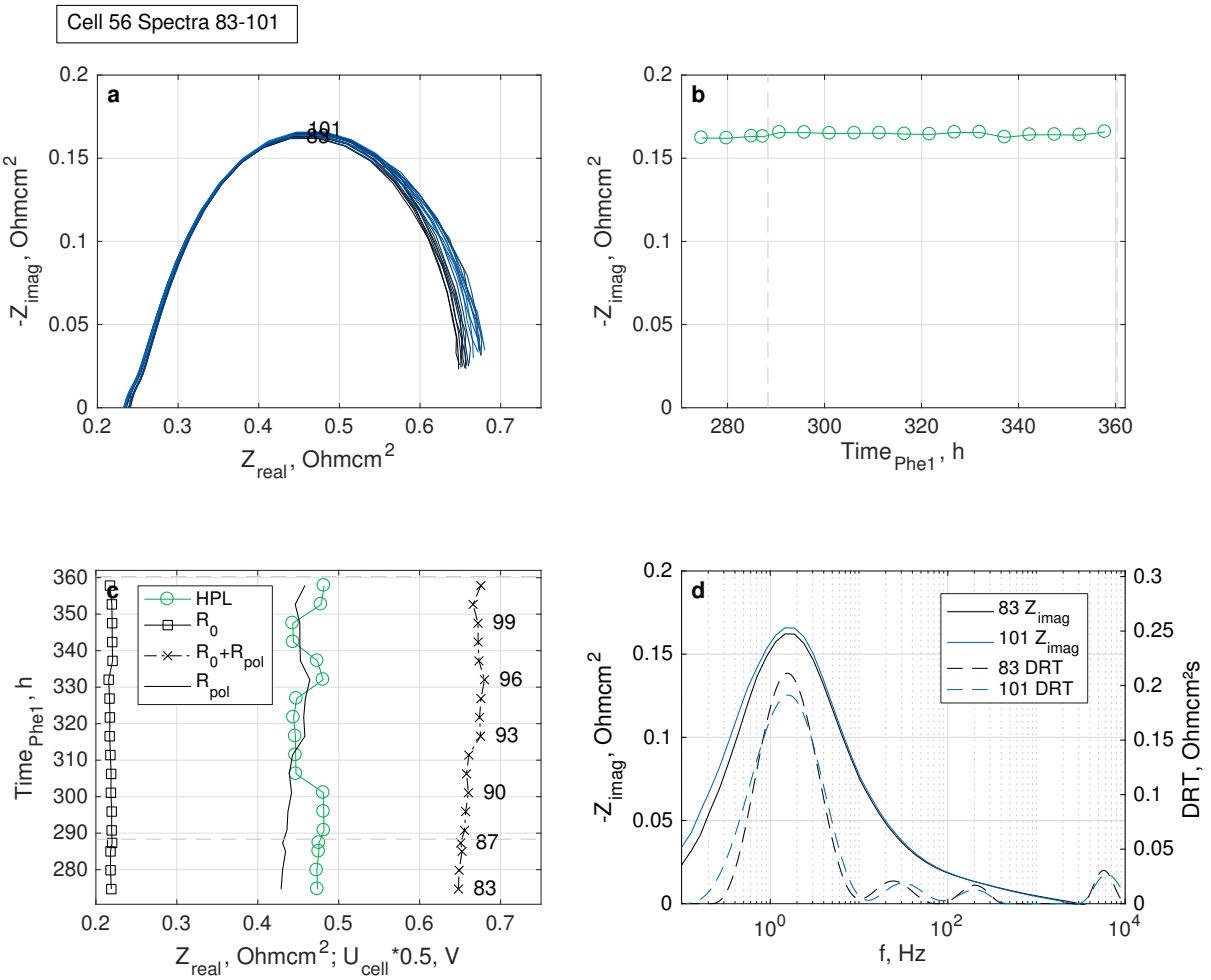

Figure 7.8: Impedance data for C56 during Phe4. HPL: ASR at maximum of low-frequency arc. a: Nyquist plot; b: trend of Z_{imag} of HPL; c: trend of Z_{real} of HPL together with R_{pol} and R_0; d: comparison of the DRT and the imaginary part for a representative spectrum during Syn4 (83) and the last spectrum of Phe4 (101). Operation conditions see 6.1.

within the housing cannot be determined a posteriori. It should be noted that after the end of the measurement on C56 very strong carbon deposits were present in the inlet manifold (cf. Fig. 7.11), which is consistent with the strong increase in pressure drop.

There is no impedance data available for C32 that could be used to further interpret the behaviour during Phe4. Nor was the data for C56 very revealing, see Figure

7.8: like the cell voltage, the impedance data during Phe4 was largely stable. The only noticeable abnormality beyond the usual increase of the polarisation resistance was a widening of the LF-arc from spectrum 93 onwards. This correlated with the instant at which the pressure drop had increased at a faster rate. It is possible that this detail was an indication that the electrochemically active area was then affected by metal dusting or that fuel gas flow in the housing was significantly inhibited. Since the impedance data was not very detailed, it is difficult to interpret the processes in the housing from the tests on this cell type.

7.1.3 Post-Mortem Analysis

After the experiments all cells were post-analysed. The state of the cell itself and of the housing were recorded using photos and optical microscopy. Moreover, the microstructure of some cells was further analysed by H. Jeong at Forschungszentrum Jülich.

Photos of the Cells and Optical Microscopy

Figure 7.9 shows the condition of C32 (TypIIIb), C35 (CTb), C56 (CTGDC) and C45 (CTGDC) after the tests. The inlet to the housing was located in the lower left corner from where the fuel gas was dispersed in a manifold over the entire height of the cell before it flowed through the channels along the cell. The state of the cells was similar, regardless of the cell type: the brighter areas were affected by a detachment of support material which for most parts was converted to dust. This phenomenon is known as metal dusting and is triggered by carbon deposits on nickel [79]. The metal dusting first affected the area in the inlet manifold and from there it spread into the channels of the flow-field. Also, particles of carbon could be found at the inlet and at the manifold. These were presumably parts of soot that had formed at the gold wires that protruded in the manifold for current collection, see Figure 7.11. For C32 and C56 at the inlet a regime of carbon could be found that seemed more mixed-up with the surrounding material.

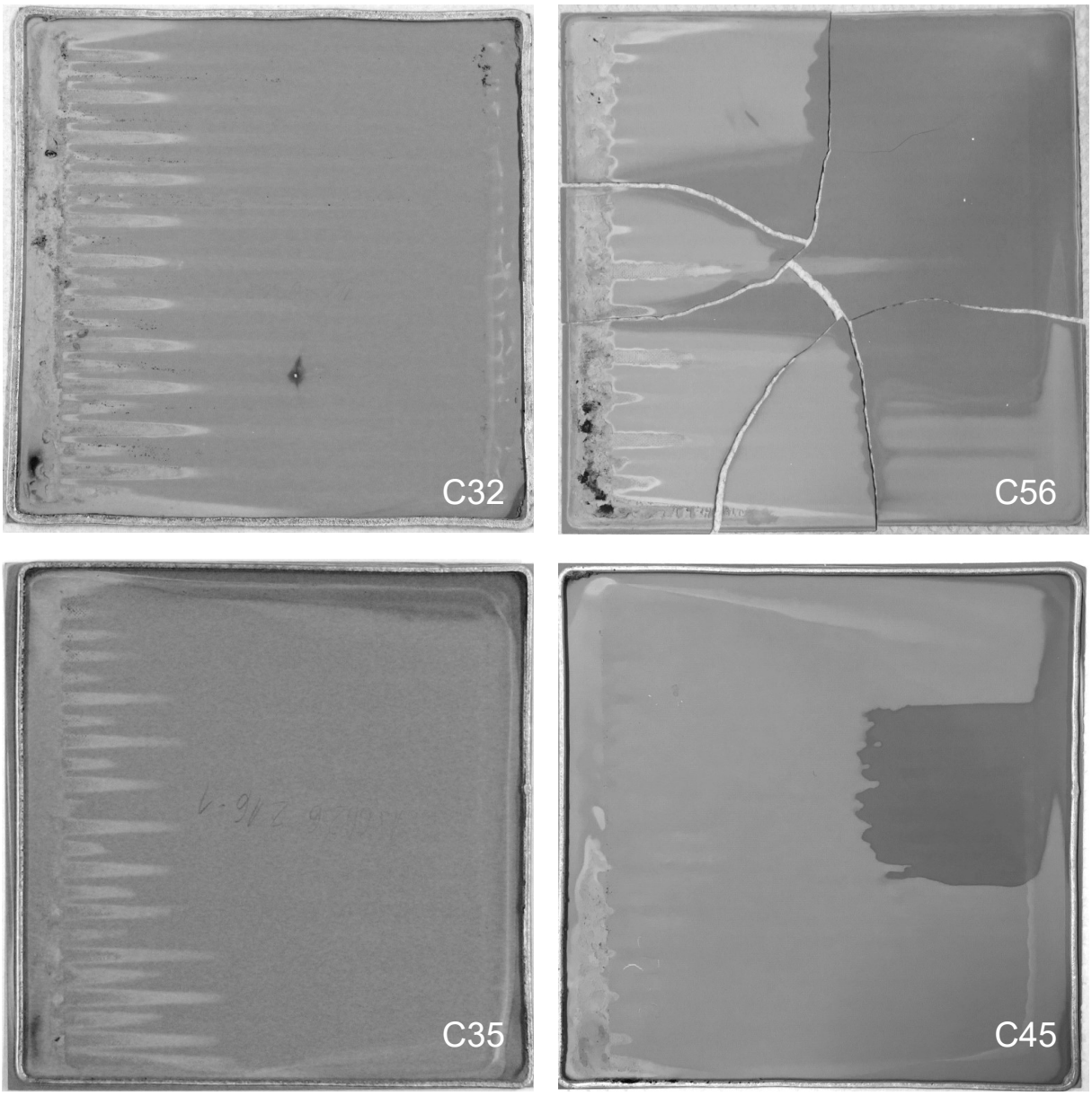

Figure 7.9: Photos of C32 (TypIIIb), C35 (CTb), C56 (CTGDC) and C45 (CTGDC) after shutdown, showing dusting above manifold and fuel channels. Inlet at the lower left corner, inlet manifold at the left side.

C32 and C35 had a similar pattern of surface degradation and progress of dusting in the channels. This is noticeable since C32 was exposed to a four times higher concentration of phenol and was charged with 28.8 g more phenol, see Table 7.1. Most likely this was due to the different substrate of the two cells. The substrate of the CTb cells has finer particles and Ni/3YSZ is used, compared to Ni/8YSZ for TypIIIb [32]. This would mean that the finer structure of 3YSZ was more susceptible to the effects of phenol.

At the same time it is noticeable that the detachment at C45 was significantly lower compared to C35 although the same amount of phenol was dosed in both cells. It is unlikely that the anode type – Ni/GDC instead of Ni/YSZ – had an influence on the processes at the substrate surface at the fuel gas inlet, especially since no electrochemical reactions took place in this area. There are two possible explanations why C45 compared to C35 with the same substrate type and C56 compared to C32 with the more susceptible substrate type showed significantly less detachment of material. First, the preheating of the fuel gas was continuously improved in the course of the experiments, as a result of which more heat was available at the cell inlet for the decomposition of the cracking products of phenol. As shown in Figure 7.6, the temperature difference between C32 and C56 was about 10 K, which can have a large influence on the formation of solid carbon in this temperature range. Second, as the number of measurements increased, microscopic deposits in the fuel gas inlet of the housing could have caused phenol to crack further upstream. As a result fewer carbon deposits might have reached the cell itself where it could trigger metal dusting.

For C35 the areas most affected by dusting were examined with an optical microscope. In the fuel channels (Figure 7.10 A) the top layer of the support was detached. In the manifold area (Figure 7.10 B) the degradation was more advanced, leaving behind large amounts of fracture material. The powder in both areas held together cohesively but was not mechanically stable. Figure 7.10 C shows agglomerates of carbon and cell material that were found at the edge area of the contacting nickel mesh. The pattern of these deposits corresponded to the free spaces in the mesh. The particles did not intrude in the substrate but loosely rested on it and could be removed easily. This pattern was also observed for cells C37, C40 and C41.

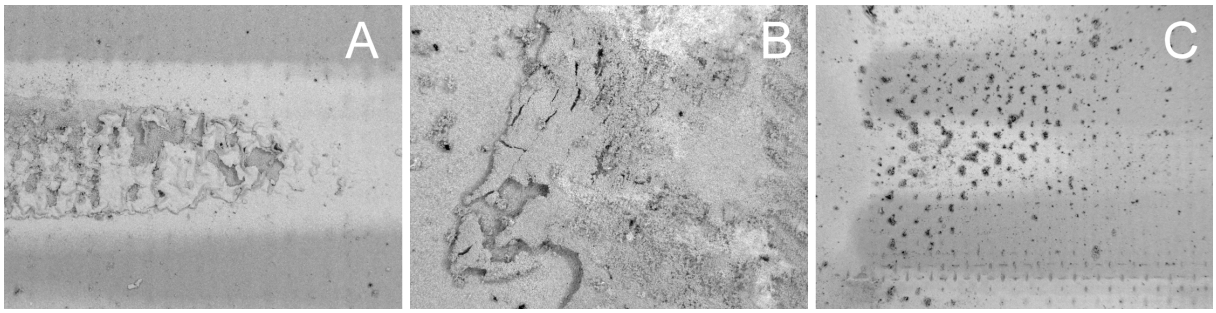

Figure 7.10: Optical microscope images of the anode substrate of C35 after 518 h of operation. A – Delaminated surface in the fuel channel. B – Accumulated material in the fuel manifold. C – Pattern of carbon particles where the nickel mesh had contact to the cell.

More or less pronounced metal dusting could be observed for all cells exposed to phenol. Even for C46, where 0.5 g/Nm^3 or a total amount of 4.3 g phenol was dosed, a discoloration of the support and carbon deposits occurred at the fuel gas inlet, which were interpreted as dusting precursor. Under the selected operating conditions all cell types tested were affected by the phenomenon as they all had a Ni/YSZ substrate. The reference cell C33, see section 4.2.3, did neither show carbon deposition nor delamination of the substrate material, which indicated that the pure syngas operation was not harmful to the cell and that carbon deposition was related to the presence of phenol. Since the condition of the substrate was only detectable after the measurements, no clear statement can be made as to whether the substrate of the CTb cells degraded differently than the one of the TypIIIb cell.

Condition of the Housing

In contrast to tests with pure syngas or with naphthalene as model tar, carbon deposits appeared in the housing during all measurements with phenol. Figure 7.11 shows these for different cells. Carbon was deposited both on the alumina oxide of the housing and on the gold wires of the contacting. While dusting was more pronounced at C32 than at C56, more carbon was present at the inlet manifold at C56 than at C32. On the one hand, this could be due to the fact that the cell was cooled down with a faster temperature ramp and a larger forming gas flow was set

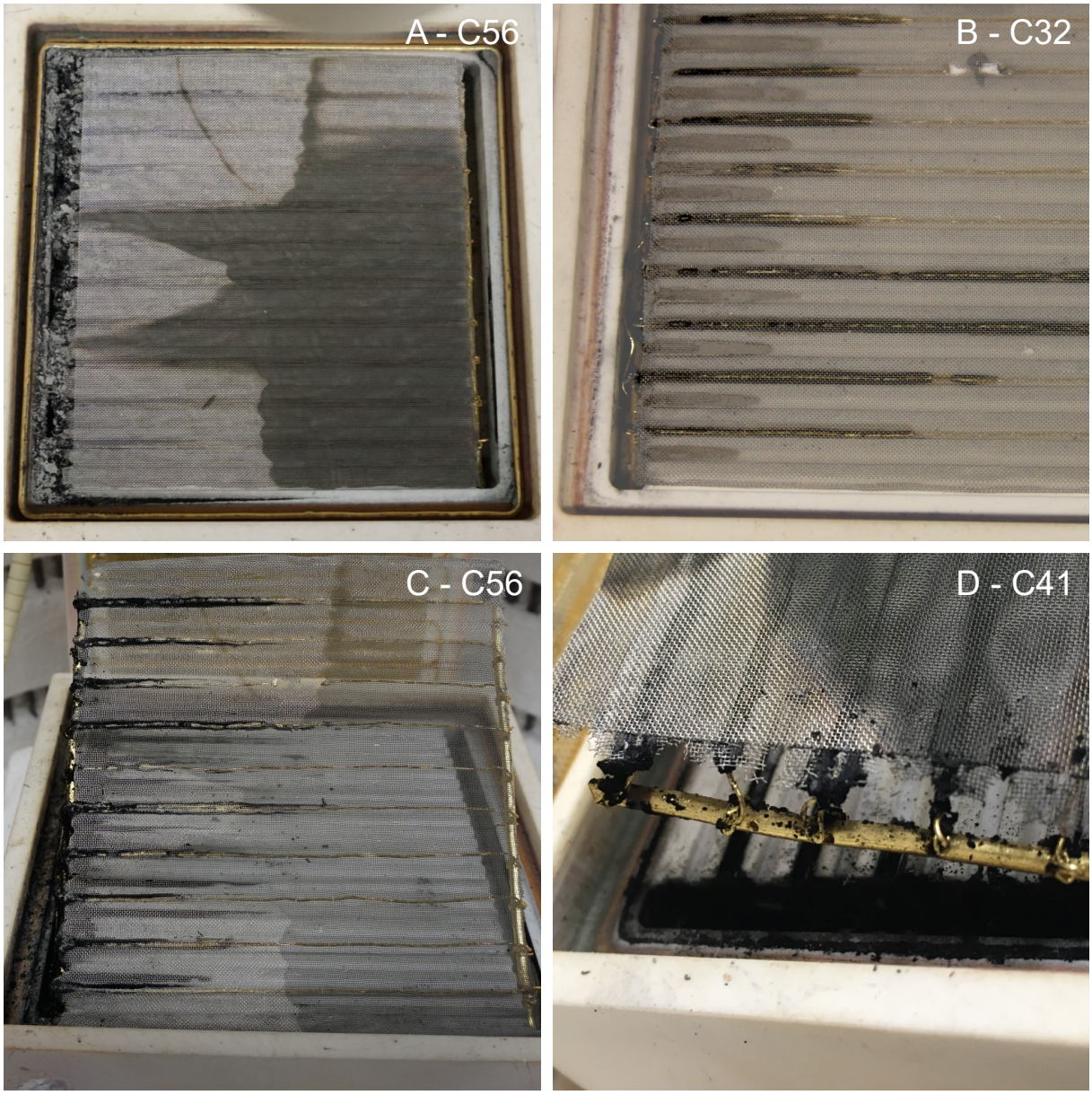

Figure 7.11: Photos of the anode-side housing after shutdown. A: Carbon deposition at the inlet manifold (C56). B: Carbon deposition on gold wires in the channels and dust on the nickel mesh (C32). C: Carbon deposition on gold wires. D: Carbon deposition on the gold wires in the manifold (C41).

at the same time, thus preventing the penetration of oxygen and the burn-off of carbon. On the other hand this could confirm the assumption mentioned above that in C56 the phenol cracked further upstream due to changed test rig conditions and less of it reached the substrate.

As shown in Figure 7.11 C, the gold wires in the flow-field were partially covered with carbon up to the center of the cell. Figure 7.11 B shows how substrate material had accumulated in the free channels on the nickel mesh after measurement on C32, while carbon deposits were visible in the channels with gold wire. This corresponds to the pattern visible at C32 in Figure 7.9 showing alternately longer and shorter brighter patches on the substrate. The longer patches were above the channels without gold wire.

Results from Microstructure Analysis

C32, C35, C45 and C56 were further analysed at Forschungszentum Jülich by Jeong. The results are discussed in detail in [32, 100]. The structure and composition of the fuel electrode and the substrate were investigated extensively via scanning electron microscopy (SEM) for analysis of the morphology, X-ray diffraction (XRD) for phase analysis, and Raman spectroscopy for detection of carbon deposition. By comparing the structure at the inlet and the outlet of the cell and calculating the pore fraction, Jeong found that the porosity of the substrate was strongly increased in the areas affected by dusting. At the same time the coarsened particles suffered from a loss of connectivity between Ni and YSZ. The nickel content had slightly decreased in the remaining material which indicates that Ni was preferentially removed but not solely. After collecting the dust from C32 Jeong found that the dusting had affected 1/3 of the support thickness at the most eroded areas. The dust contained both Ni and YSZ. At C35 filamentous structures appeared at the fuel inlet in the SEM micrographs. It was assumed that these structures were carbon fibers. For C32 these structures could also be found at the outlet area. At the same time Raman spectroscopy indicated carbon close to the support-gas-interface for C35, whereas for C32 it was detected throughout the whole substrate thickness and to a small extent also close to the anode outlet.

Table 7.2: Sequence of the test on F1002-189 together with dosed concentration of phenol. Calculated temperatures to achieve these concentrations are given as well as set and actual outlet temperature of the tar container.

Reading point	Duration, h	c_{Phenol}, g/Nm³	$T_{Tar,calc}$, °C	$T_{Tar,set}$, °C	$T_{Tar,out}$, °C
Initial I-V-curves	7	0	-	-	-
Syn1*	64	0	-	-	-
Phenol2g	24	2	74	79	74
Phenol4g	24	4	87	95	87
Phenol8g	24	8	101	110	99

* Gas flows in Nl/min/cell: 0.5 H_2O, 0.25 H_2, 0.1 CO, 0.1 CO_2. 0.05 CH_4; 2 air.

7.2 Short-Stack Test with Phenol

In addition to the single-cell experiments shown, a test was carried out on the two-level stack F1002-189 for the investigation under application-oriented conditions. The cells used in the stack were CTJb type, i.e. half cells from CeramTec, which were printed with the functional layers in Jülich. The test rig described in section 4.3 was used for this purpose and the general procedure was comparable to the test on F1002-190 in the previous chapter. Gas composition and quantity were adjusted by the connected gas mixing station.

7.2.1 Conduction of the Experiment

After installing the stack it was heated to 700 °C at 4 K/min[3]. At the same time 0.05 Nl/min/cell H_2 and 0.95 Nl/min/cell N_2 were flowing through the fuel gas side to prevent the anode pre-reduced in Jülich from re-oxidising. The air side flow was 2 Nl/min/cell air for the entire duration of the test right from the start of heating. The conduction of the test and the applied concentrations of phenol are shown in Table 7.2. As with all stacks, a basic characterisation was performed in the form of several I-V-curves with pure hydrogen (1.125 Nl/min/cell H_2), a H_2/H_2O mixture

[3]Furnace temperature 708 °C

(1.1 Nl/min/cell H_2 and 0.275 Nl/min/cell = 0.221 mg/min/cell H_2O) and a H_2/N_2 mixture (0.5 Nl/min/cell H_2, 0.61 Nl/min/cell N_2). By the means of the H_2/N_2 reference curves the performance of F1002-190 could be compared with the other stacks, see Figure 6.17. The performance of F1002-189 corresponded to the other short-stacks tested in this thesis. Due to a different voltage measurement device – Meilhaus interface instead of HOBO logger – and a lower resulting resolution of the data, the signals for F1002-189 were fitted with a hyperbolic plus a linear term for better visibility.

After the initial I-V-curves the stack was operated on pure syngas at 27 A or 0.34 A/cm^2 respectively for 64 h. Then 2, 4 and 8 g/Nm^3 of phenol were added to the syngas for 24 h each. With complete reforming these phenol amounts would result in additional 0.007, 0.013 and 0.027 Nl/min/cell H_2, respectively ($C_6H_5OH + 11H_2O \longleftrightarrow 6CO_2 + 14H_2$). The temperatures of the phenol-filled tar container, see section 4.3.3, necessary to achieve the desired tar concentrations are given in Table 7.2. The reference temperature for the calculation of the tar concentration was the temperature in the gas outlet of the container. The tar saturator was supplied with 67 ml/min CO_2 via a separate MFC, whereas the volume flow of pure CO_2 was reduced to 133 ml/min. In contrast to the single-cell tests the phenol phases were conducted without interruption, only the temperature of the tar container was increased. The tar content was regularly checked using the SPA method. For each sample the phenol concentration measured was very close to the nominal value.

7.2.2 Trends of Stack Voltage, Temperatures and Pressure Drop

Figure 7.12 shows the stack voltage during the test. It was subject to a drift of approximately 25 mV which was caused by the bottom cell whereas the voltage of the top cell was constant. The stack voltage first fell for approx. 20 h after the start of Syn1 and then rose above the original level until Phe3. The reason for this upward drift might have been the shorter reliability tests compared to Stack N. The noise in the voltage signal was due to oscillation of the water dosage[4]. During Phe3

[4]In comparison to the previous short-stack experiments, however, the oscillation was significantly lower since the water was now pumped directly into the mixing tube instead of into the

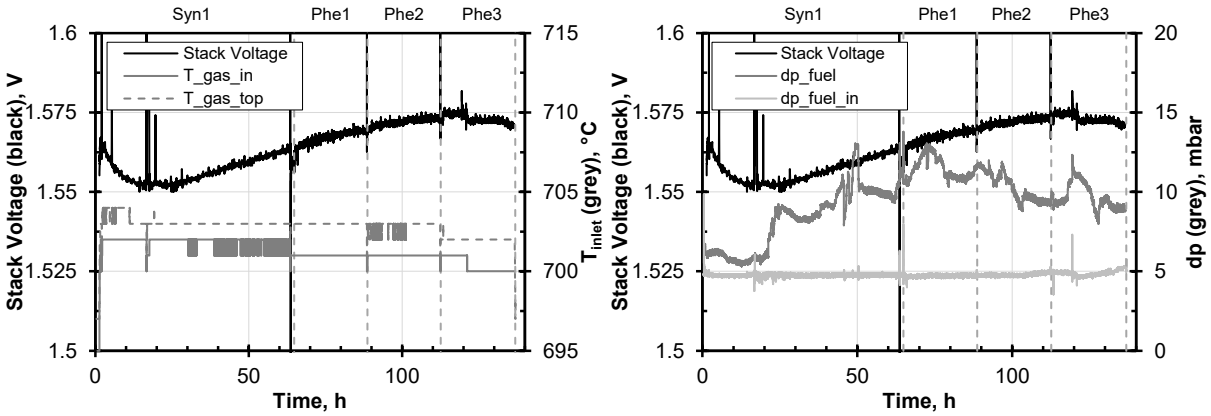

Figure 7.12: Trends of stack voltage and inlet temperature of both layers of F1002-189 (left) and pressure drop (right).

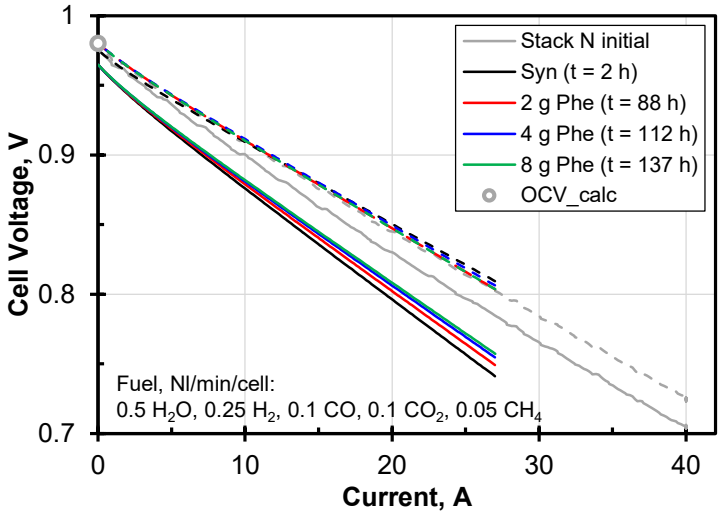

Figure 7.13: I-V-curves of stack F1002-189 on syngas plus 0, 2, 4 and 8 g/Nm^3 of phenol together with data from stack F1002-190 and the calculated OCV. Solid lines represent voltage of bottom cell. $T_{\text{stack}} = 700\,°\text{C}$; $A_{\text{active}} = 80\,\text{cm}^2$. Data for stack F1002-189 was fitted with a hyperbolic plus linear term for better visibility.

a discontinuity occurred at t = 120 h which ended the rise. For a more meaningful result the stack should have been run-in longer until the stabilisation of the voltage. Apart from this discontinuity, which may be attributed to the dusting-promoting effects of phenol on the substrate, the stack voltage did not respond to the presence of tar in the simulated bio-syngas. The shape of the I-V-curves recorded during pure syngas and at every concentration of phenol was similar but followed the upwards trends of the cell voltage under load, see Figure 7.13. This shows that as in the single-cell experiments, electrochemistry was not affected by phenol within the duration of this test.

Neither did the temperatures in the stack – in Figure 7.12 the fuel gas inlet temperatures in both planes are shown – react to phenol but fell during the experiment analogously to the increasing stack voltage. In contrast to the single-cell measurements, there was no increase in the inlet temperature. The pressure drop across the stack dp_{fuel} changed more during Syn1 than during the phenol phases. The overpressure at the inlet $dp_{\mathrm{fuel,in}}$ was constant to a large extent; only starting from the discontinuity at approx. 120 h during Phe3 did a slow increase become apparent. On the basis of the single-cell experiments, cf. section 7.1.2, it was to be expected that the pressure drop would increase due to thermally cracked phenol and metal dusting. Potentially the exposure time was not long enough for these phenomena to occur. On the other hand, the shape of gas flow in the stack is very different compared to the ceramic housing in the single-cell experiments. The materials used – Crofer and nickel instead of ceramic, gold and nickel – might also have had different influences on the decomposition of phenol upstream of the cells. Since water droplets had formed in the pipes leading to the differential pressure sensors during the measurement, the signals might have been falsified and an increase of pressure drop – if it had actually occurred – might not have been recorded.

Possible alterations in anode exhaust gas composition could be monitored by the gas analysis available at the stack test stand. Besides minor drifts its composition was constant during the test. The analysis was not accurate enough to establish mass balances with which the amount of carbon deposited in the stack could have been determined.

evaporator. The mixing tube was heated to only 160 °C.

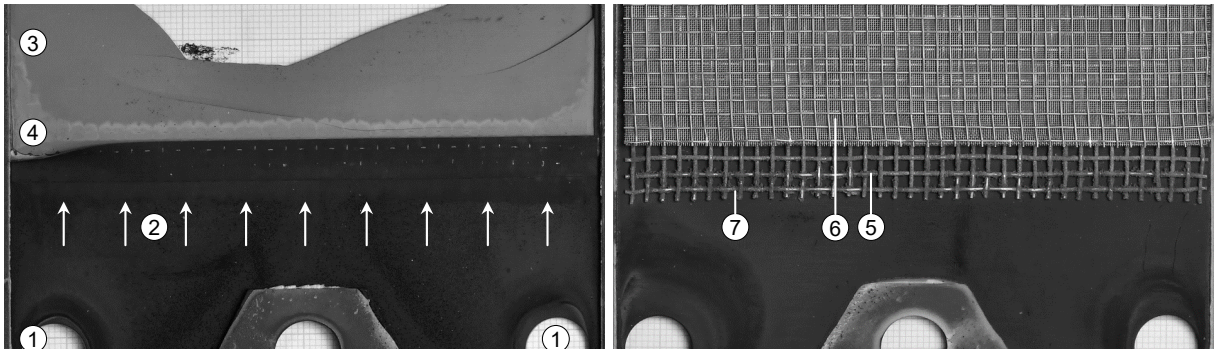

Figure 7.14: Photos of one layer of F1002-189 after the tests with phenol. Left: View at the surface of the anode substrate. Right: View at the nickel meshes for contacting. Annotations: fuel inlet (1), fuel gas flow direction in manifold (2), unaltered anode substrate (3), degraded anode substrate (4), (5) coarse nickel mesh, (6) fine nickel mesh, (7) carbon deposition.

7.2.3 Post-Mortem Analysis

After the end of the measurement the stack was post-analysed at Forschungszentrum Jülich. A detailed examination of the stack and the cells using microscopy or Raman spectroscopy has not been carried out so far. However, macroscopically visible metal dusting similar to the single-cell tests occurred on both cells, with the substrate on the fuel gas inlet discolouring across the entire width of the cell; see the band of brighter colour along the cell in Figure 7.14 left. In addition, carbon deposits were found on the nickel meshes, see Figure 7.14 right. In contrast to the test on tarry bio-syngas [112], their amount was small and therefore did not inhibit the gas flow through the stack. In addition, loose carbon particles were found in the fuel gas manifold, which suggests that phenol was partly cracked upstream of the cells as in the single cell experiments.

7.3 Conclusion and Assumed Progression of Phenol-Induced Cell Degradation

For all tests with phenol carbon deposition and irreversible degradation in form of detachment of anode substrate material were observed, even for the lowest concentration of $0.5\,g/Nm^3$. For concentrations up to $2\,g/Nm^3$ the degradation was not visible in the electrochemical performance, neither in the voltage signal nor in the EIS data. The effects were qualitatively similar for cells with Ni/YSZ or Ni/GDC anodes since in both cases the Ni/YSZ substrate was affected. Metal dusting occurred which is reported by several authors who operated SOFCs on carbon rich fuel gases [73, 154–156]. It is possible that the performance of the cells might have become affected at longer exposure times i.e. when the dusting would have reached electrochemically active areas.

The mechanism of metal dusting is explained in [79]: on suitably oriented nickel lattice planes deposited carbon forms domains of graphite. During growth it induces stress on the nickel lattice by which particles of it are detached. These Ni-particles form a second phase in the graphite and are removed from the interface when more and more carbon from the gas phase is deposited. In case of a Ni/YSZ cermet stress induced by the formation of graphitic structures reduces the density of the nickel. This increases the forces on the whole Ni/YSZ cermet matrix which leads to a loss of both Ni and YSZ as it is described in the post-test analysis by Jeong [32]. The disintegrated particles are transported into the graphite. When the carbon was partly oxidised or reformed during shut-down after the tests of this thesis, only the cermet particles persisted, which represented the dust on the cell.

Carbon deposits are therefore the initial trigger for dusting. According to the chemical equilibrium calculations shown in Figure 4.7, no solid carbon should be formed under investigated conditions, especially because of the high water content in the simulated bio-syngas. It must be emphasised that the reference cell operated only on pure gas at the same conditions – see section 4.2.3 – did not show carbon deposits or dusting over 250 h. So this mechanism of degradation was clearly triggered by the presence of phenol. In literature phenol is reported to thermally decompose at sufficiently high temperatures and form soot inside pipes and on the

cell housing, metal wires and the cell itself [64]. Once carbon is deposited, it could catalyse the formation of further soot [157]. Also, the removal of solid carbon by reforming is slower than its deposition [26]. At this point the role of metal components inside the housing in the cracking of phenol and how this affected the development of metal dusting could not be clarified. It cannot be determined whether the carbon deposits that form on the wires trigger the dusting when they are transported to the cell or whether the cell itself is partially protected when phenol cracks on the other surfaces. The problem must be taken into consideration, as the same reactions could potentially occur at the Crofer plates or the nickel mesh in a stack.

The behaviour of the short-stack F1002-189 at up to 8 g/Nm^3 phenol reflected very well the results of the single-cell experiments. The stack voltage did not show any influence of phenol, but metal dusting occurred at the entry of the cells. An increase in pressure loss, as observed in C32 and C56 with 8 g/Nm^3, did not occur. The test on another short-stack F1004-89, which was operated on tar-containing real bio-syngas, had to be stopped even after a few hours, see the results in [112]. The reason for this was that a large amount of carbon in the form of carbon whiskers had deposited inside the stack at the Ni mesh contacting the anode side of the SOFC [149]. The whiskers blocked the fuel gas flow and increased the pressure drop drastically. Under these deposits metal dusting of the anode support had started at the fuel entrance of all cells, which also affected the nickel meshes for contacting. The total amount of all tars[5] was less in the real bio-syngas than during Phe3 at F1002-189. This could indicate that tars other than phenol produce significantly more carbon deposits in the stack or that the combination of certain tars is more critical than pure phenol. A comparison of the morphology of the carbon deposits in both stacks might provide information on the underlying processes during operation especially if phenol alone also leads to the formation of carbon whiskers on the anode substrate.

All that is clear after the tests is that phenol represents a problem to the anode substrate at the operation conditions applied and it is therefore not sufficient to only alter the anode layer of an SOFC. At the same time the occurring processes on the microscopic scale were not investigated and it is still unclear how the prob-

[5]Main tar components were benzene, toluene, cresol, phenol and naphthalene.

lem can be solved by other cell materials. In the test setups used here it was not possible to determine if carbon deposition occurred due to thermal cracking or incomplete reforming at the anode substrate. Neither was there a measuring method to determine the morphology of the carbon deposits on the nickel grains, when and how the metal dusting starts and which effects lead to the YSZ also being affected by the decomposition. Moreover it is still unclear if there is a threshold in exposure time, amount of dosed phenol or its concentration and what influence the composition of the syngas has. For the future it seems reasonable to conduct tests in a test rig yet to be designed with different cell materials and tar components where these questions can be investigated in detail. For this test rig an online optical signal for the occurrence of carbon deposition could be very useful.

Besides the chemical interactions, there might also persist a strong influence of the general design of the SOFC, for example the choice of layer thickness or the parameters of microstucture. One topological problem could consist in the thickness of the anode support or more precisely the distance between the anode layer and the interface to the fuel gas. As reported in [51], carbon deposition on Ni/YSZ was more severe the thicker the anode substrate was. Other authors showed that a higher current density and therefore more oxygen at the anode can stabilise the operation of the cell even in conditions that may cause carbon deposition [154, 158]. But marginally accumulated carbon might not be removed by oxidation because oxygen ions from the cathode only react with fuel close to the anode layer and in general faster with hydrogen than with carbon species [52]. Besides substituting nickel with other active materials, the reduction of the anode thickness or the employment of electrolyte-supported cells could therefore be necessary for the smooth operation of SOFCs with bio-syngas.

Chapter 8

Summary and Outlook

In this work the tolerance of anode-supported solid oxide fuel cells with Ni/YSZ substrate towards the presence of the model tars naphthalene and phenol was investigated. The results showed that state-of-the-art anode-supported SOFCs with Ni/YSZ anode cannot be operated on gases which contain even low concentrations of naphthalene or phenol. This statement is specifically valid for the investigated cell types and in particular for the applied operating temperature of 700 °C. Measurements in literature where at least a temporary tolerance of SOFCs to tars was found were all performed at significantly higher temperatures. However, higher operating temperatures are not appropriate in view of the higher requirements placed on steels used in the SOFC stack and the higher costs involved. In order to realise B-IGFC systems without tar removal step it is therefore neccessary to find an anode material or cell concept with which the performance of the SOFC is stable at temperatures below 750 °C.

8.1 Differing Impacts of Naphthalene and Phenol

It was found that naphthalene and phenol had significantly different effects on the SOFC:

Naphthalene led to a significant decrease of cell performance even at the lowest concentration investigated (0.12 g/Nm^3 or 21 ppm). After a delay of a few hours this decrease was almost linear and led to a plateau from where the cell voltage did not decrease any further. Measurements with only a short-term dosage of

naphthalene therefore have little significance. The voltage decrease at the highest naphthalene concentration (2.5 g/Nm^3) was 19 %. After the measurements no macroscopic carbon deposits were visible on the cells.

On the basis of the EIS data it could be shown that naphthalene had negative effects on the mass transport in the anode and in the anode substrate. It is assumed that naphthalene adsorbed on all surfaces of the substrate and the anode layer. Thus it reduced the number of TPB available, which is why fuel had to overcome a higher diffusion resistance before being oxidised. The inhibition of fuel diffusion to TPB was observed in the EIS data with a strong and immediate increase in polarisation resistance at approx. 200 Hz while the resistance to electrochemical oxidation at the TPB (1-2 kHz) itself remained nearly constant. At the same time the catalytic conversion of CH_4 and CO to H_2 was inhibited. Because naphthalene itself is reformed very slowly, it occupies the active Ni sites for a very long time. Due to the lower amount of H_2 available the mass transport resistance through the anode substrate was increased, which led to an increase in polarisation resistance at 1-2 Hz in the EIS data. The reduced conversion of CH_4 and CO also became visible in the exhaust gas analysis values during the short stack test.

When the naphthalene supply was switched off, cell performance recovered only gradually. However, the original voltage level could be restored by active regeneration at 900 °C. It is assumed that the adsorbed naphthalene was only completely reformed at these temperatures. For tolerant cells, therefore, materials must be found on which the reforming of tars at moderate temperatures is significantly faster. With regard to an overall system, it is also essential that all tars are completely converted in or before the cell and do not leave it; otherwise they will lead to problems in downstream components.

Phenol on the other hand led to an irreversible destabilisation of the matrix of the Ni/YSZ substrate. Even for a low concentration of 0.5 g/Nm^3 (120 ppm) in simulated syngas metal dusting and carbon deposits were observed. For higher concentrations the dusting spread along the fuel channels from the fuel inlet. The dusting started in an area where no electrochemical reactions took place. In contrast to naphthalene phenol did not alter the electrochemical performance of the cell for concentrations <4 g/Nm^3. Tests of sufficiently long duration are therefore also necessary for this model tar. It is possible that the phenomenon might go

undetected in a real system until cells fail due to mechanical instability caused by abraded substrate. The substrate was also affected for the cells with Ni/GDC anode. It is therefore not enough to only alter the anode layer – as it was originally intended in the SynSOFC project – but the substrate must be optimised if SOFCs have to operate on phenol-containing fuel.

Due to its property to crack thermally, phenol may be a special case among tars. However, this property makes equilibrium estimates of carbon deposits for phenol-containing syngas seem ineffective. It is assumed that the bottleneck for stable operation is mainly incomplete reforming of hydrocarbons or carbon deposits on nickel because of local over-saturation with carbon. This reaction step would therefore have to be accelerated. An adaptation of the structure of the anode substrate could also lead to an increased resistance of the SOFC to dusting.

8.2 Possible Next Steps

In the context of this thesis only two tars were examined. However, real bio-syngas contains a wide range of tars, unsaturated hydrocarbons and other impurities. The question is what other forms of degradation may affect the SOFC when it is exposed to other contaminants. If no inhibition of the electrochemical performance occurs during the single cell tests, the effects can only be investigated post-mortem. In order to accelerate this screening, it therefore makes sense to perform additional purely chemical tests for the interaction of impurities and SOFC materials. In the second phase of the SynSOFC project a separate reactor will be built for this purpose. For tars these tests will have three specific objectives:

- Screening and classification of biogenic tars with respect to their effects on SOFCs, for example metal dusting, inhibition of cell reactions, complete reforming or other.
- Investigation of the interaction of tars where amplifying and diminishing effects may occur.

- Finding anode materials that are robust against metal dusting, reforming blocking and other harmful influences. Since the microstructure has a large influence, the experiments should be performed on sintered samples and not on powders.

Results of these investigations are hardly to be found in literature so far. However, they are of great importance for further cell development towards more robust cells. Furthermore, investigations with other impurities (unsaturated hydrocarbons, organic sulphur compounds) and their interaction with tars have to be carried out. With regard to the results from the coupling of a F10-stack with tarry real bio-syngas [112] also the robustness of all stack materials in contact with the bio-syngas should be tested. In contrast to single-cell measurements, different parameters such as concentration and duration of exposure as well as the (important) influence of temperature can be varied more easily. Moreover, regeneration strategies such as the targeted introduction of oxygen can be investigated with less risk. An optical port could be used to monitor carbon deposition and the state of the sample in-situ. In addition, an analysis of the exhaust gas is necessary if the blockage of the reforming reactions is to be investigated.

In parallel, the quality of the measurement data on the single-cell test stand could be further improved. A better wiring of the cell should reduce inductances which would make it also possible to map the processes at higher frequencies and the ohmic resistance. A switch to a housing for smaller cells (e.g. 5 x 5 cm^2) could offer several advantages: the gradients in temperature and gas composition would be lower; measurements at higher current densities would be possible; the tightness could be improved by a new sealing concept; new cells from Jülich can be tested earlier since the upscaling to 10x10 cm^2 is omitted. At the same time it should be examined whether the MFCs of the test rig can provide significantly lower volume flows and whether water dosing would have to be realised differently in order to avoid pulsation, for example by catalytic water generation from H_2 and O_2. In addition the single-cell test stand should be equipped with an analysis system for the anode exhaust gas as this facilitates the interpretation of the running processes. The water dosage of the gas mixing cart at the short-stack test stand should be

improved since the pulsation by the evaporation of single water drops currently leads to oscillations in the voltage signal. Differential pressure sensors with higher resolution at both test rigs will allow the faster detection of flow resistances caused by carbon deposits or dusting of the anode.

In addition to the experimental investigations, the modelling of degradation processes should also be pursued on the basis of the preliminary work available at the LES. The estimation of the actual concentrations of fuel gas and carbon at the active sites and TPB already provides valuable information. It is clear that these models are only meaningful if they can be validated with experimental data. The exhaust gas analysis already mentioned should fulfil an important function here.

Bibliography

[1] IEA. World energy outlook 2019. Technical report, IEA, Paris, 2019. URL https://www.iea.org/reports/world-energy-outlook-2019.

[2] S. Mahlke. *Atlas der Globalisierung*. Le Monde diplomatique/taz, 2019.

[3] R. Geres, A. Kohn, S. Lenz, F. Ausfelder, A.M. Bazzanella, and A Mölle. Roadmap Chemie 2050. Auf dem Weg zu einer treibhausgasneutralen chemischen Industrie in Deutschland. Technical report, FutureCamp Climate GmbH, DECHEMA e.V., 2019. URL https://www.vci.de/vci/downloads-vci/publikation/2019-10-09-studie-roadmap-chemie-2050-treibhausgasneutralitaet.pdf.

[4] FNR. Basisdaten Bioenergie Deutschland 2018. Technical report, Fachagentur nachwachsende Rohstoffe e.V., 2018.

[5] K. D. Panopoulos, L. Fryda, J. Karl, S. Poulou, and E. Kakaras. High temperature solid oxide fuel cell integrated with novel allothermal biomass gasification: Part I: Modelling and feasibility study. *Journal of Power Sources*, 159(1):570–585, 2006.

[6] M. Stemmler. *Chemische Heißgasreinigung bei Biomassevergasungsprozessen*. PhD thesis, RWTH Aachen, 2010.

[7] V. Wilk. *Extending the range of feedstock of the dual fluidized bed gasification process towards residues and waste*. PhD thesis, Technische Universität Wien, 2013.

[8] M. Kaltschmitt, H. Hartmann, and H. Hofbauer. *Energie aus Biomasse*. Springer Vieweg, Berlin Heidelberg, 3 edition, 2016. ISBN 978-3-662-47438-9.

[9] H. Spliethoff. *Power generation from solid fuels*. Springer Science & Business Media, 2010.

[10] F. Kirnbauer, V. Wilk, H. Kitzler, S. Kern, and H. Hofbauer. The positive effects of bed material coating on tar reduction in a dual fluidized bed gasifier. *Fuel*, 95:553–562, 2012.

[11] M. Mayerhofer, P. Mitsakis, X. Meng, W. de Jong, H. Spliethoff, and M. Gaderer. Influence of pressure, temperature and steam on tar and gas in allothermal fluidized bed gasification. *Fuel*, 99:204–209, 2012.

[12] T. S. Doyle, Z. Dehouche, P. V. Aravind, M. Liu, and S. Stankovic. Investigating the impact and reaction pathway of toluene on a SOFC running on syngas. *International Journal of Hydrogen Energy*, 39(23):12083–12091, 2014.

[13] H. Hofbauer, R. Koch, and C. Aichernig. Biomass CHP plant Güssing–a success story. In *Expert meeting on pyrolysis and gasification of biomass and waste*, 2002.

[14] S. Fendt. *Experimental Investigation of a Combined Biomass-to-Gas Power-to-Gas Concept for the Production of Synthetic Natural Gas (SNG)*. PhD thesis, Technische Universität München, 2020.

[15] E. Henrich, N. Dahmen, E. Dinjus, and J. Sauer. The role of biomass in a future world without fossil fuels. *Chemie Ingenieur Technik*, 87(12):1667–1685, 2015.

[16] K. D. Panopoulos, L. Fryda, J. Karl, S. Poulou, and E. Kakaras. High temperature solid oxide fuel cell integrated with novel allothermal biomass gasification: Part II: Exergy analysis. *Journal of Power Sources*, 159(1): 586–594, 2006.

[17] J. R. Rostrup-Nielsen. Conversion of hydrocarbons and alcohols for fuel cells. *Physical Chemistry Chemical Physics*, 3(3):283–288, 2001.

[18] J. Larminie, A. Dicks, and M. S. McDonald. *Fuel cell systems explained*, volume 2. J. Wiley Chichester, UK, 2003.

[19] A. Buttler and H. Spliethoff. Kampf der Studien. Technical report, Lehrstuhl für Energiesysteme, 2016.

[20] S. Herrmann. *Innovative Thermodynamic Cycles for Renewable Energy Supply.* PhD thesis, Technische Universität München, 2018.

[21] K. Sasaki, K. Haga, T. Yoshizumi, D. Minematsu, E. Yuki, R. Liu, C. Uryu, T. Oshima, T. Ogura, Y. Shiratori, et al. Chemical durability of solid oxide fuel cells: Influence of impurities on long-term performance. *Journal of Power Sources*, 196(22):9130–9140, 2011.

[22] E. Lorente, M. Millan, and N. P. Brandon. Use of gasification syngas in SOFC: Impact of real tar on anode materials. *International Journal of Hydrogen Energy*, 37(8):7271–7278, 2012.

[23] S. J. McPhail, J. Kiviaho, and B. Conti. The yellow pages of SOFC technology. international status of SOFC deployment 2017. 2017.

[24] B. C. H. Steele. Material science and engineering: The enabling technology for the commercialisation of fuel cell systems. *Journal of Materials Science*, 36(5):1053–1068, 2001.

[25] D. JL Brett, A. Atkinson, N. P. Brandon, and S. J. Skinner. Intermediate temperature solid oxide fuel cells. *Chemical Society Reviews*, 37(8):1568–1578, 2008.

[26] A. Atkinson, S. Barnett, R. J. Gorte, J. T. S. Irvine, A. J. McEvoy, Mogens Mogensen, S. C. Singhal, and J. Vohs. Advanced anodes for high-temperature fuel cells. *Nature materials*, 3(1):17, 2004.

[27] R. T. Leah, A. Bone, E. Hammer, A. Selcuk, M. Rahman, A. Clare, S. Mukerjee, and M. Selby. Development progress on the ceres power steel cell technology platform: Further progress towards commercialization. *ECS Transactions*, 78(1):87–95, 2017.

[28] N. H. Menzler, D. Sebold, and S. Zischke. Soc degradation: Long-term and small-scale effects. *ECS Transactions*, 91(1):719–729, 2019.

[29] H. Yokokawa and T. Horita. Solid oxide fuel cell materials: Durability, reliability and cost. In *Fuel Cells and Hydrogen Production*, pages 665–700. Springer, 2012.

[30] L. Blum, U. Packbier, I. C. Vinke, and L. G. J. De Haart. Long-term testing of SOFC stacks at Forschungszentrum Jülich. *Fuel Cells*, 13(4):646–653, 2013.

[31] M. Bieber. *Messmethoden zur Untersuchung der Kohlenstoffablagerung an nickelhaltigen SOFC-Anoden beim Betrieb mit Methan.* PhD thesis, Technische Universität München, 2010.

[32] H. Jeong. *Coupling a Solid Oxide Fuel Cell with a Biomass Gasifier: Degradation Mechanisms and Alternative Anode Materials.* PhD thesis, RWTH Aachen, 2019.

[33] L. Blum, LGJ B. De Haart, J. Malzbender, N. H. Menzler, J. Remmel, and R. Steinberger-Wilckens. Recent results in Jülich solid oxide fuel cell technology development. *Journal of Power Sources*, 241:477–485, 2013.

[34] J. Szász, F. Wankmüller, V. Wilde, H. Störmer, D. Gerthsen, N. H. Menzler, and E. Ivers-Tiffée. High-performance cathode/electrolyte interfaces for SOFC. *ECS transactions*, 68(1):763–771, 2015.

[35] H. Zhu, R. J. Kee, V. M. Janardhanan, O. Deutschmann, and D. G. Goodwin. Modeling elementary heterogeneous chemistry and electrochemistry in solid-oxide fuel cells. *Journal of the electrochemical society*, 152(12):A2427–A2440, 2005.

[36] A. Kromp. *Model-based Interpretation of the Performance and Degradation of Reformate Fueled Solid Oxide Fuel Cells*. PhD thesis, Karlsruhe Institute of Technology, 2013.

[37] H. S. Spacil. Electrical device including nickel-containing stabilized zirconia electrode, March 31 1970. US Patent 3,503,809.

[38] S. Harboe, A. Schreiber, N. Margaritis, L. Blum, O. Guillon, and N. H. Menzler. Manufacturing cost model for planar 5 kwel SOFC stacks at Forschungszentrum Jülich. *International Journal of Hydrogen Energy*, 45(15): 8015–8030, 2020.

[39] Y. Tao, S. D. Ebbesen, and M. B. Mogensen. Carbon deposition in solid oxide cells during co-electrolysis of H2O and CO2. *Journal of The Electrochemical Society*, 161(3):F337, 2014.

[40] J. Joos, M. Ender, I. Rotscholl, N. H. Menzler, and E. Ivers-Tiffée. Quantification of double-layer Ni/YSZ fuel cell anodes from focused ion beam tomography data. *Journal of power sources*, 246:819–830, 2014.

[41] N. Grünwald, D. Sebold, Y. J. Sohn, N. H. Menzler, and R. Vaßen. Self-healing atmospheric plasma sprayed Mn1. 0Co1. 9Fe0. 1o4 protective interconnector coatings for solid oxide fuel cells. *Journal of Power Sources*, 363: 185–192, 2017.

[42] R. Wang, M. Würth, U. B. Pal, S. Gopalan, and S. N. Basu. Roles of humidity and cathodic current in chromium poisoning of Sr-doped LaMnO3-based cathodes in solid oxide fuel cells. *Journal of Power Sources*, 360:87–97, 2017.

[43] P. W. Atkins, J. De Paula, and J. Keeler. *Atkins' physical chemistry*. Oxford university press, 2018.

[44] E. Ivers-Tiffée, A. Leonide, H. Schichlein, V. Sonn, and A. Weber. Impedance spectroscopy for high-temperature fuel cells. *Fuel Cell Science and Engineering: Materials, Processes, Systems and Technology*, pages 439–467, 2012.

[45] M. Mogensen and K. Kammer. Conversion of hydrocarbons in solid oxide fuel cells. *Annual Review of Materials Research*, 33(1):321–331, 2003.

[46] D. A. Noren and M. A. Hoffman. Clarifying the butler–volmer equation and related approximations for calculating activation losses in solid oxide fuel cell models. *Journal of Power Sources*, 152:175–181, 2005.

[47] H. Shimada, T. Suzuki, T. Yamaguchi, H. Sumi, K. Hamamoto, and Y. Fujishiro. Challenge for lowering concentration polarization in solid oxide fuel cells. *Journal of Power Sources*, 302:53–60, 2016.

[48] H. Yakabe, M. Hishinuma, M. Uratani, Y. Matsuzaki, and I. Yasuda. Evaluation and modeling of performance of anode-supported solid oxide fuel cell. *Journal of Power Sources*, 86(1-2):423–431, 2000.

[49] E4tech. Fuel cell industry review 2019. Technical report, E4tech, 2019. URL `http://www.FuelCellIndustryReview.com`.

[50] M. Homel, T. M. Gür, J. H. Koh, and A. V. Virkar. Carbon monoxide-fueled solid oxide fuel cell. *Journal of Power Sources*, 195(19):6367–6372, 2010.

[51] V. Alzate-Restrepo and J. M. Hill. Effect of anodic polarization on carbon deposition on Ni/YSZ anodes exposed to methane. *Applied Catalysis A: General*, 342(1-2):49–55, 2008.

[52] V. Alzate-Restrepo and J. M. Hill. Carbon deposition on Ni/YSZ anodes exposed to CO/H2 feeds. *Journal of Power Sources*, 195(5):1344–1351, 2010.

[53] D. Mogensen, J. D. Grunwaldt, P. V. Hendriksen, K. Dam-Johansen, and J. U. Nielsen. Internal steam reforming in solid oxide fuel cells: Status and opportunities of kinetic studies and their impact on modelling. *Journal of power sources*, 196(1):25–38, 2011.

[54] M. Riegraf, M. P. Hoerlein, R. Costa, G. Schiller, and K. A. Friedrich. Sulfur poisoning of electrochemical reformate conversion on nickel/gadolinium-doped ceria electrodes. *ACS Catalysis*, 7(11):7760–7771, 2017.

[55] R. Peters, R. Dahl, U. Klüttgen, C. Palm, and D. Stolten. Internal reforming of methane in solid oxide fuel cell systems. *Journal of Power Sources*, 106 (1-2):238–244, 2002.

[56] J. Koh, Y. Yoo, J. Park, and H. C. Lim. Carbon deposition and cell performance of Ni-YSZ anode support SOFC with methane fuel. *Solid State Ionics*, 149(3-4):157–166, 2002.

[57] W. Bessler. Hydrocarbon direct oxidation or internal reforming? A critical discussion from an elementary kinetic viewpoint. In *8th European SOFC & SOE Forum 2008*, 2008.

[58] Yoshio Matsuzaki and Isamu Yasuda. Electrochemical oxidation of H2 and CO in a H2-H2O-CO-CO2 system at the interface of a Ni-YSZ cermet electrode and YSZ electrolyte. *Journal of the Electrochemical Society*, 147(5): 1630–1635, 2000.

[59] T. A. Milne, R. J. Evans, and N. Abatzaglou. Biomass gasifier "tars": their nature, formation, and conversion. Technical report, National Renewable Energy Laboratory, Golden, CO (US), 1998.

[60] D. J. Stevens. Hot gas conditioning: Recent progress with larger-scale biomass gasification systems; update and summary of recent progress. Technical report, National Renewable Energy Lab., Golden, CO (US), 2001.

[61] F. Kirnbauer and H. Wilk, V.and Hofbauer. Performance improvement of dual fluidized bed gasifiers by temperature reduction: The behavior of tar species in the product gas. *Fuel*, 108:534–542, 2013.

[62] ECN. Tar dew point calculation. `http://www.thersites.nl/completemodel.aspx`.

[63] P. V. Aravind and W. de Jong. Evaluation of high temperature gas cleaning options for biomass gasification product gas for solid oxide fuel cells. *Progress in Energy and Combustion Science*, 38(6):737–764, 2012.

[64] N. Frank. *Umsetzung von Kohlenwasserstoffen in SOFCs*. PhD thesis, Technische Universität München, 2010.

[65] A. O. Omosun, A. Bauen, N. P. Brandon, C. S. Adjiman, and D. Hart. Modelling system efficiencies and costs of two biomass-fuelled SOFC systems. *Journal of power sources*, 131(1-2):96–106, 2004.

[66] B. Voss, J. Madsen, J. B. Hansen, and K. Andersson. Topsoe tar reforming in Skive: The tough get going. *The Catalyst Review*, 29(5):7–14, 2016.

[67] M. Asadullah. Biomass gasification gas cleaning for downstream applications: A comparative critical review. *Renewable and sustainable energy reviews*, 40: 118–132, 2014.

[68] A. Schweiger. *Reinigung von heissen Produktgasen aus Biomassevergasern für den Einsatz in oxidkeramischen Brennstoffzellen*. PhD thesis, Technische Universität Graz, 2008.

[69] A. Jess. Mechanisms and kinetics of thermal reactions of aromatic hydrocarbons from pyrolysis of solid fuels. *Fuel*, 75(12):1441–1448, 1996.

[70] P. V. Aravind, J. P. Ouweltjes, N. Woudstra, and G. Rietveld. Impact of biomass-derived contaminants on SOFCs with Ni/gadolinia-doped ceria anodes. *Electrochemical and Solid State Letters*, 11(2):B24–B28, 2008.

[71] M. Geis, S. Herrmann, S. Fendt, H. Jeong, C. Lenser, N. H. Menzler, and H. Spliethoff. Coupling SOFCs to biomass gasification – The influence of phenol on cell degradation in simulated bio-syngas. Part I: Electrochemical analysis. *International Journal of Hydrogen Energy*, 43(45):20417–20427, 2018.

[72] M. Hauser, S. Herrmann, M. Hauck, S. Fendt, H. Jeong, C. Lenser, N. H. Menzler, and H. Spliethoff. Effects of naphthalene on the performance of Ni/YSZ anode-supported SOFCs. *ECS Transactions*, 91(1):697–706, 2019.

[73] J. Mermelstein, M. Millan, and N. P. Brandon. The impact of carbon formation on Ni–YSZ anodes from biomass gasification model tars operating in dry conditions. *Chemical Engineering Science*, 64(3):492–500, 2009.

[74] J. Mermelstein, M. Millan, and N. Brandon. The impact of steam and current density on carbon formation from biomass gasification tar on Ni/YSZ, and

Ni/CGO solid oxide fuel cell anodes. *Journal of Power Sources*, 195(6):1657–1666, 2010.

[75] D. Papurello, A. Lanzini, P. Leone, and M. Santarelli. The effect of heavy tars (toluene and naphthalene) on the electrochemical performance of an anode-supported SOFC running on bio-syngas. *Renewable Energy*, 99:747–753, 2016.

[76] M. Hauth, W. Lerch, K. König, and J. Karl. Impact of naphthalene on the performance of SOFCs during operation with synthetic wood gas. *Journal of Power Sources*, 196(17):7144–7151, 2011.

[77] N. J. J. Dekker, J. P. Ouweltjes, A. Van der Drift, and G. Rietveld. Efficient conversion of biogas in electricity and heat by a solid oxide fuel cell. In *Proceedings of the 15th European biomass conference & exhibition, Berlin, Germany*, 2007.

[78] S. Forseth and P. Kofstad. Metal dusting phenomenon during carburization of FeNiCr-alloys at 850–1000°. *Materials and Corrosion*, 46(4):201–206, 1995.

[79] J. Zhang, P. Munroe, and D. J. Young. Microprocesses in nickel accompanying metal dusting. *Acta Materialia*, 56(1):68–77, 2008.

[80] O. A. Marina and M. Mogensen. High-temperature conversion of methane on a composite gadolinia-doped ceria–gold electrode. *Applied Catalysis A: General*, 189(1):117–126, 1999.

[81] D. Pumiglia, S. Vaccaro, A. Masi, S. J. McPhail, M. Falconieri, S. Gagliardi, L. Della Seta, and M. Carlini. Aggravated test of intermediate temperature solid oxide fuel cells fed with tar-contaminated syngas. *Journal of Power Sources*, 340:150–159, 2017.

[82] H. Madi, S. Diethelm, C. Ludwig, et al. The impact of toluene on the performance of anode-supported Ni-YSZ SOFC operated on hydrogen and biosyngas. *ECS Transactions*, 68(1):2811–2818, 2015.

[83] D. Papurello, A. Lanzini, D. Drago, P. Leone, and M. Santarelli. Limiting factors for planar solid oxide fuel cells under different trace compound concentrations. *Energy*, 95:67–78, 2016.

[84] N. Dekker, J. P. Ouweltjes, S. Linnekamp, and B. Rietveld. Conversion of simulated biogas in an SOFC: The effect of organic components. In *7th European SOFC & SOE Forum 2006*, 2006.

[85] M. Liu, M. G. Millan, P. V. Aravind, and N. Brandon. Influence of operating conditions on carbon deposition in SOFCs fuelled by tar-containing biosyngas. *Journal of The Electrochemical Society*, 158(11):B1310, 2011.

[86] M. Liu, A. Van der Kleij, A. H. M. Verkooijen, and P. V. Aravind. An experimental study of the interaction between tar and SOFCs with Ni/GDC anodes. *Applied energy*, 108:149–157, 2013.

[87] P. Hofmann, K. D. Panopoulos, P. V. Aravind, M. Siedlecki, A. Schweiger, J. Karl, J. P. Ouweltjes, and E. Kakaras. Operation of solid oxide fuel cell on biomass product gas with tar levels > 10 g Nm- 3. *International journal of hydrogen energy*, 34(22):9203–9212, 2009.

[88] S. M. A. Biollaz, P. Hottinger, C. Pitta, and J. Karl. Results from a 1200 hour test of a tubular SOFC with woodgas. In *17th European Biomass Conference and Exhibition. Hamburg, Germany: ETA-Florence Renewable Energies*, 2009.

[89] J. Froitzheim, G. H. Meier, L. Niewolak, P. J. Ennis, H. Hattendorf, L. Singheiser, and W. J. Quadakkers. Development of high strength ferritic steel for interconnect application in SOFCs. *Journal of Power Sources*, 178(1):163–173, 2008.

[90] P. Hofmann, A. Schweiger, L. Fryda, K. D. Panopoulos, U. Hohenwarter, J. D. Bentzen, J. P. Ouweltjes, J. Ahrenfeldt, U. Henriksen, and E. Kakaras. High temperature electrolyte-supported Ni-GDC/YSZ/LSM SOFC operation on two-stage Viking gasifier product gas. *Journal of power sources*, 173(1): 357–366, 2007.

[91] P. Hofmann, K. D. Panopoulos, L. E. Fryda, A. Schweiger, J. P. Ouweltjes, and J. Karl. Integrating biomass gasification with solid oxide fuel cells: Effect of real product gas tars, fluctuations and particulates on ni-gdc anode. *International journal of hydrogen energy*, 33(11):2834–2844, 2008.

[92] A. B.J. Oudhuis, A. Bos, J. P. Ouweltjes, G. Rietveld, and A. B. Van der Giesen. High efficiency electricity and products from biomass and waste; experimental results of proof of principle of staged gasification and fuel cells. In *2nd World Conference and Technology Exhibition on Biomass for Energy, Industry and Climate Protection, Rome, Italy*, pages 10–14, 2004.

[93] F. P. Nagel, S. Biollaz, M. Jenne, and S. Stucki. Link-up of a 1 kW SOFC with an updraft-wood gasifier via hot gas processing. In *Proceedings of the 15th European biomass conference & exhibition, Berlin, Germany*, 2007.

[94] F. P. Nagel, S. Ghosh, C. Pitta, T. J. Schildhauer, and S. Biollaz. Biomass integrated gasification fuel cell systems–concept development and experimental results. *Biomass and bioenergy*, 35(1):354–362, 2011.

[95] N. Dekker, B. Van der Drift, L. Rabou, H Van Wees, and B. Rietveld. Operation of a Staxera SOFC stack fuelled with cleaned gas from a gasifier. In *Proceedings of the 8th European SOFC & SOE Forum 2008, Lucerne, Switzerland*, 2008.

[96] R. Ø. Gadsbøll, J. Thomsen, C. Bang-Møller, J. Ahrenfeldt, and U. B. Henriksen. Solid oxide fuel cells powered by biomass gasification for high efficiency power generation. *Energy*, 131:198–206, 2017.

[97] R. Ø. Gadsbøll, A. V. Garcia, J. Ahrenfeldt, and U. B. Henriksen. Solid oxide fuel cell stack coupled with an oxygen-blown TwoStage gasifier using minimal gas cleaning. *Renewable energy*, 139:1255–1262, 2019.

[98] M. Mayerhofer. *Teerentstehung und Teerminderung bei allothermer Wirbelschichtvergasung*. PhD thesis, Technische Universität München, 2014.

[99] F. Han, R. Mücke, T. Van Gestel, A. Leonide, N. H. Menzler, H. P. Buchkremer, and D. Stöver. Novel high-performance solid oxide fuel cells with bulk ionic conductance dominated thin-film electrolytes. *Journal of Power Sources*, 218:157–162, 2012.

[100] H. Jeong, M. Geis, C. Lenser, S. Lobe, S. Herrmann, S. Fendt, N. H. Menzler, and O. Guillon. Coupling SOFCs to biomass gasification – The influence of

phenol on cell degradation in simulated bio-syngas. Part II: Post-test analysis. *International Journal of Hydrogen Energy*, 43(45):20911–20920, 2018.

[101] N. H. Menzler. Formgebende Keramiktechnologie. DGM-Seminar Ionenleitende Keramiken für Energie- und Verfahrenstechnik, 2016.

[102] C. Lenser, H. Jeong, Y. J. Sohn, N. Russner, O. Guillon, and N. H. Menzler. Interaction of a ceria-based anode functional layer with a stabilized zirconia electrolyte: Considerations from a materials perspective. *Journal of the American Ceramic Society*, 101(2):739–748, 2018.

[103] Q. Fang, L. Blum, R. Peters, M. Peksen, P. Batfalsky, and D. Stolten. SOFC stack performance under high fuel utilization. *International journal of hydrogen energy*, 40(2):1128–1136, 2015.

[104] Crofer 22 apu data sheet, 2010. URL `https://www.vdm-metals.com/fileadmin/user_upload/Downloads/Data_Sheets/Datenblatt_VDM_Crofer_22_APU.pdf`. Download 11.09.2020.

[105] *TrueData-EIS - Manual for Impedance spectrum analyzer*. FuelCon AG, Steinfeldstr. 1, D-39179 Magdeburg-Barleben, 2016.

[106] *TestWork Script - Handbuch zur Erstellung von Skript-Prüfprogrammen*. FuelCon AG, Steinfeldstr. 1, D-39179 Magdeburg-Barleben, 2017.

[107] M. Würth. Automatisierung einer Teermischstrecke, 2013. Bachelor's Thesis, Technische Universität München.

[108] M. Hauck, S. Herrmann, and H. Spliethoff. Simulation of a reversible SOFC with Aspen Plus. *International journal of hydrogen energy*, 42(15):10329–10340, 2017.

[109] D. Klotz, A. Weber, and E. Ivers-Tiffée. Practical guidelines for reliable electrochemical characterization of solid oxide fuel cells. *Electrochimica Acta*, 227:110–126, 2017.

[110] A. Weber, B. Sauer, A. C. Müller, D. Herbstritt, and E. Ivers-Tiffée. Oxidation of H2, CO and methane in SOFCs with Ni/YSZ-cermet anodes. *Solid State Ionics*, 152:543–550, 2002.

[111] Y. L. Liu and C. Jiao. Microstructure degradation of an anode/electrolyte interface in SOFC studied by transmission electron microscopy. *Solid State Ionics*, 176(5-6):435–442, 2005.

[112] F. Fischer, M. Hauser, M. Hauck, S. Herrmann, S. Fendt, H. Jeong, C. Lenser, N. H. Menzler, and H. Spliethoff. Effect of internal hydrocarbon reforming during coupled operation of a biomass gasifier with hot gas cleaning and SOFC stacks. *Energy Science & Engineering*, 7(4):1140–1153, 2019.

[113] M. Hauck. Assembly and startup of a test rig for fuel-cell stacks. Master's thesis, Technische Universität München, 2017.

[114] A. Geiger. Umbau und Automatisierung eines Teststands für SOFC Stacks und Versuchsdurchführung. Master's thesis, Technische Universität München, 2019.

[115] L. Briesemeister. *Flugstromvergasung hydrothermal karbonisierter Biomasse mit Luft*. PhD thesis, Technische Universität München, 2018.

[116] V. Berova. Auslegung eines Teststandes zur chemischen Untersuchung von Festoxidbrennstoffzellenmaterialien und Aufbau der zugehörigen Teerdosierung, 2019. Research Internship, Technische Universität München.

[117] C. Brage, Q. Yu, G. Chen, and K. Sjöström. Use of amino phase adsorbent for biomass tar sampling and separation. *Fuel*, 76(2):137–142, 1997.

[118] R. K. Großmann. Teeranalytik für Biomassevergasung, 2012. Bachelor's Thesis, Technische Universität München.

[119] M. E. Orazem and B. Tribollet. *Electrochemical Impedance Spectroscopy*. John Wiley & Sons, New York, 2011. ISBN 978-1-118-20994-3.

[120] E. Basoukov and J. R. MacDonald. *Impedance Spectroscopy: Theory, Experiment, and Applications*. John Wiley & Sons, New Jersey, second edition edition, 2005. ISBN 780471716228.

[121] L. Malafronte, B. Morel, and A. Pohjoranta. Online total harmonic distortion analysis for solid oxide fuel cell stack monitoring in system applications. *Fuel Cells*, 18(4):476–489, 2018.

[122] A. Utz. *The Electrochemical Oxidation of H2 and CO at Patterned Ni Anodes of SOFCs*. PhD thesis, Karlsruhe Institute of Technology, 2011.

[123] B. A. Boukamp. A linear kronig-kramers transform test for immittance data validation. *Journal of the Electrochemical Society*, 142(6):1885–1894, 1995.

[124] KIT. Kramers-kronig validity test lin-kk for impedance spectra. `http://www.iwe.kit.edu/Lin-KK.php`.

[125] H. Schichlein, A. C. Müller, M. Voigts, A. Krügel, and E. Ivers-Tiffée. Deconvolution of electrochemical impedance spectra for the identification of electrode reaction mechanisms in solid oxide fuel cells. *Journal of Applied Electrochemistry*, 32(8):875–882, 2002.

[126] A. Leonide. *SOFC modelling and parameter identification by means of impedance spectroscopy*. PhD thesis, Karlsruhe Institute of Technology, 2010.

[127] E. Massa. Algorithmengestützte Datenauswertung in der experimentellen Untersuchung von Festoxid-Brennstoffzellen. Master's thesis, Technische Universität München, 2018.

[128] J. Nielsen and J. Hjelm. Impedance of SOFC electrodes: A review and a comprehensive case study on the impedance of LSM: YSZ cathodes. *Electrochimica Acta*, 115:31–45, 2014.

[129] M. Lutz. Investigation of the degradation of solid oxide fuel cells via impedancespectroscopy. Master's thesis, Technische Universität München, 2017.

[130] L. Spiegler. Modellgestützte Interpretation der Impedanzspektren von Festoxidbrennstoffzellen. Master's thesis, Technische Universität München, 2017.

[131] R. M. Fuoss and J. G. Kirkwood. Electrical properties of solids. VIII. Dipole moments in polyvinyl chloride-diphenyl systems. *Journal of the American Chemical Society*, 63(2):385–394, 1941.

[132] F. Monaco. Application of electrochemical impedance spectroscopy to solid oxide fuel cells. Master's thesis, Politecnico di Torino, 2014.

[133] J. Weese. A reliable and fast method for the solution of fredhol integral equations of the first kind based on Tikhonov regularization. *Computer physics communications*, 69(1):99–111, 1992.

[134] N. L. Herz. Intelligente Datenauswertung in der experimentellen Untersuchung von Festoxid-Brennstoffzellen. Master's thesis, Technische Universität München, 2018.

[135] P. C. Hansen. The L-curve and its use in the numerical treatment of inverse problems. 1999.

[136] T. H. Wan, M. Saccoccio, C. Chen, and F. Ciucci. Influence of the discretization methods on the distribution of relaxation times deconvolution: Implementing radial basis functions with DRTtools. *Electrochimica Acta*, 184:483–499, 2015.

[137] V. Sonn, A. Leonide, and E. Ivers-Tiffée. Combined deconvolution and CNLS fitting approach applied on the impedance response of technical Ni/ 8YSZ cermet electrodes. *Journal of The Electrochemical Society*, 155(7):B675–B679, 2008.

[138] A. Kromp, A. Leonide, A. Weber, and E. Ivers-Tiffée. Electrochemical analysis of reformate-fuelled anode-supported SOFC. *Journal of The Electrochemical Society*, 158(8):B980–B986, 2011.

[139] A. Hauch, A. Hagen, J. Hjelm, and T. Ramos. Sulfur poisoning of SOFC anodes: Effect of overpotential on long-term degradation. *Journal of The Electrochemical Society*, 161(6):F734, 2014.

[140] D. Papurello, D. Menichini, and A. Lanzini. Distributed relaxation times technique for the determination of fuel cell losses with an equivalent circuit model to identify physicochemical processes. *Electrochimica Acta*, 258:98–109, 2017.

[141] A. Kromp, S. Dierickx, A. Leonide, A. Weber, and E. Ivers-Tiffée. Electrochemical analysis of sulfur-poisoning in anode supported SOFCs fuelled with a model reformate. *Journal of The Electrochemical Society*, 159(5): B597–B601, 2012.

[142] A. Leonide, A. Weber, and E. Ivers-Tiffée. Electrochemical analysis of biogas fueled anode supported SOFC. *Ecs Transactions*, 35(1):2961, 2011.

[143] R. Barfod, M. Mogensen, T. Klemensø, A. Hagen, Y. Liu, and P. V. Hendriksen. Detailed characterization of anode-supported SOFCs by impedance spectroscopy. *Journal of The Electrochemical Society*, 154(4):B371–B378, 2007.

[144] J. Kim, A. V. Virkar, K. Fung, K. Mehta, and S. C. Singhal. Polarization effects in intermediate temperature, anode-supported solid oxide fuel cells. *Journal of the Electrochemical Society*, 146(1):69–78, 1999.

[145] Gestis data sheet naphthalene, 2020. URL `http://gestis.itrust.de`. Download 11.09.2020.

[146] M. Hauth, T.s Kienberger, and J. Karl. Transient operation effects of SOFCs driven with tar loaded synthesis gas. *ECS Transactions*, 35(1):2713–2723, 2011.

[147] A. Jess. Catalytic upgrading of tarry fuel gases: A kinetic study with model components. *Chemical Engineering and Processing: Process Intensification*, 35(6):487–494, 1996.

[148] C Röhr and W. Holzapfel. Der Einsatz von Aktivkohle bei der Sanierung von Grundwasser und Bodenluft. URL `http://www.gutmbh.de/AktivkohleVortrag2.htm`.

[149] H. Jeong, M. Hauser, F. Fischer, M. Hauck, S. Lobe, R. Peters, C. Lenser, N. H. Menzler, and O. Guillon. Utilization of bio-syngas in solid oxide fuel cell stacks: Effect of hydrocarbon reforming. *Journal of The Electrochemical Society*, 166(2):F137–F143, 2019.

[150] M. Mogensen, K. V. Jensen, M. J. Jørgensen, and S. Primdahl. Progress in understanding SOFC electrodes. *Solid State Ionics*, 150(1-2):123–129, 2002.

[151] V. He. Experimental investigation of three different fixed bed methanation reactors. Master's thesis, Technische Universität München, 2019.

[152] M. Geis, S. Herrmann, S. Fendt, H. Jeong, C. Lenser, N. H. Menzler, and H. Spliethoff. Investigations on the influence of phenol as a model tar on Ni/YSZ anodes using electrical impedance spectroscopy. In *13th European SOFC & SOE Forum 2018*, 2018.

[153] Gestis data sheet phenol, 2020. URL `http://gestis.itrust.de`. Download 11.09.2020.

[154] T. Chen, W. G. Wang, H. Miao, T. Li, and C. Xu. Evaluation of carbon deposition behavior on the nickel/yttrium-stabilized zirconia anode-supported fuel cell fueled with simulated syngas. *Journal of Power Sources*, 196(5): 2461–2468, 2011.

[155] H. Timmermann. *Untersuchungen zum Einsatz von Reformat aus flüssigen Kohlenwasserstoffen in der Hochtemperaturbrennstoffzelle SOFC*. PhD thesis, Karlsruhe Institute of Technology, 2009.

[156] T. Namioka, Y. Nagai, K. Yoshikawa, and T. Min. A tolerance criterion for tar concentration in a model wood gas for a nickel/scandia-stabilized zirconia cermet anode in a solid oxide fuel cell. *International Journal of Hydrogen Energy*, 37(22):17245–17252, 2012.

[157] H. Watanabe, M. Kanie, M. Chanthanumataporn, T. Nagasawa, and K. Hanamura. Experimental and detailed kinetic modeling study of carbon deposition on Ni/YSZ anode in SOFC. *ECS Transactions*, 78(1):1107–1114, 2017.

[158] M. Pillai, Y. Lin, H. Zhu, R. J. Kee, and S. A. Barnett. Stability and coking of direct-methane solid oxide fuel cells: Effect of co2 and air additions. *Journal of power sources*, 195(1):271–279, 2010.

[159] K. Ruzicka, M. Fulem, and V. Ruzicka. Recommended vapor pressure of solid naphthalene. *Journal of Chemical & Engineering Data*, 50(6):1956–1970, 2005.

[160] R. Perry and D. Green. *Perry's Chemical Engineers' Handbook*. McGraw-Hill Education, New York, 8 edition, 2008. ISBN 978-0-071-42294-9.

[161] L. Fowler, W. N. Trump, and C. E. Vogler. Vapor pressure of naphthalene. measurements between 40. deg. and 180. deg. *Journal of Chemical & Engineering Data*, 13(2):209–210, 1968.

[162] A. B. Macknick and J. M. Prausnitz. Vapor pressures of high-molecular-weight hydrocarbons. *Journal of Chemical and Engineering Data*, 24(3): 175–178, 1979.

[163] Dortmund Data Bank: Vapor pressure of naphthalene, 2020. URL `http://www.ddbst.com/en/EED/PCP/VAP_C123.php`. Download 11.09.2020.

[164] A. Haag. Verbesserte Dosierung und Konzentrationsmessung von Teeren für Degradationsmessungen an Festoxid-Brennstoffzellen, 2017. Research Internship, Technische Universität München.

Appendix A

Saturation Pressure of Phenol and Naphthalene

In order to obtain a desired concentration of tar in the fuel gas, a constituent equation is necessary with which the saturation vapour pressure p_{sat} can be calculated as a function of temperature. If the saturation vapour pressure is known, the concentration of tar in the fuel gas in g/Nm^3 can be calculated:

$$c = \frac{p_{\mathrm{sat}}}{p} \cdot \frac{\dot{V}_{\mathrm{cg}}}{\dot{V}_{\mathrm{Anode}}} \cdot \frac{MW_{\mathrm{Tar}}}{V_{\mathrm{mol,ig}}} \cdot 1000 \, \frac{\mathrm{l}}{\mathrm{Nm}^3}. \tag{A.1}$$

Here $\dot{V}_{\mathrm{cg}}$ is the volume flow of carrier gas through the tar container and $\dot{V}_{\mathrm{Anode}}$ is the total volume flow at the anode. It is assumed that the gas behaves ideally and reaches saturation in the tank (partial pressure = saturation pressure), given the residence is high enough. $V_{\mathrm{mol,ig}}$ is the volume of 1 mole of an ideal gas.

For the calculation of the saturation vapour pressure, a distinction must be made between whether the tar is present in a solid or liquid state, i.e. whether an equilibrium is established between the solid and gas phases or between the liquid and gas phases. For the first case the Cox equation was used in this thesis for naphthalene

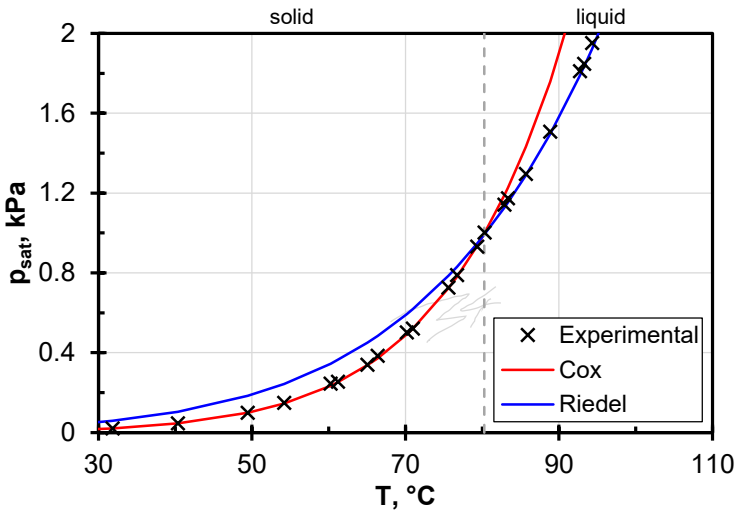

Figure A.1: Trend of saturation pressure of naphthalene calculated with Cox and Riedel equation. Experimental reference values are found in [161, 162].

$$\ln\frac{p_{\text{sat}}}{p_{\text{ref}}} = (1 - \frac{T_{\text{ref}}/K}{T/K})\exp(\sum_{i=0}^{n} b_i (T/K)^i) \tag{A.2}$$

with parameters $b_0 = 3.272310$, $b_1 = -2.663498 \cdot 10^{-2}$, $b_2 = -2.929123 \cdot 10^{-9}$, $T_{\text{ref}} = 353.37K$, $p_{\text{ref}} = 993.5Pa$ [159]. For temperatures above 80.3 °C, i.e. for the gas/liquid equilibrium, the Riedel equation was used

$$\ln\, p_{\text{sat}} = A + \frac{B}{T} + C \cdot \ln\, T + DT^E. \tag{A.3}$$

For naphthalene the coefficients are $A_{\text{N}} = 61.447$, $B_{\text{N}} = -8109$, $C_{\text{N}} = -5.5571$, $D_{\text{N}} = 2.08 \cdot 10^{-18}$ and $E_{\text{N}} = 6$ [160].

As can be seen in Figure A.1 the two equations in the respective validity ranges very well represent the experimentally measured saturation vapour pressure of naphthalene [163]. In order to determine the necessary container temperature for a required tar concentration, the correct equation can be selected with the aid of the required saturation vapour pressure.

For phenol the saturation pressure was calculated with the Riedel equation. Between 314 (melting point) and 694 K the coefficients are $A_P = 95.44$, $B_P = -10113$, $C_P = -10.09$, $D_P = 6.76\ e^{-18}$ and $E_P = 6$ [160]. For temperatures below 314 K other coefficients for a solid/gas equilibrium must be applied. No reference data could be found for phenol so it is assumed that the coefficients from [160] are of the same quality as for naphthalene.

This website http://www.thersites.nl/completemodel.aspx [62] offers an online calculation of the dew point temperatures for gases containing defined amounts of tars.

Appendix B

Calibration Curves for Evaluation of Tar Content in SPA Samples

A calibration of the gas chromatograph (GC) is necessary for the quantitative evaluation of the tar content of the SPA samples. The existing calibration by Großmann was not suitable for the high tar concentrations in the diluted gas stream in the tar mixing station [118]. In the underlying GC method the injected DCM-tar-mixture was diluted only with a split ratio[1] of 3 which meant that the GC column was always overloaded which affected the accuracy of the measured peak area. Therefore, new calibrations for higher tar concentrations were carried out for phenol and naphthalene [164].

For this purpose calibration solutions of DCM and phenol or naphthalene in the range between 0.1 and 10 mg/ml were prepared and measured in the GC. In order to optimally use the measuring range of the detector two calibrations with split ratio 50 and 250 were performed. From 0.1 to 1 mg/ml split ratio 50 was used, from 1 to 10 mg/ml split ratio 250. From the fitted lines through the calibration points shown in Figure B.1, the following correlations resulted for the determination of the concentration of naphthalene and phenol from a measured peak area A_{FID} in mg/ml:

[1] Ratio of purge gas flow to gas flow through the column.

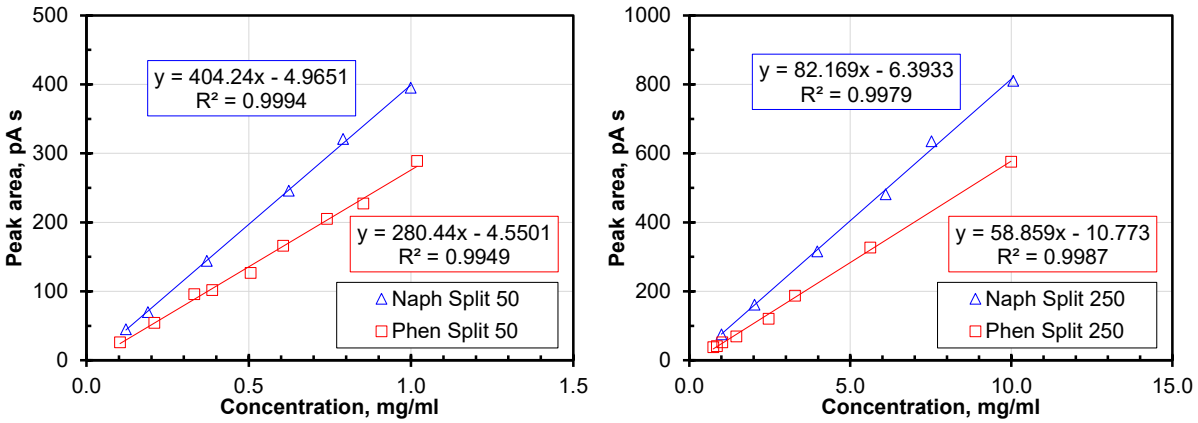

Figure B.1: Calibration data for naphthalene and phenol for concentrations up to 1 mg/ml (left) and 10 mg/ml (right).

$$c_{\text{Naph,S50}} = (A_{\text{FID}} + 4.9651)/404.24 \tag{B.1}$$

$$c_{\text{Naph,S250}} = (A_{\text{FID}} + 6.3933)/82.169 \tag{B.2}$$

$$c_{\text{Phen,S50}} = (A_{\text{FID}} + 4.5501/280.44 \tag{B.3}$$

$$c_{\text{Phen,S250}} = (A_{\text{FID}} + 10.773)/58.859. \tag{B.4}$$

If the tar concentration is unknown, it may therefore be necessary to measure an eluted sample several times using different methods in order to obtain an accurate result without overloading the column. Großmann's calibration was still used to measure the tar concentration in the anode inlet gas. The validity of the calibrations must be checked regularly by control measurements with calibration solutions or an internal standard should be used for each measurement.

Appendix C

Reference spectra

C.1 Study Temp2

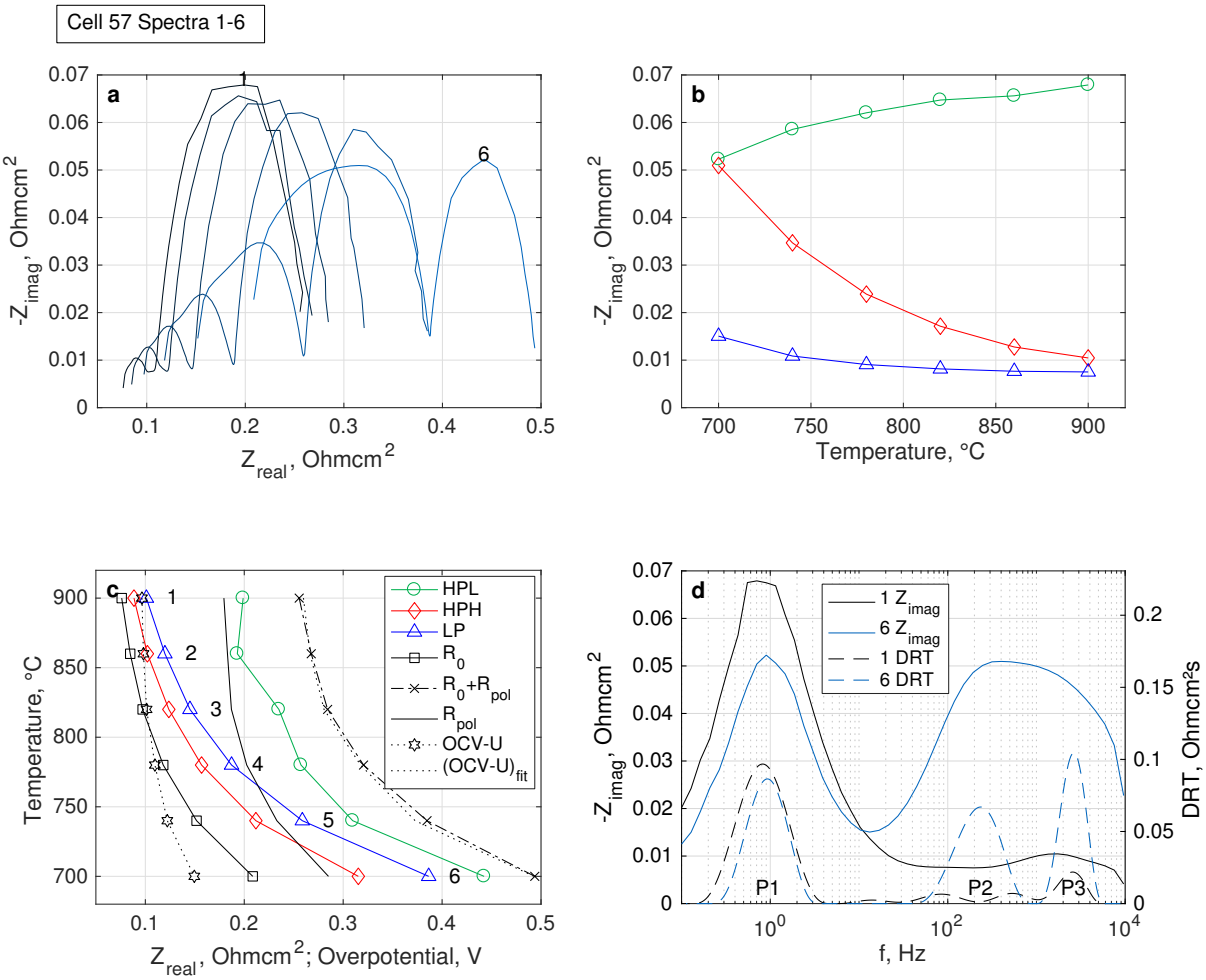

Figure C.1: Impedance data for variation of furnace temperature from 900 to 700 °C (Study *Temp2*). Other operation conditions see Table 5.1. 1: 900, 2: 860, 3: 820, 4: 780, 5: 740, 6: 700 °C. C57.

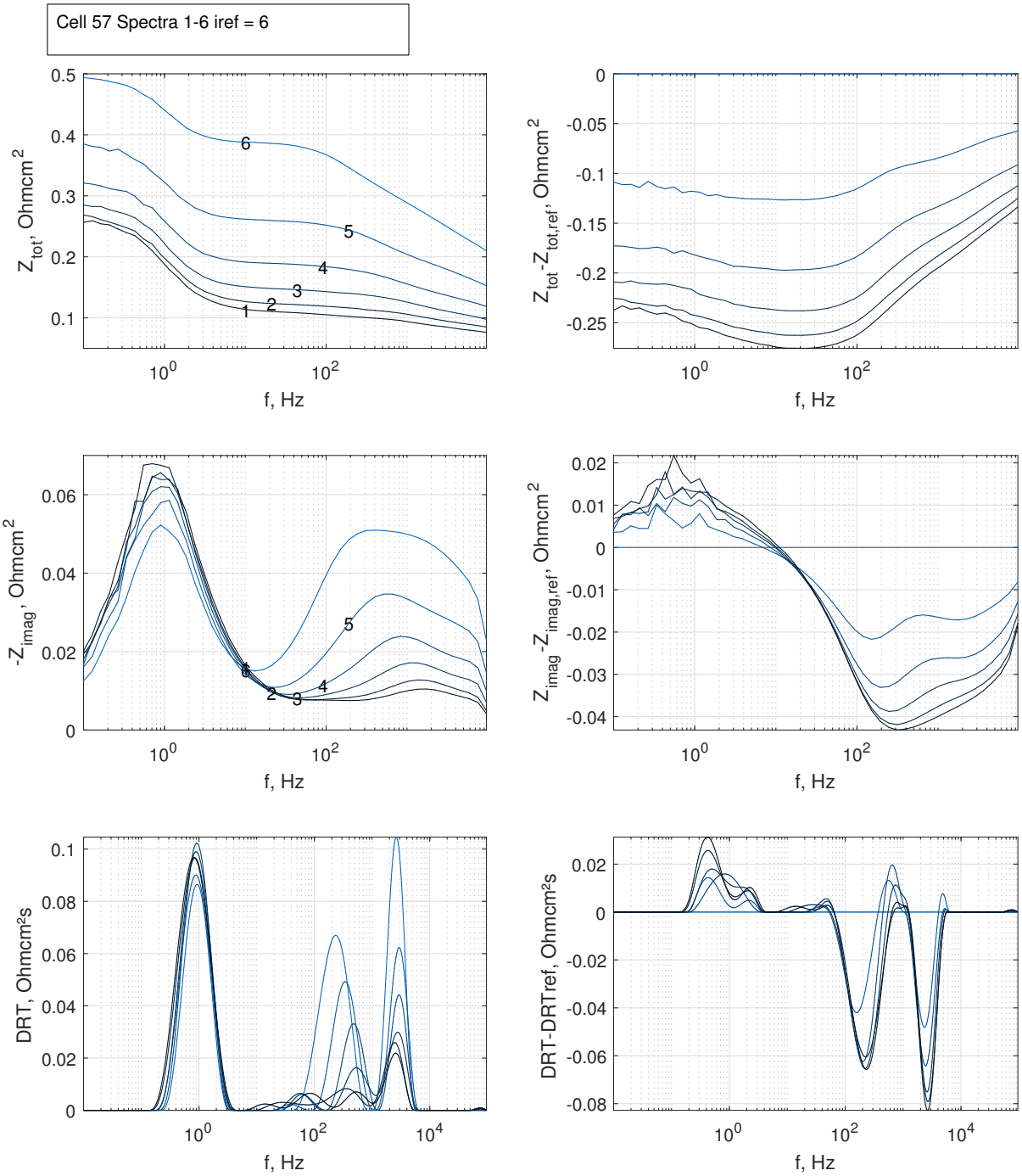

Figure C.2: Bode plots and DRT for variation of furnace temperature from 900 to 700 °C (Study *Temp2*). Other operation conditions see Table 5.1. 1: 900, 2: 860, 3: 820, 4: 780, 5: 740, 6: 700 °C. C57.

C.2 Study CH4

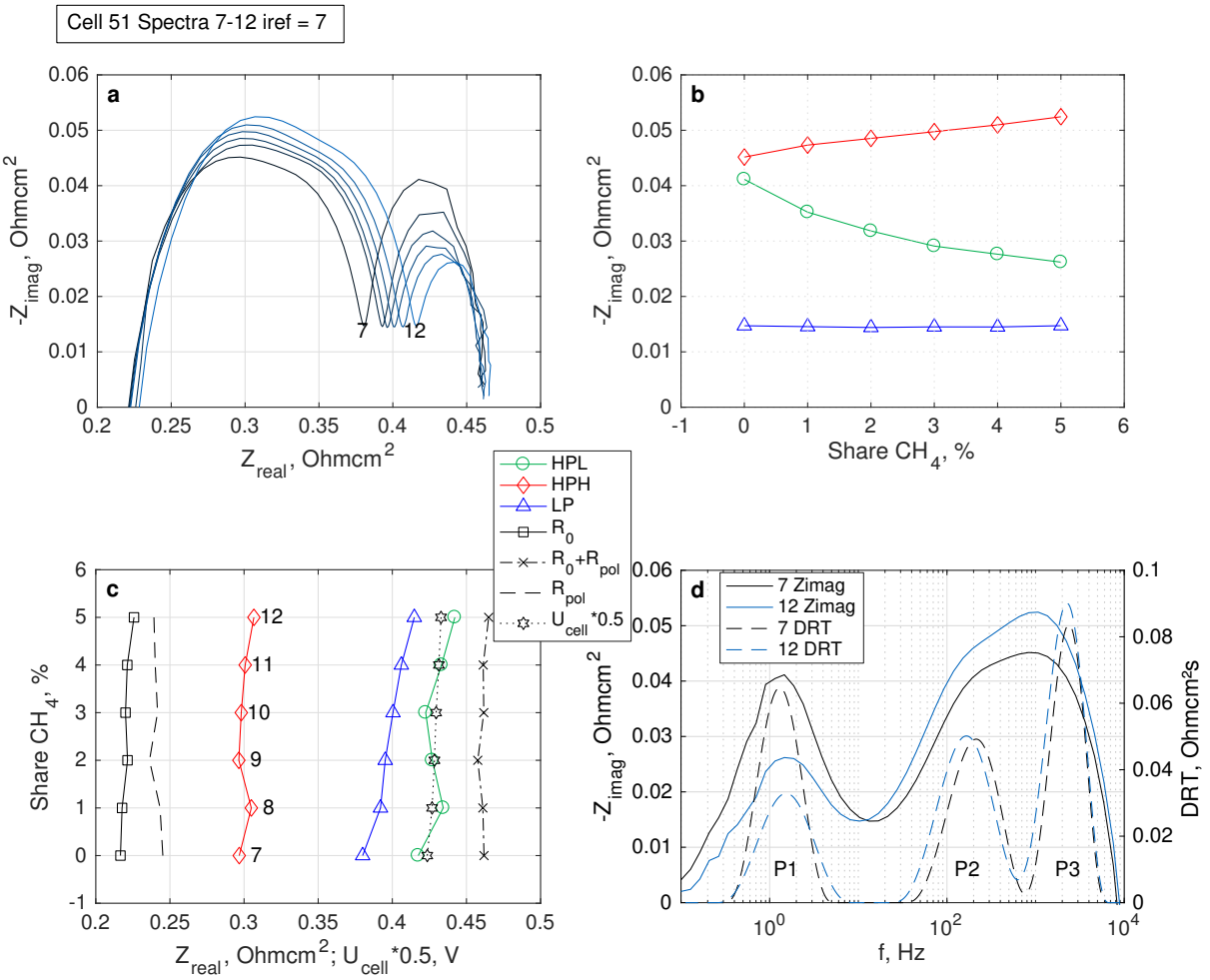

Figure C.3: Impedance data for variation of methane content in syngas (Study *CH4*). Other operation conditions see Table 5.1. 7: 0, 8: 0.01, 9: 0.02, 10: 0.03, 11: 0.04, 12: 0.05 Nl/min CH4. C51.

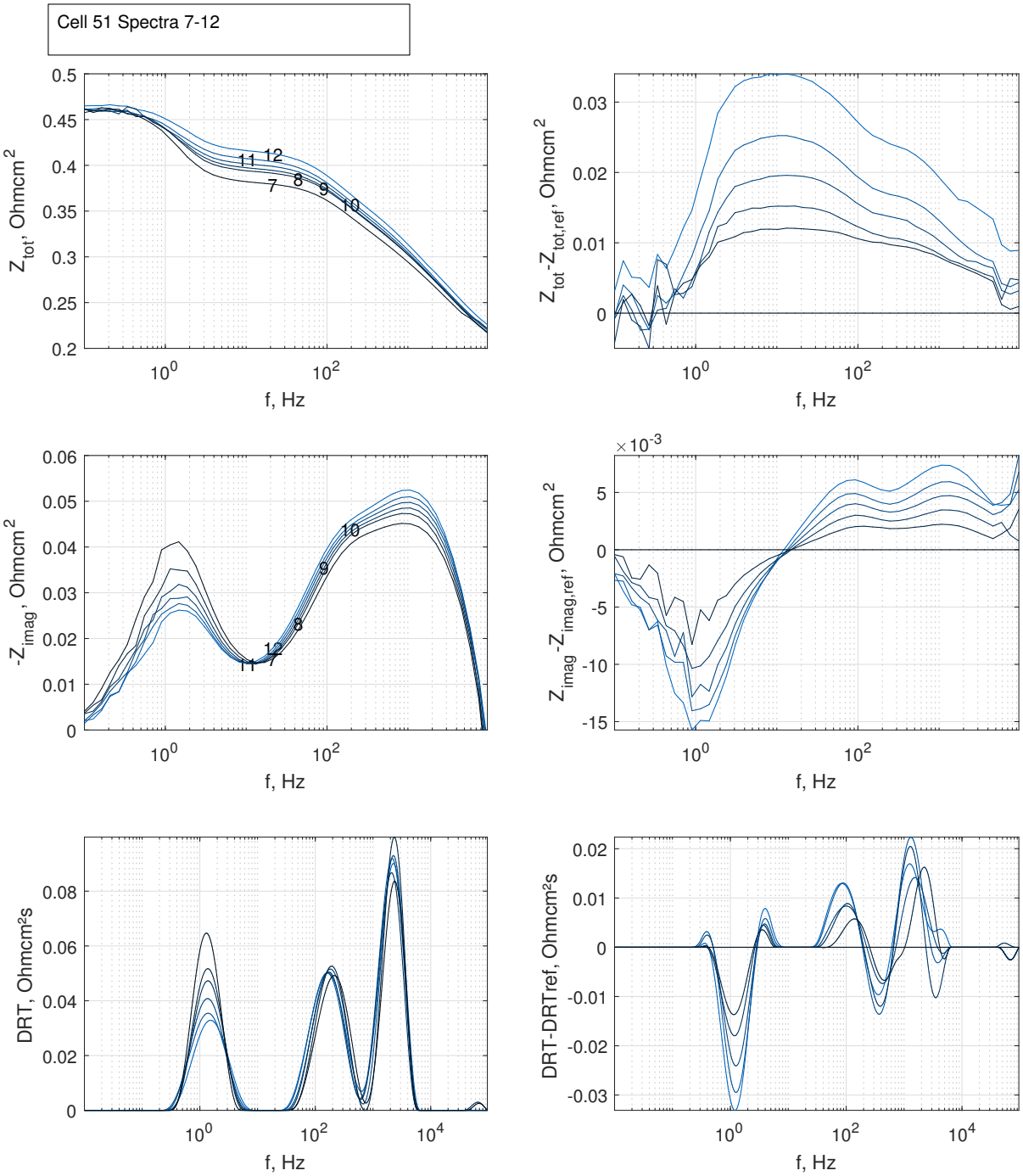

Figure C.4: Bode plots and DRT for variation of methane content in syngas (Study *CH4*). Other operation conditions see Table 5.1. 7: 0, 8: 0.01, 9: 0.02, 10: 0.03, 11: 0.04, 12: 0.05 Nl/min CH4. C51.

C.3 Study CO

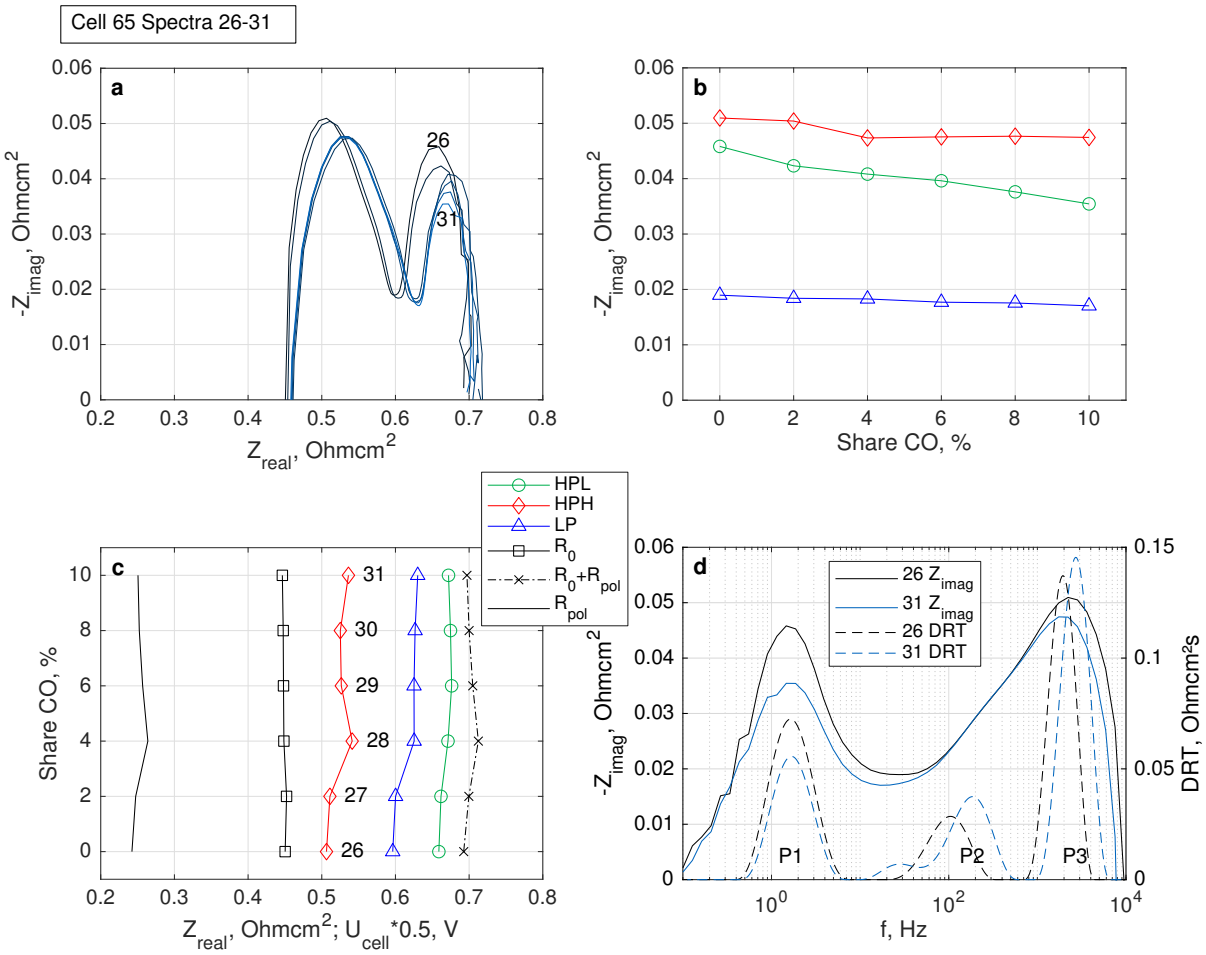

Figure C.5: Impedance data for variation of carbon monoxide content in syngas (Study *CO*). Other operation conditions see Table 5.1. 26: 0, 27: 0.02, 28: 0.04, 29: 0.06, 30: 0.08, 31: 0.1 Nl/min CO. C65.

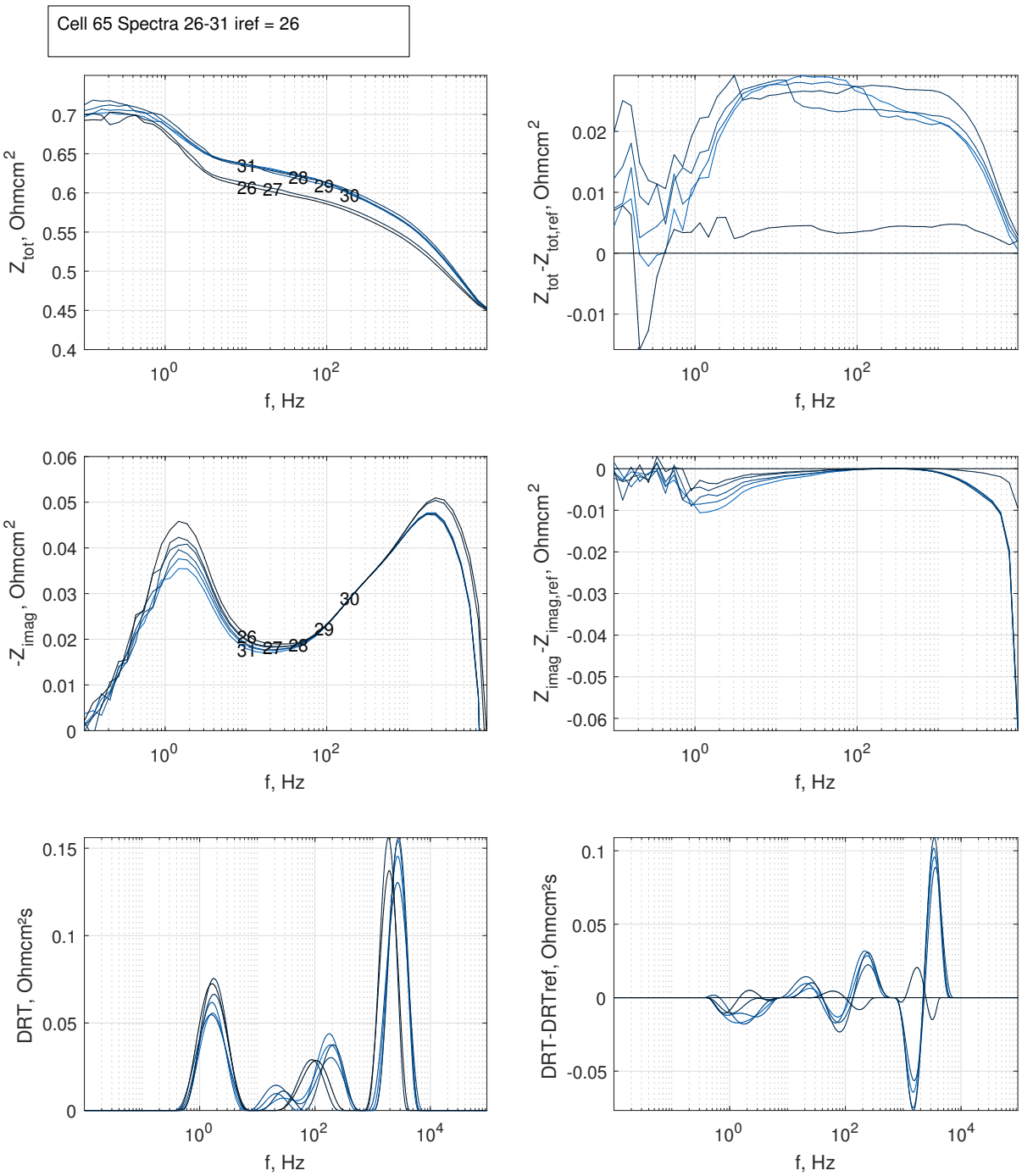

Figure C.6: Bode plots and DRT for variation of carbon monoxide content in syngas (Study *CO*). Other operation conditions see Table 5.1. 26: 0, 27: 0.02, 28: 0.04, 29: 0.06, 30: 0.08, 31: 0.1 Nl/min CO. C65.

C.4 Study O2H2

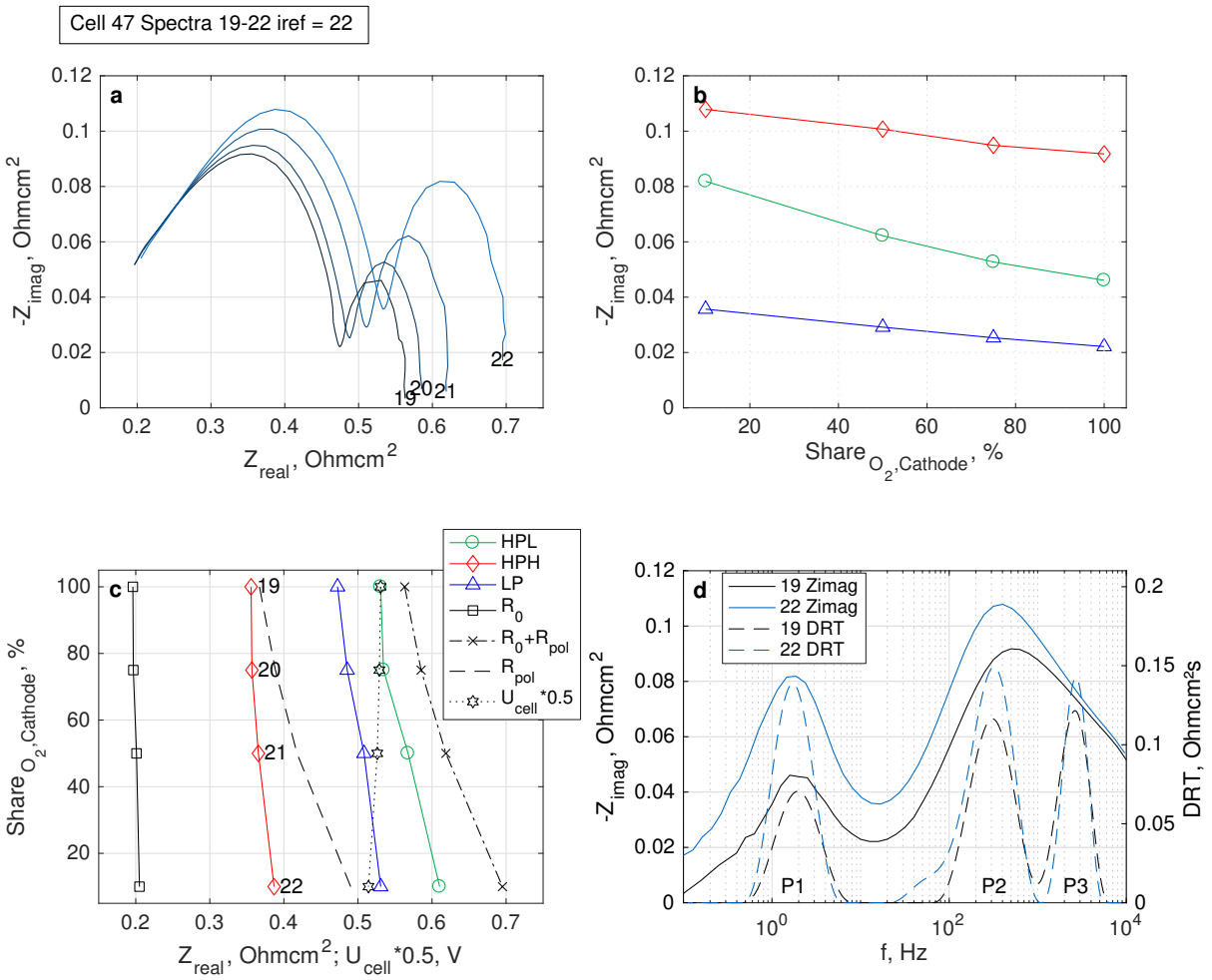

Figure C.7: Impedance data for variation of oxygen concentration at the cathode (Study *O2_H2*). Other operation conditions see Table 5.1. 19: 1 (0), 20: 0.75 (0.25), 21: 0.5 (0.5), 22: 0.1 (0) Nl/min O_2 (N_2). C47.

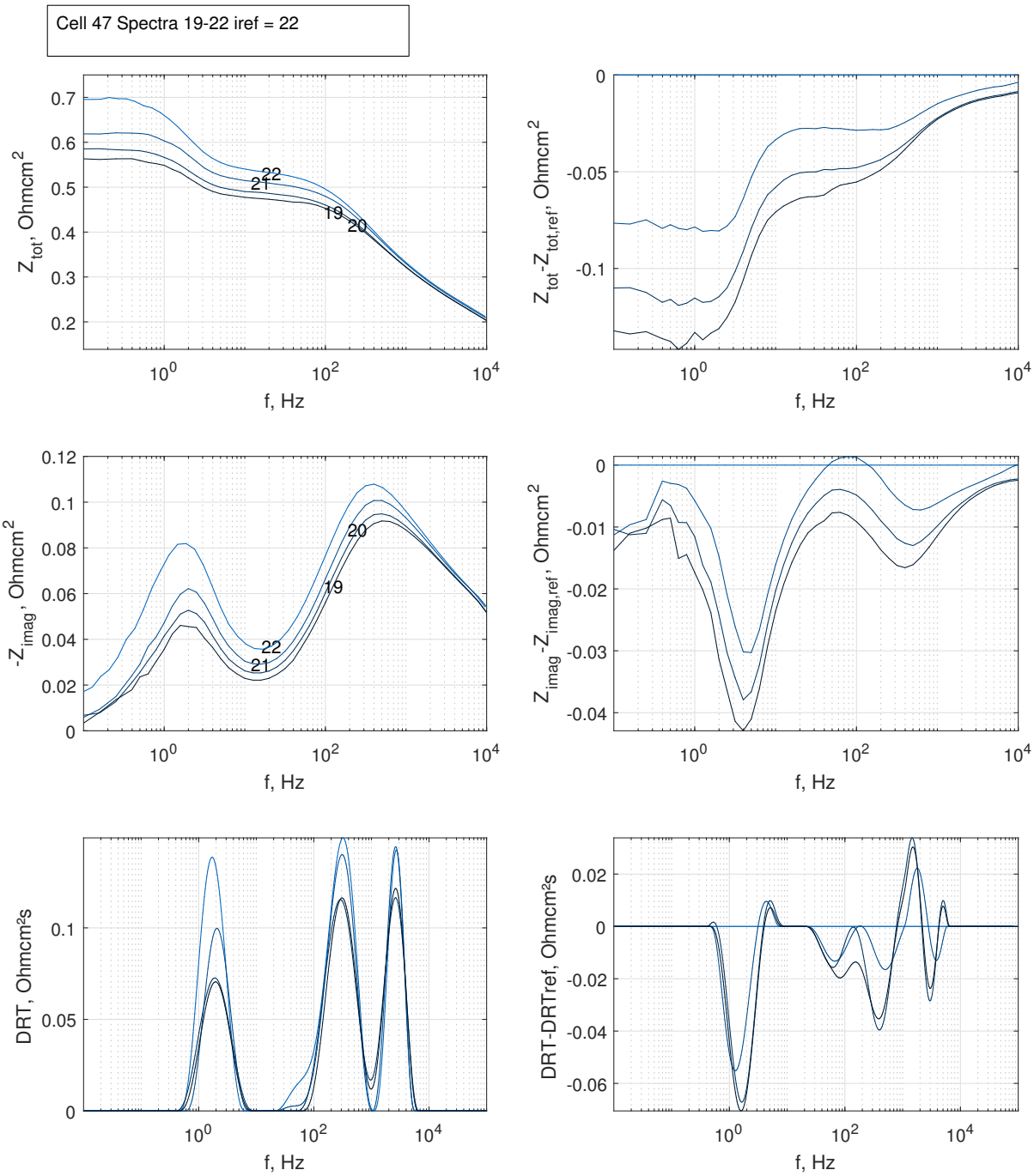

Figure C.8: Bode plots and DRT for variation of oxygen concentration at the cathode (Study *O2_H2*). Other operation conditions see Table 5.1. 19: 1 (0), 20: 0.75 (0.25), 21: 0.5 (0.5), 22: 0.1 (0) Nl/min O_2 (N_2). C47.